
Cavity Enhanced Detection of Cold Molecules

Von der Fakultät für Mathematik und Physik
der Gottfried Wilhelm Leibniz Universität Hannover

zur Erlangung des akademischen Grades
Doktor der Naturwissenschaften
Dr. rer. nat.

genehmigte Dissertation von

M. Sc. Jannis Schnars

- 1. Gutachterin:** Prof. Dr. Silke Ospelkaus
Institut für Quantenoptik
Leibniz Universität Hannover
- 2. Gutachter** Prof. Dr. Klemens Hammerer
Institut für Theoretische Physik
Leibniz Universität Hannover
- 3. Gutachter:** Prof. Dr. Guido Pupillo
Institute de Science et d'ingénierie Supramoléculaires
Université de Strasbourg

Tag der Promotion: 29.03.2022

Für Mattis

ABSTRACT

Cold quantum gases are versatile tools not only to investigate quantum many-body physics and ultracold chemistry, but also for testing fundamental theories. Many degenerate quantum gases, however, consist of atoms and provide only short-range interactions between different particles limiting research opportunities. Hence, shortly after the production of the first atomic gases an interest arose in ensembles of cold polar molecules that exhibit adjustable long-range anisotropic dipole-dipole interactions to expand research fields further. Loading such a molecular cloud into an optical lattice provides an excellent experimental control regarding particle-particle interactions and to simulate condensed matter physics.

Experiments with cold quantum gases require imaging techniques to determine properties like the number of atoms and molecules or the position of single particles. For atomic ensembles, absorption or fluorescence techniques are often utilised since atoms usually provide closed cycling transitions allowing to scatter a large number of photons for the imaging signal. The internal level structure of molecules, though, is more complex compared to atoms due to additional rovibrational states and many molecules do not provide closed cycling transitions. For these molecules new imaging techniques need to be developed.

In this thesis such a novel detection scheme for cold molecules is proposed. The presented method utilises dispersive light-matter interactions to scatter multiple photons even in the absence of closed cycling transitions. By using either large laser detunings or low powers, absorption can be suppressed during the detection of the particles. The imaging signal is enhanced by placing the molecules inside an optical cavity and a superposition of several transverse modes allows to detect single molecules spatially resolved. Finally, the imaging signal is measured by a homodyne detector.

In the first part of the thesis a theoretical background of the imaging technique is provided, starting with a classical approach. The advantages of a classical theory are an intuitive understanding of the detection method and an applicability to spherical nanoparticles, which can then be utilised as test objects for the proposed imaging scheme. The resolution capability of the detection technique is discussed and the important role of small cavity waists for high resolutions is highlighted. In a next step, a full quantum mechanical approach is presented and compared to the classical theory. It is shown that both theories are equivalent except for vacuum fluctuations, a pure quantum physical effect important to determine quantum noise correctly.

After introducing theoretical backgrounds, cavity geometries suitable for the detection of molecules are discussed. Properties, directly important for the imaging process, e. g. waist, mode number and linewidth, and technical aspects like misalignment sensitivity are taken into account. A simultaneous optimisation of all these properties is not possible since they are partially contradicting each other. However, a balance between these different aspects is found. Two cavity geometrics, feasible for imaging NaK molecules, a hemispherical resonator and a concentric cavity are proposed.

Finally, an experimental setup to demonstrate the general feasibility of the imaging technique is developed. Titania and silver are identified as materials for nanoparticles best suited to imitate NaK molecules. Imaging resonators are designed and an alignment procedure for these cavities is presented.

Keywords: molecules, imaging, optical resonators, transverse modes, resolution, dispersive light-matter interaction, cold quantum gases

ZUSAMMENFASSUNG

Kalte Quantengase ermöglichen die Erforschung von Quanten-Vielteilchensystemen und ultrakalter Chemie sowie die Verifizierung fundamentaler physikalischer Theorien. Viele entartete Quantengase bestehen aus Atomen und unterstützen lediglich kurzreichweitige Wechselwirkungen zwischen den einzelnen Teilchen. Schon kurz nach der Erzeugung erster atomarer Gase wuchs daher ein Interesse an Ensembles bestehend aus kalten polaren Molekülen, welche durchstimmbare langreichweitige anisotrope dipol-dipol Wechselwirkungen zwischen einzelnen Partikeln aufweisen und die Erforschung komplexerer Theorien ermöglichen. Wird eine entsprechende molekulare Wolke in ein optisches Gitter geladen, erlaubt dies eine exzellente Kontrolle der Wechselwirkungen zwischen verschiedenen Teilchen und ermöglicht es, kondensierte Materie gezielt nachzubilden.

Abbildungstechniken sind für die experimentelle Untersuchung von Quantengasen wichtig, um beispielsweise die Anzahl von Partikeln oder die Position von einzelnen Teilchen zu bestimmen. Für atomare Gase werden häufig Absorptions- oder Fluoreszenzverfahren verwendet, da Atome üblicherweise über geschlossene Übergänge verfügen, die es erlauben, mehrere Photonen an einem einzelnen Teilchen zu streuen. Für kalte Moleküle ist dies oft nicht möglich, da diese aufgrund einer komplexeren internen Zustandsstruktur meist über keine solchen geschlossenen Übergänge verfügen.

In dieser Arbeit wird eine neue Abbildungstechnik vorgestellt, welche sich auch für Moleküle eignet. Diese basiert auf dispersiven Licht-Materie Wechselwirkungen, um mehrere Photonen auch ohne geschlossene Übergänge streuen zu können. Absorption kann dabei durch größere Frequenzverstimnungen oder durch geringe Laserleistungen unterdrückt werden. Das Abbildungssignal wird durch einen Resonator verstärkt und mithilfe eines homodyn Detektors gemessen. Einzelne Moleküle können durch eine Überlagerung verschiedener transversaler Moden orts aufgelöst detektiert werden.

Zunächst werden die theoretischen Grundlagen des neuen Abbildungsverfahrens entwickelt, wobei zunächst ein klassischer Ansatz verfolgt wird. Ein Vorteil dieser klassischen Theorie ist ihre Anwendbarkeit auf Streuprozesse von sphärischen Nanopartikeln, wodurch diese als Testobjekte für die Detektionsmethode verwendet werden können. Ebenfalls wird das Auflösungsvermögen diskutiert, welches insbesondere von der Größe der Taille des Resonatorfeldes abhängt. Anschließend wird eine quantenmechanische Version der Theorie entwickelt und mit dem klassischen Ansatz verglichen. Dabei wird gezeigt, dass beide Theorien äquivalent sind, abgesehen von Vakuumfluktuationen, einem rein quantenphysikalischen Effekt, welcher für die korrekte Beschreibung quantenlimitierten Rauschens relevant ist.

Im Folgenden werden mögliche Resonatorgeometrien im Hinblick auf die Detektion kalter Moleküle diskutiert. Dabei werden Eigenschaften, die unmittelbar relevant für eine erfolgreiche Abbildung sind, z. B. Strahltaille, Modenanzahl und Linienbreite, und technische Aspekte, wie Robustheit gegenüber Fehljustage, berücksichtigt. Eine gleichzeitige Optimierung aller dieser Eigenschaften ist nicht möglich, da diese einander teilweise entgegenstehen. Ein Kompromiss zwischen diesen sich widersprechenden Aspekten wird vorgeschlagen. Es wird je eine hemisphärische und eine konzentrische Resonatorgeometrie bestimmt, welche für die Detektion von NaK Molekülen geeignet sind.

Im letzten Teil der Arbeit wird ein experimenteller Aufbau entwickelt, welcher geeignet ist, um die allgemeine Anwendbarkeit des Abbildungsverfahrens zu demonstrieren. Titanoxid und Silber werden als mögliche Materialien für Nanopartikel vorgeschlagen, um NaK Moleküle zu imitieren. Abbildungsresonatoren werden konzipiert und ein Justageverfahren für diese wird vorgestellt.

Schlagwörter: Moleküle, Abbildung, optische Resonatoren, transversale Moden, Auflösung, dispersive Licht-Materie Wechselwirkung, kalte Quantengase

Contents

1	Introduction	1
1.1	History	1
1.2	Imaging of cold quantum gases	2
1.3	The aim of the thesis	5
2	The Fundamentals of Gaussian Beams	7
2.1	Gaussian beams	7
2.2	Hermite-Gaussian modes	12
3	Optical Resonators	15
3.1	Two-mirror optical resonators	15
3.2	Ring resonators	21
4	Detection of Cold Particles - Classical Description	25
4.1	Interaction between a single particle and a paraxial beam	25
4.2	Multiple particles inside a multimode cavity	32
4.3	Homodyne Detection	34
4.4	Homodyne detection of particles inside an optical resonator	37
4.5	Resolution capability	39
5	Detection of Cold Particles - Quantum Description	43
5.1	Jaynes-Cummings Hamiltonian	43
5.2	Amplitudes of the cavity modes	46
5.3	Signal-to-noise ratio	48
5.4	Comparison of the classical and quantum mechanical model	51
6	Cavity Geometries for the Detection of Cold Particles	53
6.1	Stable resonators	54
6.2	Multimode resonators	55
6.3	Resonator waist	57
6.3.1	Near-concentric resonators	58
6.3.2	Near-confocal resonators	59
6.3.3	Near-hemispherical resonators	59
6.3.4	Paraxial approximation and maximum number of supported modes	60
6.4	Finitely sized resonator mirrors	60
6.4.1	Diffraction loss	60
6.4.2	Misalignment sensitivity	63
6.5	Cooperativity	66
6.6	Critical distance	67
6.6.1	Near-concentric resonators	68
6.6.2	Near-confocal resonators	68
6.6.3	Near-hemispherical resonators	69

6.7	Resonator geometries for imaging NaK molecules	69
6.7.1	Transitions in NaK molecules	69
6.7.2	Resonator properties	69
6.7.3	Near-concentric resonators	70
6.7.4	Near-confocal resonators	72
6.7.5	Near-hemispherical resonators	72
6.7.6	Other resonator geometries	73
6.7.7	Homodyne signal	74
7	Cavity Design for the Detection of Particles	77
7.1	Nanoparticles	78
7.2	Experimental setups for the detection of nanoparticles	81
7.2.1	Mode matching	81
7.2.2	Imaging resonators	83
7.2.3	Cavity alignment	85
7.2.4	Operating near-unstable cavities on the last stable mode	87
7.2.5	Experimental setup	91
8	Conclusion and Outlook	95
A	Mathematical transformations	99

List of Figures

1.1	1D optical lattice	2
1.2	Dispersive imaging	3
1.3	Molecular level structure	5
2.1	Gaussian beam	9
2.2	Optical rays	11
2.3	Hermite-Gaussian modes	13
3.1	Two-mirror cavity	16
3.2	Airy functions	21
3.3	Ring resonator	22
4.1	Coordinate transformation	27
4.2	Homodyne detection	35
4.3	Homodyne detection of molecules	38
4.4	Homodyne signals of a single particle	40
4.5	Homodyne signal of two particles and definition of the resolution capability	41
4.6	Resolution capability	42
6.1	Resonator stability diagram	55
6.2	Resonator spectra	56
6.3	Cavity waist-mirror parameter-diagram	58
6.4	Beam size at mirror-mirror parameter-diagram	62
6.5	Diffraction loss	63
6.6	Cavity linewidth broadening	64
6.7	Misaligned cavity	64
6.8	Misalignment sensitivity of cavities	65
6.9	Cooperativities of the concentric cavity	71
6.10	Cooperativities of the hemispherical cavity	72
6.11	1D homodyne signals of NaK molecules inside a concentric resonator	73
6.12	2D homodyne signal of s single molecule inside a concentric resonator	74
6.13	Homodyne signals for 6 particles inside an optical lattice	75
6.14	Homodyne signal with even mode orders	76
7.1	Cross sections of nanoparticles	79
7.2	Mode matching	83
7.3	Resonator design	84
7.4	Gimbal mount	85
7.5	Cavity pre-alignment	86
7.6	Cavity transmissions	87
7.7	Measurement of the cavity parameter product - theory	88
7.8	Measurement of the cavity parameter product - experimental data	89
7.9	Transmission spectra for different transverse modes	90

7.10 Proposed experimental setup for the detection of nanoparticles	92
A.1 Complex number - polar coordinates	103

Chapter 1

Introduction

1.1 History

In 1900, the physicist Max Planck derived the law of black-body radiation by introducing quantised energy packages [1]. This work also introduced the Planck constant h , one of the most fundamental physical constants, for the first time. Planck himself, however, was initially not convinced of a physical meaning behind his concept of discrete energy portions [2] and saw it more as a mathematical tool [3]. It was Albert Einstein who conceded a physical reality to quantised particles, by interpreting light as photons and, thus, explaining the photoelectric effect in 1905 [4]. These two groundbreaking works by Planck and Einstein are the starting point for all modern quantum theories. The existence of quanta allows to explain properties and effects that cannot be covered by classical theories and quantum physics has been applied to many fields of science, e. g. chemistry [5], medicine [6] or engineering [7]. Quantum optics [8] is an important field utilising quanta to describe interactions between matter and light. To govern these interactions correctly, a quantisation of field theories is necessary. This quantisation was first done by Paul Dirac in 1927 [9] and further developed in the following decades, e. g. in [10, 11, 12]. In combination with technical innovations like lasers [13], quantum optical theories opened a whole new set of research fields.

One of these research fields relates to (ultra-)cold quantum gases, which typically consist of particles at temperatures in the range of nK or μ K and allow to investigate quantum many body problems [14] and condensed matter physics [15] or may serve as quantum simulators [16]. Important requirements for experiments in the field of quantum gases are cooling and storing methods for atoms, the first of these techniques demonstrated was Doppler cooling in 1978 [17]. Further historical milestones were Zeeman deceleration [18], evaporative cooling [19], magneto-optical traps [20] and optical molasses [21]. Finally, the breakthrough was the realisation of the first Bose-Einstein condensates [22, 23], an exotic state of matter already predicted by Einstein in 1925 [24, 25] relying on a work from Bose [26], where a large fraction of bosonic atoms occupy the absolute ground state. Shortly after, quantum degenerate Fermi gases were also realised [27]. The capability to produce these quantum states of matter leads to an extensive growth of the research field of quantum gases and enabled physicists to investigate many quantum phenomena and properties experimentally, like quantum phase transitions [28, 29], Sakharov oscillations [30] or superconductivity [31].

The first produced cold quantum gases consisted of atoms, which often provide only short interparticle interaction length and, thus, limited research opportunities. Hence, shortly after the production of the first quantum gases, an interest arose for quantum gases to provide long range anisotropic dipole-dipole interactions between particles [32], which would allow to investigate a broader research field [32, 33]. For example, atom species like Chromium [34], Dysprosium [35] and Erbium [36] provide a permanent dipole moment and, therefore, facilitate the existence of dipolar quantum gases. However, the dipole moments of these

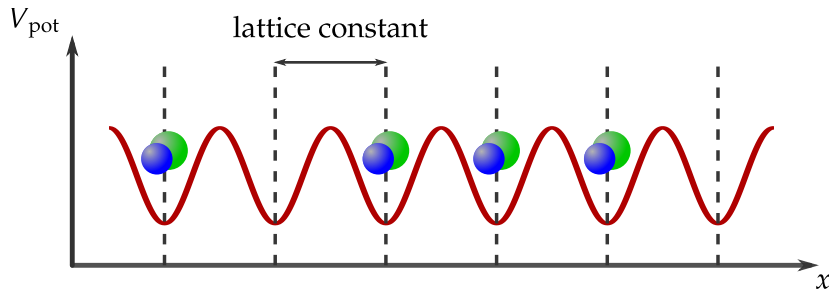


Figure 1.1: One dimensional optical lattice along the x -direction. A periodic potential V_{pot} captures atoms or molecules at discrete positions, which are called the lattice sites. Not all sites are necessarily occupied by a particle. The distance between two adjacent sites is called the lattice constant.

atoms are too weak to investigate contact interaction forces or to overcome the spacing between the sites of most utilised optical lattices [37] and particles with stronger dipole moments are desired.

Possible candidates for strong long-range interactions are heteronuclear polar molecules, which are able to exceed the strength of atomic dipole moments by magnitudes [38]. Additionally, the dipole moment of these molecules is induced by external electric fields and, therefore, the interaction strength can be adjusted as desired [39]. Furthermore, polar molecules also exhibit rotational and vibrational quantum states [39] and this complex level structure expands the research fields of fundamental theory testing, ultracold chemistry or new many-body quantum phases in comparison to atoms [40]. However, the rovibrational states make it also more difficult to handle these molecules experimentally. Especially, direct cooling is not feasible for molecules, except for some few species, e. g. [41, 42]. Therefore, the standard procedure to produce ultracold polar molecules is to cool both atom species of the molecule separately and then combine them to a weakly bound molecule through a so called Feshbach resonance [43]. Subsequently, these Feshbach molecules are transferred into the ground state by applying a Stimulated Raman Adiabatic Passage (STIRAP) [44], thus enabling the creation of quantum gases with high phase-space densities [45].

1.2 Imaging of cold quantum gases

Parallel to the feasibility to produce cold quantum gases a necessity for imaging techniques, which allow to determine properties like temperature or the number of particles, arose. Especially, imaging techniques are necessary to measure the density of the gaseous clouds or the position of single particles. The latter is important for atoms or molecules loaded into an optical lattice [46] that allows, for example, to simulate condensed matter systems [16] and to experimentally control the particles effectively. An optical lattice is a periodic potential allowing to trap particles at different potential minima, also called lattice sites, by applying a dipole force to the atoms or molecules [46], see figure 1.1. Therefore, optical lattices allow to arrange cold particles periodically and, thus, imitating solids. The spacing between two adjacent sites, in the following also called lattice constant, is equal to $\frac{\lambda}{2}$, where λ is the wavelength of the lasers forming the lattice [47]. The lattice constant is often set to 532 nm [48, 49]. Resolving particles in an optical lattice is an important obstacle that needs to be overcome by imaging techniques applied to quantum gases in such lattices to detect single atoms or molecules.

All measurement techniques for quantum gases rely on the interaction with light. The interaction of a photon with an atom or molecule can be divided into three processes, which are absorption, emission and a phase shift [50]. For absorption, the photon is annihilated and

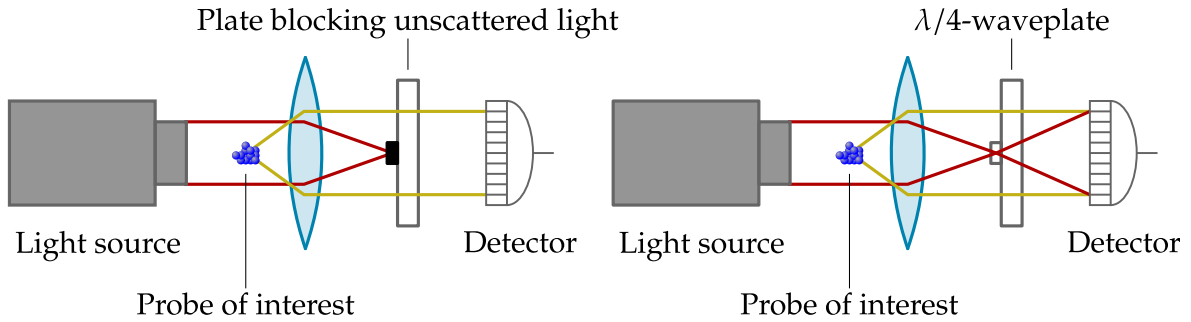


Figure 1.2: Schematic representation of the two most common dispersive imaging techniques. The left side illustrates dark ground imaging, while the right side shows phase contrast imaging. Both methods appear to be similar, the only difference is that the unscattered light in the case of dark ground imaging is blocked, while it is shifted in phase for phase contrast techniques. However, the difference in the signal quality is significant since the overlap with the unscattered beam leads to improved signals for small phase shifts for phase contrast imaging.

the particle enters an excited state with a higher energy than before, while emission is the opposite process, where a photon is created and the particles energy is reduced. Finally, the phase of the light can be shifted through the interaction with matter. The first two processes are classified as absorptive, while phase shifts are considered as dispersive interactions.

The imaging techniques for the first created Bose-Einstein condensates were based on absorptive imaging [22, 23], where quantum gases are illuminated with a light beam and the shadow cast is measured with a detector, e. g. a CCD camera [50]. In comparison, fluorescence imaging methods collect and detect photons emitted by the probe of interest. Since photons are randomly emitted into an arbitrary direction and imaging systems are limited by numerical apertures, only a fraction of all photons can be detected and, thus, fluorescence signals are usually considered to be weaker than absorption imaging techniques [50]. However, fluorescence imaging is often background free, which is in turn an advantage [50].

Dispersive imaging methods, i. e. techniques that utilise the induced phase shift, can be separated into two categories, dark ground and phase contrast imaging. Both handle the light not scattered by the quantum gas differently [50]. Both methods are schematically depicted in figure 1.2. In dark ground techniques, the unscattered light is simply blocked and only photons that have dispersively interacted with the probe of interest are detected. In contrast to this, phase contrast imaging [51] schemes utilise the unscattered light by shifting its phase by $\pm\frac{\pi}{2}$ and overlapping it with the scattered field, which provides improved signal quality for small phase shifts in comparison to dark ground imaging [50].

Dispersive imaging methods may utilise the phase shift of the light in different ways. For example, a cloud of cold particles refracts a light beam like a lens. If the beam is detected, conclusions can be drawn regarding the quantum gases properties. Another possibility to image cold quantum gases dispersively is polarisation imaging, applied e. g. in [52]. These techniques gain their information regarding the quantum gases properties by the interaction of light with anisotropic matter, where different polarisation directions experience different phase shifts.

Atomic quantum gas experiments often utilise absorption imaging [23, 22, 27, 53, 54] or fluorescence imaging [55]. Especially fluorescence imaging is often used to detect atoms single-site resolved inside an optical lattice, e.g. [56, 57, 58, 59, 60]. Absorption and fluorescence imaging were also modified to improve resolution, e. g. in [61] an optical pumping lattice was utilised for this purpose. Dispersive techniques have, for example, been demonstrated with dark field [62, 63], holography [64, 65] and Faraday imaging methods [66, 67].

An important figure of merit is the destructiveness for the respective method, i. e. how much the quantum gas properties are disturbed by the imaging process. For example absorption and emission automatically apply a momentum to the particle and, thus, are effectively increasing the kinetic energy of the atom or molecule subsequently leading to higher temperatures of particle clouds. Therefore, absorption and fluorescence imaging are usually considered as destructive.

A dispersively scattered photon does not change the quantum state of motion of the particle and, therefore, dispersive interactions are more suitable for non-destructive imaging than absorption of fluorescence methods. However, it is important to note that dispersive imaging schemes are not non-destructive in general. Even if only the phase shift is utilised to gain information, one or multiple photons can still be absorbed during the detection process leading to destructive behaviour. For example, dispersive imaging methods have no advantage for quantum gases with small optical densities compared to absorption imaging regarding its destructive nature [50].

While there is a large number of established imaging techniques for atomic quantum gases, there is still a lack of satisfying detection schemes for polar molecules. Atoms can be approximated as two-level systems with a ground and excited state and after absorbing a photon the atom will decay back into the ground state by reemitting another light quanta. Such a system provides a closed cycling transition, i. e. the process of absorption and emission can be repeated many times and, thus, increasing the number of scattered photons improving the signal strength. However, most molecules do not have such closed cycling transitions due to their rovibrational level structure, which is depicted in figure 1.3. An absorption process excites the molecule to an excited electronic state and, subsequently, the molecule can decay back into many rovibrational states of the electronic ground state as indicated by the arrows in the figure. This limits the number of absorbed and reemitted photons drastically since the process cannot be repeated after the molecule has entered an unknown state. Due to the large number of rovibrational states, this also cannot be compensated for by repumping lasers as sometimes utilised for atoms. In conclusion, the lack of closed cycling transitions make absorption and fluorescence imaging unsuitable for many molecules.

It should be noted that there are some molecules providing nearly closed cycling transitions [68, 69], which are the molecules that are directly laser coolable, e. g. CaF and SrF [38]. Though for these species, absorption or fluorescence imaging, as done in [70], can be applied, molecules with nearly closed cycling transitions are rare and more universal imaging techniques are favourable. Early molecular quantum gases were imaged through ionisation [71, 72] and absorption imaging with a small number of scattered photons has also been demonstrated [73]. Maybe the most common method to detect polar molecules without closed cycling transitions is to reverse the production process and disassemble the molecule into its constituting atoms, which can then be imaged using established techniques [45, 74, 75]. However, all these methods are highly destructive.

Several dispersive imaging techniques have been proposed and demonstrated for non-destructive detection of cold molecules. Vacuum Rabi splitting (VRS) and electromagnetically induced transparency has been suggested in [76] to measure the number of molecules of a quantum gas and VRS was successfully demonstrated [77]. For the detection of single molecules optical birefringence induced by excited rotational states [78] and Faraday imaging [79] have been proposed, but both techniques have unsuitable signal-to-noise ratios [78, 79]. So far no imaging technique is universally applicable to molecules and able to resolve single particles without destroying the molecule.

As previously explained, the absence of closed cycling transitions makes dispersive interactions more suitable for the detection of cold molecules. However, if only a single photon is absorbed the molecule might enter an unknown state and the imaging process

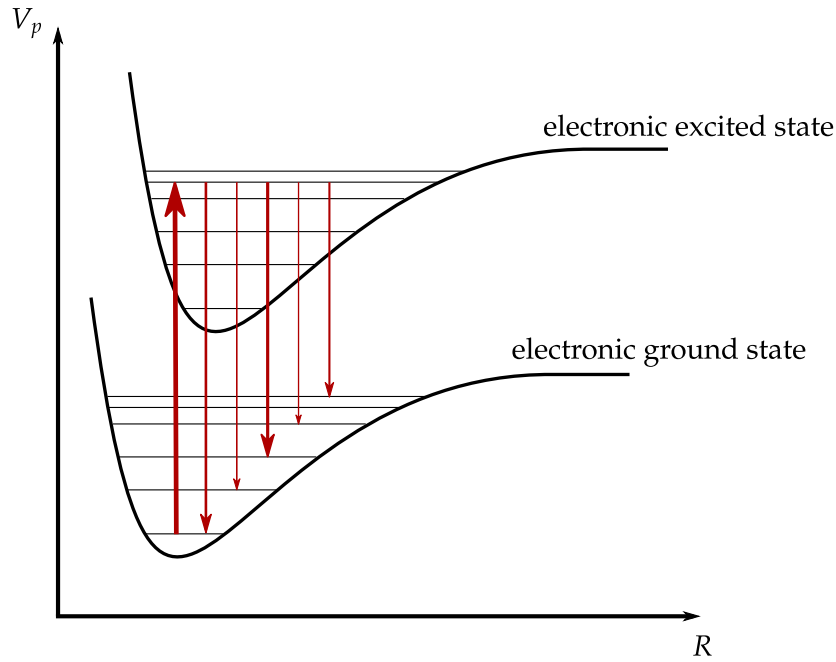


Figure 1.3: Schematic representation of the state structure of a cold molecule consisting of two atoms. The figure depicts the molecular potential depending on the distance between the cores of the atoms, where the curved lines indicate the electronic ground, and an arbitrary electronically excited state. Both states have a set of sub-levels representing possible rotational and vibrational states. If a photon is absorbed from the ground to the excited state, the molecule can decay back into several rovibrational levels of the ground state, as indicated by the arrows. The different sizes of the arrows imply that the transition probability is in general different for the various rotational and vibrational states.

is interrupted. Hence, it must be ensured that the probability of a photon to be scattered dispersively is significantly higher than being absorbed. This can be done by applying a laser beam with a relatively large detuning, i. e. the frequency of the laser is slightly shifted in comparison to the resonance frequency of the molecules transition [80, 8].

Another obstacle for dispersive imaging techniques are weak signals, which can be solved by placing the molecules inside an optical resonator to enhance the signal strength. If the resonator also supports multiple transverse modes simultaneously, the superposition of these modes allows to detect the molecule spatially resolved. Transverse modes with higher orders carry more momentum that can be utilised to improve the resolution of the imaging scheme [81]. Since the phase shift induced by single molecules through dispersive interaction is usually small, phase contrast methods are more suitable than dark ground techniques. Phase contrast imaging can be realised with a homodyne detector [50].

1.3 The aim of the thesis

The aim of this thesis is to develop and investigate an imaging scheme applicable for cold molecules relying on the ideas given at the end of the preceding section. For this purpose the thesis is organised as follows:

In chapter 2 and 3 literature reviews of Gaussian optics and optical resonators are provided. Expressions for Gaussian beams and higher-order Hermite-Gaussian modes are derived and the propagation of these beams through optical systems is explained. Stability criteria, resonance frequencies, beam shapes and cavity linewidths of two-mirror and ring resonators are discussed.

The concepts from these two chapters are then applied in chapter 4 and 5 to develop a theoretical background for the imaging technique. The focus in chapter 4 is set on an intuitive classical approach that also governs other objects beside molecules that scatter light in form of dipole radiation like nanoparticles. The theory presented in this chapter covers the aspects of light-molecule interaction, cavity optics and the homodyne detection scheme. Finally, simulations of the imaging signals are provided and the resolution capability is discussed. In the fifth chapter, the interaction between molecules and light inside a resonator is treated quantum mechanically to include vacuum fluctuations into the imaging theory. At the end of chapter 5 the quantum mechanical and classical theories are compared and it is shown that both are equivalent, apart from these vacuum fluctuations.

In chapter 6, cavity configurations suitable for the detection of cold molecules are discussed. Properties relevant for the imaging like multimode regimes and small cavity waists, are taken into account and the effects of technical aspects like finite mirror sizes and misalignment sensitivity are explained. Finally, two cavity configurations applicable for the detection of single molecules inside an optical lattice are presented. These resonators are designed to resolve sodium-potassium (NaK) molecules inside an optical lattice with periodicity of 532 nm as provided in experiments of the POLAR group at the Leibniz University Hanover [75].

In chapter 7 these theoretical resonator concepts are translated in technical feasible designs and nanoparticles are introduced as possible test objects to simulate cold molecules. An alignment concept for the cavity is explained and an experimental setup to test the imaging technique is developed.

The last chapter of this thesis ends with a summary and an outlook of future steps.

Chapter 2

The Fundamentals of Gaussian Beams

This chapter provides a brief overview of the properties of Gaussian beams. These beams are an important concept in the field of optics since they describe light fields emitted by many lasers and optical cavities. Gaussian beams play a fundamental role for the molecular detection scheme introduced in this thesis. The described concepts follow the established literature, see e.g. [82], [83] and [84] for more details.

The first section of this chapter introduces the origin and properties of the most basic Gaussian modes, often referred to as fundamental modes. A short derivation of the wave equation for electromagnetic radiation is given. For this derivation the paraxial approximation is used. The last part of the first section discusses the validity of this approach. The second section introduces the rule of propagation of Gaussian beams through space and optical systems. Furthermore, the beam parameter product and its consequences for the beam waist and far-field angle are explained. The last section of this chapter generalises Gaussian beams into a broader set of transverse light fields with a particular focus on Hermite-Gaussian modes.

2.1 Gaussian beams

The whole field of electrodynamics can mostly be described by a set of four coupled differential equations, known as the Maxwell's equations [85]. In particular, these equations reveal a coupling between electric and magnetic fields. Temporal changes in one of those fields lead to spatial alterations within the other field and vice versa. Maxwell's equations allow the derivation of electromagnetic waves or radiation, where oscillating electric and magnetic fields propagate through space. The following wave equation for electric fields \vec{E} can be derived from Maxwell's equations [82]:

$$c^2 \Delta \vec{E}(x, y, z, t) = \frac{\partial^2 \vec{E}(x, y, z, t)}{\partial t^2}, \quad (2.1)$$

where c is the vacuum speed of light and Δ is the Laplace operator. x, y, z are the spatial coordinates, while t is the time. The following ansatz for the electric field \vec{E} can be used assuming that time and space coordinates are separable

$$\vec{E}(x, y, z, t) = \vec{e} \psi(x, y, z) \exp(i\omega t). \quad (2.2)$$

\vec{e} is the unity polarisation vector, ω is the angular frequency of the radiation and $\psi(x, y, z)$ is a complex amplitude summarising all spatial terms. Inserting equation 2.2 into equation 2.1 leads to the Helmholtz equation

$$\Delta \psi(x, y, z) = -k^2 \psi(x, y, z) \quad (2.3)$$

that exploits the dispersion relation of light $\omega = ck$, with k being the wavenumber. An ansatz to solve the differential equation above is to separate the propagation factor $\exp(-ikz)$ from the amplitude

$$\psi(x, y, z) = a(x, y, z) \exp(-ikz). \quad (2.4)$$

This form divides the amplitude into two parts, one describing a harmonic oscillation, the other, a yet unknown amplitude $a(x, y, z)$, describing the field pattern of the mode. In particular, the amplitude contains information about the field distribution in planes perpendicular to the direction of propagation z . These patterns are also called transverse profiles. Substituting the new ansatz from equation 2.4 into the Helmholtz equation 2.3 yields

$$\Delta a(x, y, z) - 2ika(x, y, z) = 0. \quad (2.5)$$

A slow variation of the transverse profile over the distance of one wavelength λ along the direction of propagation, which is known as the paraxial approximation, is assumed [82]

$$\left| \frac{\partial^2 a}{\partial z^2} \right| \ll \left| 2k \frac{\partial a}{\partial z} \right|, \left| \frac{\partial^2 a}{\partial x^2} \right|, \left| \frac{\partial^2 a}{\partial y^2} \right|. \quad (2.6)$$

By dropping the second derivative in z equation 2.5 reduces to the paraxial Helmholtz equation [84]

$$\Delta_t a(x, y, z) - i2k \frac{\partial a(x, y, z)}{\partial z} = 0. \quad (2.7)$$

Δ_t is the transverse Laplace operator, only taking into account derivatives orthogonal to the direction of propagation. A trial solution of this equation is

$$a(x, y, z) = a_1(z) \exp\left(-ik \frac{x^2 + y^2}{2q(z)}\right), \quad (2.8)$$

where $q(z)$ is a complex number and $a_1(z)$ is a yet unknown function. Inserting this ansatz into the paraxial Helmholtz equation provides

$$\begin{aligned} \psi(x, y, z) &= a(x, y, z) \exp(-ikz) \\ &= \sqrt{\frac{2}{\pi}} \frac{1}{w(z)} \exp\left(-\frac{x^2 + y^2}{w^2(z)}\right) \exp\left(-ikz - ik \frac{x^2 + y^2}{2R(z)} + i\zeta(z)\right). \end{aligned} \quad (2.9)$$

Chapter 16 and 17 of [82] contain a detailed derivation of this equation representing the mathematical expression of a Gaussian beam. Gaussian beams combine properties of ray and wave optics and are often used to describe the output radiation of lasers. The yet undefined expressions in equation 2.9 are

$$\text{beam radius} \quad w(z) = w_0 \sqrt{1 + \left(\frac{z}{z_R}\right)^2}, \quad (2.10)$$

$$\text{curvature of the phase front} \quad R(z) = z \left(1 + \left(\frac{z_R}{z}\right)^2\right), \quad (2.11)$$

$$\text{Gouy phase} \quad \zeta(z) = \arctan\left(\frac{z}{z_R}\right) \quad (2.12)$$

$$\text{and beam waist} \quad w_0 = \sqrt{\frac{\lambda z_R}{\pi}}. \quad (2.13)$$

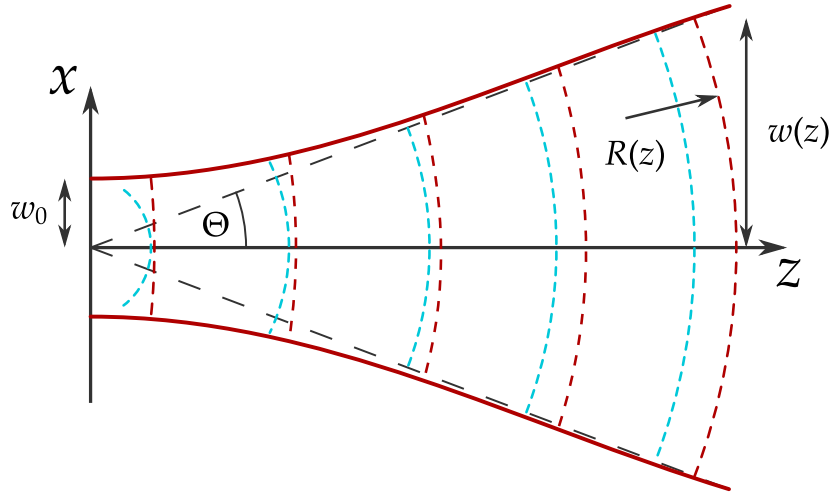


Figure 2.1: Representation of a Gaussian beam in the x - z -plane. The red lines indicate beam size (solid) and phase fronts (dashed) of the beam. For long propagation distances, the size increases approximately linearly and the shape of the wavefront becomes spherical. The blue dashed lines indicate phase fronts of spherical waves centred at the origin of the Gaussian beam. The Gouy phase shift leads to forward shifted phase fronts of the Gaussian beam in comparison to the spherical waves.

The smallest radius of the Gaussian beam is the beam waist. z_R is the Rayleigh range, i.e. the distance along the direction of propagation doubling the spot size of the beam. Figure 2.1 visualises a Gaussian beam in the x - z -plane. For a deeper understanding of Gaussian beams, some physical properties are highlighted here. As before, z is defined as the direction of propagation of the wave. The position of the waist is set as $z = 0$. At this point, the phase front of the Gaussian beam is plane. During propagation the radius $R(z)$ shrinks to $2z_R$ at $z = z_R$ before increasing again. Equation 2.9 also reveals that the field of an ideal Gaussian beam never drops to zero within a transverse plane since the field distribution is given by a Gaussian profile. Hence, handling beam sizes is not straightforward, since several different definitions for the beam radius are common. Here it is defined as the radius at which the intensity has dropped to $1/e^2$ of its maximum value [83]. Furthermore, for $z \gg z_R$, the beam size increases approximately linearly. This allows to define the far field angle or angle of divergence Θ . Usually Θ is small, otherwise the paraxial approximation would be violated, as explained at the end of this section.

In equation 2.9 three different phase terms can be distinguished. The $-ikz$ -term is the phase of a plane wave travelling along its optical axis, whereas the profile of the phase front is described by the $-ik\frac{x^2+y^2}{2R(z)}$ -term. At first, the last term governing the Gouy phase shift $\zeta(z)$ seems unintuitive. In 1890, the French physicist Louis G. Gouy discovered this effect [86], leading to a phase shift from $-\pi/2$ at $z \rightarrow -\infty$ to $\pi/2$ at $z \rightarrow \infty$. The Gouy phase originates from the uncertainty principle [87]. A strongly focused light field, like the waist of a Gaussian beam, leads to an uncertain value for the transverse momentum. This results in a locally increased phase velocity and wavelength and eventually into the above mentioned phase shift.

Since some physical values of Gaussian beams depend on each other, the set of quantities defining a Gaussian beam completely needs to be specified. First, the direction of propagation is mandatory and is set to be the z -axis for this thesis. Furthermore, the position of the waist needs to be known. In combination with the wavelength and the waist, the Gaussian beam is fully determined. A single complex number allows to express the properties of a

Gaussian beam at any point in space, if these four values are known. This quantity is called the complex beam parameter [84] and is defined as

$$q(z) = z + iz_R. \quad (2.14)$$

The reciprocal of the complex beam parameter directly reveals the radius of curvature of the phase front and the beam size since both values are connected to the real and imaginary part of the inverse of $q(z)$:

$$\frac{1}{q(z)} = \frac{1}{R(z)} - i \frac{\lambda}{\pi w^2(z)}. \quad (2.15)$$

The complex beam parameter is identical to the complex number $q(z)$ in equation 2.8. It allows to express the propagation and transformation of Gaussian beams through optical systems in a very elegant and simple way, see chapter 2.1.

To apply the theory of Gaussian beams correctly, it is important to know in which cases the paraxial approximation is valid. The following passage is based on chapter 16.1 in [82]. An optical field can be written as a superposition of plane waves travelling along the optical axis with different angles Θ . In the paraxial approximation such a wave can be expressed as

$$E(x, z)a(x, z) \exp(-ikz) \approx \exp\left(-ik\Theta x + ik\frac{\Theta^2 z}{2}\right). \quad (2.16)$$

Without loss of generality, a wave in the x - z -plane is assumed here and the wave is propagating along the z -axis. For the first derivative of $a(x, z)$ in the z -direction and the second derivatives in x - and z -direction it follows

$$-i \frac{2k}{a} \frac{\partial a}{\partial z} \approx k\Theta^2, \quad (2.17)$$

$$\frac{1}{a} \frac{\partial^2 a}{\partial x^2} \approx -k^2 \Theta^2, \quad (2.18)$$

$$\frac{1}{a} \frac{\partial^2 a}{\partial z^2} \approx -k^2 \frac{\Theta^4}{4}. \quad (2.19)$$

For the paraxial approximation to be true, the last term must be significantly smaller than the terms above. This is the case for a Θ below 0.5 rad or 30°. Hence, the derivations above remain valid as long as the far field angles do not exceed this threshold.

Propagation of Gaussian beams through optical systems

Propagation through space and optical systems changes the properties of Gaussian beams, like beam size and phase front. Therefore, it is important to know how these alterations can be expressed mathematically. Ray transfer matrices are a possible tool for this purpose [82, 83, 84]. Often rays can be used to describe the propagation of light in a very simple, yet effective way. A ray is a straight line. The model considering light as rays, is called geometrical optics. Geometrical optics describes a beam by its distance h from the optical axis and the angle φ between this axis and the ray, see figure 2.2. An optical system consists of several optical elements separated by finite distances. These elements are either reflective surfaces or boundaries between materials with different indices of refraction. When encountering an optical system, the ray will change its distance and angle to the optical axis. If only paraxial rays, i.e. rays close to the optical axis, with angles small enough for the validity of the small-angle approximation $\sin(\varphi) \approx \varphi$ contribute to the beam, the connection

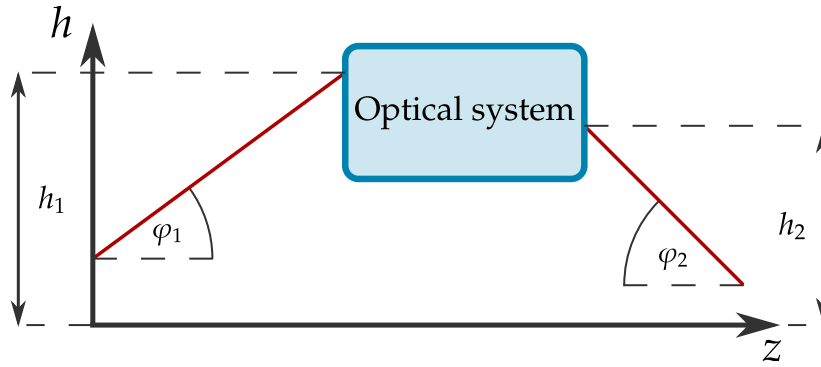


Figure 2.2: The distance h from the optical axis z and the angle φ define an optical ray. Propagation through an optical system changes both parameters.

between distance and angle before (index 1) and behind (index 2) the optical system is given by a system of linear equations:

$$h_2 = Ah_1 + B\varphi_1, \quad (2.20)$$

$$\varphi_2 = Ch_1 + D\varphi_1. \quad (2.21)$$

This equation system can be expressed using vectors and a matrix

$$\begin{pmatrix} h_2 \\ \varphi_2 \end{pmatrix} = \begin{pmatrix} A & B \\ C & D \end{pmatrix} \begin{pmatrix} h_1 \\ \varphi_1 \end{pmatrix}. \quad (2.22)$$

The matrix in the equation above is a ray transfer matrix or ABCD matrix. The ray transfer matrix of an arbitrary optical system is the product of the ABCD matrices of the elements the system consists of. For example, the matrix of a thick lens comprises three components namely, two curved surfaces and the distance between them. To receive a proper result, it is necessary to obtain a correct order of the components, as the commutative property does not hold for matrices in general. Therefore, the correct order of the components for the ray transfer matrix of a thick lens during beam propagation is firstly a curved surface, then the propagation between the interfaces and lastly the second surface. Ray transfer matrices are a powerful tool since even complicated systems can be represented by a product of a small set of matrices. The matrices of common optical elements and systems can be found in the literature, e.g. [83].

Furthermore, ray transfer matrices allow to describe the propagation of Gaussian beams through optical systems. The transformation law is expressed as

$$q_2 = \frac{Aq_1 + B}{Cq_1 + D}. \quad (2.23)$$

This equation is known as the ABCD law [83]. q_1 and q_2 are the complex beam parameters in front of and behind the optical system, respectively. Since often the reciprocal of the beam parameter is used, it might be helpful to provide the corresponding expression as well:

$$\frac{1}{q_2} = \frac{C + \frac{D}{q_1}}{A + \frac{B}{q_1}}. \quad (2.24)$$

Another important property of Gaussian beams is the beam parameter product

$$w_0\Theta = \frac{\lambda}{2}. \quad (2.25)$$

Since the wavelength λ is constant for a monochromatic Gaussian beam, decreasing the waist automatically leads to an increase of the far field angle and vice versa. The beam parameter product can be seen in the context of the uncertainty principle. If the waist (and by this the position) is defined very well, information regarding the wavenumber (i. e. the momentum) is uncertain. Since the product of the waist and the far field angle is a constant, the beam parameter product of a Gaussian beam cannot be changed by propagating through any optical system. Therefore, it is not possible to generate a Gaussian beam with an arbitrarily precise waist that is also collimated. The consequences for the detection scheme discussed in this thesis are severe (see chapter 6).

2.2 Hermite-Gaussian modes

The Gaussian beam is not the only solution of the paraxial Helmholtz equation. Indeed, the number of modes solving this equation is infinite. Depending on the symmetry of the system, different sets of solutions are used. Either Hermite-Gaussian modes for rectangular cases or Laguerre-Gaussian modes for circular ones. In fact, there is even a more general third family called Ince-Gaussian modes that contains Hermite-Gaussian and Laguerre-Gaussian modes as special cases [88].

Since the optical lattice containing the cold molecules imprints a rectangular symmetry to the system, this chapter concentrates on Hermite-Gaussian modes. These modes are given by [82]

$$\begin{aligned} \psi_{nm}(x, y, z) &= \sqrt{\frac{1}{2^{n+m}n!m!}} \sqrt{\frac{2}{\pi w^2(z)}} H_n\left(\sqrt{2}\frac{x}{w(z)}\right) H_m\left(\sqrt{2}\frac{y}{w(z)}\right) \exp\left(-\frac{x^2 + y^2}{w^2(z)}\right) \\ &\quad \cdot \exp\left(-ikz - i\frac{k(x^2 + y^2)}{2R(z)} + i(n + m + 1) \arctan\left(\frac{z}{z_R}\right)\right) \\ &= C_N H_n\left(\sqrt{2}\frac{x}{w(z)}\right) H_m\left(\sqrt{2}\frac{y}{w(z)}\right) \exp\left(-\frac{x^2 + y^2}{w^2(z)}\right) \\ &\quad \cdot \exp\left(-ikz - i\frac{k(x^2 + y^2)}{2R(z)} + i(n + m + 1) \arctan\left(\frac{z}{z_R}\right)\right), \end{aligned} \quad (2.26)$$

where $C_N = \sqrt{\frac{1}{2^{n+m}n!m!}} \sqrt{\frac{2}{\pi w^2(z)}}$ is a normalisation factor. $H_n\left(\sqrt{2}\frac{x}{w(z)}\right)$ and $H_m\left(\sqrt{2}\frac{y}{w(z)}\right)$ are Hermite polynomials. A recurrence formula defines these polynomials by [84]

$$H_{j+1}(t) = 2tH_j(t) - 2jH_{j-1}(t), \quad (2.27)$$

$$H_0(t) = 1, \quad (2.28)$$

$$H_1(t) = 2t, \quad (2.29)$$

where j is the order of the Hermite polynomial. In equation 2.26 n and m are the orders of the x - and y -directions, respectively. For $n = m = 0$ equation 2.26 reduces to the Gaussian beam from equation 2.9. Hence, the 00-mode is also called the fundamental mode. Equation 2.26 also reveals that all Hermite-Gaussian modes share a parabolic wavefront with an identical radius of curvature $R(z)$. The Gouy phase increases with the total order $n + m$ of the corresponding Hermite-Gaussian mode. Furthermore, the Hermite polynomials modulate the intensity profile of the Gaussian beam significantly. The intensity profiles for lower order modes are shown in figure 2.3. Note that the shape of the profiles is independent of the position along the optical axis and scales with the beam size $w_{00}(z)$ of the fundamental

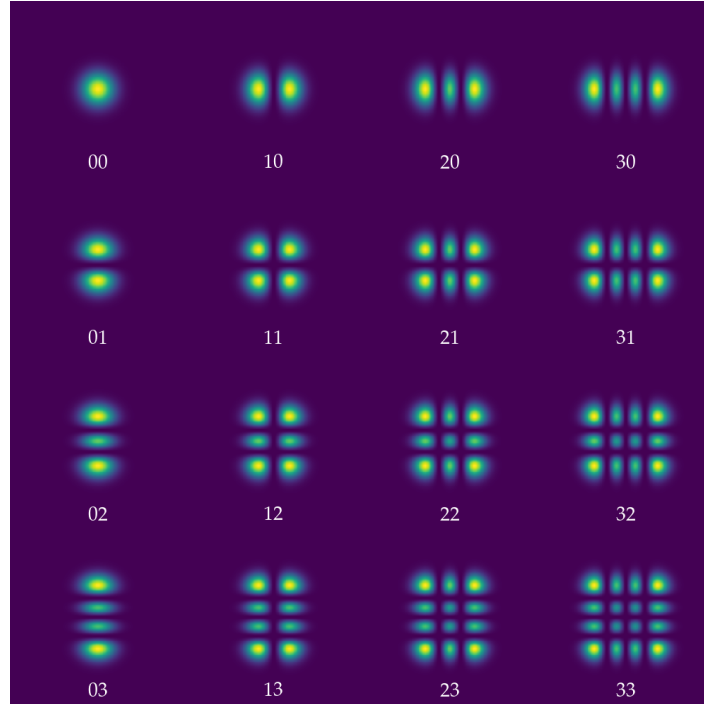


Figure 2.3: Intensity profiles of some Hermite-Gaussian modes. The numbers below each mode refer to the orders in x - and y -direction, respectively.

mode. Equation 2.26 also shows that the beam size $w_m(z)$ and the angle of divergence Θ_m of higher order Hermite-Gaussian modes are magnified in comparison to the fundamental mode. However, different sources use different definitions for these radii and angles. In [89] the beam size is defined as twice the variance of x or y in a plane transverse to the optical axis resulting in

$$w_m(z) = \sqrt{2m + 1}w(z), \quad (2.30)$$

$$\Theta_m = \sqrt{2m + 1}\Theta. \quad (2.31)$$

Different sources also utilise other definitions for the beam size, leading to alternative factors of probability between fundamental and higher order modes, e. g. \sqrt{m} [82, 90]. In this thesis, the definition of twice the variance is used since this concept predicts larger beam sizes. Later, it will be shown that the beam size is important for the number of modes supported by a cavity, see chapter 4. A convention predicting larger beam sizes is favourable to reduce the probability to overestimate the number of modes supported by a resonator.

Due to their increased beam sizes higher-order modes add an additional factor in the beam parameter product, known as the propagation factor M^2 [83]. The maximum of this propagation factor is determined by the highest order mode of a light field $M_{max}^2 = 2m_{max} + 1$. In the case of a rectangular symmetry, two M^2 values exist for both directions perpendicular to the optical axis. In combination with the propagation factor, the beam parameter product takes the form

$$w_{0,m}\Theta_m = M^2 \frac{\lambda}{2}. \quad (2.32)$$

Hermite-Gaussian modes also have another important property. All orders share the same complex beam parameter q [90] that is defined by the waist and wavelength of the fundamental mode. According to the ABCD law, all modes are then transformed in the same way by an optical system. Hence, optical elements preserve the order of a mode.

Another important feature of Hermite-Gaussian modes is that different modes are orthonormal to each other [82]

$$\int_{-\infty}^{\infty} dx \int_{-\infty}^{\infty} dy \psi_{n_1, m_1}(x, y, z) \psi_{n_2, m_2}(x, y, z) = \delta_{n_1, n_2} \delta_{m_1, m_2}, \quad (2.33)$$

where δ_{n_1, n_2} and δ_{m_1, m_2} are Kronecker deltas. This relation applies independently for the x - and y -direction. The coefficients in equation 2.26 must be chosen correctly for the normalisation. In the literature, the coefficients are not uniformly defined. Depending on the definition of Hermite-Gaussian modes a normalisation factor needs to be added to the equation above.

By obeying to the relation in equation 2.33, Hermite-Gaussian modes form a complete set in any plane transverse to the optical axis [82]. This allows to write any arbitrarily paraxial beam as a superposition of Hermite-Gaussian modes

$$E(x, y, z) = \sum_N \alpha_N \psi_N(x, y, z), \quad (2.34)$$

where N refers to the different modes. $N = (n, m)$ is a combination of the direction orders n and m and is therefore an element of the set $N \in \{(00), (10), (01), (11), (20), \dots\}$. α_N is the amplitude of mode N and can be interpreted as the 'weight' mode N is contributing to the total field.

Chapter 3

Optical Resonators

An optical resonator or cavity is a device that traps optical electromagnetic radiation by multiple reflections between several mirrors. Resonators are used primarily to enable optical feedback in lasers [82], but the scope of application of resonators is broader. For instance, cavities are used as frequency filters for radiation [83, 91], in gravitational-wave detectors [92] or generally in cavity quantum electrodynamics [93].

Optical cavities allow to increase and control the interaction strength between matter and light fields and are used for the molecular detection scheme presented in this thesis. The aim of this chapter is to introduce the theory behind stable optical resonators. The presented concepts follow the established literature, see e. g. [82, 83, 84, 90] for more details. The first section covers the simplest cavities consisting of two mirrors. A criterion for stability is defined and relations between resonator design and beam properties inside the cavity are derived. Boundary conditions of the mirrors are used to determine the frequencies that are supported by the cavity. Finally, the cavity linewidth, which is an important quantity regarding the interaction strength between radiation and molecules as well as for the number of modes supported by the cavity, is introduced. The second section derives all these properties and conditions for ring resonators consisting of four mirrors.

3.1 Two-mirror optical resonators

A two-mirror cavity consists of two spherical mirrors with radii r_1 and r_2 , respectively. Both mirrors are separated by a distance L from each other, see figure 3.1. Furthermore, the mirrors are approximated as being unconfined, i. e. the reflective surface is infinitely large. The combination of radii of curvature and mirror separation defines the resonator geometry and determines the shapes and frequencies of light fields inside the cavity entirely. Light fields supported by a resonator are solutions of the paraxial Helmholtz equation 2.7, where boundary conditions are defined by the cavity geometry. Alternatively, these solutions can be found by solving the Fresnel-Kirchhoff integral arising from Huygens' theory. Since both derivations are quite extensive, they are not discussed in detail here, but can be found in the literature, e. g. in [84] for the Helmholtz equation or in [83] for the Fresnel-Kirchhoff approach. For an ideal case, i. e. without consideration of losses (power reduction due to absorption or the finite surface of a mirror) and for perfectly reflective mirrors the solutions are the Hermite-Gaussian modes discussed in chapter 2.2. Even for most non-ideal mirrors, these modes approximate the experimentally observed light fields in cavities very well [83].

Ray transfer matrices allow to determine many properties of resonators in a very simple way. To estimate the total ABCD matrix of a two-mirror cavity two types of ray transfer matrices are needed, the first type describing a reflection at a mirror and the second type characterising propagation through space. The matrices are given by

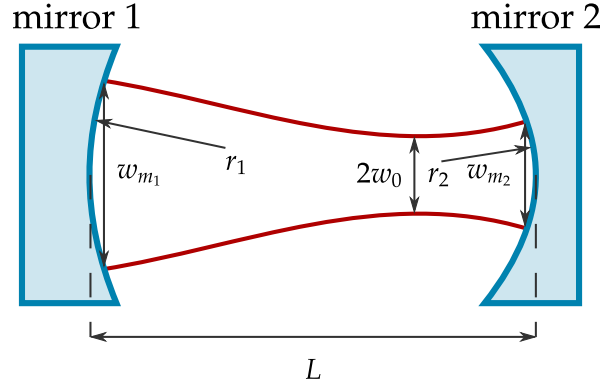


Figure 3.1: Two-mirror cavity consisting of two opposing mirrors separated by a distance L . The radii of curvature of the mirrors are r_1 and r_2 . The waist of the optical beam inside the resonator is w_0 and beam sizes at the mirrors are w_{m_1} and w_{m_2} .

$$\text{reflection at mirror: } \begin{pmatrix} 1 & 0 \\ -\frac{2}{r} & 1 \end{pmatrix} \quad \text{propagation through space: } \begin{pmatrix} 1 & L \\ 0 & 1 \end{pmatrix}. \quad (3.1)$$

Without loss of generality, the reference point, i. e. the position where the beam starts and ends during a complete cycle inside the cavity, is at the left mirror in figure 3.1. The beam directly propagates to the mirror on the right side, is then reflected and propagates back, where it is finally reflected by the first mirror. The ray transfer matrix for a two-mirror resonator is hence given by

$$\begin{pmatrix} A & B \\ C & D \end{pmatrix} = \begin{pmatrix} 1 & 0 \\ -\frac{2}{r_1} & 1 \end{pmatrix} \begin{pmatrix} 1 & L \\ 0 & 1 \end{pmatrix} \begin{pmatrix} 1 & 0 \\ -\frac{2}{r_2} & 1 \end{pmatrix} \begin{pmatrix} 1 & L \\ 0 & 1 \end{pmatrix}. \quad (3.2)$$

By defining

$$g_i := 1 - \frac{L}{r_i}, \quad (3.3)$$

where i is the corresponding mirror index, the ABCD matrix takes the form

$$\begin{pmatrix} 2g_2 - 1 & 2g_2L \\ \frac{2}{L}(2g_1g_2 - g_1 - g_2) & 4g_1g_2 - 2g_2 - 1 \end{pmatrix}. \quad (3.4)$$

g_1 and g_2 are called cavity or mirror parameters. Many resonator properties depend directly on these two quantities.

Beam sizes and radii of curvature of the phase front

By considering the reciprocal of the complex beam parameter $\frac{1}{q}$, the beam size and radius of curvature of the phase front for cavity fields can be derived in a very simple way. The following derivation is based on [90]. Cavity fields are stationary solutions of the paraxial Helmholtz equation. Therefore, a resonator mode should replicate itself after one round trip. In particular, this means that the complex beam parameter is unaltered after a complete cycle within the cavity. Applying the ABCD law leads to

$$\frac{1}{q} = \frac{C + \frac{D}{q}}{A + \frac{B}{q}}, \quad (3.5)$$

which is a quadratic equation and can be written as

$$B\left(\frac{1}{q}\right)^2 + (A - D)\left(\frac{1}{q}\right) - C = 0. \quad (3.6)$$

The solutions of this equation are given by

$$\frac{1}{q} = \frac{D - A}{2B} \pm \frac{1}{2B} \sqrt{(A - D)^2 + 4BC}. \quad (3.7)$$

The elements of the ray transfer matrix in equation 3.4 are real. By definition, the imaginary part of $1/q$ cannot be equal to zero, since otherwise the value of the beam size would be physically unreasonable. Therefore, it can be assumed that the expression $(A - D)^2 + 4BC$ is negative. Later, it is shown, that this assumption can be used to define a stability criterion for resonators. The distance to the waist for any q is identical to the negative value of the respective beam parameter. Hence, the first term in the equation above is identical to the real part of $1/q$ and the second term to its imaginary part. Finally, comparing equations 2.15 and 3.7 enables the connection of the beam size and the curvature of the phase front at mirror 1 with the entries of the ray transfer matrix for cavities:

$$R_{m_1}(z) = \frac{2B}{D - A}, \quad (3.8)$$

$$-i\frac{\lambda}{\pi w^2} = \pm \frac{1}{2B} \sqrt{(A - D)^2 + 4BC}. \quad (3.9)$$

Since the determinant of a ray transfer matrix is equal to unity [90], the beam size can be written as

$$w_{m_1}^2 = \sqrt{\frac{2\lambda}{\pi} \frac{|B|}{4 - (A + D)^2}}. \quad (3.10)$$

Inserting the matrix elements given by equation 3.4 leads to

$$w_{m_1} = \frac{\lambda L}{\pi} \sqrt{\frac{g_2}{g_1(1 - g_1 g_2)}}. \quad (3.11)$$

Substituting the matrix elements in equation 3.8 reveals that the radius of curvature of the phase front is identical to the negative radius of the first mirror $-r_1$. The minus sign arises from the convention that radii of phase fronts are negative when the centre of the Gaussian beam is located to the right of the wavefront [90].

So far, the beam size and wavefront curvature are only known for one position in the cavity. The values for any other point can be found by applying the ABCD law.

In particular, the waist of the cavity field is of interest. Since the radius of the wavefront is vanishing at the origin of a Gaussian beam, the complex beam parameter $q_0 = q(z = 0)$ becomes purely imaginary at the position of the waist. Substituting equation 2.13 into 2.14 leads to

$$q_0 = iz_R = i\frac{\pi w_0^2}{\lambda}. \quad (3.12)$$

Furthermore, it is easy to show that the imaginary part of any complex number ξ is connected to the imaginary part of $1/\xi$ through

$$\text{Im}(\xi) = -\frac{\text{Im}\left(\frac{1}{\xi}\right)}{|\xi|^2}. \quad (3.13)$$

This allows to write the beam waist as

$$w_0^2 = -\frac{\lambda}{\pi} \frac{\text{Im}\left(\frac{1}{q}\right)}{\left|\frac{1}{q}\right|^2}. \quad (3.14)$$

Substituting the entries of the ray transfer matrix for two-mirror cavities leads to

$$w_0^2 = \frac{\lambda L}{\pi} \sqrt{\frac{g_1 g_2 (1 - g_1 g_2)}{(g_1 + g_2 - 2g_1 g_2)^2}}. \quad (3.15)$$

The distance z_1 between waist and mirror 1 can be found in a similar way. The separation to the waist for any point of a Gaussian beam is identical to the negative value of the respective beam parameter q . The relation in equation 3.13 also holds for real parts. Applying some algebraic transformations the distance between waist and mirror 1 obtains the form [90]

$$z_1 = L \frac{g_2 (g_1 - 1)}{|g_1 g_2 - 2g_1 g_2|}. \quad (3.16)$$

If the beam inside the cavity starts from the second mirror instead of the first one, all expressions given above stay the same, except that the indices of the mirrors need to be interchanged. This allows to conclude for the beam size at mirror 2 and for the corresponding distance to the waist

$$w_{m_2}^2 = \frac{\lambda L}{\pi} \sqrt{\frac{g_1}{g_2 (1 - g_1 g_2)}} \quad (3.17)$$

$$z_2 = L \frac{g_1 (g_2 - 1)}{|g_1 g_2 - 2g_1 g_2|}. \quad (3.18)$$

Criterion of stability

As mentioned above, the expression below the square root in equation 3.7 must be negative and therefore

$$2 \geq |A + D| \quad (3.19)$$

applies. Inserting the ray matrix elements for A and D into this equation leads to

$$0 \leq g_1 g_2 \leq 1. \quad (3.20)$$

This is the criterion of stability for two-mirror cavities. If the resonator geometry satisfies this inequality, it is considered stable and a ray will remain in-between the mirrors for an infinite or at least a large number of reflections. This does not mean that light fields will not build up in unstable cavities. But rays inside unstable resonators will be lost after a few round trips. Due to the boundary conditions defined by the resonator geometry, Hermite-Gaussian modes are no longer solutions of the paraxial Helmholtz equation in the unstable regime. Usually the losses of unstable resonators are large compared to stable cavities, the mode structure is complicated and obtaining higher order modes inside the cavity is difficult [83]. In chapter 6 it is explained that these properties make unstable resonators unsuitable for the molecular detection scheme presented in this thesis. Therefore, unstable resonators are not further discussed here.

Resonance frequencies

Apart from the complex beam parameter the phase of a cavity field also needs to reproduce itself after one round trip in the cavity in order to generate a stationary solution. The total phase shift at the optical axis after one complete transition cycle is

$$\Delta\phi = 2kL - 2(n + m + 1) \left(\arctan\left(\frac{z_2}{r_R}\right) - \arctan\left(\frac{z_1}{r_R}\right) \right), \quad (3.21)$$

where n and m are the orders of the Gouy phases. The difference between these Gouy phases can be written as [82]

$$\left(\arctan\left(\frac{z_2}{r_R}\right) - \arctan\left(\frac{z_1}{r_R}\right) \right) = \arccos\left(\pm \sqrt{g_1 g_2}\right). \quad (3.22)$$

A plus sign is used when both mirror parameters are positive, otherwise a minus sign applies. To reproduce itself, the phase needs to satisfy the condition

$$\Delta\phi = q2\pi, \quad (3.23)$$

otherwise destructive interference will annihilate the light field. q is an integer here and not the complex beam parameter as before. This duplication of use is unfortunate, though common in the literature. Hence, this convention is also used here. The respective context clarifies which q is meant.

Combing the equations 3.21, 3.22 and 3.23 and using the dispersion relation of light $\omega = kc$ leads to

$$q\pi = \frac{\omega L}{c} - (n + m + 1) \arccos\left(\pm \sqrt{g_1 g_2}\right). \quad (3.24)$$

Finally, solving this equation for the angular frequency of the cavity field $\omega = \omega_{qnm}$ this results in

$$\omega_{qnm} = \frac{\pi c}{L} \left(q + (n + m + 1) \frac{\arccos\left(\pm \sqrt{g_1 g_2}\right)}{\pi} \right). \quad (3.25)$$

Only light fields satisfying this condition are supported by the cavity. There are two different categories of resonator modes. Longitudinal modes depend on the integer q , where q is the number of half wavelengths fitting between both cavity mirrors. The frequencies of these modes rely on the distance L between the mirrors, but are independent from the mirror shapes. The difference in frequency between two 'neighbouring' longitudinal modes q and $q + 1$ is constant and called the free spectral range:

$$\Delta\omega_{\text{FSR}} = \frac{\pi c}{L}. \quad (3.26)$$

The second category of light fields is called transverse modes, since these beams have different profiles in planes orthogonal to the optical axis for integers n and m . For Hermite-Gaussian modes n and m are identical to the orders of the Hermite polynomials. Note, that a cavity mode is not either longitudinal or transverse. Each cavity mode can be seen as a combination of these two types and a longitudinal mode q can be divided in an infinite set of corresponding transverse modes. The set of all frequencies supported by the cavity, determined by all possible combinations of q , n and m , is the spectrum of the cavity. This spectrum of modes strongly depends on the resonator geometry. More details are given in chapter 6, where proper cavity designs for the molecular detection scheme are discussed.

Cavity linewidth

A cavity can store a light field for an infinite amount of time only when the mirrors are perfectly reflective and no losses occur. However, this is an ideal case never achieved for real mirrors. Furthermore, mirrors with a finite transmission might be needed to couple light into the cavity in the first place. Non-perfectly reflective mirrors reduce the lifetime of a photon within the cavity. Usually, mirror losses are small compared to reflection and transmission. Therefore, it is assumed that light, which is not reflected by a mirror, is transmitted. \tilde{r}_1 and \tilde{r}_2 are the amplitude reflectivities (\tilde{r} is used instead of r to distinguish reflectivity and mirror curvature) for the cavity mirrors and R_1 and R_2 are the intensity reflectivities. t_1 , t_2 and T_1 , T_2 are the amplitude and intensity transmissions, respectively.

The following section investigates a cavity in transmission design, i. e. an electromagnetic wave is coupled to the cavity through one of the mirrors and leaves the resonator through the other. The presented derivation is published in the literature, e. g. in [94]. Without loss of generality, mirror 2 is the output mirror. E_p is the field strength of the pump beam. Each time the beam interacts with a mirror it is either reflected or transmitted. Therefore, the transmitted field can be written as

$$\begin{aligned} E_t &= E_p t_1 t_2 \exp\left(-i\frac{\Delta\phi}{2}\right) + E_p t_1 t_2 \tilde{r}_1 \tilde{r}_2 \exp\left(-i3\frac{\Delta\phi}{2}\right) + E_p t_1 t_2 \tilde{r}_1^2 \tilde{r}_2^2 \exp\left(-i5\frac{\Delta\phi}{2}\right) + \dots \\ &= t_1 t_2 E_p \exp\left(-i\frac{\Delta\phi}{2}\right) \sum_{l=0}^{\infty} \tilde{r}_1^l \tilde{r}_2^l \exp(-il\Delta\phi) \\ &= \frac{E_p t_1 t_2 \exp\left(-i\frac{\Delta\phi}{2}\right)}{1 - \tilde{r}_1 \tilde{r}_2 \exp(-i\Delta\phi)}. \end{aligned} \quad (3.27)$$

In the last step a geometric series is used [95]. For the intensity transmitted through the cavity follows

$$\begin{aligned} I_t = |E_t|^2 &= I_0 \frac{t_1^2 t_2^2}{(1 - \tilde{r}_1 \tilde{r}_2 \exp -i\Delta\phi)(1 - \tilde{r}_1 \tilde{r}_2 \exp i\Delta\phi)} \\ &= I_0 \frac{t_1^2 t_2^2}{(1 - \tilde{r}_1 \tilde{r}_2)^2 \left(1 + F \sin^2\left(\frac{\Delta\phi}{2}\right)\right)}, \end{aligned} \quad (3.28)$$

where $F = 4\tilde{r}_1 \tilde{r}_2 / ((1 - \tilde{r}_1 \tilde{r}_2)^2)$. From energy conservation it follows $\tilde{r}_i^2 + t_i^2 = 1$. By assuming identical mirror reflectivities and transmissions, this allows to write the fraction of transmitted intensity or transmission as

$$\mathcal{T} = \frac{I_t}{I_0} = \frac{1}{1 + F \sin^2\left(\frac{\Delta\phi}{2}\right)}. \quad (3.29)$$

These are the Airy functions of optical resonators. Figure 3.2 depicts them for different reflectivities and flat mirrors. The figure illustrates that lower reflectivities lead to broader resonances. The width of the resonances is called the cavity linewidth κ and is an important property of cavities. The linewidth is either defined as the full width at half maximum (FWHM) or half of it (HWHM). In this thesis it is defined as HWHM. Furthermore, κ is here given in units of an angular frequency. Without loss of generality the linewidth can be determined from the resonance at $\omega_{qnm} = 0$:

$$\mathcal{T} = \frac{1}{2} = \frac{1}{1 + F \sin^2\left(\frac{\kappa L}{c}\right)}. \quad (3.30)$$

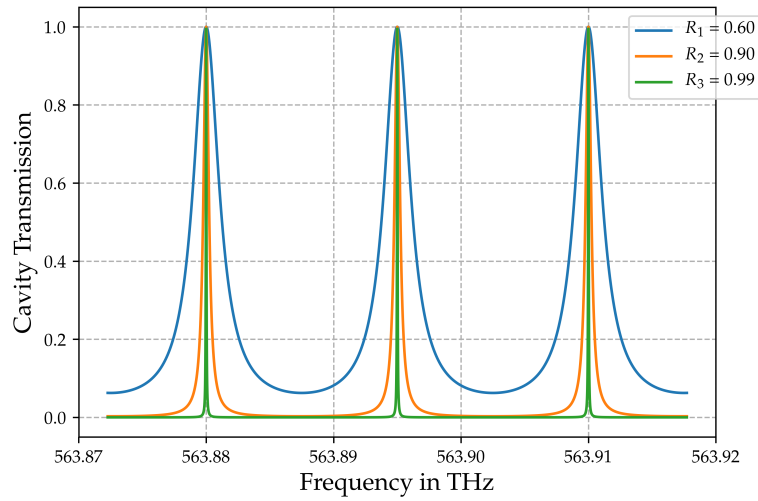


Figure 3.2: Airy functions for a cavity consisting of flat mirrors and different reflectivities. The cavity length is set to $L = 1$ cm. Decreasing the reflectivity of the mirrors leads to broader resonances.

Since $\frac{\kappa L}{c}$ is usually small, the small-angle approximation can be applied. After some algebra this leads to

$$\kappa = \frac{c}{2L} \frac{1-R}{\sqrt{R}}, \quad (3.31)$$

where R is the intensity reflectivity of one mirror. The reciprocal of the linewidth is a measure for the lifetime of a photon inside the cavity [84]:

$$\tau = \frac{1}{\kappa}. \quad (3.32)$$

Another quantity often used to characterise the quality of resonators is the finesse, defined as the quotient of the free spectral range and the cavity linewidth:

$$\mathcal{F} = \frac{\Delta\omega_{\text{FSR}}}{\kappa} = \frac{\pi\sqrt{R}}{1-R}. \quad (3.33)$$

The finesse is a measure for the resolution of a cavity regarding its resonances. Usually large finesses are desired. However, for the detection of molecules moderate values, which are discussed in detail in chapter 6, might be desirable.

3.2 Ring resonators

Another important class of optical cavities are so-called ring resonators. This type consists of more than two mirrors or optical fibres [84]. Ring resonators and two-mirror cavities have many properties in common, however, there are also some important differences. The electromagnetic wave in a two-mirror cavity is reflected back into itself, forming a standing wave. In ring resonators travelling waves propagate. In [90] a very simple, yet effective derivation for the properties of ring resonators is introduced, using ray transfer matrices. The first part of this section follows largely this approach.

Figure 3.3 depicts two possible configurations of ring resonators consisting of four mirrors, two flat and two curved mirrors each. The radii of curvature r of the spherical mirrors

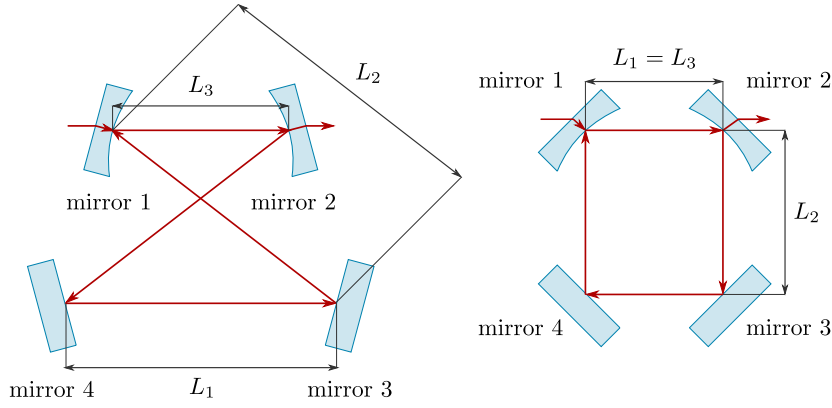


Figure 3.3: Two possible configurations of ring resonator consisting of four mirrors. The cavity on the left side is commonly referred to as a bow-tie cavity.

are identical. L_1 is the distance between the flat mirrors, L_2 between the flat and the curved mirrors and L_3 between the curved mirrors. The ray transfer matrix of these ring resonators is again a product of four matrices:

$$\begin{pmatrix} A & B \\ C & D \end{pmatrix} = \begin{pmatrix} 1 & 0 \\ -\frac{2}{r} & 1 \end{pmatrix} \begin{pmatrix} 1 & L_1 + 2L_2 \\ 0 & 1 \end{pmatrix} \begin{pmatrix} 1 & 0 \\ -\frac{2}{r} & 1 \end{pmatrix} \begin{pmatrix} 1 & L_3 \\ 0 & 1 \end{pmatrix}. \quad (3.34)$$

The reference point for this matrix is located at the left of the curved mirrors and the beam propagates directly to the other curved mirror. The complex beam parameter is not altered by reflections at flat mirrors. Therefore, the corresponding distances can be summarised as $L_s = 2L_2 + L_1$. By defining new g-parameters for ring resonators

$$g_1 = 1 - \frac{L_s}{r}, \quad (3.35)$$

$$g_2 = 1 - \frac{L_3}{r} \quad (3.36)$$

the ray transfer matrix can be written as

$$\begin{pmatrix} 2g_1 - 1 & r(-2g_1g_2 + g_1 + g_2) \\ -\frac{4g_1}{r} & 4g_1g_2 - 2g_1 - 1. \end{pmatrix}. \quad (3.37)$$

Beam sizes and radii of curvature of the phase front

The reflections at spherical mirrors alter the complex beam parameter of a Gaussian beam. Since the beam is not reflected back into itself in a ring cavity, there are two different values for the complex beam parameter q inside these resonators. This is equivalent to two different Gaussian beams inside the four-mirror ring cavity. The first beam is located within the range L_3 , see figure 3.3 and its properties are indicated by unprimed variables, whereas the second beam is located in the remaining interval $L_s = 2L_2 + L_1$ and for the quantities of this beam primed variables are used. As for the two-mirror case, the complex beam parameters need to replicate themselves after one round trip. Hence, the ABCD law implicates

$$\frac{1}{q} = \frac{2g_1(g_2 - 1)}{r(g_1 + g_2 - 2g_1g_2)} \pm \frac{2\sqrt{g_1g_2(1 - g_1g_2)}}{r(g_1 + g_2 - 2g_1g_2)}, \quad (3.38)$$

$$\frac{1}{q'} = \frac{2g_2(1 - g_1)}{r(g_1 + g_2 - 2g_1g_2)} \pm \frac{2\sqrt{g_1g_2(1 - g_1g_2)}}{r(g_1 + g_2 - 2g_1g_2)}. \quad (3.39)$$

The beam size at the curved mirrors and the waists of the Gaussian beams can be found in the same way as for the two-mirror cavity. This leads to

$$w_m^2 = \frac{\lambda r}{2\pi} \frac{g_1 + g_2 - 2g_1g_2}{\sqrt{g_1g_2(1 - g_1g_2)}} \quad (3.40)$$

for the beam size at the mirror. The waists are given by

$$w_0^2 = \frac{\lambda r \sqrt{g_1g_2(1 - g_1g_2)}}{2\pi g_1}, \quad (3.41)$$

$$w_0'^2 = \frac{\lambda r \sqrt{g_1g_2(1 - g_1g_2)}}{2\pi g_2}. \quad (3.42)$$

Another interesting feature is revealed by calculating the quotient between the two waists above:

$$\frac{w_0}{w_0'} = \sqrt{\frac{g_2}{g_1}}. \quad (3.43)$$

Therefore, the ratio of the waists can be adjusted by changing either L_3 or L_s .

Criterion of stability

The criterion of stability for ring resonators can be derived similarly as for the two-mirror resonator. The inequality is the same [90]

$$0 < g_1g_2 < 1. \quad (3.44)$$

However, there is an important difference, namely that the lengths in the g-parameters for ring resonators are independent from each other. Hence, the distance between the curved mirrors cannot become arbitrarily small and stable ring resonators need to satisfy

$$r \leq L_3 \leq \frac{rL_3}{L_1 - r}. \quad (3.45)$$

Assuming that $r \ll L_3$ yields

$$L_{3,\text{stab}} \approx \frac{r^2}{L_3} \quad (3.46)$$

for the distance between the curved mirrors, that can be adjusted, without violating the criterion of stability for ring resonators.

Resonance frequencies

As for the two-mirror cavity, the resonance frequencies are determined by the phase after a complete cycle in the ring resonator. The corresponding expression takes a similar form as before [90]:

$$\omega_{qnm} = \frac{2\pi c}{L_{\text{total}}} \left(q + (n + m + 1) \frac{\arccos(\pm \sqrt{g_1g_2})}{\pi} \right). \quad (3.47)$$

The length is defined as $L_{\text{total}} = L_1 + 2L_2 + L_3$. In comparison to the resonance frequencies of two-mirror cavities, this equation includes a factor of 2 since the beam is not reflected

back into itself here. The free spectral range of ring cavities is therefore twice as large as for two-mirror resonators:

$$\Delta\omega_{\text{FSR}} = \frac{2\pi c}{L_{\text{total}}}. \quad (3.48)$$

Cavity linewidth

The cavity linewidth of ring resonators can be determined in the same way as for two-mirror cavities. The four mirrors are labelled as depicted in figure 3.3. In the following the field transmitted through the second mirror is investigated. Each cycle the field is either reflected or transmitted, leading to

$$\begin{aligned} E_{t,2} &= t_1 t_2 E_p \exp(-i\Delta\phi_{12}) + t_1 \tilde{r}_2 \tilde{r}_3 \tilde{r}_4 \tilde{r}_1 t_2 E_p \exp(-i(\Delta\phi_{12} + \Delta\phi)) + \dots \\ &= E_p \exp(-i\Delta\phi_{12}) t_1 t_2 \sum_{l=0}^{\infty} \tilde{r}^l \exp(-il\Delta\phi) \\ &= \frac{E_p \exp(-i\Delta\phi_{12}) t_1 t_2}{1 - \tilde{r} \exp(-i\Delta\phi)}, \end{aligned} \quad (3.49)$$

with amplitude transmissions t_i and reflectivities \tilde{r}_i . $\Delta\phi_{12}$ is the phase shift between mirror 1 and 2 and $\tilde{r} = \tilde{r}_1 \tilde{r}_2 \tilde{r}_3 \tilde{r}_4$. The transmitted intensity can then be written as

$$I_{t,2} = |E_{t,2}|^2 = I_0 \frac{T_1 T_2}{(1 - \tilde{r})^2 \left(1 + F \sin^2\left(\frac{\Delta\phi}{2}\right)\right)}, \quad (3.50)$$

where T_i is the intensity transmission of mirror i and $F = \frac{4\tilde{r}}{(1-\tilde{r})^2}$. Again, the HWHM is calculated for the resonance at $\omega_{qmm} = 0$. It is important to note, that the intensity transmitted through the second mirror does not equal unity at resonance since the other mirrors are not perfectly reflective in general. Therefore, the linewidth can be found by setting the transmission to $\frac{1}{2} \frac{T_1 T_2}{(1-\tilde{r})^2}$:

$$\kappa = \frac{c}{L_{\text{total}}} \frac{(1 - \tilde{r})}{\sqrt{\tilde{r}}}. \quad (3.51)$$

Again, this is twice the size of a two-mirror cavity with an equal length, since the beam is not reflected back into itself. The reflectivity of mirrors not used to couple light into the cavity or for the transmission signal should be close to unity, since otherwise power is lost unnecessarily through these mirrors.

Chapter 4

Detection of Cold Particles - Classical Description

Quantum mechanical approaches are typically used to describe the interaction between particles, i. e. atoms or molecules, and electromagnetic fields within an optical resonator. This research field is often called cavity quantum electrodynamics (cQED). A common theory in cQED is the Jaynes-Cummings model [8, 96] explaining many experimentally observed phenomena, like vacuum Rabi oscillations [97] or sub-Poissonian distributions of emitted photons [98, 99]. Some of these observations such as the revival of Rabi oscillations [100] cannot be explained classically, other phenomena like for example vacuum Rabi splitting [101] or laser cooling of particles [102] can be interpreted in a classical framework.

Classical theories describing the interaction between particles and light are valid in the low-saturation regime, i. e. when the particles mostly remain in the ground state. Since the fundamental idea for the molecular detection scheme discussed in this thesis relies on dispersive light-molecule interactions and the suppression of absorption either due to large detunings or low intensities, classical theories are applicable. The advantages of a classical approach might provide a more intuitive understanding behind the physics of the detection scheme as well as a transfer to other objects often described classically, like nanoparticles, see chapter 7.1. The aim of the following chapter is to introduce a classical description for the imaging of cold molecules.

In the first section, the interaction between a single particle and a single Hermite-Gaussian mode is investigated. An overlap integral between dipole radiation and an arbitrary Hermite-Gaussian mode, similar to the approach in [103] is calculated for this purpose. However, the calculations presented here are more general and contain the results from [103] as special cases. In the second section, multiple particles inside a multimode resonator are considered and the cavity field is determined. Subsequently, the homodyne detection technique is introduced and specialised for the spatially resolved imaging of particles. Finally, the spatial resolution of the proposed detection scheme is discussed.

4.1 Interaction between a single particle and a paraxial beam

In the following, the interaction between a single particle and a linearly polarised electric field

$$\vec{E} = \frac{1}{2}E_0 \exp(-i\omega t)\vec{e} + \text{c.c.}, \quad (4.1)$$

is considered, where E_0 is the amplitude, ω the angular frequency of the field, t the time and \vec{e} the polarisation unity vector. c.c. is short for complex conjugate. Compared to the corresponding atomic or molecular core the mass of an electron is small. Hence, the

negatively charged electron starts to oscillate with the same frequency and in the same direction as the applied electric field, whereas the positive core remains stationary. The particle is then an oscillating dipole, i. e. is described by the Lorentz oscillator model, with the dipole moment given by

$$\vec{p} = \frac{1}{2} p_0 \exp(-i\omega t) \vec{e} + \text{c.c.} \quad (4.2)$$

The amplitude p_0 is proportional to the amplitude of the electric field: $p_0 = \alpha E_0$. The factor of proportionality is the complex polarisability of the particle [103]

$$\alpha = 6\pi\epsilon_0 c^3 \frac{\Gamma/\omega_0^2}{\omega_0^2 - \omega^2 - i(\omega^3/\omega_0^2)\Gamma}, \quad (4.3)$$

where ω_0 is the resonance frequency of the particles transition, Γ the linewidth of the particles transition and ϵ_0 is the vacuum permittivity. The real and the imaginary part of the polarisability have different physical meanings. While the real part characterises dispersive interaction, the imaginary part describes absorption [104]. Defining the detuning between the driving field and the frequency of the particles transition $\Delta := \omega - \omega_0$ and applying the rotating wave approximation [105, 106], with $\Delta \ll \omega$, ω_0 and $\omega + \omega_0 \approx 2\omega_0$ allows to write the polarisability as

$$\alpha \approx \frac{6\pi\epsilon_0}{k^3} \left(\frac{2\Delta\Gamma}{4\Delta^2 + \Gamma^2} + i \frac{\Gamma^2}{4\Delta^2 + \Gamma^2} \right). \quad (4.4)$$

The equation above reveals that dispersive and absorptive effects depend differently on the detuning. While the real part of the complex polarisability decreases linearly with increasing the detuning Δ (at least for $\Delta \gg \Gamma$), the imaginary part decreases quadratically. Hence, the absorption can be suppressed in comparison to dispersive interaction by using large detunings. Utilising large detunings is therefore an effective method to enter the low-saturation regime. The model described above corresponds to the Lorentz oscillator model [107, 108], which allows to describe a quantum mechanical two-level system classically as long as the excitations of the particle can be neglected.

An accelerated charge, like the oscillating electron, emits radiation itself. As long as a particle is small compared to the wavelength of the driving field it can be considered as pointlike. Hence, the oscillating electron emits an electric field for $R \gg \lambda$ according to [109]

$$E_{\text{rad}} = \frac{k^2}{4\pi\epsilon_0} \sin(\theta) \frac{\exp(ikR)}{R} \alpha E. \quad (4.5)$$

R is the distance between the dipole emitter and the point of observation and θ is the angle between the polarisation vector \vec{e} and the direction of observation, see figure 4.1. The field is written as a scalar since polarisation effects are not considered in the following.

Next, the fraction of light scattered into an arbitrary Hermite-Gaussian mode ψ_N by the particle is determined. This fraction is called the amplitude α_N of the mode. It is assumed that the optical axis of the Hermite-Gaussian mode is orthogonal to the direction of oscillation of the electron. Mathematically, an electric field can be seen as a vector and α_N as the projection of E_{rad} on ψ_N . Therefore, the mode amplitude for an arbitrary plane orthogonal to the optical axis of the Hermite-Gaussian mode is given by the scalar product

$$\alpha_N = \int_{-\infty}^{\infty} \int_{-\infty}^{\infty} \psi_N^* E_{\text{rad}} dx dy. \quad (4.6)$$

It is important to note, that the coordinate systems of the scattered field and the mode do not coincide in general, as depicted in figure 4.1. Before solving the above integral, it is

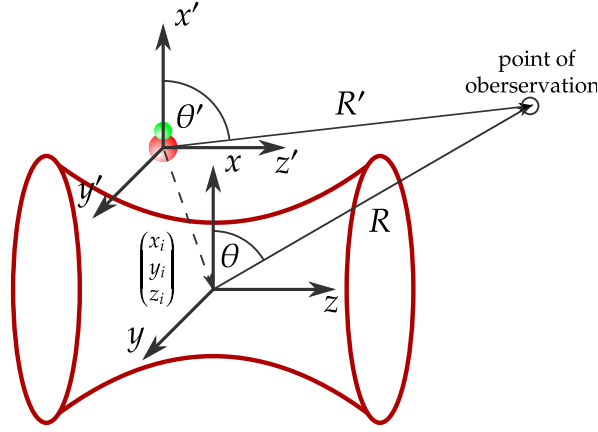


Figure 4.1: Coordinate systems of the particle (primed) and the mode (unprimed). The origins of the coordinate systems are separated by x_i , y_i and z_i .

necessary to perform a coordinate transformation. Primed variables indicate coordinates in the particles system, whereas unprimed variables refer to the coordinate system of the mode. The transformation is then

$$x' = x - x_i, \quad (4.7)$$

$$y' = y - y_i, \quad (4.8)$$

$$z' = z - z_i. \quad (4.9)$$

Later in the experiment, several molecules are placed inside a multimode resonator. The origin of the coordinate system in equation 4.5 is located at the position of the emitter and therefore each molecule defines its own coordinate system, whereas all modes of the cavity share the same. Hence, the position of a particle is transformed into the coordinate system of the modes here since this is more universal.

Hermite-Gaussian modes are paraxial beams and therefore only a small far field cone contributes to the overlap integral above. This allows to approximate $\sin(\theta') \approx \sin(\theta) \approx 1$ as well as $R' \approx ((z - z_i) + ((x - x_i)^2 + (y - y_i)^2) / (2(z - z_i)))$. The scattered field in coordinates of the mode is then

$$E_{\text{rad}} \approx \frac{k^2}{4\pi\epsilon_0} \alpha E(\vec{r}_p) \frac{\exp\left(ik(z - z_i) \left(1 + \frac{(x-x_i)^2 + (y-y_i)^2}{2(z-z_i)^2}\right)\right)}{z - z_i}. \quad (4.10)$$

$\vec{r}_p = (x_p, y_p, z_p)$ is the position of the particle in coordinates of the mode. After considering the paraxial approximation and the coordinate transformation and using equation 2.26 the mode amplitude takes the form

$$\begin{aligned} \alpha_N = & C_N \frac{k^2}{4\pi\epsilon_0} \alpha E(\vec{r}_p) \exp\left(-ikz + i(n + m + 1) \arctan\left(\frac{z}{z_R}\right)\right) \frac{1}{z - z_i} \\ & \cdot \int_{-\infty}^{\infty} \int_{-\infty}^{\infty} H_n\left(\frac{\sqrt{2}x}{w(z)}\right) H_m\left(\frac{\sqrt{2}y}{w(z)}\right) \exp\left(-ik\frac{(x^2 + y^2)}{2R(z)}\right) \\ & \cdot \exp\left(-\frac{x^2 + y^2}{w^2(z)}\right) \exp\left(ik(z - z_i) \left(1 + \frac{(x - x_i)^2 + (y - y_i)^2}{2(z - z_i)^2}\right)\right) dx dy. \end{aligned} \quad (4.11)$$

Note that the sign convention for the phase of the Hermite-Gaussian mode is the opposite here in comparison to the situation in chapter 2. This is allowed since usually the absolute phase is not relevant and only phase differences are important. Switching the phase convention is also common in the literature, e. g. in [84]. Changing the sign of the phase simplifies the following calculation significantly.

The integrals for the x - and y -direction in the equation above are identical. Hence, it is sufficient to solve one of them. The integral in the x -direction can be written in the following form:

$$\begin{aligned} I &:= \int_{-\infty}^{\infty} H_n\left(\sqrt{2}\frac{x}{w}\right) \exp\left(-\frac{x^2}{w^2}\right) \exp\left(i\frac{k(x-x_i)^2}{2(z-z_i)}\right) \exp\left(-i\frac{kx^2}{2R}\right) dx \\ &= \exp\left(i\frac{kx_i^2}{2(z-z_i)}\right) \int_{-\infty}^{\infty} H_n\left(\sqrt{2}\frac{x}{w}\right) \exp\left(-\frac{x^2}{w^2}\right) \exp\left(-i\frac{kxx_i}{z-z_i} + i\frac{kx^2}{2}\left(\frac{1}{z-z_i} - \frac{1}{R}\right)\right) dx. \end{aligned} \quad (4.12)$$

By substituting

$$\tilde{x} = \sqrt{2}\frac{x}{w} \quad \text{and} \quad d\tilde{x} = \frac{\sqrt{2}}{w} dx \quad (4.13)$$

the integral takes the form

$$\begin{aligned} I &= \exp\left(i\frac{kx_i^2}{2(z-z_i)}\right) \frac{w}{\sqrt{2}} \int_{-\infty}^{\infty} H_n(\tilde{x}) \\ &\quad \cdot \exp\left(i\frac{kx_i}{z-z_i} \tilde{x} \left(\frac{1}{z-z_i} - \frac{1}{R}\right) - i\frac{kx_i}{z-z_i} \frac{w}{\sqrt{2}} \tilde{x}\right) d\tilde{x}. \end{aligned} \quad (4.14)$$

Next, all constants and quantities not depending on \tilde{x} are summarised by defining

$$\phi := \frac{kx_i^2}{4} \left(\frac{1}{z-z_i} - \frac{1}{R}\right) \quad \text{and} \quad \xi_x := \frac{k}{z-z_i} \frac{w}{\sqrt{2}} x_i. \quad (4.15)$$

The integral thus takes on a more compact form:

$$I = \exp\left(i\frac{kx_i^2}{2(z-z_i)}\right) \frac{w}{\sqrt{2}} \int_{-\infty}^{\infty} H_n(\tilde{x}) \exp\left(-\frac{\tilde{x}^2}{2}\right) \exp\left(i\phi\tilde{x}^2 - i\xi_x\tilde{x}\right) d\tilde{x}. \quad (4.16)$$

This integral can be solved by summing over $t^n/n!$ and using the generating function for Hermite polynomials [110]

$$\sum_{n=0}^{\infty} H_n(\tilde{x}) \frac{t^n}{n!} = \exp(2\tilde{x}t - t^2). \quad (4.17)$$

Switching the sum and the integral allows to write

$$\begin{aligned} \tilde{I} &:= \int_{-\infty}^{\infty} \sum_{n=0}^{\infty} H_n(\tilde{x}) \frac{t^n}{n!} \exp\left(-\frac{\tilde{x}^2}{2}\right) \exp\left(i\phi\tilde{x}^2 - i\xi_x\tilde{x}\right) d\tilde{x} \\ &= \int_{-\infty}^{\infty} \exp(2\tilde{x}t - t^2) \exp\left(-\frac{\tilde{x}^2}{2}\right) \exp\left(i\phi\tilde{x}^2 - i\xi_x\tilde{x}\right) d\tilde{x} \end{aligned} \quad (4.18)$$

The factor in front of the integral is dropped for simplicity and $\tilde{I} := I \exp\left(-i \frac{kx_i^2}{2(z-z_i)}\right) \frac{\sqrt{2}}{w}$ is defined. Next, the integral is transformed into

$$\tilde{I} = \exp(-t^2) \int_{-\infty}^{\infty} \exp\left(-\left(\frac{1}{2} - i\phi\right)\tilde{x}^2 + (2t - i\xi_x)\tilde{x}\right) d\tilde{x}. \quad (4.19)$$

The solution for this integral can be found in the literature [110]:

$$\int_{-\infty}^{\infty} \exp(-p^2\tilde{x}^2 \pm q\tilde{x}) d\tilde{x} = \frac{\sqrt{\pi}}{p} \exp\left(\frac{q^2}{4p^2}\right), \quad \text{Re}(p^2) > 0. \quad (4.20)$$

Comparing the equations 4.19 and 4.20 reveals $p^2 = \left(\frac{1}{2} - i\phi\right)$ and $q = (2t - i\xi_x)$. Hence, the real part of p^2 is always positive and the application of equation 4.20 is valid. After some algebraic transformations equation 4.19 can then be written as

$$\tilde{I} = \frac{\sqrt{2\pi}}{\sqrt{1 - 2i\phi}} \exp\left(\frac{4t\xi_x - i\xi_x^2 - t^2(4\phi - 2i)}{4\phi + 2i}\right). \quad (4.21)$$

Next, the exponent in the exponential function is multiplied with $1 = \frac{4\phi - 2i}{4\phi - 2i}$. The result is

$$\tilde{I} = \frac{\sqrt{2\pi}}{\sqrt{1 - 2i\phi}} \exp\left(\frac{4t\xi_x(4\phi - 2i) - t^2(4\phi - 2i)^2 - i\xi_x^2(4\phi - 2i)}{16\phi^2 + 4}\right). \quad (4.22)$$

Performing another substitution

$$\tilde{t} := t \frac{4\phi - 2i}{\sqrt{16\phi^2 + 4}} \quad (4.23)$$

allows to transform equation 4.22 into

$$\tilde{I} = \frac{\sqrt{2\pi}}{\sqrt{1 - 2i\phi}} \exp\left(\frac{4\xi_x}{\sqrt{16\phi^2 + 4}}\tilde{t} - \tilde{t}^2 - i\xi_x^2 \frac{4\phi - 2i}{16\phi^2 + 4}\right). \quad (4.24)$$

Applying the generating function for Hermite polynomials once again results in

$$\tilde{I} = \frac{\sqrt{2\pi}}{\sqrt{1 - 2i\phi}} \sum_{n=0}^{\infty} H_n\left(\frac{\xi_x}{\sqrt{4\phi^2 + 1}}\right) \frac{\tilde{t}^n}{n!} \exp\left(-i\xi_x^2 \frac{(4\phi - 2i)}{16\phi^2 + 4}\right). \quad (4.25)$$

Next the substitution from equation 4.23 is inverted. For the equation above follows

$$\tilde{I} = \frac{\sqrt{2\pi}}{\sqrt{1 - 2i\phi}} \sum_{n=0}^{\infty} H_n\left(\frac{\xi_x}{\sqrt{4\phi^2 + 1}}\right) \frac{t^n}{n!} \exp(in\Psi) \exp\left(-i\xi_x^2 \frac{(4\phi - 2i)}{16\phi^2 + 4}\right), \quad (4.26)$$

where $\exp(i\Psi) := \frac{4\phi - 2i}{|4\phi - 2i|}$ is defined. This is allowed since the modulus of this expression is equal to 1.

By comparing identical n in the equations 4.18 and 4.26 the solution of the integral in equation 4.16 can be found and by adding the factor dropped in equation 4.18 again, the result is

$$\begin{aligned}
I &= \exp\left(i\frac{kx_i^2}{2(z-z_i)}\right) \frac{w}{\sqrt{2}} \int_{-\infty}^{\infty} H_n(\tilde{x}) \exp\left(-\frac{\tilde{x}^2}{2}\right) \exp\left(i\phi\tilde{x}^2 - i\xi_x\tilde{x}\right) d\tilde{x} \\
&= \exp\left(i\frac{kx_i^2}{2(z-z_i)}\right) \frac{w}{\sqrt{2}} \frac{\sqrt{2\pi}}{\sqrt{1-2i\phi}} H_n\left(\frac{\xi_x}{\sqrt{4\phi^2+1}}\right) \exp\left(-i\xi_x^2 \frac{4\phi-2i}{16\phi^2+4} + in\Psi\right).
\end{aligned} \tag{4.27}$$

The solution of the integrals in x - and y -direction permits to write the mode amplitude as

$$\begin{aligned}
\alpha_N &= \sqrt{\frac{1}{2^{n+m}n!m!}} \sqrt{\frac{2}{\pi w(z)} \frac{k^2}{4\pi\epsilon_0}} \alpha E(\vec{r}_p) \exp\left(-ikz + i(n+m+1) \arctan\left(\frac{z}{z_R}\right)\right) \\
&\cdot \frac{1}{z-z_i} \exp\left(i\frac{k(x_i^2+y_i^2)}{2(z-z_i)}\right) \left(\frac{w(z)}{\sqrt{2}}\right)^2 H_n\left(\frac{\xi_x}{\sqrt{4\phi^2+1}}\right) H_m\left(\frac{\xi_y}{\sqrt{4\phi^2+1}}\right) \\
&\cdot \frac{2\pi}{1-i2\phi} \exp\left(-i\frac{(\xi_x^2+\xi_y^2)(4\phi-2i)}{16\phi^2+4} + i(n+m)\Psi + ik(z-z_i)\right).
\end{aligned} \tag{4.28}$$

This rather complicated equation can be simplified significantly. The following expressions can be used for this purpose:

$$\phi = \frac{zz_i + z_R^2}{2z_R(z-z_i)}, \tag{4.29}$$

$$\frac{\xi_x}{\sqrt{4\phi^2+1}} = \frac{\sqrt{2}x_i}{w(z_i)} \operatorname{sgn}(z-z_i), \tag{4.30}$$

$$\frac{\xi_y}{\sqrt{4\phi^2+1}} = \frac{\sqrt{2}y_i}{w(z_i)} \operatorname{sgn}(z-z_i), \tag{4.31}$$

$$\frac{4(\xi_x^2+\xi_y^2)\phi}{16\phi^2+4} = \frac{k(x_i^2+y_i^2)}{2(z-z_i)} + \frac{k(x_i^2+y_i^2)}{2R(z_i)}, \tag{4.32}$$

$$\Psi = \arctan\left(\frac{z_i}{z_R}\right) - \arctan\left(\frac{z}{z_R}\right) - \operatorname{Hea}(\operatorname{sgn}(z-z_i))\pi, \tag{4.33}$$

$$\frac{1}{1-i2\phi} = \sqrt{\frac{(z-z_i)^2 z_R^2}{(z^2+z_R^2)(z_i^2+z_R^2)}} \exp\left(i\arctan\left(\frac{z_i}{z_R}\right) + i\arctan\left(\frac{z_R}{z}\right) - i\operatorname{Hea}\left(\operatorname{sgn}\left(\frac{z_i}{z}-1\right)\right)\pi\right). \tag{4.34}$$

The derivations of the equations above contain a large amount of algebraic transformations, which are not specified here, but can be found in the appendix A. sgn is the sign function that gives a +1 for positive and a -1 for negative function values. Hea is the Heaviside step function that is $\operatorname{Hea}(x) = 0$ for $x \geq 0$ and $\operatorname{Hea}(x) = 1$ for $x < 0$.

Applying equation 4.29 to 4.34 allows to write for the amplitude of the mode

$$\begin{aligned}
 \alpha_N = & \sqrt{\frac{1}{2^{n+m}n!m!}} \sqrt{\frac{2}{\pi}} \frac{k^2}{4\pi\epsilon_0} \alpha E(\vec{r}_p) \pi \frac{w(z)}{z-z_i} \sqrt{\frac{z_R^2(z-z_i)^2}{(z^2+z_R^2)(z_i^2+z_R^2)}} \\
 & \cdot H_n\left(\frac{\sqrt{2}x_i}{w(z_i)}\right) H_m\left(\frac{\sqrt{2}y_i}{w(z_i)}\right) \operatorname{sgn}(z-z_i)^{n+m+1} \exp\left(-\frac{x_i^2+y_i^2}{w^2(z_i)}\right) \\
 & \cdot \exp\left(i \arctan\left(\frac{z}{z_R}\right) + i \arctan\left(\frac{z_R}{z}\right) - i \operatorname{Hea}\left(\operatorname{sgn}\left(\frac{z_i}{z}-1\right)\right)\right) \\
 & \cdot \exp\left(-ikz_i - i \frac{k(x_i^2+y_i^2)}{2R(z_i)} + i(n+m+1)\left(\arctan\left(\frac{z_i}{z_R}\right) \operatorname{Hea}\left(\operatorname{sgn}(z-z_i)\right)\right)\right).
 \end{aligned} \tag{4.35}$$

The next possible simplification of this equation is $\exp\left(i \arctan\left(\frac{z}{z_R}\right) + i \arctan\left(\frac{z_R}{z}\right)\right) = \exp\left(\operatorname{sgn}(z)i\frac{\pi}{2}\right) = \operatorname{sgn}(z)i$ [110]. For the remaining terms that depend on the z -coordinate, the following expression can be found:

$$\frac{w(z)}{z-z_i} \sqrt{\frac{z_R^2(z-z_i)^2}{(z^2+z_R^2)(z_i^2+z_R^2)}} = \frac{w_0^2}{z_R w(z_i)} \operatorname{sgn}(z-z_i). \tag{4.36}$$

The derivation of this equation is also demonstrated in the appendix A. In the appendix it is also explained that all sgn -terms and -factors eliminate each other. For the mode amplitude follows

$$\begin{aligned}
 \alpha_N = & i \sqrt{\frac{1}{2^{n+m}n!m!}} \sqrt{\frac{2}{\pi w^2(z_i)}} H_n\left(\frac{\sqrt{2}x_i}{w(z_i)}\right) H_m\left(\frac{\sqrt{2}y_i}{w(z_i)}\right) \exp\left(-\frac{x_i^2+y_i^2}{w^2(z_i)}\right) \\
 & \cdot \exp\left(-ikz_i - i \frac{k(x_i^2+y_i^2)}{2R(z_i)} + i(n+m+1) \arctan\left(\frac{z_i}{z_R}\right)\right) \frac{k^2}{4\pi\epsilon_0} \alpha E(\vec{r}_p) \frac{w_0^2\pi}{z_R}.
 \end{aligned} \tag{4.37}$$

This expression reveals that the mode amplitude is independent of the z -coordinate. Hence, the fraction of the light field scattered into an arbitrary mode N is the same for all planes orthogonal to the optical axis. Furthermore, the equation above is proportional to the complex conjugate of the Hermite-Gaussian mode N at the position of the particle \vec{r}_p . The corresponding expression is given by

$$\begin{aligned}
 \psi_N^*(\vec{r}_p) = & \sqrt{\frac{1}{2^{n+m}n!m!}} \sqrt{\frac{2}{\pi w^2(z_i)}} H_n\left(\frac{\sqrt{2}x_i}{w(z_i)}\right) H_m\left(\frac{\sqrt{2}y_i}{w(z_i)}\right) \exp\left(-\frac{x_i^2+y_i^2}{w^2(z_i)}\right) \\
 & \cdot \exp\left(-ikz_i - i \frac{k(x_i^2+y_i^2)}{2R(z_i)} + i(n+m+1) \arctan\left(\frac{z_i}{z_R}\right)\right).
 \end{aligned} \tag{4.38}$$

This allows to write the mode amplitude as

$$\alpha_N = i \frac{w_0^2\pi}{2} \psi_N^*(\vec{r}_p) \frac{k^2}{2\pi\epsilon_0} \alpha E(\vec{r}_p) \frac{1}{z_R}. \tag{4.39}$$

The effective mode area of the fundamental Gaussian mode $\frac{w_0^2\pi}{2}$ is defined as η . In [103] the dimensionless parameter

$$\beta = \frac{k}{\pi w_0^2} \frac{\alpha}{\epsilon_0}, \tag{4.40}$$

which is a measure for the coupling strength between particle and mode N , is defined. Finally, substituting this quantity in combination with equation 2.13 allows to write

$$\alpha_N = i\eta\beta E(\vec{r}_p)\psi_N^*(\vec{r}_p) \quad (4.41)$$

for the mode amplitude. Modes with an antinode at the particles position \vec{r}_p are strongly populated, whereas the particle does not scatter into modes with a node at the corresponding coordinates. For the fundamental mode equation 4.41 replicates equation 5 from [103]. Note that the additional factor of η arises from a different definition of the normalisation factor for Gaussian beams.

4.2 Multiple particles inside a multimode cavity

In free space, the phase shift of an electromagnetic wave imprinted by a scattering particle is usually small. Cavities allow to enhance the interactions between particles and light fields and, thus, amplify the phase shift. In free space, the beam can only interact once with the particle. However, in a resonator the radiation is reflected several times and during each cycle the phase shift increases. Hence, the total phase shift of a light field in the resonator is increased in comparison to the free space case.

In the following, a number of N_p particles with fixed positions are placed inside a two-mirror resonator. The cavity is assumed to be in the multimode regime, i. e. the resonator frequencies ω_M for different transverse modes M are nearly degenerated. The number of Hermite-Gaussian modes supported by the cavity is N_m . The resonator length is L , the amplitude reflectivities and transmissions of the mirrors are \tilde{r} and q , respectively. q is used instead of t to avoid confusion with time abbreviations used later in this chapter. An electromagnetic wave E_{in} drives or pumps the resonator to maintain the cavity field. This driving beam is paraxial, i. e. the beam is decomposable into Hermite-Gaussian modes, which applies for most laser beams. The angular frequency of the pumping beam is ω . The cavity field is assumed to be stationary, i. e. independent of time.

The amplitude α_M of an arbitrary resonator mode M consists of three parts. The first contribution originates from the circulating cavity field itself. During a complete cycle within the resonator this beam is reflected at both mirrors and accumulates a total phase of $2kL$, with k being the wavenumber. The second term arises from the mode amplitude of the pumping beam $\alpha_{M,in}$. Finally, the last part originates from the field scattered by the particles and the corresponding mode amplitudes are denoted as $\alpha_{M,s}$. Thus, the mode amplitude inside the resonator is

$$\alpha_M = \tilde{r}^2 \exp(i2kL)\alpha_M + q\alpha_{M,in} + 2 \sum_{p=1}^{N_p} \alpha_{M,s}(\vec{r}_p). \quad (4.42)$$

The factor 2 in front of the last term occurs since the particles scatter the light field in both cavity directions [103]. The beam driving the particles is the cavity field itself. Hence, it is decomposable into the individual resonator modes according to

$$E(\vec{r}_p) = \sum_{N=1}^{N_m} \alpha_N \psi_N^*(\vec{r}_p). \quad (4.43)$$

By substituting this expression into equation 4.41 the mode amplitude of the scattered field can be written as

$$\alpha_{M,s}(\vec{r}_p) = i2\beta\eta \left(\sum_{N=1}^{N_m} \alpha_N \psi_N^*(\vec{r}_p) \right) \psi_M(\vec{r}_p). \quad (4.44)$$

For the mode amplitude of the cavity follows

$$\alpha_M = \tilde{r}^2 \exp(i2kL) \alpha_M + q\alpha_{M,in} + i4\beta\eta \sum_{p=1}^{N_p} \sum_{N=1}^{N_m} \alpha_N \psi_N^*(\vec{r}_p) \psi_M(\vec{r}_p). \quad (4.45)$$

Finally, converting this equation to α_M yields

$$\alpha_M = \frac{q\alpha_{M,in} + i4\beta\eta \sum_{p=1}^{N_p} \sum_{N=1, N \neq M}^{N_m} \alpha_N \psi_N^*(\vec{r}_p) \psi_M(\vec{r}_p)}{1 - \tilde{r}^2 \exp(i2kL) - i4\beta\eta \sum_{p=1}^{N_p} \psi_M^*(\vec{r}_p) \psi_M(\vec{r}_p)}. \quad (4.46)$$

The expression $N = 1, N \neq M$ below the sum in the numerator implies summation over all modes except the M -mode.

Equation 4.46 applies for all modes supported by the cavity. Therefore, the set of all these equations forms a system of N_m coupled equations. This set can be written in a more compact form. First, the cavity detuning is defined as $\delta_M := \omega - \omega_M$. Furthermore, it is assumed that the mirror reflectivities are close to unity and that the rotating wave approximation can be applied (see chapter 4.1). These assumptions allow to approximate the phase shift after one round-trip within the cavity as

$$\tilde{r}^2 \exp(i2kL) \approx 1 - q^2 + iq^2 \frac{\delta_M}{\kappa}, \quad (4.47)$$

with κ being the linewidth of the optical resonator. This permits to write for the amplitude of mode M

$$0 = \alpha_M \left(-q^2 + iq^2 \frac{\delta_M}{\kappa} \right) + q\alpha_{M,in} + i4\beta\eta \sum_{p=1}^{N_p} \sum_{N=1}^{N_m} \alpha_N \psi_N^*(\vec{r}_p) \psi_M(\vec{r}_p). \quad (4.48)$$

Next, the following vector and matrices are defined

$$\vec{A} = \begin{pmatrix} \alpha_1 \\ \alpha_2 \\ \vdots \\ \alpha_{N_m} \end{pmatrix}, \quad T = \begin{pmatrix} q^2 & 0 & \cdots \\ 0 & q^2 & \\ \vdots & & \ddots \end{pmatrix}, \quad D = \begin{pmatrix} q^2 \frac{\delta_1}{\kappa} & 0 & \cdots \\ 0 & q^2 \frac{\delta_2}{\kappa} & \\ \vdots & & \ddots & \\ & & & q^2 \frac{\delta_{N_m}}{\kappa} \end{pmatrix},$$

$$M = 4\beta\eta \begin{pmatrix} \sum_{p=1}^{N_p} \psi_1^*(\vec{r}_p) \psi_1(\vec{r}_p) & \sum_{p=1}^{N_p} \psi_1^*(\vec{r}_p) \psi_2(\vec{r}_p) & \cdots & \sum_{p=1}^{N_p} \psi_1^*(\vec{r}_p) \psi_{N_m}(\vec{r}_p) \\ \sum_{p=1}^{N_p} \psi_2^*(\vec{r}_p) \psi_1(\vec{r}_p) & \sum_{p=1}^{N_p} \psi_2^*(\vec{r}_p) \psi_2(\vec{r}_p) & & \\ \vdots & & \ddots & \\ \sum_{p=1}^{N_p} \psi_{N_m}^*(\vec{r}_p) \psi_1(\vec{r}_p) & & & \sum_{p=1}^{N_p} \psi_{N_m}^*(\vec{r}_p) \psi_{N_c}(\vec{r}_p) \end{pmatrix}. \quad (4.49)$$

The vector \vec{A}_{in} is defined identical to \vec{A} . Similar definitions were already used in [111] in the context of a quantum mechanical approach of the detection theory. This allows to write the system of equations above as

$$\vec{0} = (-T + i(D + M))\vec{A} + q\vec{A}_{in}, \quad (4.50)$$

where $\vec{0}$ is the null vector. Rearranging yields

$$\vec{A} = -(-T + i(D + M))^{-1} q\vec{A}_{in}. \quad (4.51)$$

The solution of this equation contains all amplitudes of Hermite-Gaussian modes supported by the cavity. These amplitudes allow to write the total cavity field as

$$E_c(\vec{r}_p, \vec{r}, t) = \sum_{N=1}^{N_m} \alpha_N(\vec{r}_p) \psi_N(\vec{r}) \exp(-i\omega_N t) + \text{c.c.} \quad (4.52)$$

\vec{r} is the vector of the coordinates x , y , and z and t is the time. Note that the expression above is just an approximation since the number of modes supported by a real non-ideal cavity is not infinitely large and Hermite-Gaussian modes are only solutions for the ideal cavity, i. e. perfectly shaped and arranged mirrors and no resonator losses. Nevertheless, most real cavity fields are well approximated by a finite set of Hermite-Gaussian modes [83].

The fields of a cavity, either from a transmissive or reflective setup, are [94]

$$E_{tr} = tE_c, \quad (4.53)$$

$$E_r = -rE_{in} + rt \exp(ikL)E_c, \quad (4.54)$$

respectively. These fields contain information regarding the particles positions, see equation 4.52. However, the imprinted phase shift cannot be directly measured due to its low magnitude. To determine the phase shift, special techniques such as homodyne detection can be applied.

4.3 Homodyne Detection

Fluctuations of the amplitude or the phase of an electromagnetic wave, as they occur in modulated light beams or quantum noise, are usually small. By overlapping the beam of interest with a reference beam, these fluctuations can be measured. For signal and reference fields with identical and different frequencies, these techniques are called homodyne and heterodyne detection, respectively. A modification of homodyne detection can be applied to measure the positions of particles inside a resonator. Therefore, the basic principle of a homodyne detector is explained in the following. Further details can be found in the literature, e. g. in [112], which provides the foundation of this section.

Electromagnetic fields are often represented with complex numbers and usually polar coordinates, as in equation 2.2, are used for this purpose. However, Cartesian coordinates can also be utilised. In the following, the complex amplitude of an arbitrary electric field is denoted as $u(\vec{r}, t)$ with $\vec{r} = (x, y)$. The time dependence t of the amplitude arises due to modulation or noise, though the propagation factor $\exp(-i\omega t)$ is not contained in this quantity.

For the representation of the electric field in Cartesian coordinates the quadrature amplitudes X_1 and X_2 are defined:

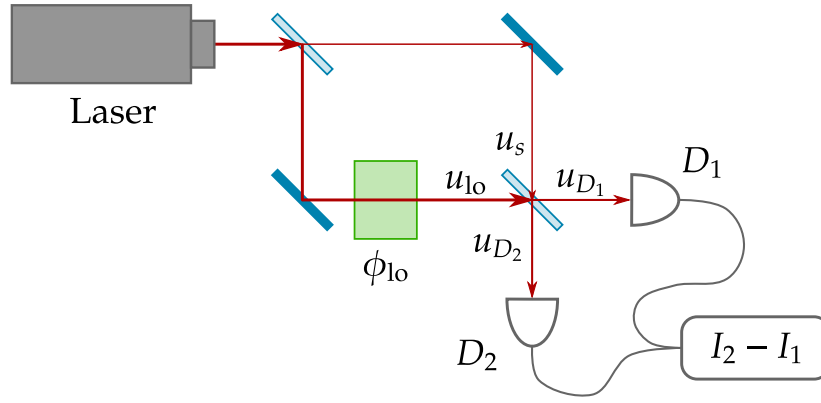


Figure 4.2: Schematic representation of the homodyne detection technique. The beam of a monochromatic light source is split into two different paths to obtain a signal and a reference (local oscillator) beam. The phase of the local oscillator ϕ_{10} can be shifted, e. g. by adjusting the length of the corresponding path. Both beams are mixed again and the intensities of the two resulting beams are measured at the detectors D_1 and D_2 and are subsequently subtracted from each other. In dependence of the phase shift of the local oscillator, this allows to detect the quadratures of the signal directly.

$$X_1(\vec{r}, t) := u(\vec{r}, t) + u(\vec{r}, t)^*, \quad (4.55)$$

$$X_2(\vec{r}, t) := -i(u(\vec{r}, t) - u(\vec{r}, t)^*). \quad (4.56)$$

The electric field is then

$$E(\vec{r}, t) = X_1(\vec{r}, t) \cos(\omega t) + X_2(\vec{r}, t) \sin(\omega t). \quad (4.57)$$

Fluctuations of the amplitude and phase entail alterations of the quadrature amplitudes denoted as δX_1 and δX_2 . The complex amplitude can then be written as

$$u(\vec{r}, t) = u_0(\vec{r}) + \delta X_1(t) + i\delta X_2(t), \quad (4.58)$$

where $u_0(\vec{r})$ represents the constant fraction of the amplitude.

Homodyne detection allows to measure the fluctuations δX_1 and δX_2 of an electromagnetic wave. This electromagnetic wave is denoted as the signal beam in the following. Figure 4.2 depicts a schematic representation of the homodyne measurement. The amplitudes of the signal beam and local oscillator are u_s and u_{10} , respectively. A stable phase relation between both electromagnetic waves is required. For this purpose, both beams can be created by an identical source, e. g. a laser, and a beam splitter. Using identical sources also ensures equal frequencies for both beams. The power of the reference beam should be significantly larger in comparison to the signal.

According to equation 4.58, the amplitudes of the signal and local oscillator beam can be written as

$$u_s(t) = u_{0,s} + \delta X_{1,s}(t) + i\delta X_{2,s}(t), \quad (4.59)$$

$$u_{10}(t) = (u_{0,10} + \delta X_{1,10}(t) + i\delta X_{2,10}(t)) \exp(i\phi_{10}). \quad (4.60)$$

The phase of the local oscillator can be controlled in a homodyne detector, either due to optical elements or simply by adjusting the path length with a piezo element. This allows to control the phase relation between both beams which is mathematically expressed by the factor of

$\exp(i\phi_{10})$ for the reference wave. This additional phase control ensures a constant phase relation between signal and local oscillator. Furthermore, it allows the specific measurement of either $\delta X_{1,s}(t)$ or $\delta X_{2,s}(t)$ as explained later.

After imprinting the additional phase of ϕ_{10} to the local oscillator, both beams are mixed by a beam splitter. Since no further phase control behind the reference beam path is possible, the effects of a beam splitter regarding the phases are discussed here. For simplicity, the phases of the incoming beams are set to zero, in particular the local oscillator ϕ_{10} is dropped for the moment. The beam splitter divides an incoming beam equivalently into two partial beams, i. e. half of the light amplitude is reflected, while the other half is transmitted. The phases imprinted by the beam splitter for reflection and transmission of the signal beam are $\phi_{r,s}$ and $\phi_{t,s}$, respectively, while phase shifts regarding reflections and transmission of the local oscillator are defined accordingly as $\phi_{r,lo}$ and $\phi_{t,lo}$. There is no general rule for these phase shifts, different sizes and materials of the beam splitter imprint different phase shifts. However, it is possible to derive phase relations by assuming energy conservation, i. e. lossless beam splitters. The amplitudes of the outgoing beams of a beam splitter with properties as assumed above are

$$u_{D_1}(t) = \sqrt{\frac{1}{2}}u_s(t) \exp(i\phi_{r,s}) + \sqrt{\frac{1}{2}}u_{10}(t) \exp(i\phi_{t,lo}), \quad (4.61)$$

$$u_{D_2}(t) = \sqrt{\frac{1}{2}}u_s(t) \exp(i\phi_{t,s}) + \sqrt{\frac{1}{2}}u_{10}(t) \exp(i\phi_{r,lo}). \quad (4.62)$$

Due to energy conservation the splitter must preserve power, hence

$$\begin{aligned} |u_{10}(t)|^2 + |u_s(t)|^2 &= |u_{D_1}(t)|^2 + |u_{D_2}(t)|^2 \\ &= |u_{10}(t)|^2 + |u_s(t)|^2 \\ &\quad + \frac{1}{2}u_{10}^*(t)u_s(t) \exp(i(\phi_{t,s} - \phi_{t,lo})) + \text{c.c.} \\ &\quad + \frac{1}{2}u_{10}^*(t)u_s(t) \exp(i(\phi_{r,s} - \phi_{r,lo})) + \text{c.c.} \end{aligned} \quad (4.63)$$

This implies

$$0 = \exp(i(\phi_{t,s} - \phi_{t,lo})) + \exp(i(\phi_{r,s} - \phi_{r,lo})). \quad (4.64)$$

Every lossless beam splitter needs to satisfy this expression. Without loss of generality, the phases are chosen as $\phi_{t,lo} = \phi_{r,lo} = \phi_{r,s} = 0$ and $\phi_{t,s} = -\pi$. The amplitudes of the outgoing beams of the second beam splitter in the homodyne detector are then

$$u_{D_1}(t) = \sqrt{\frac{1}{2}}u_{10}(t) + \sqrt{\frac{1}{2}}u_s(t), \quad (4.65)$$

$$u_{D_2}(t) = \sqrt{\frac{1}{2}}u_{10}(t) - \sqrt{\frac{1}{2}}u_s(t). \quad (4.66)$$

The phase of the local oscillator ϕ_{10} can now be added again. Next, the larger power of the reference beam is considered, hence $|u_{10}(t)|^2 \gg |u_s(t)|^2$ applies and weak terms can be neglected. Combining the two expressions above with the equations 4.59 and 4.60 allows to determine the intensities measured for both detectors:

$$I_{D_1}(t) = \frac{1}{2}c\epsilon_0 |u_{D_1}(t)|^2 \approx \frac{1}{4}c\epsilon_0 \left(|u_{0,lo}|^2 + 2u_{0,lo}\delta X_{1,lo}(t) + 2u_{0,lo} \left(\delta X_{1,s}(t) \cos(\phi_{1o}) + i\delta X_{2,s}(t) \sin(\phi_{1o}) \right) \right), \quad (4.67)$$

$$I_{D_2}(t) = \frac{1}{2}c\epsilon_0 |u_{D_2}(t)|^2 \approx \frac{1}{4}c\epsilon_0 \left(|u_{0,lo}|^2 + 2u_{0,lo}\delta X_{1,lo}(t) - 2u_{0,lo} \left(\delta X_{1,s}(t) \cos(\phi_{1o}) + i\delta X_{2,s}(t) \sin(\phi_{1o}) \right) \right). \quad (4.68)$$

Finally, subtracting both intensities from each other yields

$$\Delta I = I_{D_2} - I_{D_1} = c\epsilon_0 u_{0,lo} \left(\delta X_{1,s}(t) \cos(\phi_{1o}) + i\delta X_{2,s}(t) \sin(\phi_{1o}) \right). \quad (4.69)$$

This is a very powerful and astonishing result. The noise of the local oscillator and the time-independent part of the signal amplitude are completely suppressed. By choosing the phase shift of the local oscillator ϕ_{1o} accordingly, both quadrature fluctuations of the signal are separately measurable, which allows to determine the corresponding phase. Furthermore, the amplitude of the local oscillator allows to amplify the homodyne signal ΔI . A slight modification of a homodyne detector can be used for the detection of cold molecules, see chapter 4.4.

4.4 Homodyne detection of particles inside an optical resonator

Homodyne detection is normally used to measure time dependent signals, i. e. modulation or noise. However, the signal for imaging the particles does not depend on time. The particles imprint a phase shift to the cavity field regarding their positions. To extract the localisation of the particles a spatially resolved measurement of the cavity field is required. Since the interaction effects between field and particles are small, homodyne detection with spatially resolved detectors can be used for this purpose. This measurement of spatially resolved fields is the main difference to conventional homodyne detectors where only the power in both arms is considered. The application of spatially resolved detectors can be seen as a regular homodyne detection done for each pixel of the detectors simultaneously.

A schematic representation of the homodyne detection scheme for particles is depicted in figure 4.3. A beam splitter mixes the transmitted field (optionally the reflected field can be used) through the cavity E_s , which contains information regarding the particles' positions, with a local oscillator E_{lo} . The amplitudes of the beams behind the beam splitter are then $\frac{E_s - E_{lo}}{\sqrt{2}}$ and $\frac{E_s + E_{lo}}{\sqrt{2}}$. The intensities of these two fields are then measured spatially resolved, e. g. by CCD cameras. The intensity of an arbitrary light field with the corresponding electric field amplitude E is given by $I = \frac{1}{2}c\epsilon_0 |E|^2$ [83]. The electric fields at the positions of the detectors are given by

$$E_{D1}(\vec{r}, \vec{r}_p) = \frac{E_s(\vec{r}, \vec{r}_p) + E_{lo}(\vec{r})}{\sqrt{2}} = \frac{1}{\sqrt{2}} \sum_{N=1}^{N_m} \left(\alpha_{s,N}(\vec{r}_p) + \alpha_{lo,N} \right) \tilde{\psi}_N(\vec{r}) \exp(-i\omega t) + \text{c.c.}, \quad (4.70)$$

$$E_{D2}(\vec{r}, \vec{r}_p) = \frac{E_s(\vec{r}, \vec{r}_p) - E_{lo}(\vec{r})}{\sqrt{2}} = \frac{1}{\sqrt{2}} \sum_{N=1}^{N_m} \left(\alpha_{s,N}(\vec{r}_p) - \alpha_{lo,N} \right) \tilde{\psi}_N(\vec{r}) \exp(-i\omega t) + \text{c.c.} \quad (4.71)$$

α_s and α_{lo} are the mode amplitudes of the signal and local oscillator beam, respectively. $\tilde{\psi}$ are Hermite-Gaussian modes, however, these are not identical to the cavity modes. After being uncoupled through the cavity mirror, the modes change their properties as they propagate

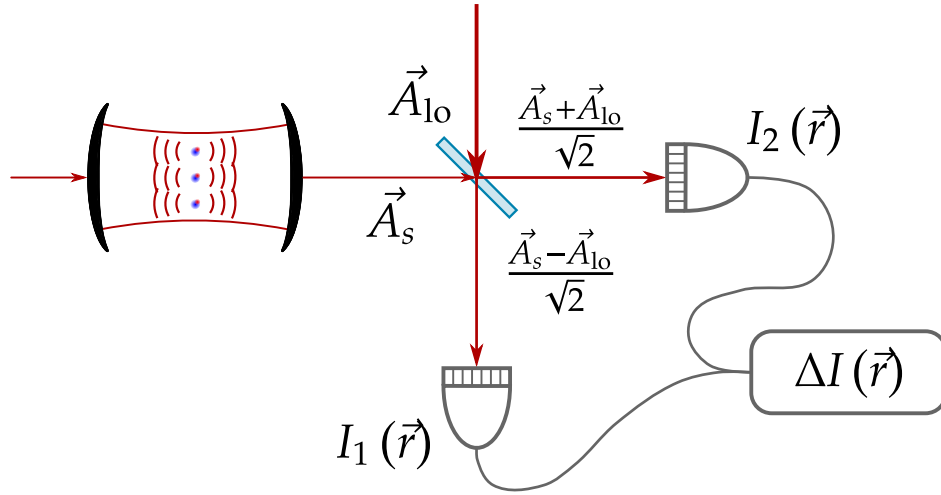


Figure 4.3: Imaging scheme for cold molecules. A homodyne detector is used to read out the alterations of the cavity field induced by the particles. In comparison to common homodyne detection techniques the detectors measure the fields spatially resolved.

over an arbitrary distance and through optical components like lenses. By using the ABCD law, these alterations can be taken into account. The new modes are then indicated by $\tilde{\psi}_N$. Note that the local oscillator beam in general is not described by the same set of Hermite-Gaussian modes as the signal beam. This can be achieved, however, by placing the correct optical elements into the path of the local oscillator.

The intensity difference between detector 1 and 2 is then

$$\Delta I(\vec{r}, \vec{r}_p) = I_{D1}(\vec{r}, \vec{r}_p) - I_{D2}(\vec{r}, \vec{r}_p) = \frac{c\epsilon_0}{4} \sum_{N=1}^{N_m} \sum_{M=1}^{N_m} \tilde{\psi}_N(\vec{r}) \tilde{\psi}_M^*(\vec{r}) \alpha_{s,N}(\vec{r}_p) \alpha_{lo,M}^* + \text{c.c.} \quad (4.72)$$

This is the general expression for the homodyne signal.

Next, assumptions regarding the cavity field are formulated. The interaction between light and particles is usually weak. Hence, the entries in the matrix M in equation 4.51 are much smaller than the entries in T and D . This allows to perform a Taylor expansion leading to

$$\begin{aligned} \vec{A} &= (-T + iD + iM)^{-1} q\vec{A}_{in} \\ &\approx (-T + iD)^{-1} q\vec{A}_{in} + (-T + iD)^{-1} M(-T + iD)^{-1} q\vec{A}_{in}. \end{aligned} \quad (4.73)$$

Furthermore, it is assumed that all cavity modes have the same frequency, i. e. the cavity detuning δ is for all modes the same. T and D are then diagonal matrices with identical values. This allows to write

$$\vec{A} \approx \frac{1}{q^2(-1 + i2\frac{\delta}{\kappa})} \text{Id} q\vec{A}_{in} + \frac{1}{(q^2(-1 + i2\frac{\delta}{\kappa}))^2} q\vec{A}_{in}, \quad (4.74)$$

for the cavity amplitudes. Id is the unity matrix. The first term takes into account the effects of an empty cavity, while the second term contains light-particle interactions. A last assumption is that only the fundamental 00-mode of the cavity is pumped and the corresponding mode amplitude is $a_{in,1}$. Hence, only the first column of the matrix M contributes to the cavity field:

$$\vec{A} = \frac{1}{q^2(-1 + i2\frac{\delta}{\kappa})} qa_{\text{in},1} \vec{e}_1 + \frac{1}{(q^2(-1 + i2\frac{\delta}{\kappa}))^2} qa_{\text{in},1} \sum_{N=1}^{N_m} \sum_{p=1}^{N_p} \psi_N^*(\vec{r}_p) \psi_1(\vec{r}_p) \vec{e}_N. \quad (4.75)$$

The amplitudes of the signal are the transmitted amplitudes of the cavity field and, hence,

$$\alpha_{s,N} = q\alpha_N, \quad (4.76)$$

where α_N are the entries of \vec{A} .

Inserting the mode amplitudes into equation 4.72 allows to write

$$\begin{aligned} \Delta I(\vec{r}, \vec{r}_p) &= \frac{c\epsilon_0}{4} \frac{1}{(-1 + i2\frac{\delta}{\kappa})} \alpha_{\text{in},1} \tilde{\psi}_1(\vec{r}) \sum_{M=1}^{N_m} \tilde{\psi}_M^*(\vec{r}) \alpha_{\text{lo},M}^* + \text{c.c.} \\ &+ \frac{c\epsilon_0}{4} \frac{1}{q^2(-1 + i2\frac{\delta}{\kappa})^2} \alpha_{\text{in},1} \sum_{N=1}^{N_m} \sum_{M=1}^{N_m} \sum_{p=1}^{N_p} \tilde{\psi}_M^*(\vec{r}) \alpha_{\text{lo},M}^* \tilde{\psi}_N(\vec{r}) \psi_N^*(\vec{r}_p) \psi_1^*(\vec{r}_p) + \text{c.c.} \end{aligned} \quad (4.77)$$

As mentioned before, the first terms do not contain information regarding the particles positions. Hence, they need to be dropped by subtracting an empty cavity field. By rearranging the sums, the homodyne detection signal for the particles is

$$\Delta I_p(\vec{r}, \vec{r}_p) = \frac{c\epsilon_0}{4} \frac{1}{q^2(-1 + i2\frac{\delta}{\kappa})^2} \alpha_{\text{in},1} \sum_{M=1}^{N_m} \tilde{\psi}_M^*(\vec{r}) \alpha_{\text{lo},M}^* \sum_{p=1}^{N_p} \psi_1^*(\vec{r}_p) \sum_{N=1}^{N_m} \tilde{\psi}_N(\vec{r}) \psi_N^*(\vec{r}_p) + \text{c.c.} \quad (4.78)$$

To simplify this expression the two following functions are defined

$$\text{Lo}(\vec{r}) := \sum_{M=1}^{N_m} \tilde{\psi}_M^*(\vec{r}) \alpha_{\text{lo},M}^* \quad (4.79)$$

$$\text{J}(\vec{r}, \vec{r}_p) := \sum_{N=1}^{N_m} \tilde{\psi}_N(\vec{r}) \psi_N^*(\vec{r}_p). \quad (4.80)$$

For the detection signal follows

$$\Delta I(\vec{r}, \vec{r}_p) = \frac{c\epsilon_0}{4} \frac{1}{q^2(-1 + i2\frac{\delta}{\kappa})^2} \alpha_{\text{in},1} \text{Lo}(\vec{r}) \sum_{p=1}^{N_p} \psi_1^*(\vec{r}_p) \text{J}(\vec{r}, \vec{r}_p) + \text{c.c.} \quad (4.81)$$

$\text{Lo}(\vec{r})$ is simply the local oscillator field without the oscillating part. $\tilde{\psi}_1^*(\vec{r}_p) \text{J}(\vec{r}, \vec{r}_p)$ can be interpreted as the resolution defining term of the detection method. In particular, the cavity waist and number of involved modes are responsible for the resolution capability through $\tilde{\psi}_1^*(\vec{r}_p) \text{J}(\vec{r}, \vec{r}_p)$.

4.5 Resolution capability

For the detection of particles homodyne signals are measured spatially resolved. The equations 4.72 and 4.81 allow to determine the signal profiles for different particle configurations

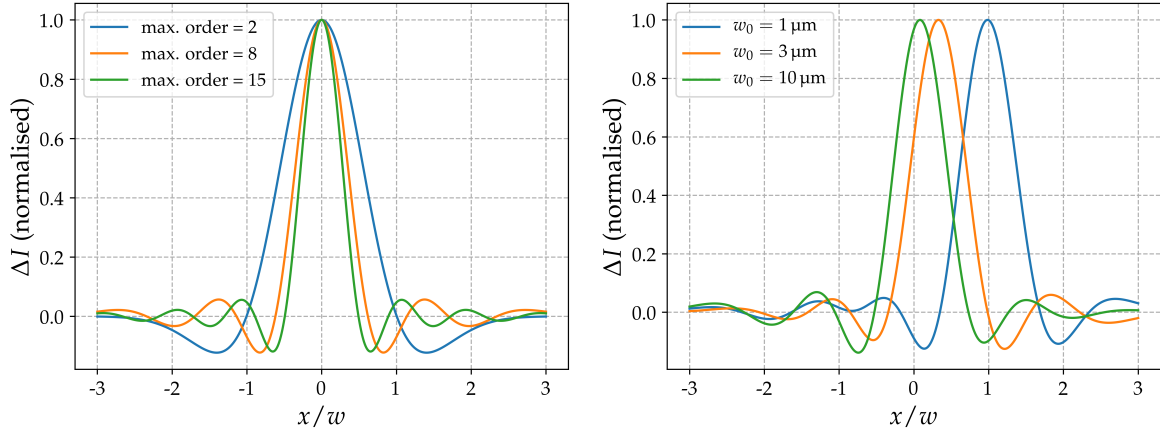


Figure 4.4: Homodyne signals for a single particle along the x -direction. The x -coordinate is depicted in units of the beam size at the detectors positions. A 00-mode drives the cavity, while also serving as a local oscillator with a waist of $w_{0,lo} = 5$ mm. All cavity modes are degenerate. The left side of the figure depicts homodyne signals for different maximum mode orders and a waist of $w_0 = 1.5$ μm . The right side shows signals for a maximum mode order equal to 8 for different cavity waists. While the particle at the left side of the figure is placed at $x_p = 0$ μm , the position of the particle on the right side is $x_p = 1$ μm .

within the resonator. Note that equation 4.72 contains the signal from the cavity background that needs to be subtracted to receive a pure particle driven signal, i. e. the signal of an empty cavity needs to be subtracted. Figure 4.4 depicts normalised homodyne signals ΔI of a single particle placed at the position of the cavity waist. For simplicity, the signal is investigated along the x -direction and the values of x are given in units of the beam size at the detectors surfaces. The cavity modes are assumed to be degenerate, i. e. the resonance frequencies of all modes are identical. A 00-mode serves as the local oscillator and also drives the cavity. The waist of the local oscillator field is $w_{0,lo} = 5$ mm. All these assumptions are also used for the other simulations in this chapter, if not explicitly stated otherwise.

The homodyne signals at the left side of figure 4.4 refer to the maximum mode orders $n + m$ of 2, 8 and 15. Each mode of every order contributes to the signal, hence, the mode numbers given by any possible combination of n and m are 6, 45 and 136, respectively. The cavity waist and particle position for all curves are $w_0 = 1.5$ μm and $x_p = 0$ μm , respectively. A peak in the homodyne signal appears at the corresponding position of the particle that resembles a Lorentzian or Gaussian profile. However, the correct mathematical expression to describe these profiles is $\tilde{\psi}_1^*(\vec{r}_p)J(\vec{r}, \vec{r}_p)$. Furthermore, larger mode orders lead to narrower signal peaks. The homodyne signal can also adopt negative values since it is an intensity difference and not a pure intensity. The number of ripples next to the main peak depend on the maximum mode order and should not be misinterpreted as diffraction.

The left side of figure 4.4 depicts the homodyne signal for different cavity waists. The maximum mode order is equal to 8 for all curves. In this diagram, the particle is not positioned at the optical axis as on the right side of the figure, but at $x_p = 1$ μm . The linewidth of the peak is unaffected by using various cavity waists. However, the peak is shifted to the centre of the diagram for larger resonator waists. Hence, it is more difficult to distinguish between adjacent particles. Both, the maximum mode order supported by the cavity and the waist of the resonator field have an impact on the resolution capability, but in different ways. While larger mode numbers lead to decreased linewidths of the peaks, smaller waists allow to distinguish the different particles more effectively.

To investigate the impact of the cavity waist and mode order further, a suitable definition for the resolution is needed. However, such a resolution criterion can be unambiguous since

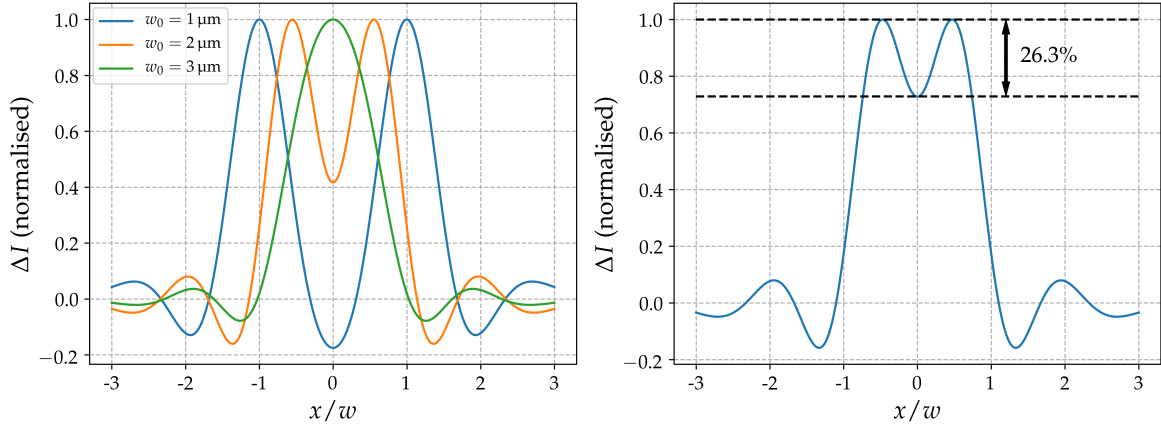


Figure 4.5: Homodyne signals for two adjacent particles. The plot parameters are identical to those from figure 4.4. The particles' positions for the left side of the figure are $x_{p_1} = 1 \mu\text{m}$ and $x_{p_2} = -1 \mu\text{m}$. Homodyne signals for three different waists are depicted. The right side of the figure shows the homodyne signal of two particles that are considered at the resolution limit, where the intensity drops between the main peaks by 26.3%.

the resolution might depend on the evaluation technique applied to the homodyne signal. Several definitions for the resolution capability exist for microscopes, telescopes and other optical imaging systems.

For classical optical microscopes, the Abbe limit is common and given by $\frac{\lambda}{2\text{NA}}$ [113, 114]. NA is the numerical aperture of the optical system and depends on the half angle θ of the imaging beam. This definition could also be applied to the proposed particle detection scheme by using the far-field angle of the cavity field as θ in the numerical aperture. However, this definition might oversimplify the mechanisms behind the detection technique since the effects of higher order modes could only be taken into account indirectly. Therefore, other definitions might be more suitable.

Another common definition for the resolution for two adjacent particles is the Rayleigh criterion first suggested by Lord Rayleigh [115]. The Rayleigh criterion is applicable for diffraction limited systems, assuming that each of the particles emits radiation itself. Due to diffraction, the corresponding intensity profiles have one global main maximum and several local maxima and minima. Two particles are considered to be at the resolution limit when one of the particles is placed at the first minimum of the intensity profile of the other particle [116]. This corresponds to an intensity drop of $I(x = 0) = 0.737 I_{\text{max}}$ between the particles, if I_{max} is the intensity at one of the two intensity peaks, assuming the corresponding particle positions are x_p and $-x_p$. This intensity drop is represented at the right side of figure 4.5 and corresponds to a drop by 26.3%.

The Rayleigh criterion is not an absolute limit since an observer might distinguish two particles even closer to each other. For example, the Dawes limit defines the border for resolvability by an intensity drop of 5% since it was empirically found that a significant number of people are still able to resolve two particles at the corresponding positions [117]. Even if the resolution capability of the proposed detection scheme might depend on the evaluation of the measured signal, the Rayleigh criterion is still an appropriate definition to investigate the impact of cavity waist and maximum mode order on the resolution since it defines an universal criterion, which can be applied for an arbitrary particle-cavity system. As described above the ripples next to the main peak in figure 4.4 do not arise through diffraction and the resolution cannot be defined as the distance between main maxima and first minima. However, the intensity drop between the main maxima of 26.3% can be utilised to define the resolution capability.

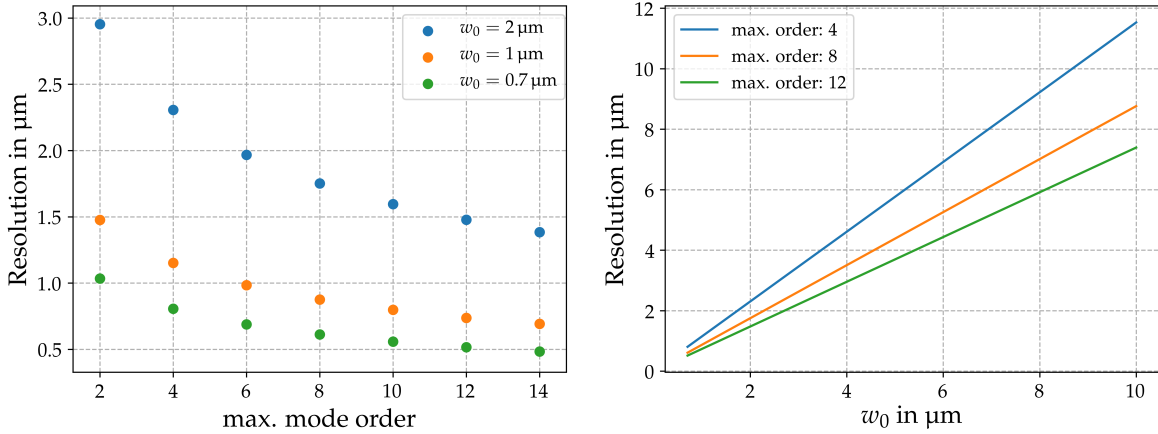


Figure 4.6: Resolution regarding different mode orders and cavity waists. The plot parameters for the curves are identical to those in figure 4.4. The left side depicts the dependency of the resolution regarding the maximum mode order supported by the cavity for different cavity waists. The right side shows the resolution capabilities in dependence of the waist for three different maximum mode orders.

Figure 4.5 depicts the homodyne signal for two particles placed in the waist of the cavity and a maximum mode order equal to 8. The left side of the figure shows the signals for particles located at $x_{p_1} = 1 \mu\text{m}$ and $x_{p_1} = -1 \mu\text{m}$ for different cavity waists. As expected, larger waists make it more difficult to distinguish the signal maxima until both peaks merge together. The right side of the figure depicts a homodyne signal of two particles at the resolution limit according to the above defined resolution criterion.

To find the resolution capabilities for a given set of maximum order modes and resonator waists the position of two particles is tuned until the intensity drop between the main maxima of the homodyne signal is equal to $\Delta I(x=0) = 0.737 \Delta I_{\text{max}}$. The distance to the cavity axis is always the same for both particles, hence, the homodyne signals are symmetric to $x=0$. Results are depicted in figure 4.6. At the left side of the figure, resolution capabilities for three different waists are represented depending on the maximum mode order supported by the cavity. At the right side of the figure, the resolution is shown for three different maximum orders depending on the the cavity waist. As expected, small waists and large mode numbers lead to high resolutions. However, the effect of both quantities regarding the resolution is not the same. While the resolution improves linearly with decreasing waists, the resolutions curves for maximum mode orders flatten for higher orders. Furthermore, the effect of additional mode orders is stronger for larger waists. High resolutions can be obtained for lower mode numbers as long as the waist is small enough. To achieve high resolutions for large cavity waists, although, a very high number of modes would be necessary.

Furthermore, it should be noted that the left side of figure 4.6 only represents the resolutions capability of even modes. In a symmetric configuration, i. e. the distance of both particles to the optical axis is identical, the odd modes do not contribute to the signal since these modes are point symmetric and, therefore, the signals of both particles annihilate each other. However, odd modes contribute to the signal for non symmetric arrangements. The behaviour regarding additional mode orders for the resolution stays the same.

Chapter 5

Detection of Cold Particles - Quantum Description

Classical approaches require less abstract physics in comparison to quantum physical theories and are therefore often more straightforward to understand and may yield simpler dynamics [103]. However, only quantum mechanical theories ensure a complete description of the interaction between light and matter with certainty. A quantum mechanical approach for the molecular detection scheme was developed in the master thesis of Jan Bischoff [111] which relies on the Jaynes-Cummings model explained in the literature, e. g. [118].

In the first section, the Jaynes-Cummings model for an arbitrary number of particles and cavity modes is introduced. The three parts defining the corresponding Hamiltonian are discussed and the Hamiltonian is transformed into the interaction picture. In the second section, the amplitudes of the cavity modes are determined by using the previously defined Jaynes-Cummings Hamiltonian. In the section afterwards the signal-to-noise ratio and number of spontaneously scattered photons is investigated. These first three sections are based on [111]. Finally, the quantum mechanical theory is compared to the classical approach.

5.1 Jaynes-Cummings Hamiltonian

The Hamiltonian of a particle inside an optical cavity consists of three parts describing the particle, the resonator field and the light-matter interaction, respectively. This Hamiltonian is also called the Jaynes-Cummings Hamiltonian [8] and can generally be expressed as

$$\hat{H} = \hat{H}_{\text{particle}} + \hat{H}_{\text{cavity}} + \hat{H}_{\text{interaction}}. \quad (5.1)$$

Variables with roofs indicate operators and operators being a mapping between mathematical spaces. Operators are widely used in quantum mechanics, further information can be found in the literature, e. g. in [119].

Particle Hamiltonian

To suppress absorption the low-saturation regime is considered for the particle. Hence, the particle can be approximated as two-state system, especially valid for molecules despite their complex internal level structure. $|g\rangle$ and $|e\rangle$ denote the ground and excited state of the particle, respectively. The energy of the ground state is set equal to zero and the energy difference between ground and excited state is $E_e - E_g = \hbar\omega_e$. The Hamiltonian of the particle is then [111]

$$\hat{H}_{\text{particle}} = \hbar\omega_e |e\rangle\langle e| = \hbar\omega_e \hat{\sigma}_e. \quad (5.2)$$

\hbar is the reduced Planck constant and the operator $\hat{\sigma} := |e\rangle\langle e|$ is the probability for the particle to be in the excited state.

Cavity field Hamiltonian

The Hamiltonian of the cavity consists of two parts, the field inside the cavity itself and the field pumping the resonator. The first part, the cavity field, is proportional to the number of photons inside the resonator given by the number operator $\hat{a}^\dagger \hat{a}$ where \hat{a} and \hat{a}^\dagger are the annihilation and creation operators of the cavity field, respectively, with the †-symbol indicating that \hat{a}^\dagger is the Hermitian conjugated operator of \hat{a} . The second part, the resonator mode, is driven by an external field E_e with frequency ω_L . Power losses are taken into account in this term by $\sqrt{2\kappa}$, with κ being the linewidth of the resonator. The Hamiltonian for a cavity mode with frequency ω_c is therefore [111]

$$\hat{H}_{\text{cavity}} = \hbar\omega_c \hat{a}^\dagger \hat{a} + i \left(\sqrt{2\kappa} E_e \hat{a} \exp(-i\omega_L t) - \text{h.c.} \right) \quad (5.3)$$

where h.c. is an acronym for Hermitian conjugated.

Interaction Hamiltonian

The third Hamiltonian in equation 5.1 describes the interaction between the particle and cavity mode. This term contains information regarding the particles' position inside the resonator. The interaction Hamiltonian is given by [8]

$$\hat{H}_{\text{interaction}} = -\vec{d} \vec{\hat{E}}. \quad (5.4)$$

\vec{d} is the dipole operator discussed further below and $\vec{\hat{E}}(\vec{r}_p)$ is the electric field operator at the particles' position \vec{r}_p , given by

$$\vec{\hat{E}} = \sqrt{\frac{\hbar\omega_c}{2\epsilon_0 V}} \sqrt{\eta} \psi(\vec{r}_p) (\hat{a} + \hat{a}^\dagger) \vec{e}. \quad (5.5)$$

V is the mode volume of the resonator, \vec{e} is the unity vector in direction of the polarisation of the light field and ψ is the electric field distribution of the cavity mode, e. g. a Hermite-Gaussian mode. The factor of the square root of the effective mode area $\sqrt{\eta} = \sqrt{\frac{2}{\pi w^2}}$ is usually not found in the literature. It is implemented here, since the Hermite-Gaussian modes in chapter 2 are not dimensionless, but have units of a reciprocal length from the factor of $\sqrt{\frac{2}{\pi w^2}}$. This factor ensures that the Hermite-Gaussian modes form an orthonormal set. To avoid two different conventions for Hermite-Gaussian modes it is assumed that the field distribution ψ always contains the factor $\sqrt{\frac{2}{\pi w^2}}$.

Next, the particles creation and annihilation operators are introduced by [8]

$$\hat{\sigma}_+ = |e\rangle\langle g|, \quad (5.6)$$

$$\hat{\sigma}_- = |g\rangle\langle e|, \quad (5.7)$$

respectively. Using parity consideration, i. e. $\langle g|\hat{d}|g\rangle = \langle e|\hat{d}|e\rangle = 0$, the projection of the dipole operator onto the cavity fields polarisation $\hat{d} = \vec{d}\vec{e}$ can be written as [8]

$$\hat{d} = d|g\rangle\langle e| + d^*|e\rangle\langle g| = d\hat{\sigma}_- + d^*\hat{\sigma}_+ \quad (5.8)$$

where $d = \langle e | \hat{d} | g \rangle$. d is the transition dipole matrix element describing the coupling strength between the ground and excited state of the particle [8]. Without loss of generality, d is assumed as real-valued [8] which allows to write the interaction Hamiltonian as

$$\hat{H}_{\text{interaction}} = d \sqrt{\frac{\hbar \omega_c}{2\epsilon_0 V}} \psi(\vec{r}_p) (\hat{\sigma}_+ + \hat{\sigma}_-) (\hat{a} + \hat{a}^\dagger). \quad (5.9)$$

Next, the coupling parameter is introduced:

$$\tilde{g} = d \sqrt{\frac{\omega_c}{2\hbar\epsilon_0 V}} \sqrt{\eta} \psi(\vec{r}_p) = \tilde{g}_0 \psi(\vec{r}_p). \quad (5.10)$$

This quantity is a measure for the interaction strength between particle and cavity mode. The coupling parameter allows to write the interaction Hamiltonian as

$$\hat{H}_{\text{interaction}} = \hbar \tilde{g} (\hat{\sigma}_+ + \hat{\sigma}_-) (\hat{a} + \hat{a}^\dagger). \quad (5.11)$$

In the interaction picture the creation and annihilation operators depend on the time t . The time evolution of the operators are [8]

$$\hat{\sigma}_-(t) = \hat{\sigma}_-(0) \exp(-i\omega_e t), \quad (5.12)$$

$$\hat{\sigma}_+(t) = \hat{\sigma}_+(0) \exp(i\omega_e t), \quad (5.13)$$

$$\hat{a}(t) = \hat{a}(0) \exp(-i\omega_c t), \quad (5.14)$$

$$\hat{a}^\dagger(t) = \hat{a}^\dagger(0) \exp(i\omega_c t). \quad (5.15)$$

The product of these operators in equation 5.11 are therefore proportional to the following factors [8]:

$$\hat{\sigma}_+ \hat{a} \propto \exp(i(\omega_e - \omega_c)t), \quad (5.16)$$

$$\hat{\sigma}_- \hat{a}^\dagger \propto \exp(-i(\omega_e - \omega_c)t), \quad (5.17)$$

$$\hat{\sigma}_- \hat{a} \propto \exp(-i(\omega_e + \omega_c)t), \quad (5.18)$$

$$\hat{\sigma}_+ \hat{a}^\dagger \propto \exp(i(\omega_e + \omega_c)t). \quad (5.19)$$

$\hat{\sigma}_+ \hat{a}$ excites the particle and annihilates a photon, while $\hat{\sigma}_- \hat{a}^\dagger$ does the opposite. $\hat{\sigma}_- \hat{a}$ and $\hat{\sigma}_+ \hat{a}^\dagger$ do not preserve energy conservation since either the particle is excited and a photon is created or the state of the particle and a photon are destroyed at the same time. However, applying the rotating wave approximation, and therefore $\omega_e \approx \omega_c$, leads to fast oscillations in the non-energy conserving products and the corresponding terms can be omitted [8]. The interaction Hamiltonian can then be written as

$$\hat{H}_{\text{interaction}} \approx \hbar \tilde{g} \hat{\sigma}_+ \hat{a} + \text{h.c.} \quad (5.20)$$

Jaynes-Cummings Hamiltonian for a single particle inside a single mode cavity

Inserting the three individual Hamiltonians from equations 5.2, 5.3 and 5.11 into equation 5.1 allows to determine the Jaynes-Cummings Hamiltonian for a single particle inside a single mode resonator. The Hamiltonian can be written as

$$\hat{H} = \hbar \omega_e \hat{\sigma}_e + \hbar \omega_c \hat{a}^\dagger \hat{a} + i \left(\sqrt{2\kappa} E_e \hat{a} \exp(-i\omega_L t) - \text{h.c.} \right) + \hbar (\tilde{g} \hat{\sigma}_+ \hat{a} + \text{h.c.}). \quad (5.21)$$

Jaynes-Cummings Hamiltonian for multiple particles inside a multimode cavity

To generalise the Jaynes-Cummings Hamiltonian for multiple particles and multimode cavities accumulations over the number of all particles N_p and modes N_m for the corresponding terms are necessary:

$$\begin{aligned} \hat{H} = & \sum_{p=1}^{N_p} \hbar\omega_{e,p} \hat{\sigma}_{e,p} + \sum_{N=1}^{N_m} \hbar\omega_{c,N} \hat{a}_N^\dagger \hat{a}_N + i \sum_{N=1}^{N_m} \left(\sqrt{2\kappa} E_{e,N} \hat{a}_N \exp(-i\omega_L t) - \text{h.c.} \right) \\ & + \sum_{N=1}^{N_m} \sum_{p=1}^{N_p} \hbar \left(\tilde{g}_{N,p} \hat{\sigma}_{+,p} \hat{a}_N + \text{h.c.} \right). \end{aligned} \quad (5.22)$$

To transform the Hamiltonian into the interaction picture, i. e. to get rid of the time dependent exponential function in the term driving the cavity, the unitary operator [120]

$$\hat{U} = \exp \left(-i\omega_L \left(\hat{a}_N^\dagger \hat{a}_N + \hat{\sigma}_{e,p} \right) \right) \quad (5.23)$$

can be applied. The new Hamiltonian is then obtained by [111]

$$\hat{H}_{\text{IP}} = i \frac{d\hat{U}}{dt} \hat{U} + \hat{U} \hat{H} \hat{U}^\dagger. \quad (5.24)$$

Finally, the Jaynes-Cummings Hamiltonian in the interaction picture takes the form

$$\begin{aligned} \hat{H}_{\text{IP}} = & \sum_{p=1}^{N_p} \hbar\Delta_p \hat{\sigma}_{e,p} + \sum_{N=1}^{N_m} \hbar\delta_N \hat{a}_N^\dagger \hat{a}_N + i \sum_{N=1}^{N_m} \left(\sqrt{2\kappa} E_{e,N} \hat{a}_N + \text{h.c.} \right) \\ & + \sum_{N=1}^{N_m} \sum_{p=1}^{N_p} \hbar \left(\tilde{g}_{N,p} \hat{\sigma}_{+,p} \hat{a}_N + \text{h.c.} \right). \end{aligned} \quad (5.25)$$

As before, Δ_p and δ_N are the particle-laser and mode-laser detunings, respectively.

5.2 Amplitudes of the cavity modes

The cavity field contains information regarding the particles positions and, hence, the amplitudes of the modes \hat{a}_N supported by the cavity also contain this information. The time evolutions of the annihilation operators of an arbitrary mode N for a reflective resonator and particle p are given by [111]

$$\frac{d\hat{a}_N}{dt} = i \left[\hat{H}_{\text{IP}}, \hat{a}_N \right] - \kappa \hat{a}_N + \sqrt{2\kappa} \hat{a}_{\text{vac},N}, \quad (5.26)$$

$$\frac{d\hat{\sigma}_{-,p}}{dt} = i \left[\hat{H}_{\text{IP}}, \hat{\sigma}_{-,p} \right]. \quad (5.27)$$

The brackets in the equations above indicate commutators which are defined for two arbitrary operators \hat{A} and \hat{B} as $[\hat{A}, \hat{B}] = \hat{A}\hat{B} - \hat{B}\hat{A}$. $\hat{a}_{\text{vac},N}$ is the operator of the vacuum field of mode N . After some algebraic transformations, the time evolutions of the operators are given by [111]

$$\frac{d\hat{a}_N}{dt} = -(\kappa + i\delta_N)\hat{a}_N + \sqrt{2\kappa}(E_{e,N} + \hat{a}_{\text{vac},N}) - i \sum_{p=1}^{N_p} \tilde{g}_{N,p}^* \hat{\sigma}_{-,p}, \quad (5.28)$$

$$\frac{d\hat{\sigma}_{-,p}}{dt} = -i\Delta_p \hat{\sigma}_{-,p} - i \sum_{N=1}^{N_m} \tilde{g}_{N,p} \hat{\sigma}_{3,p} \hat{a}_N. \quad (5.29)$$

Similar results are obtained for atomic cases in [121]. $\hat{\sigma}_{3,p}$ is the inversion operator for particle p and given by $\hat{\sigma}_3 = |e\rangle\langle e| - |g\rangle\langle g|$ [8]. Due to the low-saturation regime $\hat{\sigma}_{3,p} \approx -1$ can be assumed. Furthermore, for $\hat{\sigma}_{-,p}$ an adiabatic elimination [106] is assumed and, therefore, [111]

$$\hat{\sigma}_{-,p} = i \sum_{N=1}^{N_m} \frac{\tilde{g}_{N,p}}{\Delta_p} \hat{a}_N. \quad (5.30)$$

Next, this expression is inserted into equation 5.28 and a steady state solution is considered, since a state of equilibrium for the cavity field is assumed. This leads to

$$0 = -(\kappa + i\delta_N)\hat{a}_N + \sqrt{2\kappa}(E_{e,N} + \hat{a}_{\text{vac},N}) - i \sum_{M=1}^{N_m} \sum_{p=1}^{N_p} \frac{\tilde{g}_{N,p}^* \tilde{g}_{M,p}}{\Delta_p} \hat{\sigma}_{-,p} \hat{a}_M. \quad (5.31)$$

This expression reveals that the annihilation operator for an arbitrary mode N depends on all other modes M supported by the cavity. The annihilation operators of all modes form therefore a set of coupled equations. Analogue to the classical case this system of equations can be written in a more compact form by defining the following vectors and matrices [111]:

$$\vec{A} = \begin{pmatrix} \hat{a}_1 \\ \hat{a}_2 \\ \vdots \\ \hat{a}_{N_m} \end{pmatrix}, \quad \sqrt{K} = \begin{pmatrix} \sqrt{\kappa} & 0 & \cdots \\ 0 & \sqrt{\kappa} & \\ \vdots & & \ddots \end{pmatrix}, \quad D = \begin{pmatrix} \Delta_{c,1} & 0 & \cdots \\ 0 & \Delta_{c,2} & \\ \vdots & & \ddots \\ & & & \Delta_{c,N_m} \end{pmatrix}$$

$$M = \begin{pmatrix} \sum_{p=1}^{N_p} \frac{g_{1,p}^* g_{1,p}}{\Delta_{a,p}} & \sum_{p=1}^{N_p} \frac{g_{1,p}^* g_{2,p}}{\Delta_{a,p}} & \cdots & \sum_{p=1}^{N_p} \frac{g_{1,p}^* g_{N_m,p}}{\Delta_{a,p}} \\ \sum_{p=1}^{N_p} \frac{g_{2,p}^* g_{1,p}}{\Delta_{a,p}} & \sum_{p=1}^{N_p} \frac{g_{2,p}^* g_{2,p}}{\Delta_{a,p}} & & \\ \vdots & & \ddots & \\ \sum_{p=1}^{N_p} \frac{g_{N_m,p}^* g_{1,p}}{\Delta_{a,p}} & & & \sum_{p=1}^{N_p} \frac{g_{N_m,p}^* g_{N_m,p}}{\Delta_{a,p}} \end{pmatrix}. \quad (5.32)$$

Vectors for the vacuum fields \vec{A}_{vac} and driving field \vec{E}_e are defined in the same way as \vec{A} . This allows to write the system of equations for the modes as

$$\vec{A} = (K + i(D + M))^{-1} \sqrt{2} \sqrt{K} (\vec{E}_e + \vec{A}_{\text{vac}}). \quad (5.33)$$

The vector \vec{A} contains all amplitudes of the modes supported by the cavity. The cavity field, in turn, can be used to determine the positions of the particles.

5.3 Signal-to-noise ratio

There are two important properties describing the quality of the proposed imaging technique. The first of these properties is the so-called signal-to-noise ratio (SNR). As the name indicates, the SNR is defined as the ratio between signal strength and measurement noise. This ratio should be at least equal to unity for proper signal qualities since the measurement signal can not be distinguished from the detection noise otherwise. The second important quantity is the number of photons spontaneously scattered by a molecule N_{sp} . In general, the SNR can be increased by longer measurement times, however, this also increases the probability of spontaneously scattered photons.

To obtain an expression for the SNR the signal strength of the homodyne detector as well as the corresponding noise need to be determined. As the previous sections, the following derivations rely on [111]. For the purpose to determine signal strength and noise, the field leaving the cavity is required and given by

$$\begin{aligned}\vec{A}_{\text{out}}(\vec{r}, t) &= \vec{A}_{\text{in}}(\vec{r}, t) + \vec{E}(\vec{r}) - \sqrt{2} \sqrt{\kappa} \vec{A}(\vec{r}, t) \\ &= \left(\text{Id} - 2 \left(\text{Id} + i \sqrt{\kappa}^{-1} (D + M) \sqrt{\kappa}^{-1} \right)^{-1} \right) \left(\vec{A}_{\text{in}}(\vec{r}, t) + \vec{E}(\vec{r}) \right).\end{aligned}\quad (5.34)$$

For simplicity, a single particle at the centre of a single mode cavity is considered, this leads to

$$\begin{aligned}\hat{a}_{\text{out}}(t) &= \left(1 - 2 \left(1 + i \frac{g_0^* g_0}{\kappa \Delta} \right)^{-1} \right) \left(\hat{a}_{\text{in}}(t) - \hat{E}_{\text{in}} \right) \\ &\approx (1 - i\Phi) \left(\hat{a}_{\text{in}}(t) - \hat{E}_{\text{in}} \right).\end{aligned}\quad (5.35)$$

for the outgoing cavity field. Φ is defined as

$$\Phi := \frac{2g_0^* g_0}{\kappa \Delta} \quad (5.36)$$

and can be interpreted as the phase shift induced by the molecule.

Next, the homodyne signal must be determined. A schematic representation of a homodyne detector is illustrated in figure 4.2 and the corresponding classical theory is described in chapter 4.3. Further information regarding the quantum physical theory can be found in the literature, e. g. [122]. The signal of a homodyne detector is given by the difference between the signals of the detectors

$$\Delta \hat{I}_{\text{hs}}(\vec{r}, t) = \hat{I}_2(\vec{r}, t) - \hat{I}_1(\vec{r}, t) = 2c\epsilon_0 \left(\hat{E}_2(\vec{r}, t) \hat{E}_2^\dagger(\vec{r}, t) - \hat{E}_1(\vec{r}, t) \hat{E}_1^\dagger(\vec{r}, t) \right) \quad (5.37)$$

with

$$\hat{E}_1(\vec{r}, t) = i\tilde{\psi}(\vec{r}) \left(\frac{\hbar\omega_L}{2\epsilon_0 c A} \right) \frac{\hat{a}_{\text{out}}(t) - \hat{a}_{\text{lo}}(t)}{\sqrt{2}} \exp(-i\omega_L t), \quad (5.38)$$

$$\hat{E}_2(\vec{r}, t) = i\tilde{\psi}(\vec{r}) \left(\frac{\hbar\omega_L}{2\epsilon_0 c A} \right) \frac{\hat{a}_{\text{out}}(t) + \hat{a}_{\text{lo}}(t)}{\sqrt{2}} \exp(-i\omega_L t) \quad (5.39)$$

being the electric fields at the surfaces of the detectors 1 and 2, respectively. A is the effective mode area of the fields, $\hat{a}_{\text{lo}}(t)$ is the annihilation operator of the local oscillator and $\psi(\vec{r})$ is the field distribution of the electric fields. Inserting these fields into equation 5.37 leads to

$$\Delta \hat{I}_{\text{hs}}(\vec{r}, t) = \frac{\hbar\omega_L}{2A} |\psi(\vec{r})|^2 \left(\hat{a}_{\text{out}}(t) \hat{a}_{\text{lo}}^\dagger(t) - \hat{a}_{\text{out}}^\dagger(t) \hat{a}_{\text{lo}}(t) \right). \quad (5.40)$$

The local oscillator is assumed to be in a coherent state

$$\hat{a}_{\text{loc}}(\vec{r}, t) |\alpha_{\text{lo}}\rangle = \alpha(t) |\alpha_{\text{lo}}\rangle = |\alpha| \exp(i\Theta)(t) |\alpha_{\text{lo}}\rangle. \quad (5.41)$$

Applying this state to $\Delta \hat{I}_{\text{hs}}$ yields

$$\Delta \hat{I}_{\text{loc}}(\vec{r}, t) = \langle \alpha_{\text{lo}} | \Delta \hat{I}_{\text{hs}}(\vec{r}, t) | \alpha_{\text{lo}} \rangle = \frac{\hbar\omega_L}{2A} |\psi(\vec{r})|^2 \left(\hat{a}_{\text{out}}(t) \alpha^*(t) - \hat{a}_{\text{out}}^\dagger(t) \alpha(t) \right). \quad (5.42)$$

Inserting the cavity field from equation 5.35 and applying some algebraic transformations allows to write

$$\begin{aligned} \Delta \hat{I}_{\text{loc}}(\vec{r}, t) = & \frac{\hbar\omega_L}{2A} |\psi(\vec{r})|^2 |\alpha| \left(\cos(\Theta) \hat{E}_{\text{in}} + \left(a_{\text{in}}(t) \exp(i\Theta) + a_{\text{in}}^\dagger(t) \exp(-i\Theta) \right) \right. \\ & \left. - \Phi \sin(\Theta) \hat{E}_{\text{in}} - i\Phi \left(a_{\text{in}}(t) \exp(i\Theta) - a_{\text{in}}^\dagger(t) \exp(-i\Theta) \right) \right) \end{aligned} \quad (5.43)$$

with Θ being the phase of the local oscillator. Setting this phase to $\Theta = -\frac{\pi}{2}$ and assuming that \hat{E}_{in} yields

$$\Delta \hat{I}_{\text{loc}}(\vec{r}, t) = \frac{\hbar\omega_L}{A} |\psi(\vec{r})|^2 |\alpha| \left(i \left(a_{\text{in}}(t) - a_{\text{in}}^\dagger(t) \right) + \Phi \hat{E}_{\text{in}} + \Phi \left(i \left(a_{\text{in}}(t) + a_{\text{in}}^\dagger(t) \right) \right) \right). \quad (5.44)$$

The product of the phase shift with the noise terms is usually small and can be dropped, allowing to write

$$\Delta \hat{I}_{\text{loc}}(\vec{r}, t) = \frac{\hbar\omega_L}{A} |\psi|^2 |\alpha| \left(i \left(a_{\text{in}}(t) - a_{\text{in}}^\dagger(t) \right) + \Phi \hat{E}_{\text{in}} \right). \quad (5.45)$$

In the simplified case of a single molecule placed at the centre of the cavity, a spatially resolved detection of the electric fields is not necessary and the above expression can be integrated:

$$\Delta \hat{I}(t) = \int \Delta \hat{I}_{\text{loc}}(\vec{r}, t) d^2r = \hbar\omega_L |\alpha| \left(i \left(a_{\text{in}}(t) - a_{\text{in}}^\dagger(t) \right) + \Phi \hat{E}_{\text{in}} \right). \quad (5.46)$$

As in the classical case, the noise of the local oscillator is completely suppressed while its amplitude enhances the cavity signal. The time dependent quadrature is given by:

$$\hat{p}_{\text{out}}(t) = \hat{p}_{\text{in}}(t) + \hat{\Phi}, \quad (5.47)$$

where $\hat{p}_{\text{in}}(t)$ is the noise term and $\hat{\Phi}$ the total phase shift induced by the molecule. Detectors measure signals integrated over time and, thus,

$$\hat{p}_{\text{out}} = \frac{1}{\sqrt{T}} \int_T \hat{p}_{\text{out}}(t) dt, \quad (5.48)$$

$$\hat{p}_{\text{in}} = \frac{1}{\sqrt{T}} \int_T \hat{p}_{\text{in}}(t) dt. \quad (5.49)$$

From this follows:

$$\hat{p}_{\text{out}} = \hat{p}_{\text{in}} + \hat{\Phi}. \quad (5.50)$$

Finally, the SNR can be obtained through

$$\text{SNR} = \frac{\langle \hat{p}_{\text{out}} \rangle}{\Delta \hat{p}_{\text{out}}}. \quad (5.51)$$

The noise is given by

$$\begin{aligned} \Delta p_{\text{out}} &= \sqrt{\langle p_{\text{out}}^2 \rangle - \langle p_{\text{out}} \rangle^2} \\ &= \sqrt{\langle p_{\text{in}}^2 \rangle + \langle p_{\text{in}}^\dagger \tilde{\Phi} + p_{\text{in}} \tilde{\Phi}^* \rangle + \langle p_{\text{out}} \rangle^2 - \langle p_{\text{out}} \rangle^2} \\ &= \sqrt{\langle p_{\text{in}}^2 \rangle} \\ &= \hbar \omega_L |\alpha|. \end{aligned} \quad (5.52)$$

For the SNR follows

$$\begin{aligned} \text{SNR} &= \frac{\langle p_{\text{in}} + \tilde{\Phi} \rangle}{\hbar \omega_L |\alpha|} \\ &= \frac{1}{\sqrt{T}} \int_T \langle i(a_{\text{in}} - a_{\text{in}}^\dagger) + \Phi \hat{E}_{\text{in}} \rangle dt \\ &= \frac{\Phi}{\sqrt{T}} \int_T \hat{E}_{\text{in}} dt. \end{aligned} \quad (5.53)$$

Inserting the phase shift from equation 5.36 yields

$$\text{SNR} = \frac{2g_0^2}{\kappa \Delta \sqrt{T}} \int_T \hat{E}_{\text{in}} dt. \quad (5.54)$$

The modulus square of the electric field \hat{E}_{in} is the photon flux and, hence, the normalised integral is equal to the square root of the photon number N_p :

$$\text{SNR} = \frac{2g_0^2}{\kappa \Delta} \sqrt{N_p}. \quad (5.55)$$

The SNR can be increased by stronger light-particle interactions, longer lifetimes of the photons inside the cavity or by exposing the molecule to a larger number of photons. However, all these parameters are also affecting the number of spontaneously scattered photons. This number is given by

$$N_{\text{sp}} = \gamma_s \text{pr}(t) T \quad (5.56)$$

with γ_s being the decay rate of the excited state and $\text{pr}(t)$ being the probability to measure the molecule in the excited state given by

$$\text{pr}(t) = \frac{\Omega^2}{\Omega^2 + \Delta^2} \sin^2\left(\frac{\Omega t}{2}\right). \quad (5.57)$$

Ω is the rabi frequency which can be obtained through

$$\Omega = g_0 \sqrt{\frac{P}{\hbar \omega \kappa}}. \quad (5.58)$$

Assuming that $\Omega \ll \Delta$ applies, which corresponds to the low-saturation regime, allows to write

$$\text{prop}(t) \approx \frac{\Omega^2}{\Delta^2} \sin^2\left(\frac{\Omega t}{2}\right). \quad (5.59)$$

For the number of spontaneously scattered photons follows

$$\begin{aligned} N_{\text{sp}} &= \gamma_s \frac{\Omega^2}{2\Delta^2} T \\ &= \frac{\gamma_s g_0^2 PT}{\Delta^2 \hbar \omega_L \kappa} \\ &= \frac{\gamma_s g_0^2}{\kappa \Delta^2} N_p \\ &= \text{SNR} \frac{\gamma_s}{2\Delta} \sqrt{N_p} \end{aligned} \quad (5.60)$$

with

$$N_p = \frac{PT}{\hbar \omega_L} \quad (5.61)$$

being the number of photons interacting with the molecule. N_{sp} depends on the SNR itself and a careful balance between both quantities needs to be found. Inserting equation 5.55 into equation 5.60 yields

$$N_{\text{sp}} = \text{SNR}^2 \frac{\gamma_s \kappa}{8g_0^2}. \quad (5.62)$$

The equation above contains a quantity called the single particle cooperativity given by [103]

$$C = \frac{4g_0^2}{\kappa \gamma_s}. \quad (5.63)$$

This is a common quantity in the field of cavity quantum electrodynamics and determine if either light-matter interactions or photon losses dominate a particle-cavity system. Inserting the cooperativity into equation 5.62 yields

$$N_{\text{sp}} = \frac{\text{SNR}^2}{2C}. \quad (5.64)$$

Hence, the cooperativity is an important measure for the quality of the proposed imaging method. The cooperativity needs to increase quadratically with the SNR to maintain a constant number of spontaneously scattered photons making large SNRs difficult to obtain. For a SNR equal to unity, the cooperativity should at least be $C = 0.5$ so that not more than one photon is scattered. However, larger cooperativities are preferable to reduce N_{sp} below unity.

5.4 Comparison of the classical and quantum mechanical model

A comparison of the classical and quantum mechanical model for the detection of particles helps to understand whether a classical description of the detection scheme is appropriate or not. The amplitudes of the cavity modes in the classical description are determined by equation 4.51, whereas the quantum physical amplitudes are given by equation 5.33. Qualitatively, both expressions are similar, except the additional vacuum field term for the quantum mechanical model. This meets general expectations since vacuum field fluctuations are a purely quantum optical effect. Furthermore, the matrices in equation 4.51 and 5.33

are different. However, the corresponding classical and quantum mechanical matrices are approximately proportional to each other, the proportionality factor is $\frac{c}{2L}$, i. e. $K = \frac{c}{2L}T$. To prove this, two approximations regarding the cavity linewidth from equation 3.31 are applied. The square root in the denominator can be omitted since the reflectivity of cavity mirrors is usually close to unity. Furthermore, $1 - R = T = q^2$ applies and therefore

$$\kappa \approx q^2 \frac{c}{2L}. \quad (5.65)$$

From this approximation also follows $q^2 \frac{1}{\kappa} \frac{c}{2L} = 1$ and therefore the classical and quantum mechanical D -matrices are proportional to each other, the proportionality factor is $\frac{c}{2L}$. $K = \frac{c}{2L}T$ follows also directly from equation 5.65. To show that the classical and quantum mechanical M -matrices are also proportional to each other by a factor of $\frac{c}{2L}$ the expression[103]

$$d^2 = \frac{3\pi\hbar\epsilon_0\Gamma}{k_e^3} \quad (5.66)$$

between dipole matrix element d and transition linewidth Γ is utilised. k_e is the wavenumber corresponding to the particles transition. Furthermore, either a laser beam far detuned from the particles transition frequency or a low intensity beam can be assumed to suppresses excitations and fulfil the low-saturation regime assumption of the particles. Hence, the imaginary part of the polarisability of the particles can be omitted and

$$\alpha \approx \frac{3\pi\epsilon_0}{k_e^3} \frac{\Gamma}{\Delta} \quad (5.67)$$

applies. Some algebraic transformations using equations 5.66 and 5.67, explained in the appendix A, yield

$$4\beta \frac{c}{2L} = \frac{|\tilde{g}|^2}{\Delta} \quad (5.68)$$

which proves the suggested proportionality between the classical and quantum mechanical M -matrices.

Comparing equation 4.51 and 5.33 reveals different signs between the D - and M -matrices. Both matrices are imaginary and therefore the sign equalises if the complex conjugation of either the classical or quantum physical amplitudes is considered. This can be explained by the change of the sign convention for the Hermite-Gaussian modes in chapter 4.1. The sign is reversed to simplify the overlap integral between dipole radiation and Hermite-Gaussian mode. Switching back to the original sign convention finally equalises the classical and quantum mechanical matrices.

Equation 5.65 reveals that the numerators in equation 4.51 and 5.33 are proportional to each other by a factor of $\sqrt{\frac{c}{L}}$. Hence, the proportionality between classical and quantum mechanical model is given by

$$\left(K_{\text{qm}} + i(D_{\text{qm}} + M_{\text{qm}})\right)^{-1} \sqrt{2} \sqrt{K_{\text{qm}}} = 2 \sqrt{\frac{L}{c}} \left(T_{\text{cl}} + i(D_{\text{cl}} + M_{\text{cl}})\right)^{-1}. \quad (5.69)$$

In conclusion, both theories predict identical results for the particles' positions as long as vacuum field noise can be neglected. The vacuum fluctuations are a pure quantum physical effect and that it is not occurring in the classical theory meets the expectations.

Chapter 6

Cavity Geometries for the Detection of Cold Particles

The fundamental properties of optical cavities are explained in chapter 3. After developing the theoretical foundations behind the detection of cold particles, these properties can be further investigated with respect to their impact on the imaging of the particles. This is necessary to determine resonator geometries that are suitable for the proposed detection scheme. In the following paragraphs the most important properties are briefly summarised.

(i): There are several reasons why a cavity should operate in the stable regime for the detection of particles. First, diffraction losses are significantly larger for unstable resonators [123] weakening the homodyne signals. For higher order modes the diffraction loss even increases further, which might lead to a complete suppression of these modes [123]. Finally, the field distributions of the eigenmodes of unstable cavities are often complicated and might require numerical calculations [123].

(ii): The second requirement for the resonator, the multimode regime, is necessary to enable spatially resolved detection of particles that relies on different field distributions of the cavity modes. A superposition of different transverse modes contains information regarding the particles positions.

(iii): The presence of higher order modes also improves the resolution capability that is the third requirement for the resonator. Apart from the maximum mode order supported by the cavity, small waists are advantageous for this purpose as discussed in chapter 4.5. In the future the detection method should be implemented in the POLAR experiment at the Leibniz University Hannover [75]. This experiment utilises sodium-potassium (NaK) molecules that are loaded into an optical lattice with a lattice constant of $0.532 \mu\text{m}$. A suitable combination of waist and maximum mode order needs to be chosen that allows to resolve two particles in adjacent lattice sites.

(iv): The fourth requirement is a suitable cooperativity. As previously explained in chapter 5.3 the number of spontaneously scattered photons by a molecule depends on the cooperativity and the signal-to-noise ratio. A SNR of at least unity requires a single particle cooperativity $C > 0.5$ to ensure the number of scattered photons is not too large.

The following list summarises all these requirements that a cavity must fulfil to be applicable for the detection of cold atoms or molecules:

- (i) Stable resonator
- (ii) Multimode regime
- (iii) Suitable spatial resolution for an optical lattice with a periodicity of $0.532 \mu\text{m}$
- (iv) $C > 0.5$

Meeting all these requirements at the same time is challenging, especially since improving one property often impairs another. For example, a small cavity waist increases the resolution but might lead to larger cavity linewidths due to additional diffraction losses. The different requirements and their mutual dependences are discussed in the following chapter.

This chapter is organised as follows. First, the most common stable resonators are introduced and their most important properties are summarised to give a brief overview about stable resonators. In the second section, requirements to enter the multimode regime are discussed and a connection between the number of supported modes, mirror reflectivities and cavity parameters, which determine resonator stability, is derived. Hereinafter, the potential waist of a cavity is discussed and the equations relating mode number, mirror reflectivity and cavity parameters are expanded by resonator waist and length. This ensures an expression relating the most important quantities, which define the resolution capability, with each other.

In the fourth section the focus is set on finitely sized mirror apertures and their impact on the photon lifetime in the resonator. Diffraction losses are calculated and the sensitivity of mirror misalignment is discussed. The cooperativity is investigated in the fifth section. In the section afterwards, the critical distance, i. e. the distance of a cavity geometry to the area of instability, necessary to verify the technical feasibility of resonator geometries is introduced. Finally, all aspects are combined to determine cavity geometries suitable for the detection of cold molecules. In this last section, a possible transition of NaK ground-state molecules suitable to utilise the presented detection scheme is proposed, resonator properties are defined and the resulting homodyne signals are simulated.

6.1 Stable resonators

As explained previously in chapter 3, the range of stability for cavities is defined by the mirror parameters: $0 < g_1 g_2 < 1$. Figure 6.1 depicts the area of stability and indicates some of the most commonly used resonator geometries. Note that the presented geometries are located at the edges of stability in the $g_1 - g_2$ -diagram and are therefore strictly speaking not stable. Nevertheless, they are commonly referred to in the literature, e. g. in [82], since often resonators with geometries close to these extreme configurations are utilised, e. g. near-confocal or near-concentric resonators.

(Near-)plane-parallel resonator: This resonator type consists of two (nearly) plane mirrors. The mirror parameters g_1 and g_2 are identical and approach a value equal to unity: $g_1 \approx g_2 \approx 1$. The beam profiles of these resonators are nearly cylindrical, see figure 6.1, and the waist is usually large in comparison to other cavity configurations with identical mirror distances L . Plane-parallel cavities were commonly used in early lasers [82], but are avoided in modern laser applications due to a large mirror misalignment sensitivity.

(Near-)confocal resonator: The length of a confocal cavity is (nearly) identical to the radius of curvature of the resonator mirrors. Therefore, the cavity parameters are approaching values equal to zero. The cavity length is approximately twice the Rayleigh range of the cavity field and confocal resonators have the smallest average beam radius of stable resonators [82]. Commercial Fabry-Pérot interferometers are often confocal resonators since this type is robust against misalignment of the cavity mirrors.

(Near-)concentric resonator: In this configuration, the length of the cavity is twice as large as the mirror radii. The concentric resonator can be seen as the counterpart of the plane-parallel cavity as the absolute value of the mirror parameters of both geometries are identical but have reversed signs. Both types are similarly sensitive to misalignment

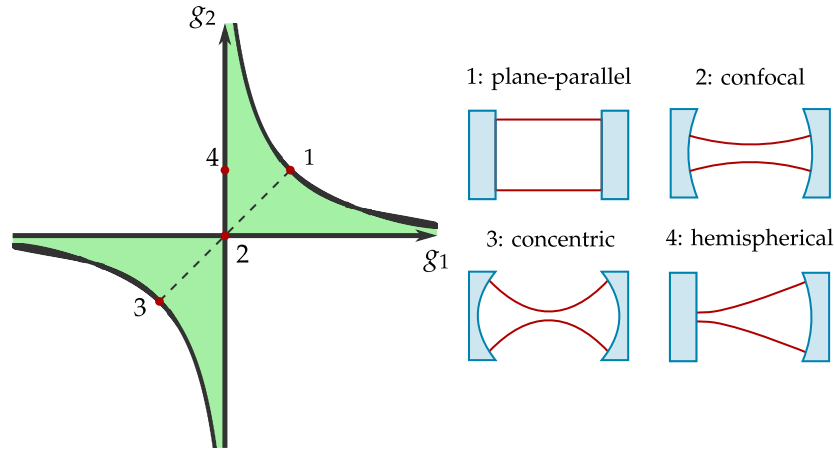


Figure 6.1: Area of stable two-mirror resonators defined by the cavity parameters g_1 and g_2 . The green shaded area indicates stable resonator geometries. Geometries along the dashed line are symmetric, i. e. the cavity mirrors have identical radii of curvature and the waist of the cavity field is placed at the centre. Four common resonator types are indicated by numbered red dots and the corresponding geometries and fields are depicted at the right side of the figure.

and have identical beam sizes at the mirror surfaces. However, the waist of concentric cavities is small compared to other configurations leading to a hourglass shaped beam profile, see figure 6.1.

(Near-)hemispherical resonator: This resonator type consists of a plane and a spherical mirror and the cavity length is identical to the radius of curvature of the spherical mirror. Therefore, one cavity parameter is equal to unity, while the other approaches a value equal to zero. This configuration combines aspects of confocal and concentric resonators, for example, it provides the beam profile of a concentric cavity and the robustness against misalignment of a confocal resonator. Hemispherical resonators are often used for the construction of lasers [82].

6.2 Multimode resonators

The resonance frequencies of a cavity mode depend on the Gouy phase and are given by equation 3.25. This expression reveals that transverse modes of identical orders are always degenerate, e. g. the Hermite-Gaussian 02- and 11-mode have identical frequencies. According to equation 3.25, degeneracy between transverse modes for identical longitudinal orders q is only obtained for a plane-parallel resonator, corresponding not even to a stable geometry, see chapter 3. However, the distance between frequencies of different transverse mode orders can be arbitrarily reduced by approaching unity for the cavity parameters g_1 and g_2 . Other geometries, beside the plane-parallel resonator, also provide (nearly) degenerate modes, but the transverse mode orders belong to different longitudinal modes. For example, in concentric cavities the resonance frequency of the mode with longitudinal order $q + 1$ and transverse order $n + m$ are identical to the frequency of the mode with orders q and $n + m + 1$. Figure 6.2 shows the spectra for different cavity geometries and reveals that decreasing the mirror parameters leads to an increased spacing between the modes $q, n + m$ and $q, n + m + 1$, until the difference is equal to a full free spectral range for $g = -1$ and, hence, leading effectively to mode degeneracy.

Figure 6.2 also shows that the frequency distance of two adjacent mode orders for confocal resonators becomes half the free spectral range, leading to a degeneracy of every second

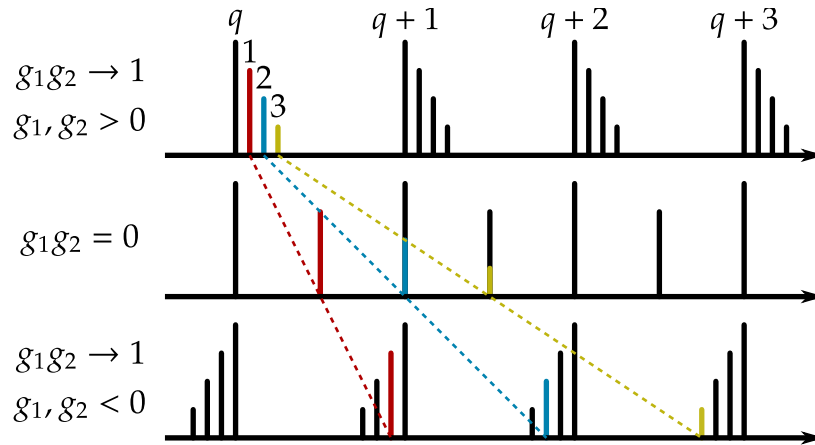


Figure 6.2: Mode spectra for different resonator geometries. Bars with various heights imply different transverse mode orders, denoted by the numbers 1 to 3, while $q, \dots, q + 3$ indicate different longitudinal modes. When the cavity parameter product g_1g_2 is close to unity, the different transverse modes become approximately degenerate. By decreasing the parameter product, the distance between neighbouring transverse modes increases until it reaches half of a free spectral range of longitudinal modes for resonators with $g_1g_2 = 0$. In such geometries, like the confocal resonator, every second order is degenerate. If the product is increased again, but for negative cavity parameters, the distance between adjacent transverse mode order becomes equal to a full free spectral range for $g_1g_2 = 1$ configurations. This leads to a degeneracy for transverse modes belonging to different longitudinal modes.

mode order. Therefore, confocal resonators and all other geometries with $g_1g_2 = 0$, like the hemispherical cavity, are also supporting the multimode regime, even if the number of modes is effectively reduced. Beside the confocal resonator, there are even more geometries where every n -th mode order is degenerate, e. g. every third order for cavities with $g_1g_2 = 0.25$ or every fourth order for $g_1g_2 = \frac{1}{\sqrt{2}}$.

It appears that near-plane-parallel and near-concentric resonators support the largest number of modes since all transverse mode orders are simultaneously degenerated. However, there are other effects that might reduce the number of modes supported by a cavity. First, finite mirror sizes are able to introduce diffraction losses especially for higher-order modes effectively suppressing a mode, see chapter 6.4. Second, the frequency distance between the transverse mode orders does not scale linearly with g_1g_2 due to the dependence on the arccos-function. The frequency difference of transverse modes for confocal resonators is usually smaller than for concentric or plane-parallel cavities. Hence, confocal geometries usually support a higher number of modes than other configurations.

As previously mentioned, a complete degeneracy of transverse modes exists only for geometries at the border of stability. However, full degeneracy can, at least theoretically, be approximated as close as desired by approaching the corresponding unstable resonator configurations, i. e. plane-parallel, concentric or confocal. As explained in chapter 3 the different resonance frequency peaks of a non-ideal cavity are not infinitely sharp, but broadened due to non-perfectly reflecting mirrors, see the definition of the cavity linewidth in equation 3.31. When the broadened resonance peaks of two or more different transverse modes of a resonator overlap the cavity is able to support these modes simultaneously, i. e. the resonator is considered to be in the multimode regime. The multimode regime is a continuous property depending on how strong the peaks of the different modes are overlapping. If the overlap is small the amplitudes of the modes cannot be large at the same time, while strongly overlapping modes can have large values for their corresponding mode amplitudes simultaneously. Thus, it is necessary to define a measure for the number of modes supported

by the cavity. The fundamental 00-mode is used as a reference mode and if the frequency of a transverse mode lies within the linewidth of this reference mode, it is considered as degenerate with the 00-mode. The frequency separation of two different adjacent transverse orders is identical for all orders and in the following called the transverse free spectral range (TFSR). Two modes are considered adjacent when the frequency difference of both is smaller than the frequency difference to any other mode. Hence, adjacent modes do not necessarily belong to the same longitudinal mode. For example, for a confocal resonator the modes $q, n + m + 2$ and $q + 1, n + m$ are considered adjacent, while for a concentric resonator the modes $q, n + m + 1$ and $q + 1, n + m$ are adjacent to each other, see figure 6.2.

Note that the number of modes supported by a cavity in reality might differ from the definition above. Modes might be suppressed by the finite size of the mirrors, see chapter 6.4 or modes can also contribute to the signal even if their resonance frequency is outside of the linewidths of the reference beam. The proposed definition for the number of modes supported by the cavity is supposed to ensure that the contribution of the higher order modes to the homodyne signal is not too weak.

The TFSR of an arbitrary resonator geometry can be estimated from equation 3.25 and is given by

$$\Delta\omega_{\text{TFSR}} = \frac{\pi c}{L} \left(1 - u \frac{\arccos(\pm \sqrt{g_1 g_2})}{\pi} \right), \quad (6.1)$$

where every u -th order is degenerated, e. g. $u = 1$ for concentric, $u = 2$ for confocal and $u = 3$ for $g_1 g_2 = 0.25$ resonators. The maximum transverse mode order supported by the cavity is denoted as v defined as the ratio between the linewidth of the resonator and the TFSR:

$$v := \frac{\kappa}{\Delta\omega_{\text{TFSR}}} = \frac{1 - R}{2\pi \left(1 - u \frac{\arccos(\pm \sqrt{g_1 g_2})}{\pi} \right)}. \quad (6.2)$$

For simplicity both mirror reflectivities are assumed to be identical. Resolving this equation for $\pm \sqrt{g_1 g_2}$ leads to

$$\pm \sqrt{g_1 g_2} = \cos \left(\frac{\pi}{u} \left(1 - \frac{1 - R}{2\pi v} \right) \right). \quad (6.3)$$

This expression allows to connect the product of the cavity parameters with the reflectivity of the mirrors and the number of supported modes. For concentric and confocal resonators this equation simplifies to

$$\sqrt{g_1 g_2} = -\cos \left(\frac{1 - R}{2v} \right), \quad (6.4)$$

$$\sqrt{g_1 g_2} = \sin \left(\frac{1 - R}{4v} \right), \quad (6.5)$$

respectively. Equation 6.3 is later used to connect the mirror reflectivity and maximum mode order with the waist provided by a certain cavity geometry, see chapter 6.3.

6.3 Resonator waist

As previously shown in chapter 4.5, the waist of the cavity field has a strong impact on the resolution capability. An expression for the waist of a resonator is derived in chapter 3, see equation 3.15. According to this expression, several quantities allow to control the waist of resonator, e. g. smaller wavelengths lead to reduced waists. However, since the wavelength

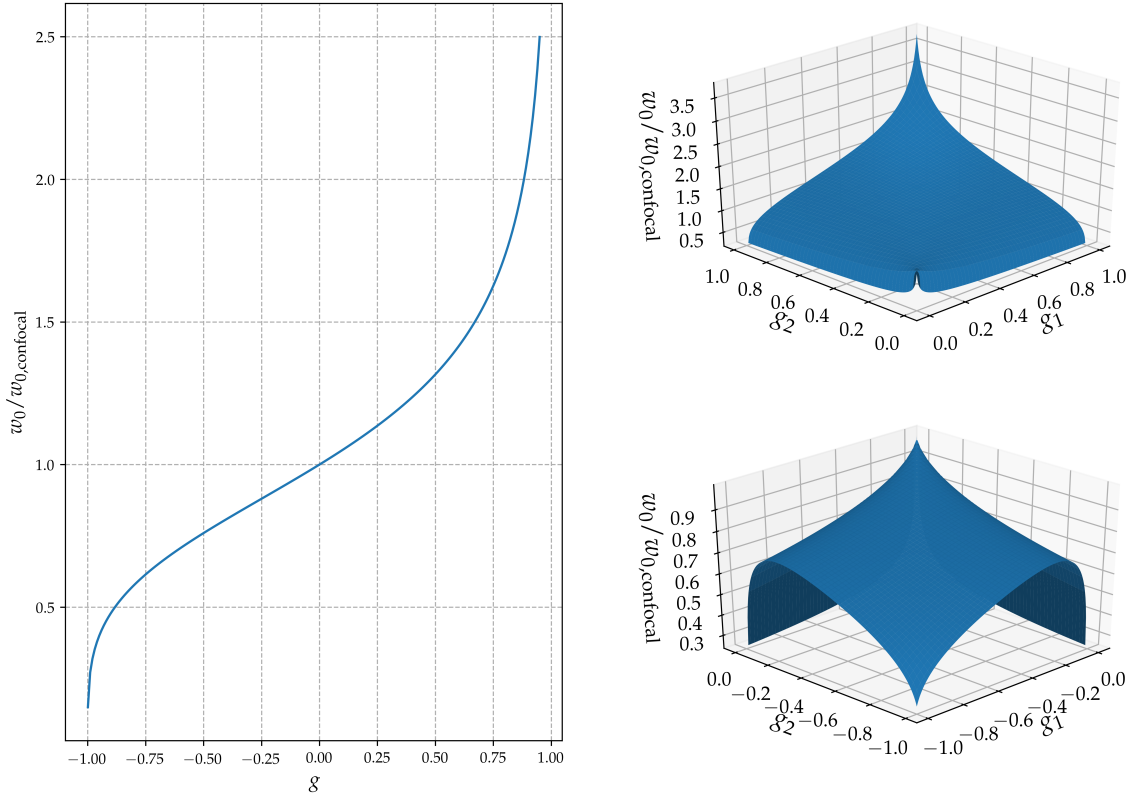


Figure 6.3: Waist of the cavity field as a function of the mirror parameters. The waist is normalised with respect to the waist of a confocal resonator. The left figure depicts the case of symmetrical resonators, i. e. $g_1 = g_2$. The plots on the right side depict 3D diagrams for positive (upper) and negative (lower) cavity parameters.

is determined by accessible transitions of the particles that should be detected, this quantity is unsuitable for the adjustment of the waist. The length of the resonator might also be utilised to modify the cavity waist, but is less suitable since it only scales with the square root and, therefore, very short mirror separations are required for small waists.

Finally, the cavity parameters g_1 and g_2 also impact the resonator waist, however, the corresponding dependency is not straightforward to recognize. Figure 6.3 therefore shows the waist as a function of g_1 and g_2 , where a normalisation by the waist of a confocal resonator is applied. The left side of the figure shows w_0 for symmetric resonators, where small waists are achieved for cavity parameters approaching values of -1 , i. e. for concentric cavities. The dependency in this area is highly non-linear and, hence, sensitive length control might be required to enter the small waist regime. The 3D diagrams on the right side of figure 6.3 reveal another class of resonators with small waists, where asymmetrical cavities with one mirror parameter approaching a value of zero tend to small beam waists.

Equation 6.2 connects the product of the mirror parameters with the mirror reflectivities. This expression can be used to find a mathematical relationship between the waist of a cavity and the number of supported modes by inserting it into equation 3.15. Since the u in equation 6.2 depends on the cavity geometry a case discrimination can be made.

6.3.1 Near-concentric resonators

The connection between mirror reflectivity, mode number and cavity parameter for near-concentric resonators is given by equation 6.4. Inserting this expression into equation 3.15 allows to write

$$\frac{g_1 g_2 (1 - g_1 g_2)}{(g_1 + g_2 - 2g_1 g_2)^2} = \frac{(1 - R)^2}{64v^2}, \quad (6.6)$$

where the addition identities $1 + \cos(x) = 2 \cos^2\left(\frac{x}{2}\right)$ and $\frac{\sin(x)}{\cos\left(\frac{x}{2}\right)} = 2 \sin\left(\frac{x}{2}\right)$ [110] are applied. Hence, the waist can be expressed as

$$w_0^2 = \frac{\lambda L (1 - R)}{8v\pi}. \quad (6.7)$$

This equation contains the cavity waist and also the maximum transverse mode order supported by the cavity with both quantities impacting the resolution capability significantly, see chapter 4.5. Therefore, the expression above is suitable to determine the reflectivities of the mirrors and cavity length for a desired waist and mode number. Furthermore, equation 6.7 is applied in chapter 6.5 to find an expression for the single particle cooperativity.

6.3.2 Near-confocal resonators

Since the mirror reflectivity is usually close to unity, the small-angle approximation can be applied for the product of cavity parameters for near-confocal resonators from equation 6.5, i. e. leading to $\sin\left(\frac{1-R}{4v}\right) \approx \frac{1-R}{4v}$. Inserting this expression into equation 3.15 and applying some algebraic transformations yields

$$w_0^2 = \frac{\lambda L}{2\pi} \frac{4v + (1 - R)}{4v - (1 - R)} \approx \frac{\lambda L}{2\pi}. \quad (6.8)$$

Since R is close to unity, the waist of the cavity is approximately independent of the mirror reflectivity and number of supported modes, which is advantageous as there are less restrictions in the construction of confocal resonators. The waist of this resonator type, on the other hand, is independent of the mirror parameters leaving only L and λ to adjust the minimal beam size within the resonator making it more difficult to reach small waist regimes.

6.3.3 Near-hemispherical resonators

Without loss of generality, the first mirror is set as the plane mirror and hence $g_1 = 1$ applies. The other spherical mirror has a radius of curvature similar to the length of the cavity and is therefore approaching a value close to zero. Hence, the cavity parameter product is also approximately equal to zero and every second transverse mode order is degenerated. This yields

$$\sqrt{g_2} = \sin\left(\frac{1 - R}{4v}\right) \approx \frac{1 - R}{4v}, \quad (6.9)$$

for the second mirror parameter, where the small-angle approximation is applied. Inserting the expression above and $g_1 = 1$ into equation 3.15 leads to

$$w_0^2 = \frac{\lambda L (1 - R)}{4v\pi} \quad (6.10)$$

for the resonator waist. Initially, this expression seems to differ from the result for near-concentric cavities by a factor of $1/2$. However, a hemispherical cavity is half a concentric resonator and both provide similar fields for identical spherical mirrors, provided that the length of the hemispherical resonator is half the value of the concentric cavity. This effectively eliminates the factor of $1/2$ leading to similar values for the waist for both resonator types. This also underlines the hybrid character of hemispherical cavities, where the mode spectrum resembles the spectrum of a confocal resonator and the waist is identical to concentric cavities.

λ in nm	w_0 in μm	v
532	1.0	4
532	1.5	10
532	2.0	18
767	1.0	1
767	1.5	4
767	2.0	8

Table 6.1: The maximum mode order v that does not violate the paraxial approximation due to large far-field angles for different cavity waists w_0 and wavelengths λ .

6.3.4 Paraxial approximation and maximum number of supported modes

Equations 6.7 and 6.10 connect the number of supported modes with the cavity waist for concentric and hemispherical cavities, respectively, while equation 6.8 reveals that both quantities are independent in the case of confocal resonators. However, these expressions take only the overlap of mode frequencies and linewidth of the fundamental mode into account.

There are other properties potentially limiting the number of supported modes by a cavity, the most fundamental probably is the far-field angle Θ of the resonator field. A critical assumption in the derivation of Hermite-Gaussian modes is the paraxial approximation (an approximation also made indirectly for the overlap integral in equation 4.6) that is violated for far-field angles above 30° , see chapter 2.1. Due to the beam parameter product in equation 2.25, this angle depends on the fields waist, i. e. small waists entail large values for Θ . This effect is even stronger for higher order modes, where the far-field angle scales with the mode order m by a factor of $\sqrt{2m+1}$. Hence, the number of modes might limit the minimal beam size and vice versa due to the beam parameter product and balance between both quantities needs to be found. An overview of different combinations for waist and mode number is depicted in table 6.1, where two different wavelengths are taken into account.

Table 6.1 indicates the significant limitation of the maximum mode order due to the paraxial approximation. According to equation 6.7, a concentric cavity with a mirror reflectivity of $R = 0.98$, a wavelength of $\lambda = 532$ nm and a waist of $w_0 = 1$ μm could still support a maximum transverse mode order of 8. However, table 6.1 reveals that this value is limited to 4. Nonetheless, the equations 6.7, 6.8 and 6.10 are still required to determine the resonator length and mirror reflectivity once the number of modes and waist is given.

Note that the number of modes might be also limited by other effects, e. g. by the finite size of the mirrors, see chapter 6.4. However, the paraxial approximation gives a finite upper limit for the number of modes supported by a cavity.

6.4 Finitely sized resonator mirrors

6.4.1 Diffraction loss

The previous assumption of infinitely sized mirrors is valid as long as the beam size at the surface of the mirrors is small compared to the width of the mirrors. However, since small waists are required for a suitable particle resolution the corresponding far-field angles, especially of the higher-order modes, are large leading to increased beam sizes at the mirrors surfaces. A compensation of the magnified beam radii due to large mirror apertures is restricted since the maximum width of a spherical mirror is twice the radius of curvature r . Only plane mirrors can be constructed as large as desired. In conclusion, the assumption of

unconfined cavity mirrors is not certainly valid for the proposed detection scheme. Finitely sized mirrors also change the mirror parameters according to [124]

$$G_1 = \frac{a_1}{a_2} g_1, \quad (6.11)$$

$$G_2 = \frac{a_2}{a_1} g_2, \quad (6.12)$$

where a_1 and a_2 are the widths of the mirrors. In the following, identical mirror apertures are assumed to avoid more complications regarding the cavity parameters g_1 and g_2 . The beam sizes at the mirrors are also functions of these parameters and given by the equations 3.11 and 3.17, respectively, figure 6.4 depicts the beam size depending on g_1 and g_2 , where the beam size is normalised by the value $w_{m,\text{confocal}} = \sqrt{\frac{\lambda L}{\pi}}$ of a confocal cavity. The left side of the figure shows the symmetric case for identical cavity parameters, while the diagrams on the right side show the beam sizes at mirror 1 (upper) and mirror 2 (lower).

Initially, it might seem logically that only small waist geometries provide large beam sizes at the mirrors due to large far-field angles. However, concentric and plane-parallel resonators have identical values revealed by the equations 3.11 and 3.17. Therefore, small waist configurations can be applied without disadvantage. The right side of figure 6.4 reveals that asymmetrical resonators have a large beam size at one mirror, while the beam size at the other mirror is small.

As previously mentioned the finite size of the mirrors might limit the number of modes supported by a cavity. As a rule of thumb, a mode is oscillating in a resonator when the beam size at the mirrors does not exceed the aperture of the mirror a . However, even when the mirror width is large enough to support a certain mode, diffraction loss might still occur leading to an broadened linewidths of the mode. This additional diffraction loss can be interpreted geometrically. The cavity field is given by a cone and the fraction of the cone not covered by the mirror aperture cannot be reflected and therefore leaks out of the resonator.

Beside additional diffraction loss, the field distribution of the modes can also deviate from ideal Hermite-Gaussian beams, if the mirror aperture is too small. Correct results for real field profiles and losses can be obtained by solving a coupled system of two Kirchhoff integral equations [83, 125]. There exists no analytical solutions for this equation system and general statements regarding the solution are difficult to make [83]. In more recent publications superpositions of modes for unconfined mirrors [126] or numerical simulations of the eigenvalue problem [127] were used to determine correct mode structures and losses. However, in [128] a less complicated approach was suggested to estimate at least diffraction loss for confined mirrors by performing an integration of an arbitrary (ideal) cavity mode over the range of the mirror surface:

$$\gamma = \int_0^a \int_0^{2\pi} |\psi_N|^2 \rho d\phi d\rho. \quad (6.13)$$

$\sqrt{\gamma}$ is the loss factor of the cavity. To avoid confusion, it should be noted that in the literature two different quantities are common as a measure for reduced photon lifetimes, the loss ΔV and the loss factor $\sqrt{\gamma}$, both connected through $\Delta V = 1 - \sqrt{\gamma}$ [83]. If $\sqrt{\gamma}$ is close to unity, i. e. if ΔV approaches a value of zero, the diffraction loss of a cavity is small.

In equation 6.13 ψ_N are again the Hermite-Gaussian modes of the cavity. Since cavity mirrors have usually round shapes, polar coordinates are suitable, which are usually used for Laguerre-Gaussian modes. However, Hermite-Gaussian modes are more commonly observed in resonators due to mirror imperfections and therefore these are used to estimate the diffraction loss that requires a coordinate transformation according to $x^2 + y^2 = \rho^2$, $x = \rho \cos(\phi)$ and $y = \rho \sin(\phi)$. Furthermore, it should be noted that a correct normalisation

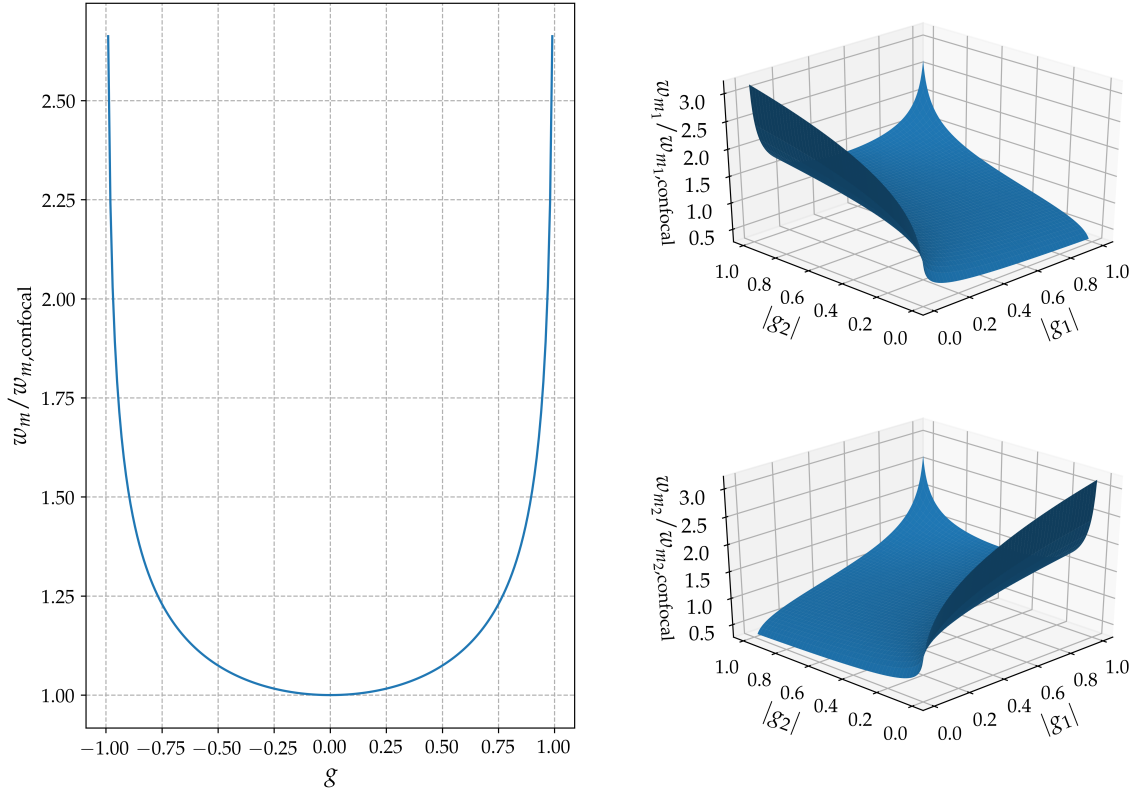


Figure 6.4: Beam sizes at the mirror surfaces for different cavity parameters g_1 and g_2 . The figure on the left side shows the symmetric case, where both parameters are identical. The beam size is independent from the sign of the cavity parameters and, hence, concentric and plane-parallel configurations have identical beam sizes at the position of the mirrors. The upper figure on the right side shows beam sizes at the first and the bottom figure at the second mirror for asymmetrical cavities. Strong asymmetrical geometries have large beam sizes at one mirror, while the size at the other mirror is small.

of the modes is required to obtain correct results for the loss factor in equation 6.13. If other factors than the ones in equation 2.26 are utilised, equation 6.13 must be normalised again by a division of an integral over an infinite large mirror surface $\int_0^\infty \int_0^{2\pi} |\psi_N|^2 \rho d\phi d\rho$.

The additional diffraction loss leads to a reduced lifetime of a photon within the cavity, i. e. the resonator linewidth is broadened. Mathematically, this can be taken into account by multiplying the mirror reflectivity with $\sqrt{\gamma}$ leading to an effective reflectivity $R_e = R \sqrt{\gamma}$. For the resonator linewidth then follows

$$\kappa_e = \frac{c}{2L} \frac{1 - R_e}{\sqrt{R_e}}. \quad (6.14)$$

Figure 6.5 depicts the diffraction loss estimated by equation 6.13 for different Hermite-Gaussian modes in dependency of the mirror width a , where a is given in units of the beam size of the fundamental 00-mode at the mirrors surface. The left side of the figure indicates that the mode order significantly impacts the diffraction loss meeting the expectations since higher order modes also have large beam radii. Furthermore, the loss factors for different transverse modes of identical orders differ from each other. This is shown in more detail on the right side of figure 6.5, where the diffraction loss for the modes of order 6 is depicted. The highest order in either the x - or y -direction mostly determines the diffraction loss of a mode due to the more rectangular shape of the corresponding profile. In conclusion, it must be ensured that the diffraction loss of the most rectangular mode of the highest order

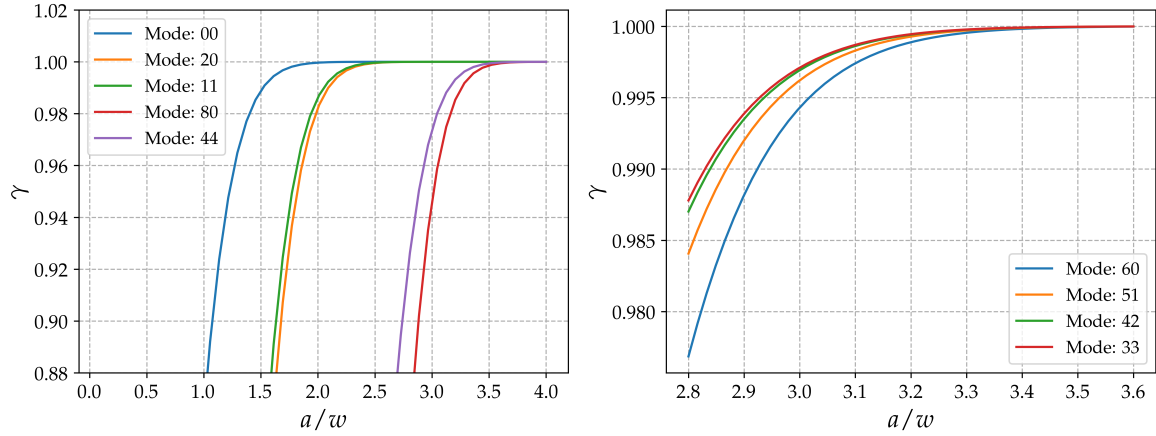


Figure 6.5: Diffraction losses of resonators due to finitely sized mirrors. The left side shows the square of the loss factor γ for the Hermite-Gaussian modes 00, 20, 11, 80 and 44. For identical mirror apertures a , larger mode order leads to increased losses. The diagram also indicates that the loss is different for various transverse modes of identical order. This is specifically shown on the right side of the figure, where γ is plotted for the modes of order 6. More rectangular modes have larger losses since they have larger beam dimensions either along the x - or y -direction.

supported by the cavity does not broaden the linewidth of the cavity to much to ensure suitable homodyne signal quality for the detection of cold particles.

The diffraction loss alone has only limited significance since identical loss factors entail different effects on the cavity linewidths for different mirror reflectivities. Therefore, figure 6.6 depicts the broadened resonator linewidths from equation 6.14 for various reflectivities and modes. The values within the figure are normalised by the linewidth of an unconfined cavity, i. e. with a loss factor equal to unity.

The left side of figure 6.6 depicts the linewidth broadening of a 00-mode depending on the mirror aperture for mirror reflectivities of 0.98, 0.99 and 0.995. Even for the smallest reflectivity, a ratio of approximately $a/w_m = 1.7$ is required to avoid an increase of the linewidth by 1.1. The right side of the figure depicts linewidths broadening for different transverse modes of order 6 with a mirror reflectivity of 0.98. Here, a ratio of roughly $a/w_m = 3.1$ is necessary to keep the broadening of the linewidth of the 60-mode below 1.1. Such ratios between aperture and beam size are still feasible.

6.4.2 Misalignment sensitivity

In the previous section the diffraction loss is interpreted by a cone of the cavity field that does not completely overlap with the mirror due to a finite aperture. Another effect that might increase cavity loss is a misalignment of the mirrors leading to a shift between cone and mirror surface. Figure 6.7 illustrates a resonator where the second, i. e. the right mirror, is tilted by an angle α_2 leading to a rotation of the optical axis of the cavity that is defined as the line passing through the centres of curvature of the resonator mirrors c_1 and c_2 [83]. The rotation of the optical axis entails a shift of the intersection between the axis and the mirror surface by Δ_{12} for the first and Δ_{22} for the second mirror in comparison to a perfectly aligned resonator. These distances are given by [83]

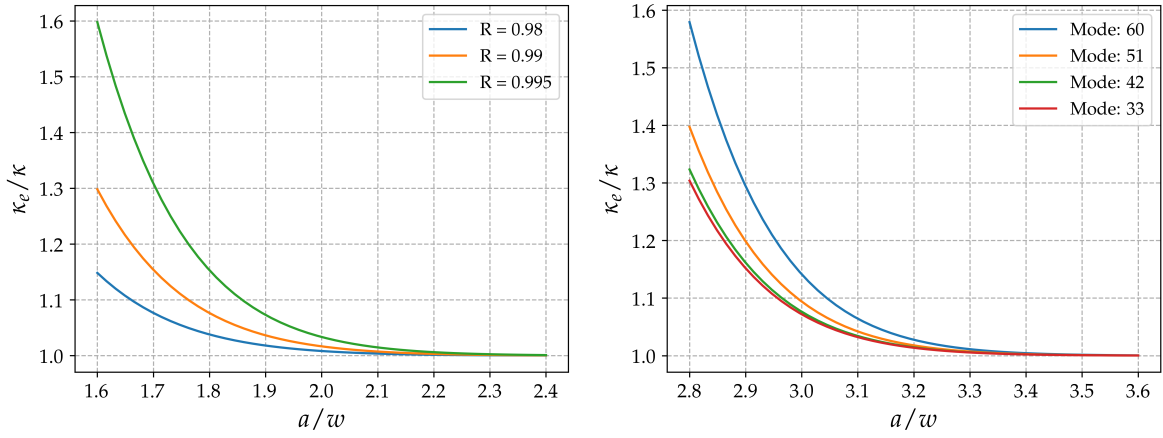


Figure 6.6: Broadened cavity linewidth κ_e normalised by the cavity linewidth without additional diffraction loss. The left side of the figure shows linewidth broadening of the 00-mode for different reflectivities. The right side depicts the increased linewidth for the modes of order 6. The corresponding mirror reflectivity is $R = 0.98$.

$$\theta_2 = \alpha_2 \frac{1 - g_1}{1 - g_1 g_2}, \quad (6.15)$$

$$\Delta_{12} = \alpha_2 \frac{L}{1 - g_1 g_2}, \quad (6.16)$$

$$\Delta_{22} = \alpha_2 \frac{g_1 L}{1 - g_1 g_2}. \quad (6.17)$$

Cavity eigenmodes propagate along the optical axis and the shifted intersection points result in increased diffraction losses due to a decreased overlap of the cavity field with the mirror surface. Again, an exact estimation of these losses would require to solve the coupled Kirchhoff integral equations. However, in [129] the impact of misalignment was investigated with perturbation theory leading to a less complicated approach to determine the diffraction loss. The loss factor for tilting mirror i by an angle α_i is given by

$$V_i = V_0 \left(1 - \alpha_i^2 \frac{s^2}{\exp(2s^2) - 1} \frac{\pi L}{\lambda} \frac{\sqrt{g_j}}{g_i} \frac{1 + g_1 g_2}{(1 - g_1 g_2)^{3/2}} \right), \quad (6.18)$$

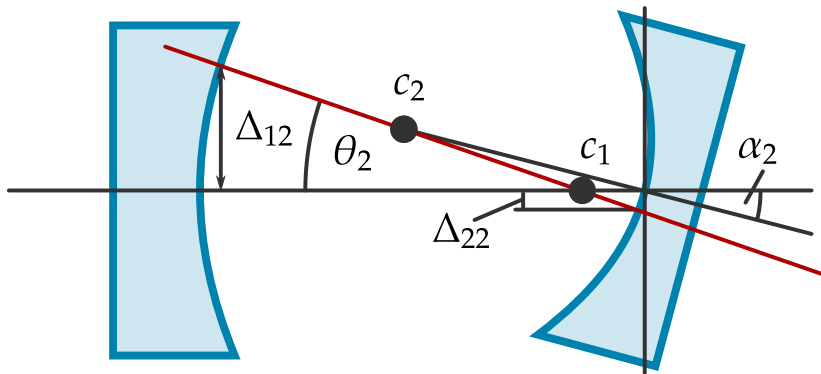


Figure 6.7: Misaligned cavity due to rotation of the right (second) mirror by an angle of α_2 . The tilt of the mirror leads to a rotation of the optical axis by θ_2 shifting the intersection points of the optical axis and the mirrors surfaces.

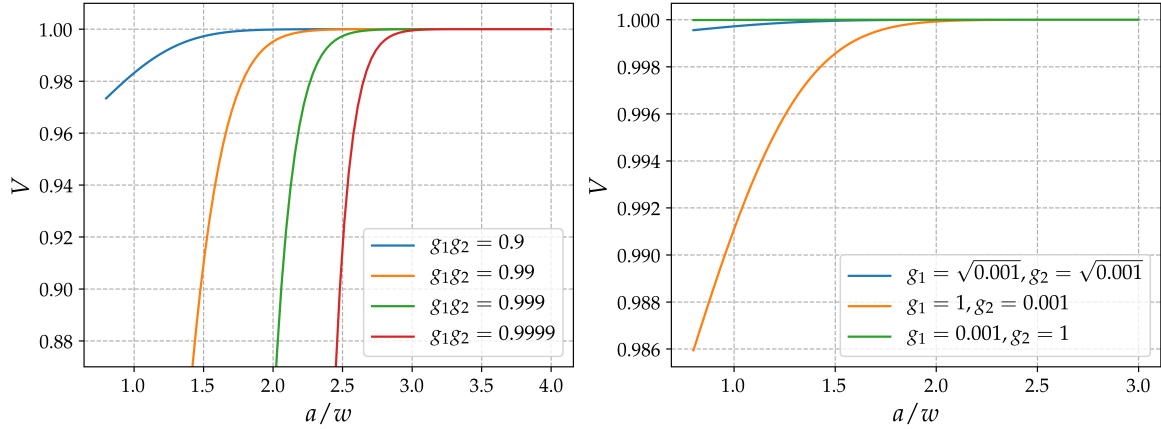


Figure 6.8: Loss factor depending on the mirror width for different cavity geometries. The left side shows configurations with a cavity parameter product close to unity, while the right side shows the case of g_1g_2 approaching a value equals to zero. The length of the resonator is set to $L = 1$ cm, the wavelength to $\lambda = 532$ nm and the mirror rotation is $\alpha = 0.01^\circ$.

where $s = \frac{a}{w_m}$ is the ratio between the mirror aperture a and the beam size at the mirrors surface w_m . V_0 is the loss factor for perfectly aligned mirrors. If the only source of diffraction loss beside cavity misalignment is the finite size of the aperture of the mirror, $V_0 = \sqrt{\gamma}$ applies. Note that equation 6.18 is only valid for 00-modes, but in a multimode resonator higher order modes have larger beam sizes and therefore inflict more losses than the pure Gaussian beam. However, calculations have shown that diffraction losses of 00-modes are larger than losses of higher order modes, if both fields are scaled to identical sizes. Therefore, the application of equation 6.18 might still be useful to approximate appropriate angles.

According to equation 6.18, the misalignment sensitivity depends on several quantities in different ways, for example, the loss factor scales linearly with the cavity length and wavelength. The impact of the mirror rotation α , in comparison, contributes quadratically to the diffraction loss. Mirror aperture and cavity parameters have the most critical effect regarding the loss factor due to their strong non-linear behaviour.

To illustrate this, figure 6.8 depicts the loss factor as a function of the mirror width a for different resonator geometries with $V_0 = 1$. The left side visualises configurations with mirror parameters close to unity, while the right side shows configurations where g_1g_2 approaches a value of zero. The effect of mirror misalignment becomes more severe for mirror parameter products closer to a value of unity, the effect is also independent from the sign of the g 's, i. e. concentric and plane-parallel resonators are the geometries most sensitive to misalignment, while confocal cavities are most robust against tilted mirrors.

The diagram for $g_1g_2 \approx 0$ on the right side of the figure illustrates the loss factor due to mirror misalignment for a near-confocal and a near-hemispherical cavity with identical mirror parameter products. The loss factors for both mirrors of the confocal cavity are identical due to the symmetry of the resonator. In comparison to this, the loss factor of the plane mirror is slightly reduced, while the losses of the spherical mirror are significantly enhanced and in total the diffraction loss of the hemispherical and other asymmetrical cavities is larger than the losses of confocal resonators assuming both have identical tilted mirrors. The total increased loss for asymmetrical cavities is a general result for all geometries and not only for the special case depicted in figure 6.8. Compared to concentric or plane-parallel resonators the losses of asymmetrical cavities with $g_1g_2 \approx 0$ are quite small.

In conclusion, cavity geometries where the product of the mirror parameters is close to zero are more stable and more suitable than plane-parallel or concentric configurations with

regard to misalignment sensitivity. However, cavities with $g_1 g_2 \approx 1$ are also valid options, but might be more technically challenging to be implemented.

6.5 Cooperativity

The idea behind the application of a cavity for the proposed detection scheme is to enhance the signal by increasing the probability of interaction between photon and particle. However, the repeated interaction also increases the chance of a spontaneously scattered photon that, in turn, changes the state of the molecule. As previously explained in chapter 5.3 the single particle cooperativity determines for a certain SNR the number of spontaneously scattered photons. For a SNR equal to unity the cooperativity should be $C > 0.5$ to avoid a larger number of scattered photons. However, this value should be seen as a lower threshold for the cooperativity since larger values reduce the probability to lose the molecular state.

The cooperativity is proportional to the product of $\frac{\tilde{g}_0}{\gamma_s}$ and $\frac{\tilde{g}_0}{\kappa}$. These ratios are also important for cQED [103] e. g. by defining the strong coupling regime [130] and in the following the cooperativity is determined by the product of these two ratios for the case that the ratios should be required for later experiments.

Since γ_s is a constant, the ratio $\frac{\tilde{g}_0}{\gamma_s}$ can only be adjusted through the coupling parameter \tilde{g}_0 , which depends on the wavelength of the particles' transition and the mode volume of the cavity V . The mode volume is $V = \int_{\text{cavity}} |\psi|^2 dV = \frac{\pi w_0^2 L}{4}$ with ψ being the cavity mode. Hence, the coupling parameter is adjustable through λ , w_0 and L . For multimode cavities, appropriate for the detection of cold particles, these quantities are not independent from each other and the corresponding connections for concentric, confocal and hemispherical resonators are given by the equations 6.7, 6.8 and 6.10, respectively. Inserting these equations into $\frac{\tilde{g}_0}{\gamma_s}$ and applying some algebraic transformations allows to write

$$\left(\frac{\tilde{g}_0}{\gamma_s}\right)_{\text{concentric}} = d \sqrt{\frac{(1-R)c}{2\hbar\epsilon_0 v \pi}} \frac{1}{w_0^2 \gamma_s}, \quad (6.19)$$

$$\left(\frac{\tilde{g}_0}{\gamma_s}\right)_{\text{hemispherical}} = d \sqrt{\frac{(1-R)c}{\hbar\epsilon_0 v \pi}} \frac{1}{w_0^2 \gamma_s}, \quad (6.20)$$

$$\left(\frac{\tilde{g}_0}{\gamma_s}\right)_{\text{confocal}} = \sqrt{2}d \sqrt{\frac{c}{\pi\hbar\epsilon_0}} \frac{1}{w_0^2 \gamma_s} \quad (6.21)$$

for concentric, hemispherical and confocal resonators. For all three geometries, $\frac{\tilde{g}_0}{\gamma_s}$ becomes large for small cavity waists. For the confocal configuration, the waist is also the only property that can be effectively adjusted. Large mode numbers reduce the ratio between coupling parameter and decay rate originating indirectly from broader cavity linewidths required to support a higher number of modes. This is an opposite behaviour compared to the resolution capability, where a large v leads to improved resolutions. However, the effect of v for the ratio $\frac{\tilde{g}_0}{\gamma_s}$ is not that severe since it scales only with the square root.

The ratio between coupling parameter and linewidth $\frac{\tilde{g}_0}{\kappa}$ can be determined in a similar way by using equations 6.7, 6.8 and 6.10. This yields

$$\left(\frac{\tilde{g}_0}{\kappa}\right)_{\text{concentric}} = \frac{dL^{3/2}\sqrt{\lambda}}{2\sqrt{c\hbar\epsilon_0\pi\sigma}w_0^3}, \quad (6.22)$$

$$\left(\frac{\tilde{g}_0}{\kappa}\right)_{\text{hemispherical}} = \frac{dL^{3/2}\sqrt{\lambda}}{\sqrt{c\hbar\epsilon_0\pi\sigma}w_0^3}, \quad (6.23)$$

$$\left(\frac{\tilde{g}_0}{\kappa}\right)_{\text{confocal}} = \frac{8\pi d}{\sqrt{2\pi\hbar\epsilon_0c}(1-R)}, \quad (6.24)$$

for the concentric, hemispherical and confocal resonator, respectively. The ratio decreases with the third power of the waist for concentric and hemispherical resonators. Therefore, small cavity waists are an effective way to generate large values for $\frac{\tilde{g}_0}{\kappa}$. The waist not occurring in the expression for confocal cavities might be unexpected. This arises, however, through equation 6.8 that connects the waist with the resonator length and wavelength. Since the wavelength is defined by the transition of the particle, L and w_0 cannot be chosen independently. If small waists are utilised to ensure a large $\frac{\tilde{g}_0}{\kappa}$, this would directly be compensated by the necessity of shorter cavities.

Similar to $\frac{\tilde{g}_0}{\gamma_s}$ the ratio between coupling parameter and linewidth decreases for large v , but for $\frac{\tilde{g}_0}{\kappa}$ it scales linearly and the conflict between a large ratio and high resolution capabilities might become more severe. Furthermore, longer resonators lead to larger values for $\frac{\tilde{g}_0}{\kappa}$ but are also more prone to mirror misalignment. This might be critical especially for the concentric cavity, which is the geometry most vulnerable to mirror misalignment, see chapter 6.4.2.

The cooperativity, defined in equation 5.63, can be determined by multiplying $\frac{\tilde{g}_0}{\gamma_s}$ and $\frac{\tilde{g}_0}{\kappa}$. Multiplying the corresponding ratios $\frac{\tilde{g}_0}{\gamma_s}$ and $\frac{\tilde{g}_0}{\kappa}$ for concentric, hemispherical and confocal resonators and applying equations 6.7, 6.8 and 6.10, respectively, yields

$$C_{\text{concentric}} = \frac{d^2L}{2\hbar\epsilon_0\pi\sigma w_0^4\gamma_s}, \quad (6.25)$$

$$C_{\text{hemispherical}} = \frac{d^2L}{\hbar\epsilon_0\pi\sigma w_0^4\gamma_s}, \quad (6.26)$$

$$C_{\text{confocal}} = \frac{8d^2}{\hbar\epsilon_0 w_0^2(1-R)\lambda\gamma_s}. \quad (6.27)$$

The cooperativity depends strongly on the waist of the cavity, for concentric and hemispherical geometries it even scales with the fourth power. For both configurations small mode numbers and long resonators are also desirable. Furthermore, the cooperativity of concentric and hemispherical cavities effectively does not depend on the wavelength, if waist and mode number are given. For confocal resonators, a small waist, wavelength and also large reflectivities are suitable for large cooperativities.

6.6 Critical distance

The critical distance is another important property regarding cavity geometries applicable for particle detection. Many of these geometries are on the verge of instability and require therefore precise length control. The critical distance is defined as the length difference of a certain cavity geometry to the closest unstable configuration. For example, for a near-concentric cavity with $g = -0.9999$ and a corresponding (unstable) concentric cavity with

$L = 2$ cm and $r = 1$ cm, the critical distance would be $\Delta L = 1 \mu\text{m}$ with $g = 1 - \frac{L-\Delta L}{r}$. The critical distance does not effect the resolution capability or homodyne signal directly, but is important due to two other reasons. First, length variations in the range of the critical distance needs to be technically controllable. Piezo stages allow to apply translational shifts in the sub-nanometre range, which is usually good enough for most critical lengths. Second, length fluctuations might occur in a cavity leading to fluctuations of the mirror parameters. For shorter critical distances, these fluctuations are more severe and might lead to unstable waists and mode numbers. For example a cavity with a length of $L = (0.01 - 27 \cdot 10^{-9})$ m, a mirror radius of $r = 0.01$ m and a wavelength of 532 nm corresponds to values of $g = -0.999997$ and $w_0 = 1.4 \mu\text{m}$ for the mirror parameter and waist, respectively. If the length is changed to be equal to $L = (0.01 - 37 \cdot 10^{-9})$ m the new values are $g = -0.999996$ and $w_0 = 1.52 \mu\text{m}$. This seem to be minor changes, however, might already impact the resolution capability. Hence, the critical distance should not exceed values below 10 nm.

The absolute value of the difference between the g of a cavity close to an unstable point and the corresponding g_{unstable} of the unstable resonator itself is $\Delta g = |g_{\text{unstable}} - g|$ and can be used to determine the critical length according to

$$\Delta L = \Delta g r. \quad (6.28)$$

In the following, a case discrimination is made to estimate the critical distances of different cavity geometries.

6.6.1 Near-concentric resonators

The mirror parameters of a near-concentric cavity are given by equation 6.4. Expanding this expression to the first order allows to write

$$\Delta g = \frac{1}{2} \left(\frac{1-R}{2v} \right)^2. \quad (6.29)$$

Inserting this expression in combination with equation 6.7 into 6.28 leads to

$$\Delta L = \frac{4\pi^2 w_0^4}{\lambda^2 L}. \quad (6.30)$$

The critical distance for near-concentric resonator scales with the fourth power on the waist of the cavity. This might limit the realisability of concentric resonators and needs to be examined for these cavity types before construction. For example a resonator with $w_0 = 1 \mu\text{m}$, $\lambda = 532$ nm and $L = 2$ cm has already a critical distance below 10 nm.

6.6.2 Near-confocal resonators

The cavity waist of resonators close to $g_1 = g_2 = 0$ is nearly not effected by changes of the cavity length, however, the resonance frequencies of the transverse modes need to lie within the linewidth of the resonator to enter the multimode regime. Hence, the critical distance of confocal cavities depends on the mirror reflectivities and desired mode numbers. Equation 6.5 connects these quantities with the mirror parameter and can be inserted into equation 6.28 after applying the small-angle approximation to obtain

$$\Delta L = \frac{1-R}{4v} L. \quad (6.31)$$

The proportionality of the critical distance to the total length of the resonator might entail problems in the construction of confocal resonators since short cavity lengths are required for small waists for this resonator type.

6.6.3 Near-hemispherical resonators

The critical distance for near-hemispherical resonators can be determined similarly to the near-concentric geometry. Inserting equations 6.9 and 6.10 into the expression for the critical distance, 6.28, leads to

$$\Delta L = \frac{\pi^2 w_0^4}{\lambda^2 L}, \quad (6.32)$$

which is four times smaller than the value of a concentric cavity of the same length. Since a hemispherical resonator is a half-concentric cavity, the critical distance is effectively half the critical distance of a concentric resonator with comparable beam size.

6.7 Resonator geometries for imaging NaK molecules

After discussing the different properties of resonators that are relevant for the detection of particles or technical feasibility, geometries suitable for the detection of NaK molecules can be determined.

6.7.1 Transitions in NaK molecules

An envisaged application of the proposed detection scheme is the imaging of cold NaK molecules inside an optical lattice with a lattice constant of $0.532 \mu\text{m}$. Discussing possible transitions of these molecules is necessary since wavelength λ and dipole transition matrix element d are defined by the molecule and cannot be adjusted later. Transitions of NaK molecules were investigated in [131, 132]. There are two transitions with relatively large matrix elements, the first at $\lambda_0 = 576.2 \text{ nm}$ with $d = 2.52 \text{ D}$ and the second at $\lambda_0 = 769.6 \text{ nm}$ with corresponding $d = 2.92 \text{ D}$. Even if the dipole matrix element for the $\lambda_0 = 576.2 \text{ nm}$ transition is slightly weaker, it is more desirable due to the shorter wavelength. This is advantageous for many cavity properties like misalignment sensitivity or resonator waist.

Absorption is suppressed by an assumed detuning of $\omega_0 - \omega = 2\pi \cdot 0.5 \text{ GHz}$ leading to an 600 times larger real part of the polarisability in comparison to the imaginary part according to equation 4.3. This ensures that dispersive interactions are more dominant with respect to absorptive interactions. The linewidth of the transition Γ can be estimated by equation 5.66 and is $2\pi \cdot 1.7 \text{ MHz}$.

6.7.2 Resonator properties

After examining possible transitions in the NaK molecule the waist and mode number can be determined since these are the properties primarily defining the resolution capability. As previously discussed in chapter 4.5 small waists are more crucial for high resolutions than the number of modes. Furthermore, large mode numbers reduce the cooperativity and increase diffraction loss due to finite mirror sizes and misalignment sensitivity.

A resonator waist of $1.5 \mu\text{m}$ is equivalent to a far-field angle of $\theta = 7^\circ$ for $\lambda_0 = 576.2 \text{ nm}$ and modes with a total order of 8 would be still within the paraxial approximation. However, the maximum mode order supported by the cavity is set to $v = 4$ for concentric and hemispherical resonators since the gain in resolution is negligible compared to the reduction of cooperativity and increased mirror sensitivity for larger mode numbers. For confocal geometries higher mode orders are feasible as the waist is independent from the mode number and this resonator type is robust against misalignment.

To investigate the other cavity properties, a case discrimination is applied for the different resonator geometries.

6.7.3 Near-concentric resonators

The concentric resonator geometry allows to achieve small waists even for longer cavities due to the small mirror parameters, increasing the cooperativity and leave more space for cold particles between the mirrors. In cQED, this resonator type is not common, however, the group of Christian Kurtsiefer has successfully implemented a concentric cavity successfully to couple single atoms to the cavity field, see [128, 133, 134]. Another advantage of concentric cavities is that they automatically support multimode regimes. The probably biggest disadvantage of these resonators is the large misalignment sensitivity, making it technically challenging that is also the reason why this geometry is not often utilised.

Longer cavity lengths lead to larger cooperativities but also increase the sensitivity of misaligned mirrors. Hence, a balance between both quantities needs to be found. Calculations of the different properties have shown that a length of 2 cm is a good compromise. The corresponding mirror radii are then 1 cm. The radius of curvature of the mirrors also limits the maximum mirror aperture. The theoretically largest aperture is $a = r$, however, the cavity would then be a sphere leaving no possibility to load molecules into the resonator. A mirror width of $0.9r = 0.9$ cm is realistic with regard to feasibility of mirror production and leaves a gap of 1.3 cm between the mirrors for the laser beams forming the optical lattice of the molecules.

Values of $w_0 = 1.5 \mu\text{m}$, $\lambda = 576.2 \text{ nm}$, $v = 4$ and $L = 2 \text{ cm}$ set the mirror reflectivities to 0.9794, the cavity parameter g to -0.9999967 and the corresponding critical distance is 30 nm. Diffraction loss due to finite mirror widths is negligible for all transverse modes and a control of the mirrors angle of $1 \mu\text{rad}$ allows to limit misalignment losses to $V_l = 0.9995$. The resulting linewidth broadening is also negligible.

An angle control in the range of $1 \mu\text{rad}$ is possible but the corresponding mirror mounts are usually expensive. Initially, it seems possible to reduce the misalignment sensitivity instead by constructing longer resonators since the maximum mirror aperture scales with L , while the beam size at the mirror surface increases with \sqrt{L} , see equation 3.11. However, changes of the resonator length entail adjustment of the mirror parameter g to keep a constant value for the waist of the cavity field, as indicated by equation 3.15. Expanding equation 6.4, which enables to determine the cavity parameters for constant waists and mode numbers, to the first order and inserting it into equation 3.11 in combination with equation 6.7 yields

$$w_m = \frac{\lambda L}{2\pi w_0}. \quad (6.33)$$

Hence, the beam size at the mirrors surface effectively scales with the length of the resonator and longer cavities cannot compensate mirror misalignment.

The ratios between coupling strength and decay rate or rather cavity linewidth are $\frac{\tilde{g}_0}{\gamma_s} = 1.22$ and $\frac{\tilde{g}_0}{\kappa} = 0.29$ with a spontaneous decay rate of $\gamma_s = 2\pi \cdot 5.5 \text{ MHz}$ [75], leading to a cooperativity of $C = 1.94$. These values are slightly lower than expected when consulting the corresponding equations. This is the case as even and odd transverse modes have different nodes. All modes inside a two-mirror cavity are standing waves and while the even modes are described by a cosine function, the odd modes are sine functions. Thus, the nodes of the even modes are located at the positions of the antinodes of the odd modes. To enable a particle to couple to both mode groups simultaneously it needs to be positioned between the nodes and antinodes leading to an additional factor of $\frac{1}{\sqrt{2}}$ for the ratios.

The single particle cooperativity defined by equation 5.63 is a measure for a particle located at the centre of the cavity field. However, the distance of the molecules inside the optical lattice from this centre is large enough to significantly weaken the particle-light interaction strength and, hence, the actual cooperativity of the different particles. To determine the correct values, the cooperativity is modulated by the intensity profiles of the different transverse modes. A total of 16 lattice sites is considered with the centre of the

0.80 (11)	1.17 (10)	1.17 (10)	0.80 (11)
1.17 (01)	1.70 (00)	1.70 (00)	1.17 (01)
1.17 (01)	1.70 (00)	1.70 (00)	1.17 (01)
0.80 (11)	1.17 (10)	1.17 (10)	0.80 (11)

Figure 6.9: Cooperativities of a NaK molecule located at different lattice sites for the concentric resonator. The two numbers below the cooperativity indicate the mode which couples strongest to the molecule. The first number is the order in the x -direction, while the second number gives the order in the y -direction.

waist coinciding with the centre of the lattice. Figure 6.9 depicts the strongest effective cooperativity, i. e. the value of the mode that leads to the largest cooperativity, for each site of the lattice. The two numbers below each cooperativity indicate which mode couples the strongest to a particle at the corresponding lattice site. The figure reveals that each site supports a cooperativity value above 0.5 and, hence, can contribute to the total signal.

For an overview, all cavity properties of the near-concentric cavity are summarised in table 6.2.

	concentric	hemispherical
Wavelength in nm	576.2	576.2
Length in cm	2	1
Mirror radii in cm	1	1
Reflectivity	0.9794	0.9794
Mirror aperture in cm	0.9	0.9
Critical distance in nm	30	15
Cavity parameters	-0.9999967	1 and $1.5 \cdot 10^{-6}$
Mirror misalignment	1 μ rad	1 mrad
Loss factor	0.9994	0.9984
\tilde{g}_0/γ_s	1.22	1.22
\tilde{g}_0/κ	0.29	0.29
Cooperativity	1.94	1.94

Table 6.2: Overview of cavity properties for geometries suitable for the detection of NaK molecules.

6.7.4 Near-confocal resonators

Confocal resonators allow to set the waist and the number of supported modes nearly independently from each other and are robust against misalignment making them a feasible choice for the detection of particles. However, the only possibility to adjust the cavity waist is to change the length of the resonator. According to equation 6.8, the length of a confocal resonator with a waist of $1.5 \mu\text{m}$ needs to be $L = 25.7 \mu\text{m}$. Fibre cavities [135] are often used to achieve short resonators that are able to realise cavity lengths below $100 \mu\text{m}$, e.g. [136]. It is possible to produce mirror curvatures up to $5 \mu\text{m}$ [137] and, hence, it is at least theoretically possible to construct a resonator with the desired length of $L = 25.7 \mu\text{m}$. However, the aperture of fibre mirrors is usually equal to or smaller than the radius of curvature [137] and, therefore, the losses would be too large to realise a multimode cavity. Furthermore, the profile of the fibre mirrors is not spherical introducing effects like mode mixing, where the eigenmodes of the resonator are no longer described by pure Hermite-Gaussian modes [137]. Finally, the laser beams forming the optical lattice have diameters of $100 \mu\text{m}$ and, therefore, such short cavities are also not feasible.

In summary, confocal resonators are not suitable for the detection of particles with resolutions in the micrometre range. If a resolution of $10 \mu\text{m}$ or larger is desired, the confocal resonator is superior compared to the concentric cavity.

6.7.5 Near-hemispherical resonators

Near-hemispherical resonators are hybrid resonators combining properties of confocal and concentric cavities. Small waists can be achieved similarly to concentric resonators, but hemispherical geometries are less sensitive to mirror misalignment. The parameters of a hemispherical cavity suitable for the detection of cold NaK molecules comply to a half-resonator version of the concentric cavity from the preceding section. The cavity length is $L = 1 \text{ cm}$ and the radius of the spherical mirror is accordingly also $r = 1 \text{ cm}$ with a

0.80 (11)	1.03 (00)	1.03 (00)	0.80 (11)
1.03 (00)	1.70 (00)	1.70 (00)	1.03 (00)
1.03 (00)	1.70 (00)	1.70 (00)	1.03 (00)
0.80 (11)	1.03 (00)	1.03 (00)	0.80 (11)

Figure 6.10: Cooperativities of a NaK molecule placed at the different lattice sites for the hemispherical resonator. The two numbers below the cooperativity indicate the mode which couples the strongest to the molecule. The first number indicates the order in the x -direction, while the second number is the order in the y -direction. Some numbers are different from the concentric cavity since hemispherical resonators only support even modes.

reflectivity of 0.9794. Since the mirror radii of the hemispherical and concentric resonator and reflectivities are equal, identical mirrors for both resonators can be used, leading to a mirror aperture of 0.9 cm. Diffraction losses are again negligible and a mirror rotation of 1 mrad leads to a loss factor of $V_l = 0.9984$ at the spherical mirror. The cavity parameters are $g_1 = 1$ and $g_2 = 1.5 \cdot 10^{-6}$ and the critical distance is 15 nm. The ratios between coupling parameter and loss channels $\frac{\tilde{g}_0}{\gamma_s}$, $\frac{\tilde{g}_0}{\kappa}$ and the cooperativity are identical to the concentric cavity. The cooperativities for the different lattice sites differ slightly from the concentric case and are depicted in figure 6.10. An overview of all quantities is given in table 6.2.

In conclusion, hemispherical resonators are also suitable for the detection of cold molecules and are in some aspects superior to concentric cavities, e. g. regarding misalignment sensitivity. A disadvantage of this geometry is the position of the waist that is directly located at the surface of the plane mirror complicating a potential implementation of an optical lattice. To compensate for the latter a mirror with a large radius can be used instead of the plane mirror leaving some space for the optical lattice and almost maintaining the previously discussed properties. Another disadvantage of all resonators with cavity parameter products close to zero is that only even or odd modes are degenerate simultaneously leading to symmetric homodyne signals. This issue is discussed in more detail in chapter 6.7.7. However, the proposed hemispherical mirror is still a valid choice to verify the basic principle experimentally since it is less complicated to be built than the concentric cavity.

6.7.6 Other resonator geometries

Other cavity geometries apart from the concentric, hemispherical or confocal type are usually similar to one of these configurations or a combination of them, e. g. resonators with the first g being close to unity and the second close to zero share similar properties with the hemispherical cavity. Plane-parallel resonators are not suitable for the proposed detection scheme since they require even shorter cavity lengths than the confocal geometry and are also sensitive to mirror misalignment. Resonators with $g = 0.5$ or $g = -0.5$ support a multimode regime but also require cavity lengths that are too short for implementation.

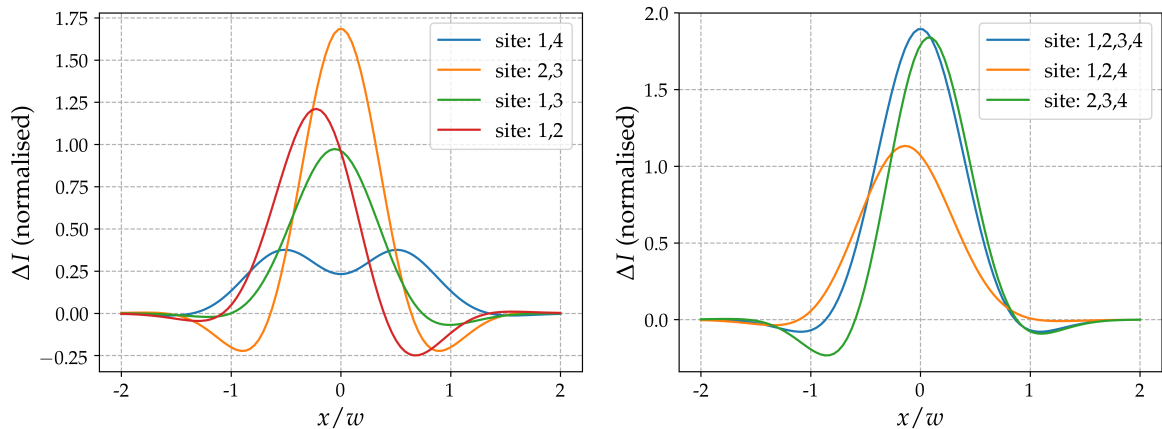


Figure 6.11: Homodyne signals of NaK molecules inside a concentric resonator. The centre of the cavity field is located at the centre of the four different sites of the optical lattice. The occupied sites for each signals are indicated in the legend. The numbering begins on the left site of the lattice and the lattice constant is $0.532 \mu\text{m}$.

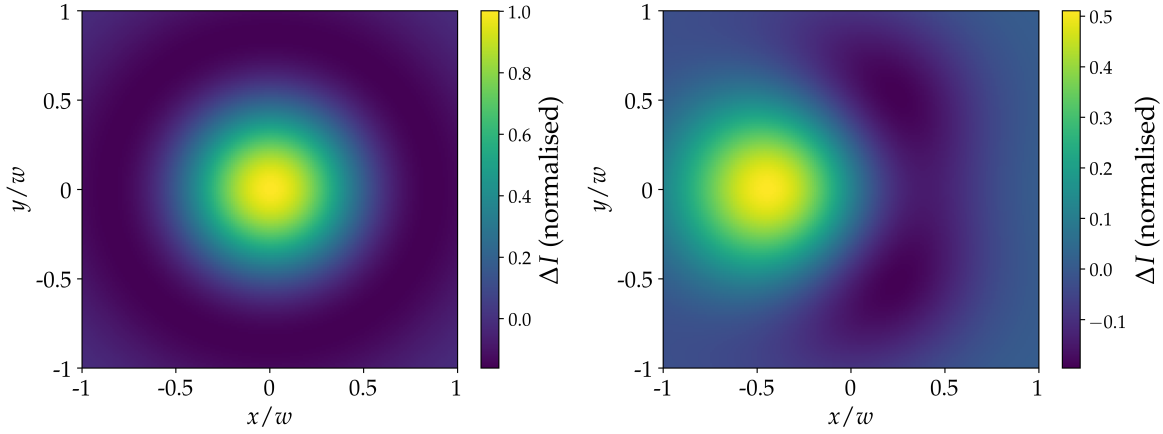


Figure 6.12: Two dimensional homodyne signal of a single particle inside a concentric cavity. On the left side of the figure, the particle is located at the centre of the cavity field, while on the right side, it is shifted by $0.798 \mu\text{m}$ to the left.

6.7.7 Homodyne signal

According to figure 4.6, the resolution capability of a cavity with a waist of $1.5 \mu\text{m}$ and a maximum mode order of 4 should be too low to resolve particles inside an optical lattice with a lattice constant of $0.532 \mu\text{m}$. This figure indicates also that a resonator would require a waist of $w_0 = 0.7 \mu\text{m}$ and a maximum mode order of 14 to resolve two adjacent lattice sites. As explained in the preceding sections, such mode numbers cannot be realised simultaneously for such small waists, e. g. due to violation of the paraxial approximation.

However, as mentioned in chapter 4.5, the defined resolution capability is not absolute and relies on the feasibility to resolve two peaks in the homodyne signal. Even if the peaks of the homodyne signal merge together, information regarding the position of the particles can still be extracted from the linewidth, the amplitude and the position of the peak.

Figure 6.11 depicts the homodyne signals of a NaK molecules placed inside a concentric cavity with the parameters determined in chapter 6.7. The local oscillator and the beam pumping the cavity are 00-modes with powers of 1 W and 10 mW, respectively. The waist of the local oscillator is 5 mm, while the value for the propagated cavity mode is 1 mm. The origins of the coordinate systems of both beams overlap. These parameters are also used for all other simulations in this section.

A lattice with four sites is considered and the different sites are numbered consecutively, where the numbers correspond to the positions $1 \hat{=} -0.798 \mu\text{m}$, $2 \hat{=} -0.266 \mu\text{m}$, $3 \hat{=} 0.266 \mu\text{m}$ and $4 \hat{=} 0.798 \mu\text{m}$. The centre of the lattice and cavity field overlap. The left side of the figure shows different signals for two particles inside the lattice, while the right side shows an occupation of three and all four sites. All signals are normalised to the signal strength of a single particle placed in the centre of the waist. This normalisation is also applied for all other figures in this section. As expected, all peaks of the homodyne signals are merged together, except when two particles are placed in the outer sites. However, the linewidths, the position of the peaks and the signal strengths are different and allow to distinguish between the different lattice site occupations. Even the shape of the homodyne signal might provide information regarding the particles position, e. g. the ripple on the left side of the 2, 3, 4-signal indicates on which side an empty lattice site is located.

So far only homodyne signals along a single axis have been discussed. However, in the experiment the lattice is two dimensional and the fields are also two dimensionally detected. Therefore, figure 6.12 depicts two simulated homodyne signals of a single particle placed inside a concentric cavity. On the left side of the figure, the particle is located at the centre of

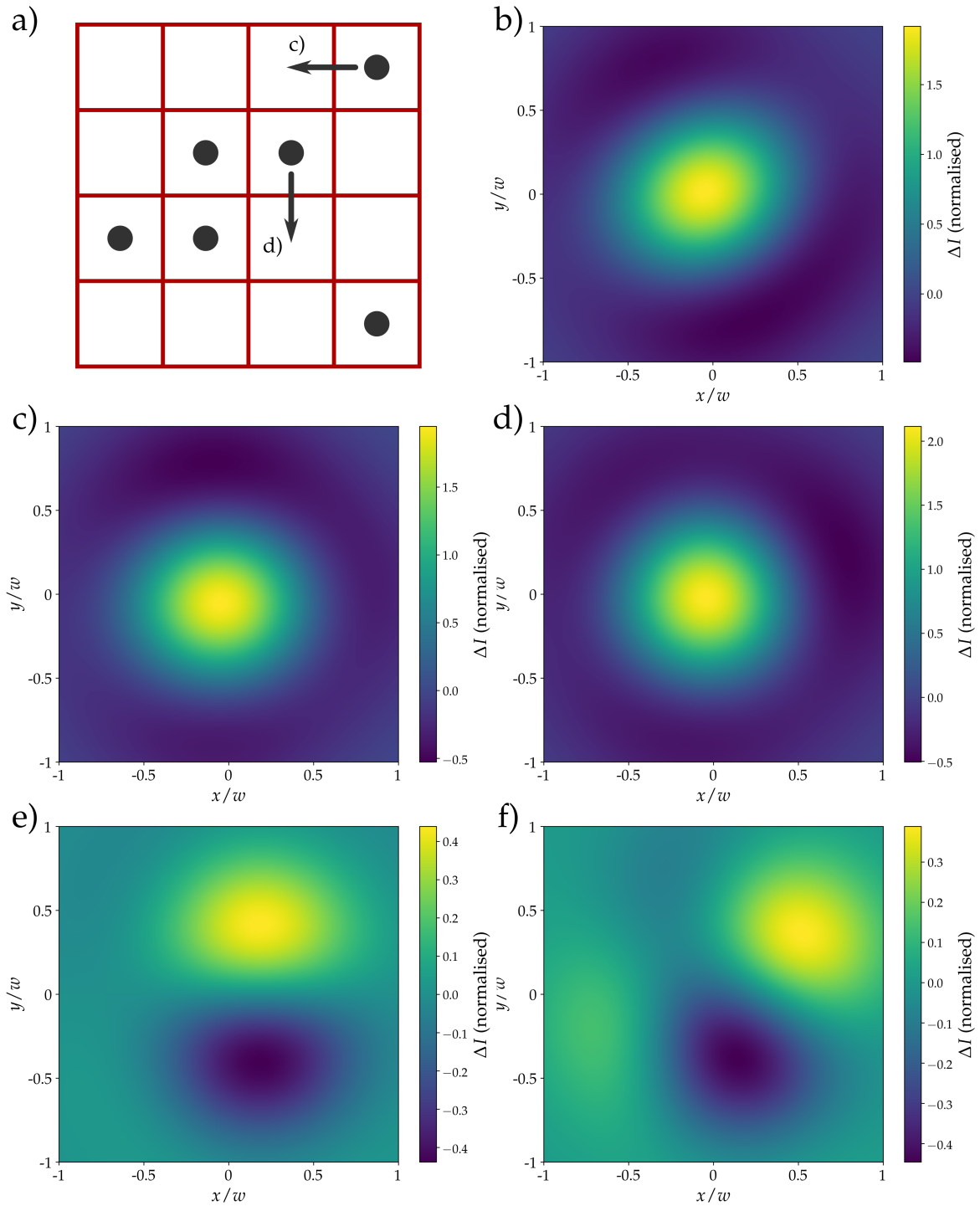


Figure 6.13: Homodyne signals for an optical lattice with 16 sites. The black dots in a) indicate which lattice sites are occupied by a molecule for the homodyne signal in b). For the signal in c), the molecule in the upper right corner is shifted to the adjacent site as indicated by the arrow. For d) another particle is pushed to a bottom lattice site, again indicated by an arrow (the upper right molecule is in this case not shifted). e) depicts the difference between the homodyne signals from b) and c), while f) shows the difference between b) and d). e) and f) have significantly other profiles indicating that even the shift of a single particle to an adjacent lattice site is detectable.

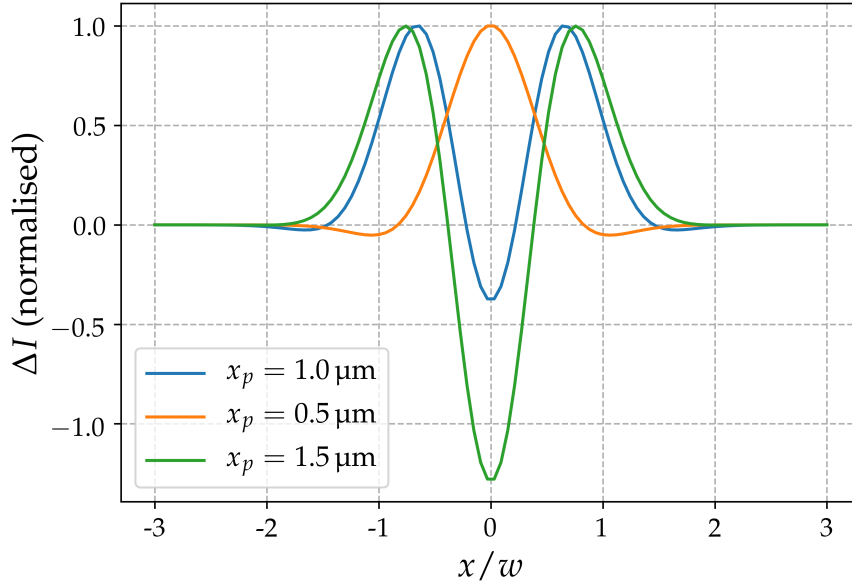


Figure 6.14: Homodyne signal of a single particle inside a hemispherical resonator. Since only even or odd modes are degenerate, the homodyne signals become symmetrical making it more difficult to decide if the molecule is located on the right or left side. This can be solved by shifting the lattice with the molecules either to the left or to the right side and then comparing both signals as indicated by the different curves in the figure.

the waist, while it is shifted by $0.798 \mu\text{m}$ to the left on the right side of figure 6.12. This shift is clearly observable by comparing both signals.

It should also be examined if signals with similar lattice site occupations can be identified uniquely. A two dimensional lattice with a total of 16 sites is assumed and the centres of the lattice and waist overlap. The lattice constant is again $0.532 \mu\text{m}$. Three different signals are compared and the corresponding occupation of sites is depicted by black dots and arrows in a) of figure 6.13. The homodyne signals for the three different occupation configurations are shown in b), c) and d) of figure 6.13. e) and f) depict the difference of the profiles for each picture implying that even similar site occupations can be identified uniquely.

In the simulations of the homodyne signals for concentric resonators, all mode orders contribute to the signal. However, in hemispherical cavities and other resonator with $g_1 g_2 = 0$ only the even or odd modes are degenerate and are able to contribute to the signal. This leads to a symmetrical profile of the homodyne signal complicating the process to determine at which side the particle is located. An example is depicted in figure 6.14 showing the homodyne signal for a particle positioned at different x -values on the right side. A single homodyne signal does not allow to decide where the molecule is located exactly. However, shifting the whole lattice either to the left or right site and comparing both signals allows to examine the exact position of the particle.

The simulations in this chapter demonstrate that the suggested geometries are suitable for the detection of cold NaK molecules. An additional advantage regarding the particles' detection is the discrete nature of the positions due to the optical lattice leading to a discrete set of expectable signals.

Chapter 7

Cavity Design for the Detection of Particles

After determining appropriate cavity geometries for the detection of particles technically feasible resonators and experimental concepts can be developed to realise the proposed imaging technique. The final objective is to construct a cavity able to detect cold NaK molecules within an optical lattice. However, to realise such an apparatus many problems need to be overcome. As explained in the previous chapter, the construction of a resonator that fulfils all constraints and requirements, is at the limit of what is feasible. To realise such a cavity inside the vacuum chamber containing a cold quantum gas is even more challenging. Hence, it might be advantageous to verify the principle of the imaging technique in a less complicate environment in the first place.

The demonstration of the feasibility of the detection scheme can be split into several steps. First, objects with the capability to imitate cold molecules inside the resonator need to be determined. Nanoparticles, for example, can be used for this purpose. Second, the general applicability of the imaging technique can be shown. As this does not necessarily require a high resolution, a confocal resonator can be constructed for this purpose that is less complicate to realise compared to a concentric or hemispherical cavity. For an explanation why a confocal resonator is less complicated to construct, see chapter 6.

After demonstrating the general feasibility of the detection method the resolution can be increased by using small waist cavities to examine if the imaging technique is also suitable for resolving single molecules inside an optical lattice. A hemispherical cavity allows to achieve high resolution and low misalignment sensitivity at the cost of a symmetrical homodyne signal, see chapter 6. Finally, a concentric resonator can be utilised to realise particle imaging with resolutions in the range of 500 nm and non-symmetrical homodyne signals.

The aim of this chapter is to develop experimental setups for the above described tasks. In the first section, the characteristics of nanoparticles are explained and similarities and differences to cold molecules are discussed. The focus of the second section lies on an experimental scheme for the detection of nanoparticles. Modular cavity designs, applicable for confocal, hemispherical and concentric geometries, are developed. Mode matching is discussed and an alignment procedure for concentric resonators is presented. Furthermore, a method to determine the cavity parameters close to unstable geometries is explained to ensure a correct cavity configuration for the detection of the nanoparticles. Finally, all these aspects are combined to propose an experimental setup with all necessary technical components for the imaging scheme.

7.1 Nanoparticles

For an apparatus to prove the imaging concept, test objects, which scatter light similar to cold molecules, are required. Nanoparticles are objects with a size between 1 and 100 nm [138] and can emit dipole fields similar to atoms and molecules. Classically, the fundamental equations describing interactions between nanoparticles and light are the Maxwell's equations [139]. The properties of these interactions strongly depend on the nanoparticles' shape that can be, for example, a plate, rod or cube. However, for spherical particles, the corresponding interaction simplifies significantly, i. e. such nanoobjects can scatter light similarly to atoms or molecules, making them suitable test objects for the proposed detection scheme.

An electromagnetic wave induces oscillations in the free electron gas of a metallic nanoparticle. These oscillations are called plasmons [139]. Since accelerated charges emit radiation, nanoparticles exposed to an electromagnetic wave start to radiate light themselves. This reemitted field interacts with the initial wave leading to partially destructive interference and a phase shift that can be interpreted as absorptive and dispersive light-matter interactions, respectively.

The exact form of a field scattered by a nanoparticle can be determined by applying Mie theory [140] that can be derived from the Maxwell's equations. However, Mie solutions reveal that the scattered field often contains higher order multipole fields [139] in contrast to atoms or molecules that can be approximated as dipole emitters. But it can also be shown that these higher order terms become negligible if the radius of the spherical nanoparticle a is significantly smaller than the wavelength of the light λ [139, 141]

$$\frac{a}{\lambda} \ll 1. \quad (7.1)$$

This is called the Rayleigh approximation since the particle in this regime behave like a Rayleigh scatterer. As for molecules, the induced dipole moment of the nanoparticles is proportional to the field exciting the electron oscillations: $p_0 = \alpha E_0$. The quasi-static polarisability α of a nanoparticle can be derived from the Clausius-Mossotti relation according to [142, 143]

$$\alpha_{np} = 4\pi\epsilon_0 a^3 \frac{\epsilon_{np} - \epsilon_m}{\epsilon_{np} + 2\epsilon_m}. \quad (7.2)$$

ϵ_{np} and ϵ_m are the relative permittivities of the nanoparticle and the surrounding environment, respectively. According to equation 7.2, the polarisability diverges for $\epsilon_{np} + 2\epsilon_m = 0$ leading to a strongly increased interaction between nanoparticle and light. Since the relative permittivity is primarily a function of the wavelength of the incident light, resonances in nanoparticles occur similarly to atoms or molecules. However, the resonances of nanoparticles, also called plasmon resonances [139], are broad and do not show the discrete nature of atomic or molecular particles, see figure 7.1.

To serve as test objects for the imaging scheme nanoparticles need to be placed inside the cavity. The most efficient method would probably be an optical tweezer [150], i. e. trapping a particle with a focused laser beam. With an optical tweezer, a nanoparticle can be positioned between the mirrors without additional objects, which could induce disturbance effects during the imaging. However, the implementation of such a tweezer is complex and simpler methods are also feasible. For example, the nanoparticles can be placed on a dielectric substrate, e. g. glass. This method has been applied successfully in [151] to image gold nanoparticles with fluorescence imaging.

If the nanoparticles are placed on a substrate within the cavity, this substrate might alter the properties of the resonator. By introducing a corresponding ray transfer matrix for this dielectric plate into the ABCD matrix of a cavity, see chapter 3, the effects of the substrate can be determined. After some algebraic transformations, it becomes apparent that the length

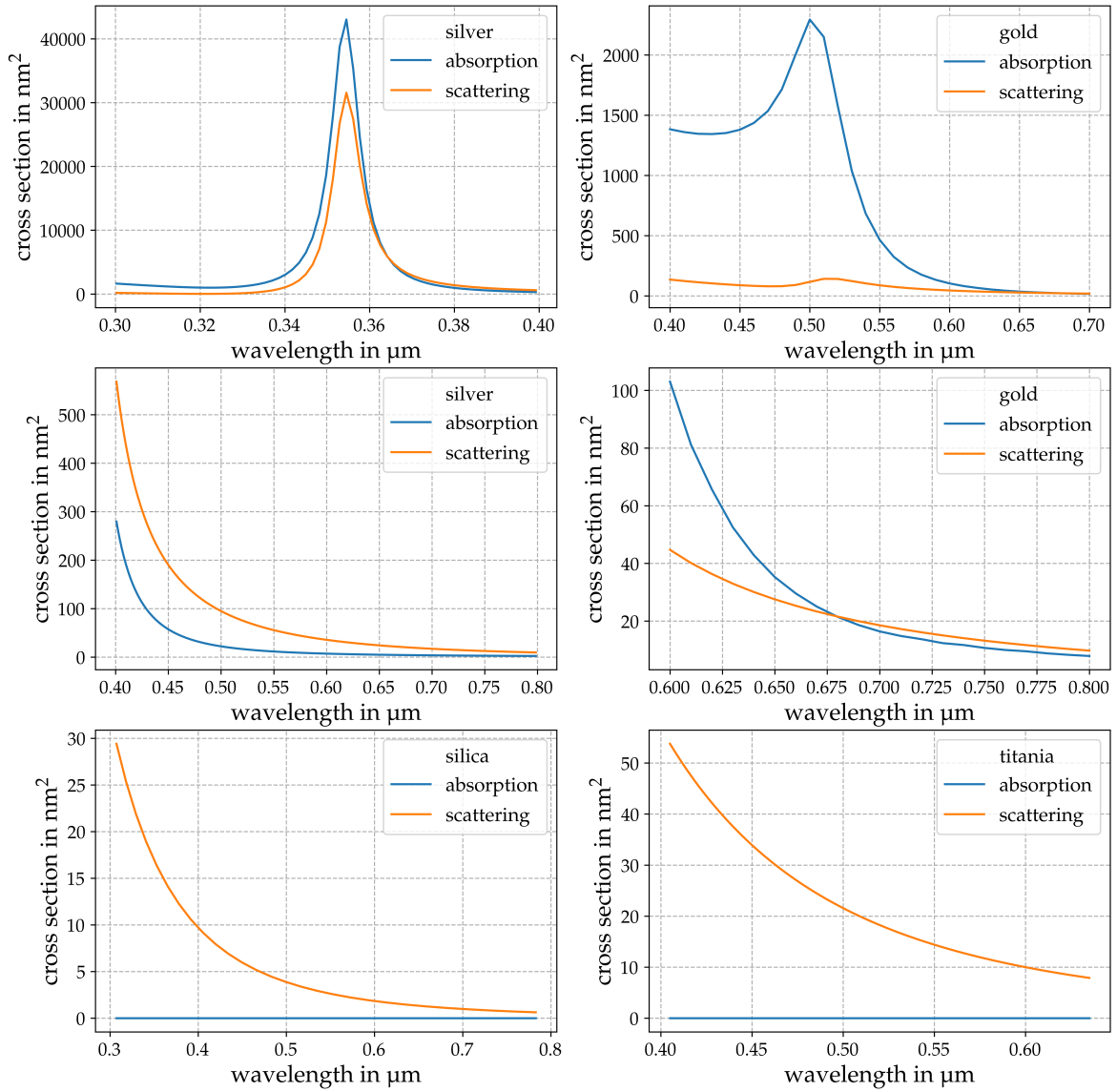


Figure 7.1: Absorption and scattering cross sections for a nanoparticle consisting of silver, gold, silica and titania depending on the wavelength of the light. The values are obtained through equations 7.5 and 7.6. The relative permittivities required to determine the corresponding polarizabilities are calculated from the complex index of refraction $\tilde{n} = n + i\kappa$ by using equations $\epsilon_{\text{real}} = n^2 - \kappa^2$ and $\epsilon_{\text{imag}} = 2n\kappa$ [144]. All data is obtained from [145], which obtained data from [146] (silver), [147] (gold), [148] (silica) and [149] (titania).

of the cavity needs to be slightly increased to obtain identical properties compared to a resonator without a substrate. The additional length depend on the thickness and material of the glass plate. In conclusion, a substrate can be used if the cavity length is corrected.

The placement of the nanoparticles on a substrate also leads to a modification of the polarisability through a so-called mirror charge. The new polarisability is then given by [152]

$$\alpha_{np,s} = \epsilon_0 \frac{V_p (\epsilon_{np} - \epsilon_m)}{\epsilon_m + L_s (\epsilon_{np} - \epsilon_m)} \quad (7.3)$$

$$\text{with } L_s = \frac{1}{3} \left(1 - \frac{1}{8} \left(\frac{d}{a} \right)^3 \right) \left(\frac{\epsilon_s - \epsilon_m}{\epsilon_s + \epsilon_m} \right). \quad (7.4)$$

V_p is the volume of the nanoparticle, d the distance between the particles centre and the surface of the substrate and ϵ_s the relative permittivity of the substrate.

The interaction of an incident electromagnetic wave with a nanoparticle is slightly different than with an atom or a molecule. While atomic or molecular particles can reemit an absorbed photon, light absorbed by a nanoparticle is dissipated into another energy form, e. g. heat [153]. Light emitted by the oscillating electrons is considered as scattered [153]. In contrast to atoms or molecules, a nanoparticle absorbing a photon can still scatter light and, hence, the imaging process must not be completed before the first absorption occurs.

However, an absorbed photon may still not contribute to the detection signal and dominating dispersive interactions would also be favourable for nanoparticles. Interaction strengths for nanoparticles are usually given in terms of the cross sections, where larger values correspond to higher probabilities for interaction. The absorption and scattering cross sections are

$$\sigma_{\text{abs}} = \frac{k}{\epsilon_0} \text{Im}(\alpha), \quad (7.5)$$

$$\sigma_{\text{sca}} = \frac{k^4}{6\pi\epsilon_0^2} |\alpha|^2, \quad (7.6)$$

respectively. The absorption cross section depends on the imaginary part of the polarisability, while the scattering cross section is proportional to the modulus square of α . Hence, both values scale with a^3 and a^6 , respectively, and dispersive interactions dominate for larger particles. This might be disadvantageous since the scattered field of larger nanoparticles also contains higher order multipole terms. A careful balance between strong dispersive interactions and suppressed multipole fields needs to be found.

The material of a nanoparticle also impacts the light-matter interaction significantly. A nanoparticle can be made either from a metallic or dielectric material. Scattering and absorption is usually stronger for metallic nanoparticles compared to dielectric materials and for particle sizes satisfying the Rayleigh approximation absorptive interaction normally dominates over dispersive processes or both cross sections have similar values at most. In contrast, the extinction coefficient of dielectrics is equal to zero and, hence, absorption does not occur in these materials.

Gold, silver, silica and titania (titanium dioxide) are discussed as materials for the nanoparticles to examine the feasibility of these materials as test objects for the proposed imaging scheme. These materials are considered since corresponding nanoparticles are available, inexpensive, can be purchased in different sizes and the optical properties of these objects are well known. Gold and silver are typical materials for metallic nanoparticles, while silica and titania are dielectrics.

The absorption and scattering cross sections for a nanoparticle with a size of 25 nm are depicted for the above mentioned materials in figure 7.1. The plasmon resonances of the metallic particles is clearly visible in the spectra, for silver at 355 nm and for gold in the range of 500 nm. At these wavelengths, the cross sections are significantly enhanced, for silver the absorption and scattering cross section differ less than for gold. For longer wavelengths, the scattering cross section becomes larger than the absorptive cross section. For silica and titania

absorption is completely suppressed, as expected, a plasmon resonance does not occur in the visible light spectrum and dispersive interactions are stronger for shorter wavelengths.

Note that the ratios between absorption and scattering cross section in figure 7.1 are not universal, but significantly depend on the particles size, as previously explained.

Each material has advantages and disadvantages. While metallic particles provide a larger number of dispersively scattered photons due to larger scattering cross sections, absorption does not occur for dielectrics. The nanoparticles should serve as test objects for the imaging scheme prior to the application in the detection process for NaK molecules. Hence, if the scattering rates of the dielectrics and the molecules are in the same order of magnitude, titania or silica are more favourable than silver or gold. Since the cross section for titania is larger than for silica, as indicated in figure 7.1, titania should be preferred over silica.

A comparison of the scattering rates of molecules and nanoparticles is possible by comparing the corresponding polarizabilities. In chapter 6.7 a large detuning of $2\pi \cdot 500$ MHz is assumed and, hence, the imaginary part of the polarisability of the molecules can be neglected. Due to the vanishing extinction coefficient of titania, it is sufficient to compare the real parts of the polarizabilities of molecules and nanoparticles. Values in the same order as for NaK molecules with a detuning of $2\pi \cdot 500$ MHz are obtained by titania nanoparticles with a size of 15 nm. This is significantly smaller than all optical wavelengths and, therefore, titania nanoparticles should be feasible as test objects for the imaging method. If the difference between a field scattered by such a nanoparticle compared to an ideal dipole emitter is still too large, silver can be used instead since the larger cross section allows to utilize smaller particle radii. In this case, however, it would be necessary to use more power for the imaging process due to the non-negligible absorption cross section.

The scattering cross section of titania nanoparticles is more effected by the size of the sphere than the wavelength and, hence, in principle all optical wavelengths can be used for the imaging scheme. Longer wavelength would suppress non-dipole terms from the scattered field and are therefore more suitable. Nevertheless, as explained in chapter 6, multimode cavities with small waists are also more difficult to realise in this case due to larger misalignment sensitivity and the paraxial approximation. Hence, longer wavelength should only be considered for resonators that are robust against misalignment, i. e. confocal or hemispherical geometries.

In conclusion, nanoparticles are feasible test objects for the proposed imaging scheme. Titania nanoparticles should provide dispersive scattering rates strong enough to imitate NaK molecules. For confocal and hemispherical cavities longer wavelengths should be utilised to suppress higher multipole fields in the scattered light. For concentric cavities shorter wavelengths are more feasible to reduce misalignment sensitivity. If the scattered field of titania particles differs too much from an ideal dipole field smaller nanoparticles should be used and silver can be utilised instead of titania.

7.2 Experimental setups for the detection of nanoparticles

7.2.1 Mode matching

Before the cavity design is presented, mode matching should be discussed. Mode matching characterises which transverse modes supported by a cavity are pumped by an incoming laser beam. An arbitrary resonator mode ψ_N and an incoming beam E_e are considered as ideally matched when the intensity distribution and phase profiles overlap perfectly [154]. In this case only mode N of the cavity is populated by the pumping beam, while other modes are not oscillating within the resonator. In reality, ideal mode matching is never reached and the mode matching efficiency can mathematically be expressed by an overlap integral [154]:

$$\eta_{\text{mode}} = \frac{|\int E_e \psi_N dA|^2}{\int |E_e|^2 dA \int |\psi_N|^2 dA}. \quad (7.7)$$

Mode matching is important since resonators are usually operated in the single-mode regime and other modes apart from the desired one should be suppressed. At first sight, mode matching might appear irrelevant for the proposed imaging scheme due to the desired multimode regime of the cavity. This is not the case for two reasons. Firstly, resonators are usually aligned far in the stable regime, i.e. the cavity parameter product $g_1 g_2$ is neither equal to zero or unity, and the length is then successively adjusted to reach the desired geometry. If the transverse modes are not degenerated, which is the case for most resonators not close to the border of stability, no transmissive or reflective resonator signal occurs for non-mode matched pumping beams and the cavity cannot be aligned. Secondly, coupling modes with larger orders than required for the imaging process might lead to an increase of the linewidth [128].

The fields of many cavities are approximately cylindrical and the backsides of the mirrors are plane. In this case, it is possible to achieve large mode matching efficiencies by coupling a collimated beam with the size of the resonator field into the cavity. However, due to the small waist, the resonator fields of concentric and hemispherical geometries have large far field angles and pumping the cavities with a collimated beam does not provide sufficient mode matching. Large matching efficiencies are usually obtained through lens systems in front of the resonator. The alignment procedure of these lenses is complex and cavities with different field profiles require individually designed lens systems. A less complicated and more universal method would be preferable.

In [128], an anaclastic lens is utilised to achieve suitable mode matching efficiencies for a near-concentric resonator. Such a lens has an aspheric shape on one side (in the case of [128] an elliptical profile), while the other side is spherical. The latter is coated with a reflective layer and used as a cavity mirror. The aspheric side is designed in a way that a collimated beam is focused at the centre of the cavity. The aspheric shape also eliminates possible aberrations and, thus, increasing the mode matching efficiency further. Hence, an anaclastic lens ensures large mode matching efficiencies simply and universally applicable in contrast to lens systems. However, due to the aspheric profile the maximum numerical aperture is limited and the far field angles of higher order modes of the required imaging cavities are too large to be covered by anaclastic lenses.

An alternative approach for mode matching is to use a cavity mirror where both sides are spherical. The purpose of the outer spherical profile is simply to suppress refractions. This allows to use a common aspheric lens for effective mode matching. This is illustrated in figure 7.2. The proposed solution is similar to the anaclastic lens and in this case the aspheric and spherical side are only distributed over two different optical elements. This allows to increase the separation between aspheric and spherical profile and, thus, the numerical aperture can be further increased compared to the anaclastic design. However, it is necessary to control the position of the lens independently of the mirror. A control over the angles with axes of rotation perpendicular to the optical axis is also required for high mode matching rates. These angles are also called yaw (x -axis) and pitch (y -axis) and are shown in figure 7.2.

All these mode matching methods only allow to couple the fundamental 00-mode into the cavity since this is usually the mode emitted by lasers. If higher order transverse modes should be coupled to the cavity, spatial light modulators can be utilised for this purpose, see [155] and [156].

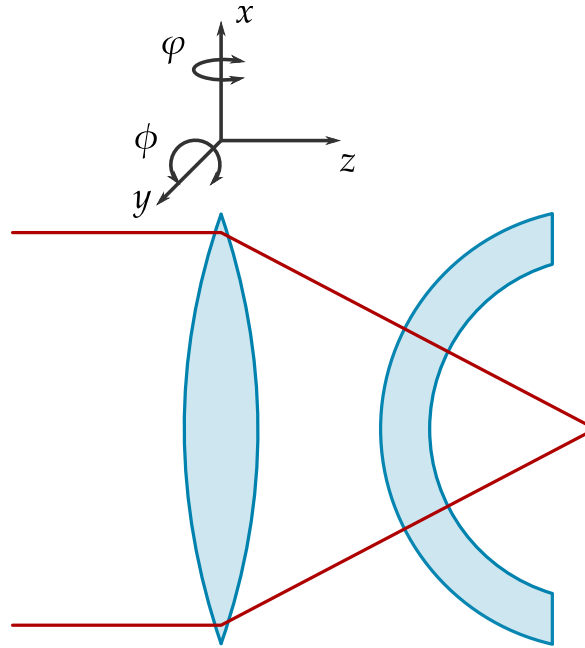


Figure 7.2: Mode matching for small-waist cavities. Both sides of the resonator mirror are spherical allowing to focus a collimated beam at the centre of the cavity with a common lens. This lens requires five degrees of freedom, three for transitions in space and two angles that allow to control the yaw (rotation around x -axis, φ) and the pitch (rotation around y -axis, ϕ).

7.2.2 Imaging resonators

As explained at the beginning of the chapter, the demonstration of the imaging technique can be split into several steps, each utilising another resonator geometry. Confocal resonators are technically the least challenging and can be used to show the general feasibility of the detection scheme. Hemispherical cavities are then used to improve the resolution and finally concentric cavities are utilised to obtain non-symmetrical homodyne signals. To reduce the number of technical elements, the components of the resonators are chosen and constructed to operate with all three cavity configurations. Furthermore, a modular design is advantageous to switch between the geometries. In the following, this modular resonator design is presented with respect to the concentric cavity since this is the most challenging design. However, the construction can also be used for hemispherical and confocal resonators.

Figure 7.3 depicts a 3D representation of the resonators components. The left side shows the assembled cavity, while on the right side an expanded view is represented. Due to large misalignment sensitivity, a control of five degrees of freedom for each mirror is required for the concentric cavity. These are three translational directions and two angles. The axes of rotation of the angles need to be perpendicular to the optical axis of the cavity and are illustrated in figure 7.2.

For a proper cavity alignment, translational shifts need to be controllable in the range of nanometres. Such small displacements can be handled with piezo elements. These elements rely on the inverse piezoelectric effect, where the elongation of the material depends on the applied voltage [157]. Piezo components allow a precise length control of the cavity including fast responses to fluctuations. A suitable piezo stage for the imaging cavities would be the P-611.3o NanoCube XYZ system from the company Physikinstrumente [158]. This stage supports translations over $120\ \mu\text{m}$ for three directions with a resolution of $0.2\ \text{nm}$. Furthermore, the piezo system is capable to hold masses up to $1.5\ \text{kg}$ if the centre of mass is

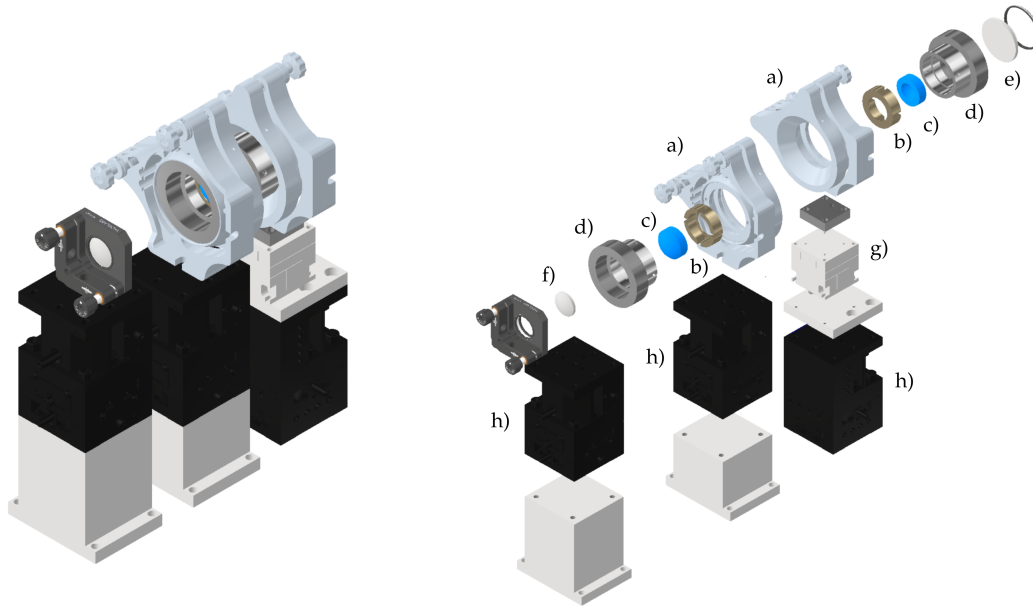


Figure 7.3: Modular design of the imaging cavities. The left side shows an assembled version, while the right side depicts an expanded view. a): Gimbal mounts, b): Mirror rings c): Cavity mirrors d): Ring-gimbal mount adapters e): Outcoupling lens f): Mode matching lens g): Piezo stage h): Translation stage.

located centrally above the stage which is sufficient for the remaining components required for the cavity.

A translation range of $120\ \mu\text{m}$ is sufficient for fine tuning, but too small for pre-aligning the cavity. In principle, piezo stages can cover larger ranges, however, this usually reduces the resolution. Hence, an additional stage for rough alignment is required. An inexpensive tool for this purpose is the linear M-DS65-XYZ stage from Newport [159]. The travel range for this stage is $25.4\ \text{mm}$ that is sufficiently large and the resolution is $1\ \mu\text{m}$, which overlaps with the range of the piezo element. Furthermore, the resolution is small enough to align the cavity in respect to the mode matching lens and pumping beam. Fine tuning is only required for aligning the mirrors in respect to each other and, hence, the M-DS65-XYZ stages allow to use a single piezo element for fine control.

There is a large number of mounts and stages for controlling the yaw and pitch of an optical element precisely. However, usually the axis of rotation does not coincide with the centre of the corresponding mirror, see figure 7.4. If the point of rotation, defined as the position where both rotational axes cross each other, does not coincide with the centres of the mirrors surfaces, tilting the yaw or pitch angle leads to a translational shift of the mirror in two directions. This is also illustrated in figure 7.4. For a less complicated alignment procedure, the degrees of freedom should be independent from each other. Independences can be ensured by using so-called gimbal mounts, where the centre of the mirror is located at the point of rotation.

A suitable gimbal mount is the U200-G2k mirror mount from Newport [160] providing different advantages. The precision of angle adjustment is $1.12\ \mu\text{rad}$ and the total alignment range is 8, which is suitable for both pre- and fine alignment. Furthermore, the adjustment screws can be exchanged to increase angle sensitivity even beyond $1.12\ \mu\text{rad}$ if required. It is also possible to use motorized piezo actuators instead of manual screws to adjust angles contactless.

Cavity mirrors for the concentric resonators have been designed in-house and produced by Asphericon. Both sides are spherical to allow uncomplicated mode matching, the inner

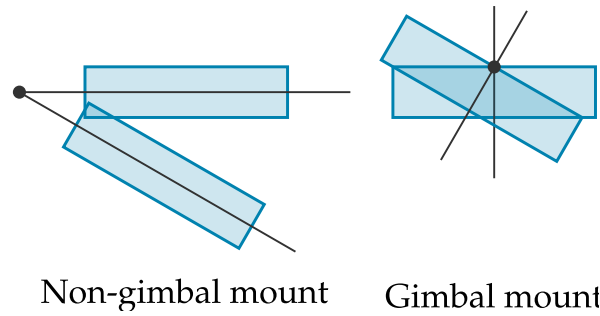


Figure 7.4: Difference between non-gimbal and gimbal mirror mounts. For non-gimbal mounts the axis of rotation is not crossing the centre of the mirrors surface, leading to a translational shift of the mirror when the angle is tilted. In contrast, gimbal mounts decouple translational degrees of freedom from angle adjustments.

side has an intensity reflectivity of 0.979, while the outer side provides an anti-reflection coating. The radius of curvature of the reflective side is 1 cm and the corresponding aperture is 0.9 cm. Plane mirrors with identical apertures and reflectivities have been also realised by Asphericon and can be used for the hemispherical cavity.

Remaining parts for the modular cavity have been designed and manufactured in-house. The mirrors are glued at four spots to mirror-holding rings, which, in turn, can be attached to a ring-gimbal mount adapter through screws. This adapter provides an external thread and can be screwed to the gimbal mirror mount. Furthermore, the adapter is designed such that the centre of the cavity mirrors' surface is located at the point of rotation of this gimbal mount. A lens can be placed inside the adapter with a retaining ring to collimate the beam transmitted through the cavity. The other parts are needed to connect the technical components to each other or with the optical table.

An aspheric lens AL4532-A from Thorlabs [161] lens is placed in front of the incoupling mirror of the cavity for mode matching. Another M-DS65-XYZ stage is used to control translational adjustments of this lens. For the alignment of the angle an inexpensive non-gimbal mirror mount can be used since the translational shifts due mirror tilting are negligible in terms of mode matching.

7.2.3 Cavity alignment

Concentric cavities are more sensitive to misplacement of the mirrors leading to more complicated alignment procedures compared to other geometries. The process of alignment described in this section is based on a concept presented in [162]. During cavity adjustment, the mirrors and mode matching lens are aligned independently from each other, effectively decoupling the degrees of freedom of the different components simplifying the setup of the cavity significantly. The feasibility of the proposed alignment procedure has been examined with a test cavity.

The adjustment procedure is schematically represented in figure 7.5. Several axes need to coincide to ensure a proper cavity alignment. As previously explained, the optical axis of a cavity is defined as the line passing through the centres of curvature c_1 and c_2 of the mirrors. To reduce diffraction loss, this optical axis need to cross the centres of the mirror surfaces, see chapter 6.4.2. To ensure large mode matching efficiency, the optical axis of the resonator should coincide with the optical axis of the beam pumping the cavity.

First, the pumping beam is aligned to define a reference line for mirrors and the mode matching lens. In principle this beam can be orientated arbitrarily and the optical components can be adjusted accordingly. For practical reasons, however, the beam should propagate parallel to the surface of the optical table and the distance from this surface

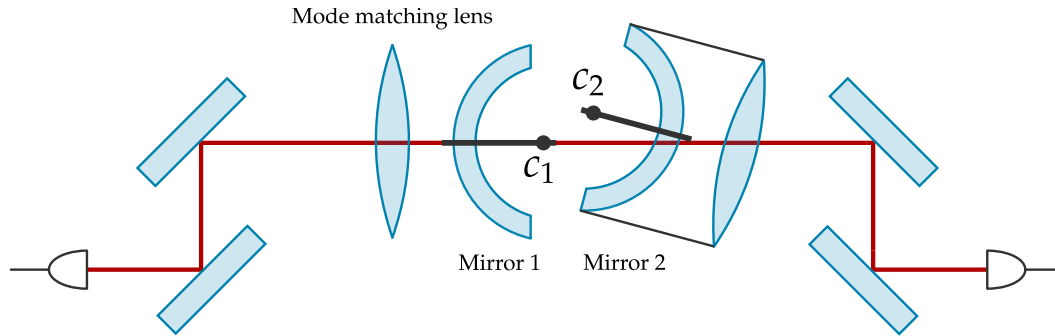


Figure 7.5: Pre-alignment of the (concentric) cavity. Two counter-propagating beams from the fibres define a reference line. Mirror 2 is then placed along this line and adjusted that the beam from fibre 2 is reflected back into itself. Afterwards, the mode matching lens is positioned and finally mirror 1 is placed and adjusted. The focus of the lens should coincide with the centre of curvature of the first mirror.

should match the height of the assembled resonator represented in figure 7.3. Furthermore, the beam should propagate into two opposite directions, which is used to align both mirrors separately. Therefore, the beam is outcoupled by two fibres and a total of four mirrors is utilised to overlap the counter-propagating beams, see figure 7.5.

In the next step mirror 2 from figure 7.5 is positioned along the reference line and adjusted that the beam from fibre 2 is reflected back into itself. Translational misalignment can be corrected by observing the symmetry of the back reflected beam with a camera [162]. After the alignment of the mirror, the beam from fibre 2 is not needed any more and can be blocked. The mode matching lens can now be placed along the beam from fibre 1 and can be adjusted. Initially, the lens is roughly aligned, but corrections can be applied later. Finally, the mirror 1 is positioned and adjusted such that the beam from fibre 1 is reflected back into itself. The focus of the lens should roughly coincide with the centre of curvature of mirror 1.

After the placement and adjustment of mirror 1, pre-alignment is completed. Next, the transmission signal of the cavity can be observed with a beam camera and a photodiode. A sawtooth or triangular voltage signal can be applied to the piezo stage connected to the second mirror to measure the spectrum of the cavity with the photodiode. The oscillating piezo signal leads to a periodic change of the cavity length and allows to observe the different transverse modes. Two examples of cavity spectra are shown in figure 7.6. The left side of the figure depicts a cavity with non-perfect mode matching. Peaks with various heights correspond to different transverse modes. The transmission signal of the cavity should look roughly like this after the pre-alignment. If no transmission signal occurs, the distance between the mirror might be too large and should be reduced. Also, it should be examined, if the amplitude of the voltage signal is large enough to alter the cavity length by $\frac{\lambda}{2}$ or more to ensure that at least one mode is in resonance with the laser during the measurement. If still no signal can be measured the mode matching is probably not sufficient and the pre-alignment must be repeated.

If a suitable transmission signal of the cavity can be measured, fine adjustments can be made. By altering the positions and angles of the mirrors and the lens consecutively, mode matching can be improved. During this process higher order transverse modes should become more suppressed, while the signal of the 00-mode increases, which can also be checked with a beam camera. An ideal case is shown on the right side of 7.6. Due to the pre-alignment, only small changes for each degree of freedom, which are still approximately independent from each other, are necessary.

After pre- and fine alignment, the cavity is usually far in the stable regime, i. e. $g_1 g_2 \neq 0$ and 1. The distances between the mirrors can successively be increased to approach the

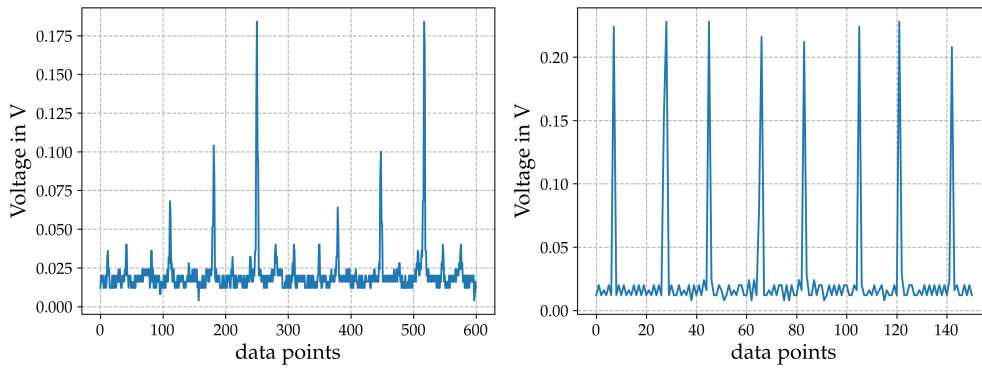


Figure 7.6: Transmissions of cavities far in the stable regime. The transmission signal is measured with a photodiode, while the length of the cavity is altered by applying periodic voltage signals to the piezo stage. The left side depicts a detail of a spectrum for non-perfect mode matching, where peaks with different heights correspond to different transverse modes. The values of the x -axis are proportional to the length of the resonator in this case and the total length change is approximately 540 nm, hence every transverse mode is represented twice in this spectrum. The right side shows the transmission signal for a better mode matching efficiency. All peaks correspond to the same transverse mode. The spectrum corresponds to four periods of the triangular piezo signal.

desired cavity geometry. This requires a measurement of the mirror parameter g and is further discussed in the next section. However, when the length of the cavity is changed the mode matching condition might change and the cavity becomes more sensitive to misalignment. Further adjustments are therefore required. However, tests have shown that only the position and angle of one mirror needs to be corrected to keep the cavity aligned.

7.2.4 Operating near-unstable cavities on the last stable mode

To provide small cavity waists, near-concentric and -hemispherical resonators need to be close to the edge of stability. Depending on their length and the pumping beam, cavities only support discrete resonance frequencies, see chapter 3. The distance between two longitudinal modes is $\frac{\lambda}{2}$. For each resonator a last stable mode exists, i. e. if the cavity length is increased by $\frac{\lambda}{2}$ the resonator enters the regime of instability. For cavity waists in the range of $1.5 \mu\text{m}$ it is necessary to operate the resonators presented in chapter 6.7 at their corresponding last stable modes.

When a cavity is properly aligned, as described in the preceding section, the last stable mode of resonators can, in theory, be found by increasing the cavity length. The linewidths of the different longitudinal modes occurring in the transmission signal can be measured. After the last stable mode a sudden drop of transmission strength should occur and the linewidth is significantly broadened, as observed in [134]. However, this approach is afflicted with uncertainties. Linewidth broadening and reduced signal strength can also occur due to mirror misalignment. Furthermore, the width and strength of the signal might not change so drastically for the first unstable mode of hemispherical resonators due to their general reduced misalignment sensitivity. Hence, a more suitable method is required to determine the last stable mode of a cavity.

The last stable mode can be examined if the length of the cavity is known. Several techniques to measure the mirror separation are discussed in [162]. For example, side bands can be imprinted to the beam pumping the cavity. If the frequency difference to the carrier frequency is equal to half a free spectral range, the transmission signal of the sidebands is

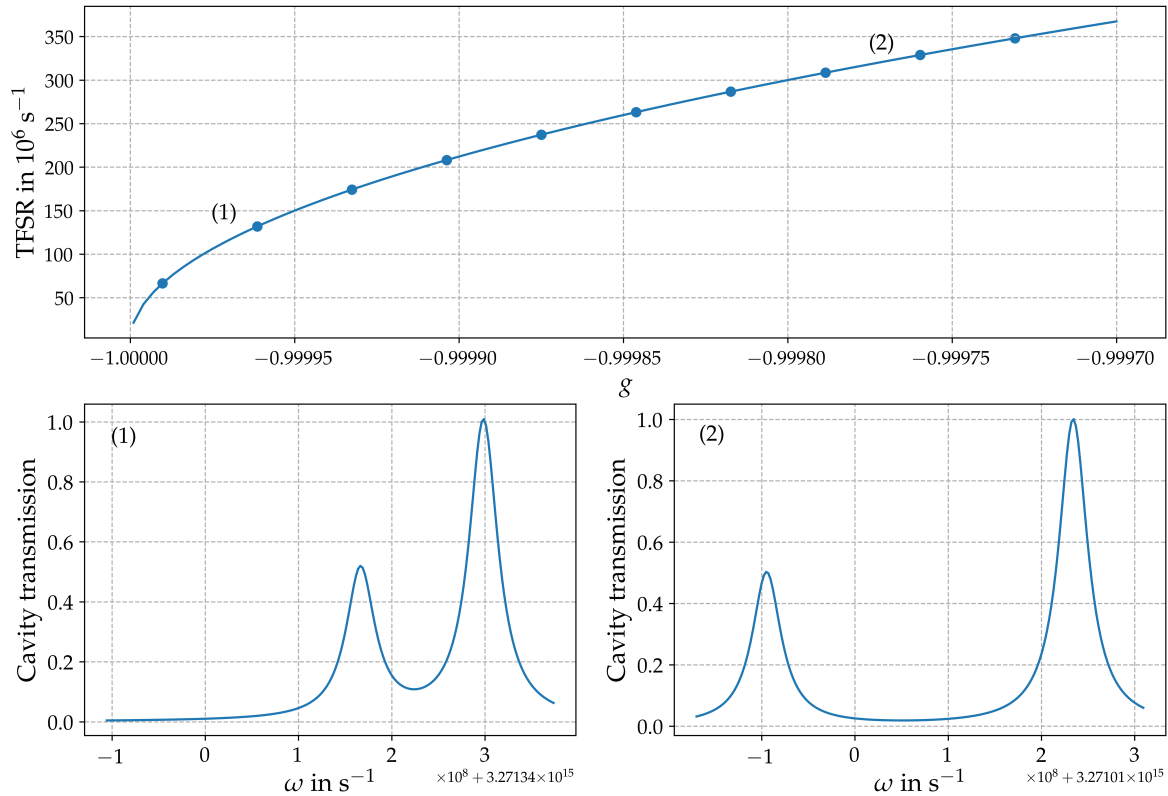


Figure 7.7: Theoretical concept to measure the cavity parameters indirectly through the TFSR. The mode matching of the cavity is chosen such that the fundamental 00-mode and a transverse mode of order 1 are pumped. The frequency of the laser, or alternatively the cavity length, is scanned and the cavity transmission is detected to receive a transmission spectra similar to the two bottom diagrams of the figure. The TFSR is determined by measuring the difference between the transmission peaks of order 0 and 1. According to equation 6.1 the cavity parameter product depends on the TFSR. This relation is also shown in the upper part of the figure. The solid line corresponds to equation 3.25, while the dots indicate the different longitudinal modes for a wavelength of 576.2 nm.

significantly enhanced and the cavity length can be determined. However, this method is only applicable for resonators with narrow linewidths and, therefore, not feasible for the imaging cavities.

Another technique suggested in [134] allows a direct determination of the mirror parameter product. This is even superior to the measurement of the length since the properties of the cavity primarily depend on this product and the mirror radii are not perfectly known. The measurement technique utilises the TFSR, see equation 6.1. The upper part of figure 7.7 shows the TFSR depending on the mirror parameter of a near-concentric cavity according to equation 3.25. The blue dots indicate the longitudinal 00-modes with index numbers of $q = 2L/\lambda$ supported by the cavity for a wavelength of $\lambda = 576.2 \text{ nm}$. The length difference of the cavity for each dot is $\frac{\lambda}{2}$

To determine the TFSR a periodic signal is applied to the piezo stage of the cavity mirror inducing oscillations of the resonator length, see chapter 7.2.3. A non-perfect mode matching is chosen such that transverse modes of order 1 are pumped beside the fundamental 00-mode. During the scan of the piezo two peaks should occur, referring to transverse mode orders 0 and 1, respectively. The distance between the peaks can then be measured to obtain the TFSR of the cavity. Two examples are depicted in the lower part of figure 7.7, corresponding to two different longitudinal modes as indicated by the numbers. The larger peak corresponds to

order 0, while the lower peak belongs to transverse mode order 1. The transmission spectrum corresponding to the resonator closer to the border of stability shows a significantly reduced difference between the resonance frequencies.

To determine the TFSR from transmission spectra, the data can be fitted by two Lorentzian profiles [134] according to

$$T = \frac{T_1}{\frac{(\omega - \omega_1)^2}{\kappa^2} + 1} + \frac{T_2}{\frac{(\omega - \omega_2)^2}{\kappa^2} + 1}. \quad (7.8)$$

T_1 and T_2 are determining the amplitudes of the peaks and ω_1 and ω_2 are the resonance frequencies of the 00- and 01-mode, respectively. The TFSR corresponds then to $\omega_1 - \omega_2$.

This measurement scheme is examined with a hemispherical test cavity. The radius of curvature of the spherical mirror is $r = 1$ cm, while the reflectivity of both mirror is $R = 0.979$. The wavelength of the pumping laser is 532 nm. The test cavity is similar to the resonator in figure 7.3. To obtain the transmission spectra necessary for determining the TFSR, an triangular voltage signal is applied to the piezo stage. Cavity transmissions are measured with a photodiode and an oscilloscope and, hence, the physical units of the spectra are voltage and time. The voltage is directly proportional to the intensity, but the time must be

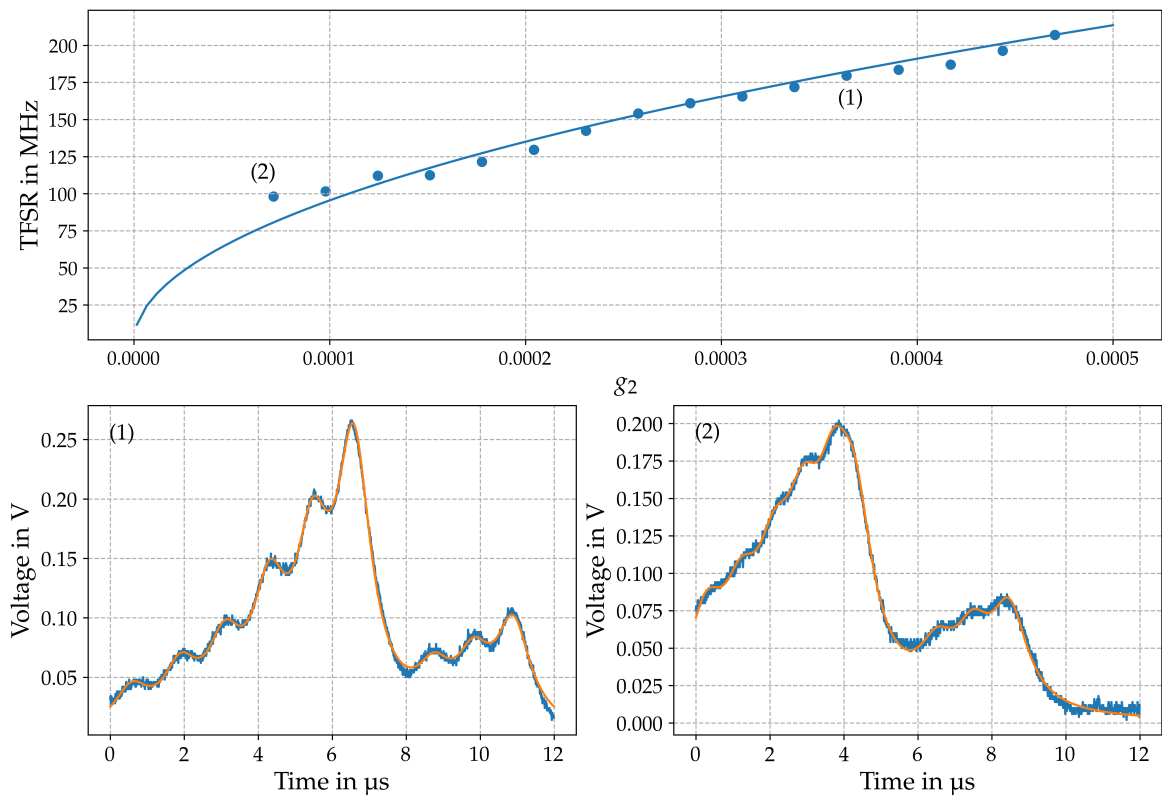


Figure 7.8: Measurement of the mirror parameter product for a near-hemispherical cavity with a length of approximately $L = 1$ cm. The dots in the upper part of the figure are obtained by measuring transmission spectra from which the TFSRs are determined. The solid line is the theoretically expected curve. For example, two spectra are shown in the lower part of the figure, the corresponding dots in the upper diagram are indicated by numbers. Lorentzian profiles are fitted to the data and multiple transverse mode orders are used to improve the quality of these fits. However, measurements for the last stable modes are not possible due to the large linewidth of the cavity. This is also indicated by the transmission spectrum in the lower right part of the figure, where different peaks cannot be clearly distinguished.

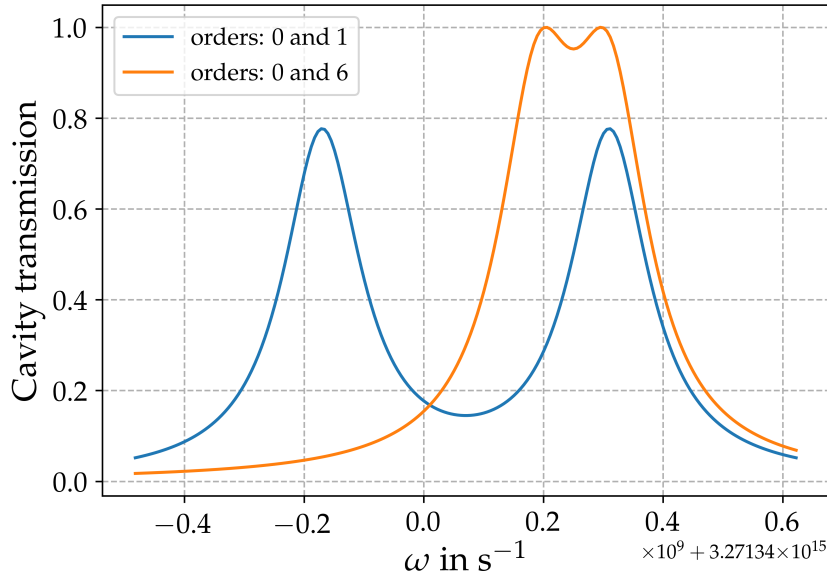


Figure 7.9: Two Spectra of a near-concentric resonator supporting the 00-/01-mode and the 00-/06-mode. Parameters are $g = -0.999968$ and $R = 0.9794$. If a 00-mode and 06-mode are coupled to the cavity, the peaks can clearly be distinguished allowing the determination of the TFSR even close to the border of stability.

converted into frequency units. This can be done by applying a reference frequency. For this purpose, the pumping beam of the cavity is phase modulated by a double pass acousto-optic modulator (AOM) to imprint a sideband. This side band also occurs in the transmission spectrum and since the frequency of the AOM is known to be $2\pi \cdot 350$ MHz, the difference between the 00-modes of the carrier and side band is equal to $2\pi \cdot 700$ MHz. From this, the difference between the 00- and 01-mode of can be obtained in frequency units.

A measurement of the cavity parameters is depicted in figure 7.8. As before, the upper part of the figure shows the theoretical expected curve and the blue dots correspond to the measured TFSRs for the different longitudinal modes. In the bottom part of the figure, two transmission spectra are shown and corresponding longitudinal modes are indicated by numbers. Lorentz profiles are fitted to the data with the `optimize.curve_fit` function from the SciPy Python library, which relies on the non-linear square method [163]. Several peaks occur in the transmission spectra due to two reasons. Firstly, the sideband reference is also included in the signal. Secondly, the quality of the fits is improved by including multiple transverse mode orders to the transmission spectrum. The peaks left to the maximum value correspond to transverse orders of 2, 4, 6, 8 and 10.

The measurement in figure 7.8 stops before the last stable modes of the resonator are reached since no reasonable data could be provided. This is probably a result of the broad linewidth of the cavity preventing a distinction of the different mode peaks. The transmission spectrum in the lower right part of the figure is also an indicator for this. To overcome this problem and to allow measurements for modes closer to the border of stability, the frequency difference between the 00-mode and a larger order could be utilised, e. g. the 06-mode since the linewidths of these modes would not overlap. The corresponding spectrum is shown in figure 7.9, where it is compared to the spectrum with only a 00- and 01-mode for a cavity with mirror parameters of $g = -0.999968$.

The measurement of the TFSR can only be improved by using higher order modes, if all orders between the modes of interest are suppressed. Such exotic mode matching profiles

cannot be obtained with common laser beams and lens systems. However, in [155] and [156], spatial light modulators (SLMs) are used to successfully demonstrate the simultaneous coupling of different transverse modes to a cavity. To couple a specific combination of these modes to a cavity, the profile of the pumping beam must be equal to a superposition of the corresponding modes. SLMs allow to modulate the phase or amplitude of an incoming beam pixel-wise and, hence, arbitrary beam profiles can be created, specifically combinations of Hermite-Gaussian modes. Further details, on how to apply SLMs can be found in [155].

A final remark regarding the operation of a cavity at the last stable mode concerns the resonance frequency. Specific values for the mirror parameters are required to ensure a waist of 1.5 μm . However, even if the cavity is adjusted to the corresponding length it is not guaranteed that the wavelength of the pumping beam matches the resonance frequency of the resonator. Therefore, it must be ensured that the frequency of the laser at least can be tuned over the free spectral range of the cavity.

7.2.5 Experimental setup

An experimental setup suitable to verify the proposed imaging scheme is illustrated in figure 7.10. Parts of the design of the experiment are inspired by [134] and [164]. Apart from a laser used for the detection itself, a second laser can be utilised to stabilise the cavity. The first laser is called the probe laser, while the second is referred to as the lock laser. The frequencies of both, the probe and the lock laser, need to be stabilised. For this purpose, a reference frequency is required. Such a reference can be generated by a second ultra-stable high finesse resonator consisting of ultra-low expansion glass to reduce thermal fluctuations. Both lasers can be locked to the reference cavity through the so called Pound-Drever-Hall technique [165, 166]. This kind of locking scheme is also utilised for all other stabilisation mechanisms in the presented setup. A detailed introduction of this technique can be found in [167].

The wavelength of the probe laser is set to 576.2 nm. Nanoparticles could also be detected by other wavelengths but using this value proves the technical feasibility of resonators suitable for detecting cold NaK molecules. The frequency of the lock laser can be chosen more freely, but must match the reflectivity of the mirrors.

The different technical components can be found in figure 7.10.

The optical isolators prevent back scattering into the lasers and by this disturbances of the beams. The probe beam is split into two partial beams by a polarizing beam splitter (PBS), one of them used for stabilising the laser frequency, while the other is used to pump the imaging cavity. A half-waveplate in front of the PBS allows to control the power distribution among the partial beams. Electro-optic modulators (EOMs) imprint sidebands with frequencies of 50 MHz to the laser fields used, to stabilise their corresponding frequencies. A suitable EOM for this purpose is the PM8-VIS from QUBIG [168].

After imprinting the sidebands with frequencies of 50 MHz, the lock laser is also split into two partial beams. The first beam is used to stabilize the lock laser's frequency itself, while the other is used to stabilise the imaging cavity in respect to the frequency of the reference resonator. The first beam is phase modulated by another EOM and one of the sidebands is finally used to stabilize the frequency of the lock laser to the reference cavity. This allows to adjust the resonance frequency of the imaging cavity independently from the reference resonator. To ensure this independence, the frequency of the second EOM can be adjusted and is generally larger with values in the GHz range. Suitable EOMs are PM9-VIS from QUBIG [168].

The partial beam of the probe laser used to stabilise its frequency with the reference cavity is a second time phase modulated by another EOM. Similar to the lock laser, this allows to adjust the frequency of the probe beam to be resonant with the imaging resonator. The beam not utilised for frequency stabilisation is again split into two partial beams. One

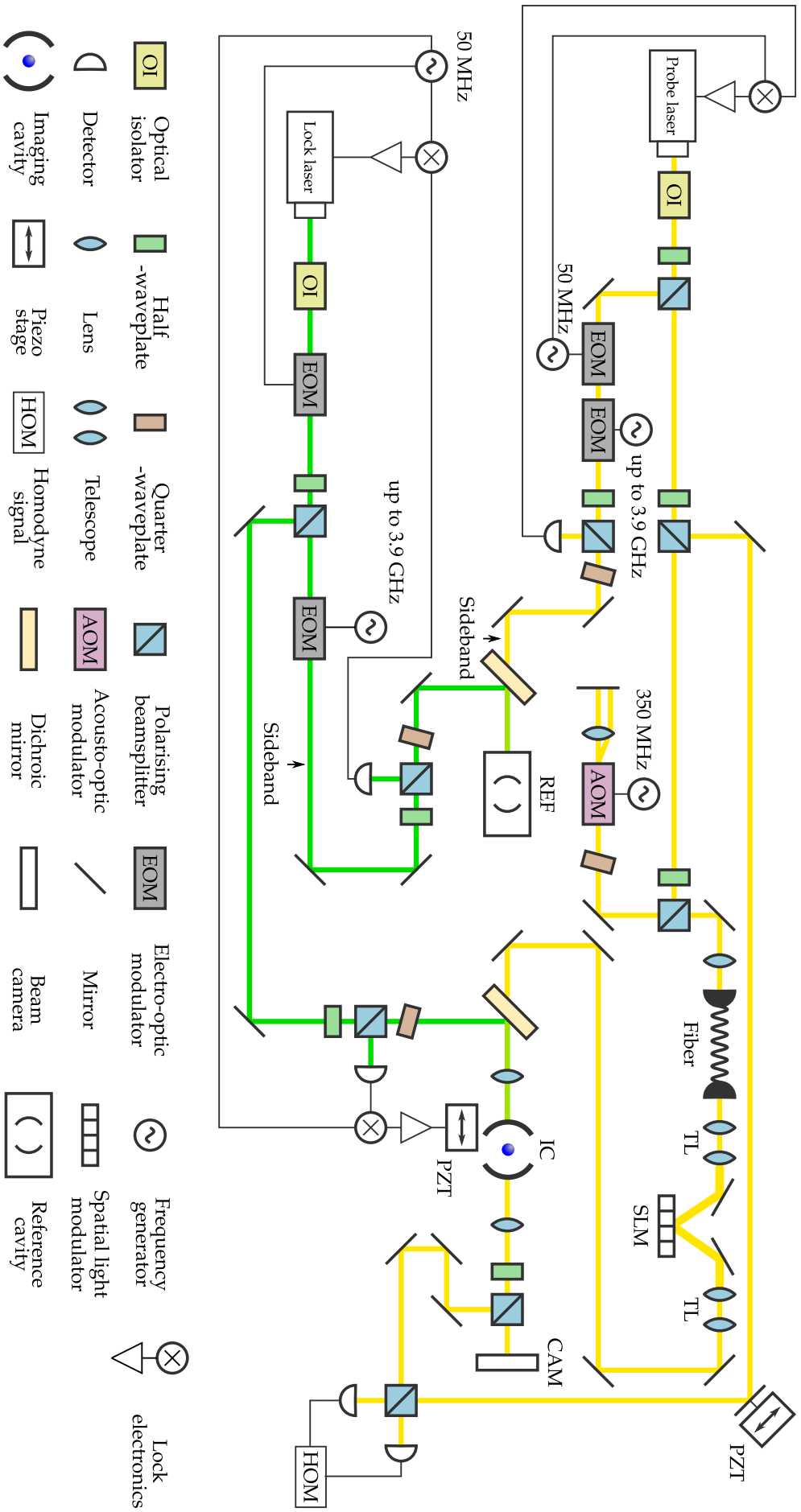


Figure 7.10: Proposed experimental setup for the detection of nanoparticles or cold molecules. Two lasers are used, one for the imaging of the particles itself, the other to stabilise the imaging cavity. The setuo is inspired by experimental designs in [134] and [164].

of these partial beams is used later as the local oscillator for the homodyne detection, while the other pumps the cavity. The length of the path of the local oscillator can be adjusted by a piezo stage allowing to stabilise the phase of this beam in respect to the phase of the signal beam.

A reference signal for the determination of the cavity parameter product (see chapter 7.2.4) can be imprinted on the pump beam through a double pass acousto-optic modulator (AOM, AOMO 3350-125 from Gooch and Housego [169]). Double pass means that the beam is reflected and passing through the AOM a second time. This is necessary since the sidebands of AOMs are also refracted and the double pass allows, therefore, to overlap the sideband with the carrier again. An AOM is utilised instead of an EOM to imprint only one sideband to the beam since a single reference for the g -measurement is sufficient. This reduces the number of modes in the signal of the imaging resonator. After determining the cavity parameters, the AOM can be switched off to get rid of the sideband in the pumping beam.

After imprinting the reference sideband, the beam profile is cleaned, i. e. brought into a pure Gaussian profile, with a fibre for a less complicated implementation of the SLM. As explained in the previous section, one purpose of the SLM is to couple specific Hermite-Gaussian modes into the cavity to measure the mirror parameters. When this measurement is completed, the SLM can still be used for appropriate mode matching, e. g. by compensating aberrations. SLMs usually require large beam sizes and, hence, a telescope is provided to enlarge the size of the pumping beam. A suitable SLM is the 512 x 512 Spatial Light Modulator from Meadowlark [170].

Finally, the beam enters the imaging cavity to detect the nanoparticles and the transmission signal of the resonator is measured with a homodyne detector to determine the particles' positions as explained in chapter 4.

Chapter 8

Conclusion and Outlook

In this thesis an imaging technique suitable to detect single cold particles spatially resolved is proposed. In particular, the detection scheme is applicable for polar molecules by utilising dispersive light-matter interactions. This allows to scatter a larger number of photons for the imaging signal compared to absorption or fluorescence methods, which often fail due to missing closed cycling transitions. During the measurement low power or a large transition-laser detuning ensures that the molecules remain in the low-saturation regime, i. e. absorption processes are suppressed. The signal strength is enhanced by an optical resonator. A superposition of transverse modes allows to determine the positions of the molecules by utilising a modified homodyne detector, where the fields in both arms of the detector are measured in a spatially resolved manner.

In the first part of this thesis, two different theoretical backgrounds for the imaging procedure are derived. First, an intuitive classical approach is developed by interpreting molecules as dipole emitters. The overlap integral between scattered field and an arbitrary Hermite-Gaussian mode is calculated and the amplitudes of different transverse modes are determined. Afterwards, the effect of a cavity on the mode distribution is evaluated and a system of coupled equations for the Hermite-Gaussian modes is derived. A homodyne detection scheme is taken into account and an expression for an imaging signal is presented. The impact of the size of the resonator waist and number of supported modes is investigated and it is shown that smaller waists are mandatory to achieve resolutions in the sub- μm regime, while the effect of large mode numbers is not that critical. Subsequently, a quantum mechanical version of the imaging theory is explained and compared to the classical approach. It is shown that both theories are equivalent apart from vacuum field fluctuations, a pure quantum physical effect and important to determine the fundamental limit of signal noise.

After determining the theoretical background, cavity properties important for an effective imaging process are discussed with a special focus on resonators capable to resolve bosonic NaK molecules inside an optical lattice with a periodicity of $0.532\ \mu\text{m}$. A possible transition in the state structure of NaK molecules is identified with a corresponding dipole transition matrix element of 2.52D and excitation wavelength of 576.2nm . The cavities' waist is set to $1.5\ \mu\text{m}$ and the reflectivity is 0.9794 such that transverse modes of order 4 lie within the resonators linewidth. The lengths of the concentric and of the hemispherical cavity are $(0.02 - 30 \cdot 10^{-9})\text{m}$ and $(1 - 15 \cdot 10^{-9})\text{m}$, respectively. This corresponds to mirror parameters of -0.9999967 for the concentric and 1 and $1.5 \cdot 10^{-6}$ for the hemispherical resonator. The single particle cooperativity is 1.94 . Simulations of homodyne signals are presented and differences in signals corresponding to different lattice fillings are pointed out.

In the following, cavities with the above theoretically chosen properties are designed. A modular construction method is utilised to reduce the number of components and allow to switch quickly between the different resonator types. Cavity geometries suitable for

the proposed detection scheme are close to the border of stability and difficult to realise. Components allowing to operate the different imaging resonators at these extreme points of the stability diagram are suggested. A measurement technique for the mirror parameters is presented, relying on the frequency difference between two adjacent transverse mode orders, which is necessary to operate the resonators at the last stable mode. This method is also examined with a test cavity and is in principle feasible except for the last few longitudinal modes, where the peaks of the different transverse modes start to merge due to the broad cavity linewidth. It is suggested to overcome this by coupling exact two transverse modes with significantly different orders to the cavity with a SLM.

An apparatus to prove the principle behind the proposed imaging scheme is developed. Nanoparticles are proposed as test objects to imitate cold molecules since these particles are capable to scatter light like a dipole-emitter if their size is significantly smaller than the corresponding wavelength. A short revision of optical properties of nanoparticles is given and different materials for the particles are discussed with titania and silver being the best options. The polarisability of nanoparticles and NaK molecules is compared to ensure similar scattering behaviours. The classical approach of the imaging scheme allows to compare the homodyne signals of both, nanoparticles and molecules.

In conclusion, an imaging technique suitable to detect single molecules spatially resolved is proposed and cavities appropriate for this purpose are developed. Components are suggested to ensure technical feasibility and a test apparatus is designed to verify the detection method, first with a confocal resonator, followed by a hemispherical and than finally by a concentric cavity.

The next logical step is to realise the proposed test apparatus and verify the imaging technique experimentally with nanoparticles. Afterwards, the detection method could be applied to cold molecules. Cold quantum gases are created in high vacuum chambers and a resonator suitable for the detection of cold molecules must be applicable in such an environment. Hence, a more compact design of the cavity is necessary and the components need to be compatible with the vacuum of the molecules' production chamber. Gimbal mounts satisfying this requirements must probably be custom designed and produced. Furthermore, once the cavity is placed inside this chamber readjustments are only possible through piezo elements, which can be controlled from the outside. Therefore, the cavity should be robust enough that only small corrections of the different degrees of freedom are necessary. In [134] and [171] cavities applied in vacuum chambers are described.

Another option apart from two-mirror cavities are ring resonators, see chapter 3.2. The total length of ring resonators can be larger compared to two-mirror cavities allowing to construct the resonator outside of the chamber and the cavity field can then enter the corresponding chamber through windows. This approach is realised in [172], for example. Constructing a resonator outside of the chamber allows to maintain it more easily and the components are not required to be vacuum compatible.

There might be even more advantages of ring resonators. Compared to two-mirror cavities ring resonator usually provide propagating waves instead of standing waves. In the case of standing waves, the nodes of even and odd modes are located at different positions and molecules must be placed between nodes and antinodes to simultaneously couple the molecule to all modes. In a propagating wave nodes do not exist and the single particle cooperativity can effectively be increased by this.

Compared to two-mirror resonators ring cavities provide an additional degree of freedom since the mirror parameters are defined by two different lengths, see equations 3.35 and 3.36. This allows to adjust the waist and the TFSR independently from each other. Different values for the mirror parameters and longer resonator lengths allow to achieve smaller TFSRs compared to two-mirror cavities and, hence, the multimode regime can be entered

more easily. This, in turn, enables to adjust the linewidth independently from the TFSR and the cooperativity can be chosen more freely.

To elaborate the advantages of ring resonators further, an example is provided. The cavity is assumed to consist of two flat and two spherical mirrors, illustrated in figure 3.3. As explained in chapter 3.2, this type of cavity provides two different Gaussian beams located at the the different sides of the spherical mirrors and the beam used for imaging the molecules propagates between mirror 1 and 2 in figure 3.3. The spherical mirrors are separated by a distance of $(0.1 - 35 \cdot 10^{-9})$ m, while the total length of the beam's path between the spherical mirrors over the flat mirrors is $(0.5 - 35 \cdot 10^{-9})$ m. The corresponding radius of curvature of the spherical mirrors is 0.0833 m and the wavelength is, as before, set to 576.2 nm.

These values provide an imaging waist of approximately $1.5 \mu\text{m}$ as in the case of the concentric or hemispherical cavity. The TFSR is, however, $2\pi \cdot 235$ kHz and, hence, reduced by a factor of 25 compared to the TFSR of the two-mirror resonators, see chapter 6.7. Assuming mirror reflectivities of 0.98 for the spherical and 0.99 for the plane mirrors, respectively, results in a linewidth approximately ten times smaller compared to the concentric resonator and, thus, in an increase of the cooperativity by a factor of 4.8.

Ring cavities, however, automatically contain an astigmatism since the effective radius of curvature of the mirrors depends on the plane of incident of the light beam, see [90]. This leads to different cavity parameters along the x - and y -direction and the waist cannot be $1.5 \mu\text{m}$ for both directions simultaneously. In [173], parabolic instead of spherical mirrors are proposed to overcome this issue and, in [172], a parabolic ring resonators is successfully demonstrated. Also, the aperture of parabolic mirrors is in theory not limited, which allows to compensate potential misalignment sensitivity.

So far, misalignment sensitivity has not been investigated in the literature and the aperture of parabolic mirrors might be limited due to technical reasons. Furthermore, in [172] it is explained that the cavity waist is currently limited as a result of angled reflections, but it is also stated that there are no theoretical restrictions prohibiting diffraction limited values.

Ring resonators might be a powerful tool to image cold molecules, however, before implementation, further theoretical investigations are necessary. Theories regarding misalignment sensitivity are more complicated compared to two-mirror cavities due to the higher number of involved mirrors. Also, potential effects of rotated parabolic mirrors regarding astigmatism must be investigated. To demonstrate the proposed imaging scheme with nanoparticles two-mirror resonators are a valid choice since the wealth of experience of these cavities is large. The above investigations should allow to decide whether a vacuum-compatible two-mirror resonator or a ring cavity is more suitable for the detection of cold molecules.

Appendix A

Mathematical transformations

In this chapter, the equations 4.29 to 4.34 and 4.36 are derived. These equations are used to simplify the overlap integral from equation 4.6. Furthermore, it is shown that all terms and factors related to the sign- and Heaviside step function occurring during the derivation of equation 4.41 eliminate each other. In a last step the algebraic transformations for equation 5.68 are shown.

Equation 4.29

First, equations 2.12 and 2.10 are inserted into

$$\phi = \frac{k\omega^2}{4} \left(\frac{1}{z - z_i} - \frac{1}{R} \right) \quad (\text{A.1})$$

for the radius of curvature of the phase front and the beam size, respectively. Additionally, the relation $k\omega_0^2 = 2z_R$ is used:

$$\phi = \frac{z_R \left(1 + \frac{z^2}{z_R^2} \right)}{2} \left(\frac{1}{z - z_i} - \frac{1}{z \left(1 + \frac{z_R^2}{z^2} \right)} \right) \quad (\text{A.2})$$

$$= \frac{z_R \left(1 + \frac{z^2}{z_R^2} \right)}{2} \left(\frac{z \left(1 + \frac{z_R^2}{z^2} \right) - z - z_i}{(z - z_i) z \left(1 + \frac{z_R^2}{z^2} \right)} \right). \quad (\text{A.3})$$

This expression is then multiplied with $\frac{z}{z}$ and $\frac{z_R}{z_R}$:

$$\phi = \frac{z_R \left(1 + \frac{z^2}{z_R^2} \right)}{2} \frac{z_R}{z_R} \left(\frac{z \left(1 + \frac{z_R^2}{z^2} \right) - z + z_i}{(z - z_i) z \left(1 + \frac{z_R^2}{z^2} \right)} \right) \frac{z}{z} \quad (\text{A.4})$$

$$= \frac{z^2 + z_R^2}{2z_R} \frac{z^2 + z_R^2 - z^2 + z_i z}{(z - z_i) (z^2 + z_R^2)} \quad (\text{A.5})$$

$$= \frac{z z_i + z_R^2}{2z_R (z - z_i)}. \quad (\text{A.6})$$

Equations 4.30 and 4.31

Without loss of generality, the derivation is shown for the x -direction. Inserting equations 4.15 and 4.29 leads to

$$\frac{\xi_x}{\sqrt{(4\phi^2 + 1)}} = \frac{kwx_i}{\sqrt{2}(z - z_i) \sqrt{\left(\frac{zz_i + z_R^2}{zz_R - z_i z_R}\right)^2 + 1}} \quad (\text{A.7})$$

$$= \text{sign}(z - z_i) \frac{kwx_i}{\sqrt{2} \sqrt{(z - z_i)^2 \left(\frac{zz_i + z_R^2}{zz_R - z_i z_R}\right)^2 + (z - z_i)^2}}, \quad (\text{A.8})$$

with $\text{sgn}(x)$ being the sign function, i. e. $\text{sgn}(x) = +1$ for positive values of x and $\text{sgn}(x) = -1$ for negative values. In a second step equation 2.10 and $k\omega_0 = \frac{2z_R}{w_0}$ are used to obtain

$$\frac{\xi_x}{\sqrt{(4\phi^2 + 1)}} = \frac{2z_R x_i \sqrt{1 + \frac{z^2}{z_R^2}}}{\sqrt{2} w_0 \sqrt{(z - z_i)^2 \left(\frac{zz_i + z_R^2}{zz_R - z_i z_R}\right)^2 + (z - z_i)^2}} \text{sign}(z - z_i) \quad (\text{A.9})$$

$$= \frac{\sqrt{2} x_i}{w_0} \sqrt{\frac{z_R^2 + z^2}{(z - z_i)^2 \frac{(zz_i + z_R)^2}{z_R^2 (z - z_i)^2} + (z - z_i)^2}} \text{sign}(z - z_i) \quad (\text{A.10})$$

$$= \frac{\sqrt{2} x_i}{w_0} \sqrt{\frac{z_R^2 + z^2}{\frac{(zz_i + z_R)^2}{z_R^2} + (z - z_i)^2}} \text{sign}(z - z_i) \quad (\text{A.11})$$

$$= \frac{\sqrt{2} x_i}{w_0} \sqrt{\frac{z_R^2 + z^2}{\frac{z^2 z_i^2 + 2zz_i z_R^2 + z_R^4}{z_R^2} + (z - z_i)^2}} \text{sign}(z - z_i) \quad (\text{A.12})$$

$$= \frac{\sqrt{2} x_i}{w_0} \sqrt{\frac{(z_R^2 + z^2) z_R^2}{z^2 z_i^2 + 2zz_i z_R^2 + z_R^4 + z_R^2 z^2 - 2zz_i z_R^2 + z_i^2 z_R^2}} \text{sign}(z - z_i) \quad (\text{A.13})$$

$$= \frac{\sqrt{2} x_i}{w_0} \sqrt{\frac{(z_R^2 + z^2) z_R^2}{z_R^2 (z_R^2 + z^2) + z^2 z_i^2 + z_i^2 z_R^2}} \text{sign}(z - z_i) \quad (\text{A.14})$$

$$= \frac{\sqrt{2} x_i}{w_0} \sqrt{\frac{1}{1 + \frac{z_i^2 (z^2 + z_R^2)}{z_R^2 (z^2 + z_R^2)}}} \text{sign}(z - z_i) \quad (\text{A.15})$$

$$= \frac{\sqrt{2} x_i}{w_0} \sqrt{\frac{1}{1 + \frac{z_i^2}{z_R^2}}} \text{sign}(z - z_i) \quad (\text{A.16})$$

$$= \frac{\sqrt{2} x_i}{w(z_i)} \text{sign}(z - z_i). \quad (\text{A.17})$$

Equation 4.32

Again, without loss of generality, the derivation is shown for the x -direction. In a first step equation 4.29 is used:

$$\frac{\phi}{4\phi^2 + 1} = \frac{1}{4\phi + \frac{1}{\phi}} \quad (\text{A.18})$$

$$= \frac{1}{4 \frac{zz_i + z_R^2}{2zz_R - 2z_i z_R} + \frac{2zz_R - 2z_i z_R}{zz_i + z_R^2}} \quad (\text{A.19})$$

$$= \frac{1}{\frac{4(zz_i + z_R^2)^2 + (2zz_R - 2z_i z_R)^2}{(2zz_R - 2z_i z_R)(zz_i + z_R^2)}} \quad (\text{A.20})$$

$$= \frac{(2zz_R - 2z_i z_R)(zz_i + z_R^2)}{4z^2 z_i^2 + 8zz_i z_R^2 + z_R^4 + 4z^2 z_R^2 - 8zz_i z_R^2 + 4z_i^2 z_R^2} \quad (\text{A.21})$$

$$= \frac{(2zz_R - 2z_i z_R)(zz_i + z_R^2)}{4z^2 z_i^2 + 4z_R^4 + 4z^2 z_R^2 + 4z_i^2 z_R^2}. \quad (\text{A.22})$$

Next, equation 4.30 and $k^2 = \frac{4z_R^2}{w_0^4}$ are utilised:

$$\xi_x^2 = \left(\frac{kx_i w_0 \sqrt{1 + \frac{z^2}{z_R^2}}}{\sqrt{2}(z - z_i)} \right)^2 \quad (\text{A.23})$$

$$= \frac{k^2 x_i^2 w_0^2 \left(1 + \frac{z^2}{z_R^2}\right)}{2(z - z_i)^2} \quad (\text{A.24})$$

$$= \frac{2(z_R^2 + z^2)x_i^2}{(z - z_i)^2 w_0^2}. \quad (\text{A.25})$$

From this follows:

$$\frac{4\xi_x^2 \phi}{16\phi^2 + 4} = \frac{2(z_R^2 + z^2)x_i^2}{(z - z_i)^2 w_0^2} \frac{(2zz_R - 2z_i z_R)(zz_i + z_R^2)}{4z^2 z_i^2 + 4z_R^4 + 4z^2 z_R^2 + 4z_i^2 z_R^2} \quad (\text{A.26})$$

$$= \frac{1(z_R^2 + z^2)x_i^2}{2(z - z_i)^2 w_0^2} \frac{(2zz_R - 2z_i z_R)(zz_i + z_R^2)}{z^2 z_i^2 + z_i^2 z_R^2 + z_R^2(z_R^2 + z^2)} \quad (\text{A.27})$$

$$= \frac{1}{2} \frac{x_i^2}{(z - z_i)^2 w_0^2} \frac{(2zz_R - 2z_i z_R)(zz_i + z_R^2)}{z_R^2 + \frac{z^2 z_i^2 + z_i^2 z_R^2}{z_R^2 + z^2}} \quad (\text{A.28})$$

$$= \frac{1}{2} \frac{x_i^2}{(z - z_i)^2 w_0^2} \frac{(2zz_R - 2z_i z_R)(zz_i + z_R^2)}{z_R^2 + z_i^2} \quad (\text{A.29})$$

$$= \frac{1}{2} \frac{x_i^2}{(z - z_i)^2 w_0^2} \frac{2z_R(z - z_i)(zz_i + z_R^2)}{z_R^2 + z_i^2} \quad (\text{A.30})$$

$$= \frac{1}{2} \frac{kx_i^2}{(z - z_i)^2} \frac{zz_i + z_R^2}{z_R^2 + z_i^2} \quad (\text{A.31})$$

$$= \frac{1}{2} \frac{kx_i^2}{(z - z_i)^2} \frac{\frac{z_R^2}{z_i} + z}{z_i + \frac{z_R^2}{z_i}} \quad (\text{A.32})$$

$$= \frac{1}{2} \frac{kx_i^2}{(z - z_i)^2} \frac{\frac{z_R^2}{z_i} + z + z_i - z_i}{z_i \left(1 + \frac{z_R^2}{z_i^2}\right)} \quad (\text{A.33})$$

$$= \frac{1}{2} \frac{kx_i^2}{(z - z_i)^2} \frac{z_i \left(1 + \frac{z_R^2}{z_i^2}\right) + z - z_i}{z_i \left(1 + \frac{z_R^2}{z_i^2}\right)} \quad (\text{A.34})$$

$$= \frac{1}{2} \frac{kx_i^2}{(z - z_i)^2} \left(1 + \frac{z - z_i}{z_i \left(1 + \frac{z_R^2}{z_i^2}\right)}\right) \quad (\text{A.35})$$

$$= \frac{kx_i^2}{2(z - z_i)} + \frac{kx_i}{2R(z_i)}. \quad (\text{A.36})$$

Equation 4.33

Inserting equation 4.29 into

$$\exp(i\Psi) = \frac{4\phi - 2i}{|4\phi - 2i|} \quad (\text{A.37})$$

leads to

$$\exp(i\Psi) = \frac{\left(2 \frac{zz_i + z_R^2}{zz_R - z_i z_R} - 2i\right)}{|4\phi - 2i|}. \quad (\text{A.38})$$

This complex number is represented in Cartesian coordinates. The correct transformation of an arbitrary complex number $\chi = x + iy$ into polar coordinates depends on the values of the real (x) and imaginary (y) part. The different transformations are [174]

$$\Psi = \arctan2(x, y) = \arctan\left(\frac{y}{x}\right) \quad \text{for } x > 0, \quad \text{quadrant 1.) and 4.)} \quad (\text{A.39})$$

$$\Psi = \arctan2(x, y) = +\frac{\pi}{2} \quad \text{for } x = 0, y > 0, \quad (\text{A.40})$$

$$\Psi = \arctan2(x, y) = \arctan\left(\frac{y}{x}\right) + \pi \quad \text{for } x < 0, y > 0, \quad \text{quadrant 2.)} \quad (\text{A.41})$$

$$\Psi = \arctan2(x, y) = \pm\pi \quad \text{for } x < 0, y = 0, \quad (\text{A.42})$$

$$\Psi = \arctan2(x, y) = \arctan\left(\frac{y}{x}\right) - \pi \quad \text{for } x < 0, y < 0 \quad \text{quadrant 3.),} \quad (\text{A.43})$$

$$\Psi = \arctan2(x, y) = -\frac{\pi}{2} \quad \text{for } x = 0, y < 0. \quad (\text{A.44})$$

$$(\text{A.45})$$

and the various cases are visualised in figure A.1.

Equation A.38 reveals that the imaginary part of $\exp(i\Psi)$ is always negative limiting the number of transformations to obtain the correct phase Ψ . Still, a case discrimination is necessary. However, before the different cases are investigated, the ratio between imaginary and real part can be simplified:

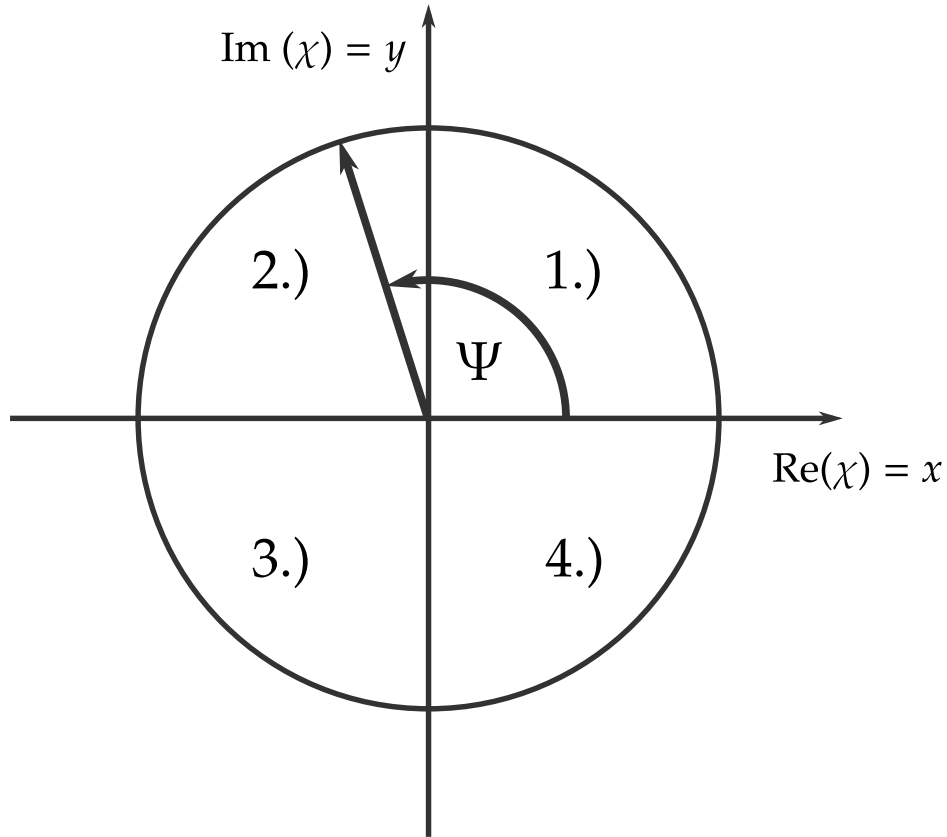


Figure A.1: Polar coordinates of a complex number. The numbers indicate different transformations rules between Cartesian and polar coordinates.

$$\frac{\text{Im}(\exp(i\Psi))}{\text{Re}(\exp(i\Psi))} = \frac{\frac{-2}{|4\phi-2i|}}{2 \frac{z z_i + z_R^2}{z z_R - z_i z_R}} \quad (\text{A.46})$$

$$= -\frac{z z_R - z_i z_R}{z z_i + z_R^2} \quad (\text{A.47})$$

$$= -\frac{z_i z}{z_R \left(1 + \frac{z z_i}{z_R^2}\right)} \quad (\text{A.48})$$

$$= \frac{\frac{z_i}{z_R} - \frac{z}{z_R}}{1 + \frac{z_i z}{z_R^2}} \quad (\text{A.49})$$

For the discrimination of cases the following addition theorems are needed [110]:

$$\arctan\left(\frac{x-y}{1+xy}\right) = \arctan(x) - \arctan(y) \quad \text{for } xy > -1 \quad (\text{A.50})$$

$$\arctan\left(\frac{x-y}{1+xy}\right) = \arctan(x) - \arctan(y) - \pi \quad \text{for } xy < -1 \text{ and } x > 0, \quad (\text{A.51})$$

$$\arctan\left(\frac{x-y}{1+xy}\right) = \arctan(x) - \arctan(y) + \pi \quad \text{for } xy < -1 \text{ and } x < 0. \quad (\text{A.52})$$

The real part of $\exp(i\Psi)$ determines if equation A.39, A.43 or A.44 must be applied for a correct transformation. Without loss of generality, the denominator and factor of 2 in

equation A.38 can be dropped and, hence, the real part of $\exp(i\Psi)$ is determined by $\frac{zz_i+z_R^2}{z_R(z-z_i)}$. Depending on the ratio between real and imaginary part, either equation A.50, A.51 or A.52 can be used to simplify the expression for the phase Ψ . In some cases, the requirements for the phase Ψ and the addition theorem are contradicting each other. This leads to the necessity of a nested case discrimination, where the different cases are indicated by numbers, roman letters and greek letters. A mathematical assumption applies for all cases after it is mentioned until explicitly another case of this prerequisite is investigated.

Note that $z_R > 0$ applies to all cases discussed below since the Rayleigh range is always larger than zero.

$$1.) \operatorname{Re}(\exp(i\Psi)) > 0 \rightarrow \frac{zz_i+z_R^2}{z_R(z-z_i)} > 0$$

In this case the phase is given by equation A.39.

$$a) z - z_i > 0$$

$$\Rightarrow zz_i + z_R^2 > 0$$

$$\Rightarrow \frac{zz_i}{z_R^2} > -1$$

Equation A.50 applies:

$$\Psi = \arctan\left(\frac{\frac{z_i}{z_R} - \frac{z}{z_R}}{1 + \frac{z_i z}{z_R^2}}\right) \quad (\text{A.53})$$

$$= \arctan\left(\frac{z_i}{z_R}\right) - \arctan\left(\frac{z}{z_R}\right). \quad (\text{A.54})$$

$$b) z - z_i < 0$$

$$\Rightarrow zz_i + z_R^2 < 0$$

$$\Rightarrow \frac{zz_i}{z_R^2} < -1$$

$$\alpha) z_i > 0$$

Equation A.51 applies:

$$\Psi = \arctan\left(\frac{\frac{z_i}{z_R} - \frac{z}{z_R}}{1 + \frac{z_i z}{z_R^2}}\right) \quad (\text{A.55})$$

$$= \arctan\left(\frac{z_i}{z_R}\right) - \arctan\left(\frac{z}{z_R}\right) - \pi. \quad (\text{A.56})$$

$$\beta) z_i < 0$$

From $z - z_i < 0$ follows $z < 0$.

Contradiction to $zz_i + z_R^2 < 0$.

\Rightarrow Case not possible.

$$\gamma) z_i = 0$$

Contradiction to $zz_i + z_R^2 < 0$.

\Rightarrow Case not possible.

$$2.) \operatorname{Re}(\exp(i\Psi)) < 0 \rightarrow \frac{zz_i + z_R^2}{z_R(z - z_i)} < 0$$

In this case the phase is given by equation A.43.

$$\mathbf{a)} z - z_i > 0$$

$$\Rightarrow zz_i + z_R^2 < 0$$

$$\Rightarrow \frac{zz_i}{z_R^2} < -1$$

$$\mathbf{a)} z_i > 0$$

From $z - z_i > 0$ follows $z > 0$.

From $z_i > 0$ and $z > 0$ follows $\frac{zz_i}{z_R^2} > 0$.

Contraction to $1 + \frac{zz_i}{z_R^2} < 0$.

\Rightarrow Case not possible.

$$\mathbf{\beta)} z_i < 0$$

$$\frac{zz_i}{z_R^2} < -1 \text{ applies.}$$

Hence, equation A.52 applies:

$$\Psi = \arctan\left(\frac{\frac{z_i}{z_R} - \frac{z}{z_R}}{1 + \frac{z_i z}{z_R^2}}\right) - \pi \quad (\text{A.57})$$

$$= \arctan\left(\frac{z_i}{z_R}\right) - \arctan\left(\frac{z}{z_R}\right) + \pi - \pi \quad (\text{A.58})$$

$$= \arctan\left(\frac{z_i}{z_R}\right) - \arctan\left(\frac{z}{z_R}\right). \quad (\text{A.59})$$

$$\gamma) z_i = 0$$

Contradiction to $zz_i + z_R^2 < 0$.

\Rightarrow Case not possible.

$$\mathbf{b)} z - z_i < 0$$

$$\Rightarrow zz_i + z_R^2 > 0$$

$$\Rightarrow \frac{zz_i}{z_R^2} > -1$$

Equation A.50 applies:

$$\Psi = \arctan\left(\frac{\frac{z_i}{z_R} - \frac{z}{z_R}}{1 + \frac{z_i z}{z_R^2}}\right) - \pi \quad (\text{A.60})$$

$$= \arctan\left(\frac{z_i}{z_R}\right) - \arctan\left(\frac{z}{z_R}\right) - \pi. \quad (\text{A.61})$$

$$3.) \operatorname{Re}(\exp(i\Psi)) = 0 \rightarrow \frac{zz_i + z_R^2}{z_R(z - z_i)} = 0$$

In this case the phase is given by equation A.44 and, hence, $\Psi = -\frac{\pi}{2}$.

From $zz_i + z_R^2 = 0$ follows $\frac{z_i}{z_R} = -\frac{z_R}{z}$.

In the following two cases the relation[110] $\operatorname{sgn}(x)\frac{\pi}{2} = \arctan(x) + \arctan\left(\frac{1}{x}\right)$ is used.

α) $z_i > 0$

$$\Psi = -\frac{\pi}{2} \quad (\text{A.62})$$

$$= \frac{\pi}{2} - \pi \quad (\text{A.63})$$

$$= \arctan\left(\frac{z_i}{z_R}\right) + \arctan\left(\frac{z_R}{z_i}\right) - \pi \quad (\text{A.64})$$

$$= \arctan\left(\frac{z_i}{z_R}\right) - \arctan\left(\frac{z}{z_R}\right) - \pi. \quad (\text{A.65})$$

β) $z_i < 0$

$$\Psi = -\frac{\pi}{2} \quad (\text{A.66})$$

$$= \arctan\left(\frac{z_i}{z_R}\right) + \arctan\left(\frac{z_R}{z_i}\right) \quad (\text{A.67})$$

$$= \arctan\left(\frac{z_i}{z_R}\right) - \arctan\left(\frac{z}{z_R}\right). \quad (\text{A.68})$$

All these cases are summarised in table A.1. Depending on the sign of $z - z_i$ an additional $-\pi$ can occur. Further below it is shown that this potential additional $-\pi$ always cancels out with other factors in the overlap integral and, thus, is effectively eliminated.

Equation 4.34

First, equation 4.29 is inserted into $\frac{1}{1-i2\phi}$:

$$\frac{1}{1-i2\phi} = \frac{1}{1-i2\frac{zz_i+z_R^2}{2z_R(z-z_i)}} \quad (\text{A.69})$$

$$= \frac{1}{\frac{z_R(z-z_i)-i(zz_i+z_R^2)}{z_R(z-z_i)}} \quad (\text{A.70})$$

$$= \frac{z_R (z - z_i)}{z_R (z - z_i) - i (zz_i + z_R^2)}. \quad (\text{A.71})$$

Hence, the real and imaginary parts are given by

$$\operatorname{Re}\left(\frac{1}{1 - i2\phi}\right) = \frac{(z - z_i)^2 z_R^2}{(z - z_i)^2 z_R^2 + (zz_i + z_R^2)^2}, \quad (\text{A.72})$$

$$\operatorname{Im}\left(\frac{1}{1 - i2\phi}\right) = \frac{z_R (z - z_i) (zz_i + z_R^2)}{(z - z_i)^2 z_R^2 + (zz_i + z_R^2)^2}. \quad (\text{A.73})$$

Since the denominator of the real and imaginary part is always greater than zero the phase of $\frac{1}{1 - i2\phi}$ is given by equation A.39 and, thus,

$$\arg\left(\frac{1}{1 - i2\phi}\right) = \arctan\left(\frac{\operatorname{Re}\left(\frac{1}{1 - i2\phi}\right)}{\operatorname{Im}\left(\frac{1}{1 - i2\phi}\right)}\right) \quad (\text{A.74})$$

$$= \arctan\left(\frac{z_R (z - z_i) (zz_i + z_R^2)}{(z - z_i)^2 z_R^2}\right) \quad (\text{A.75})$$

$$= \arctan\left(\frac{(z - z_i) zz_i z_R + (z - z_i) z_R^3}{(z - z_i)^2 z_R^2}\right) \quad (\text{A.76})$$

$$= \arctan\left(\frac{(z - z_i) \left(\frac{zz_i}{z_R} + z_R\right)}{(z - z_i)^2}\right) \quad (\text{A.77})$$

$$= \arctan\left(\frac{\left(\frac{zz_i}{z_R} + z_R\right)}{(z - z_i)}\right) \quad (\text{A.78})$$

$$= \arctan\left(\frac{\left(\frac{zz_i}{z_R} + z_R\right)}{z \left(1 - \frac{z_i}{z}\right)}\right) \quad (\text{A.79})$$

$$= \arctan\left(\frac{\frac{z_i}{z_R} + \frac{z_R}{z}}{1 - \frac{z_i}{z}}\right). \quad (\text{A.80})$$

Depending on the values of z_i and $\frac{z_i}{z}$, different addition theorems can be applied[110]:

$$\arctan\left(\frac{x + y}{1 - xy}\right) = \arctan(x) + \arctan(y) \quad \text{for } xy < 1, \quad (\text{A.81})$$

$$\arctan\left(\frac{x + y}{1 - xy}\right) = \arctan(x) + \arctan(y) - \pi \quad \text{for } xy > 1 \text{ and } x > 0, \quad (\text{A.82})$$

$$\arctan\left(\frac{x + y}{1 - xy}\right) = \arctan(x) + \arctan(y) + \pi \quad \text{for } xy > 1 \text{ and } x < 0. \quad (\text{A.83})$$

Another discrimination of cases is necessary:

$$1.) \frac{z_i}{z} < 1$$

$$\arg\left(\frac{1}{1-i2\phi}\right) = \arctan\left(\frac{z_i}{z_R}\right) + \arctan\left(\frac{z_R}{z}\right). \quad (\text{A.84})$$

2.) $\frac{z_i}{z} > 1$ and $z_i > 0$

$$\arg\left(\frac{1}{1-i2\phi}\right) = \arctan\left(\frac{z_i}{z_R}\right) + \arctan\left(\frac{z_R}{z}\right) - \pi. \quad (\text{A.85})$$

3.) $\frac{z_i}{z} > 1$ and $z_i < 0$

$$\arg\left(\frac{1}{1-i2\phi}\right) = \arctan\left(\frac{z_i}{z_R}\right) + \arctan\left(\frac{z_R}{z}\right) + \pi. \quad (\text{A.86})$$

Depending on the sign of $\frac{z_i}{z} - 1$ an additional $-\pi$ might be applied. This potential additional term of $-\pi$ also in this case cancels out with other factors in the overlap integral, as shown later.

Apart from the phase, it is also necessary to determine the amplitude of $\frac{1}{1-i2\phi}$ correctly. The amplitude is given by

$$\text{abs}\left(\frac{1}{1-i2\phi}\right) = \sqrt{\text{Re}\left(\frac{1}{1-i2\phi}\right) + \text{Im}\left(\frac{1}{1-i2\phi}\right)} \quad (\text{A.87})$$

$$= \sqrt{\frac{z_R^4 (z - z_i)^4 + z_R^2 (z - z_i)^2 (zz_i + z_R)^2}{\left((z - z_i)^2 z_R^2 + (zz_i + z_R^2)^2\right)^2}}. \quad (\text{A.88})$$

For simplicity, the numerator and denominator are treated separately. The numerator is

$$z_R^4 (z - z_i)^4 + z_R^2 (z - z_i)^2 (zz_i + z_R)^2 \quad (\text{A.89})$$

$$= (z^2 - 2zz_i + z_i^2)^2 z_R^4 + (z^2 z_R^2 - 2zz_i z_R^2 + z_i^2 z_R^2) (z^2 z_i^2 + 2zz_i z_R^2 + z_R^4) \quad (\text{A.90})$$

$$= z^4 z_R^4 - 2z^3 z_i z_R^4 + z^2 z_i^2 z_R^4 - 2z^3 z_i z_R^4 + 4z^2 z_i^2 z_R^4 - 2zz_i^3 z_R^4 + z^2 z_i^2 z_R^4 \quad (\text{A.91})$$

$$- 2zz_i^3 z_R^4 + z_i^4 z_R^4 + z^4 z_i^2 z_R^2 + 2z^3 z_i z_R^4 + z^2 z_R^6 - 2z^3 z_i^3 z_R^2 \quad (\text{A.92})$$

$$- 4z^2 z_i^2 z_R^4 - 2zz_i z_R^6 + z^2 z_i^4 z_R^2 + 2zz_i^3 z_R^4 + z_i^2 z_R^6 \quad (\text{A.93})$$

$$= z^4 z_R^4 - 2z^3 z_i z_R^4 + 2z^2 z_i^2 z_R^4 - 2zz_i^3 z_R^4 + z_i^4 z_R^4 + z^4 z_i^2 z_R^2 + z^2 z_R^6 \quad (\text{A.94})$$

$$- 2z^3 z_i^3 z_R^2 - 2zz_i z_R^6 + z^2 z_i^4 z_R^2 + z_i^2 z_R^6 \quad (\text{A.95})$$

$$= z_R^2 (z^4 z_R^2 + 2z^2 z_i^2 z_R^2 + z_i^4 z_R^2 + z^4 z_i^2 + z^2 z_R^4 - 2z^3 z_i^3) \quad (\text{A.96})$$

$$- 2zz_i z_R^4 + z^2 z_i^4 + z_i^2 z_R^4 - 2z^3 z_i z_R^2 - 2zz_i^3 z_R^2) \quad (\text{A.97})$$

$$= z_R^2 \left((z - z_i)^2 z_R^4 + (z - z_i)^2 z^2 z_R^2 + z^2 z_i^2 z_R^2 \right) \quad (\text{A.98})$$

$$+ z_i^4 z_R^2 + z^4 z_i^2 - 2z^3 z_i^3 + z^2 z_i^4 - 2zz_i^3 z_R^2) \quad (\text{A.99})$$

$$= z_R^2 \left((z - z_i)^2 z_R^4 + (z - z_i)^2 z^2 z_R^2 + (z - z_i)^2 z^2 z_i^2 + (z - z_i)^2 z_i^2 z_R^2 \right) \quad (\text{A.100})$$

$$= z_R^2 (z - z_i)^2 (z_R^4 + z^2 z_R^2 + z^2 z_i^2 + z_i^2 z_R^2) \quad (\text{A.101})$$

and for the denominator

$$\left((z - z_i)^2 z_R^2 + (zz_i + z_R^2)^2 \right)^2 \quad (\text{A.102})$$

$$= \left(z^2 z_R^2 - 2zz_i z_R^2 + z_i^2 z_R^2 + z^2 z_i^2 + 2zz_i z_R^2 + z_R^4 \right)^2 \quad (\text{A.103})$$

$$= \left(z_R^4 + z^2 z_R^2 + z^2 z_i^2 + z_i^2 z_R^2 \right) (z^2 + z_R^2) (z_i^2 + z_R^2) \quad (\text{A.104})$$

can be found. Inserting the transformed numerator and denominator into the amplitude of $\frac{1}{1-i2\phi}$ yields

$$\text{abs}\left(\frac{1}{1-i2\phi}\right) = \sqrt{\frac{z_R^2 (z - z_i)^2}{(z^2 + z_R^2)(z_i^2 + z_R^2)}}. \quad (\text{A.105})$$

Equation 4.36

$$\frac{w(z)}{z - z_i} \sqrt{\frac{z_R^2 (z - z_i)^2}{(z^2 + z_R^2)(z_i^2 + z_R^2)}} \quad (\text{A.106})$$

$$= w_0 \sqrt{\frac{\left(1 + \frac{z^2}{z_R^2}\right) z_R^2 (z - z_i)^2}{(z - z_i)^2 (z^2 + z_R^2)(z_i^2 + z_R^2)}} \text{sgn}(z - z_i) \quad (\text{A.107})$$

$$= w_0 \sqrt{\frac{\left(1 + \frac{z^2}{z_R^2}\right) z_R^2}{(z^2 + z_R^2)(z_i^2 + z_R^2)}} \text{sgn}(z - z_i) \quad (\text{A.108})$$

$$= w_0 \sqrt{\frac{(z^2 + z_R^2)}{(z^2 + z_R^2)(z_i^2 + z_R^2)}} \text{sgn}(z - z_i) \quad (\text{A.109})$$

$$= \frac{w_0}{z_R \sqrt{1 + \frac{z_i^2}{z_R^2}}} \text{sgn}(z - z_i) \quad (\text{A.110})$$

$$= \frac{w_0^2}{z_R w(z_i)} \text{sgn}(z - z_i) \quad (\text{A.111})$$

Summary of phases

The different phases of Ψ and $\left(\frac{1}{1-i2\phi}\right)$ are summarised in table A.1.

As previously mentioned, the different cases for the phases partially contain additional terms of $-\pi$, which effectively results in a factor of -1 since $\exp(-i\pi) = -1$ applies. Furthermore, equations 4.30 and 4.31 contain the factor of $\text{sgn}(z - z_i)$, which can be factored out from the Hermite polynomials. Another $\text{sgn}(z - z_i)$ is applied due to the denominator of equation 4.10. During the derivation of equation 4.41 the relation $\text{sgn}(z)i = \exp\left(i\text{sgn}(z)\frac{\pi}{2}\right) = \exp\left(i\left(\arctan\left(\frac{z}{z_R}\right) + \arctan\left(\frac{z_R}{z}\right)\right)\right)$ is used putting another sign function to the overlap integral given by $\text{sgn}(z)$. If all these factors are taken into account for the eight possible cases defined in table A.1 all minus sign cancel each other out. This is summarised in table A.2.

	$\frac{zz_i+z_R^2}{z_R(z-z_i)} > 0$	$z - z_i > 0$	$1 < \frac{z_i}{z}$	$z_i > 0$	ζ
Case I	$\frac{zz_i+z_R^2}{z_R(z-z_i)} > 0$	$z - z_i > 0$	$1 < \frac{z_i}{z}$	$z_i < 0$	$\Psi = \arctan\left(\frac{z_i}{z_R}\right) - \arctan\left(\frac{z}{z_R}\right)$ $\arg\left(\frac{1}{1-i2\phi}\right) = \arctan\left(\frac{z_i}{z_R}\right) + \arctan\left(\frac{z_R}{z}\right) - \pi$
Case II	$\frac{zz_i+z_R^2}{z_R(z-z_i)} > 0$	$z - z_i > 0$	$1 > \frac{z_i}{z}$	$z_i > 0$	$\Psi = \arctan\left(\frac{z_i}{z_R}\right) - \arctan\left(\frac{z}{z_R}\right)$ $\arg\left(\frac{1}{1-i2\phi}\right) = \arctan\left(\frac{z_i}{z_R}\right) + \arctan\left(\frac{z_R}{z}\right)$
	$\frac{zz_i+z_R^2}{z_R(z-z_i)} > 0$	$z - z_i > 0$	$1 > \frac{z_i}{z}$	$z_i < 0$	ζ
	$\frac{zz_i+z_R^2}{z_R(z-z_i)} > 0$	$z - z_i < 0$	$1 < \frac{z_i}{z}$	$z_i > 0$	ζ
	$\frac{zz_i+z_R^2}{z_R(z-z_i)} > 0$	$z - z_i < 0$	$1 < \frac{z_i}{z}$	$z_i < 0$	ζ
Case III	$\frac{zz_i+z_R^2}{z_R(z-z_i)} > 0$	$z - z_i < 0$	$1 > \frac{z_i}{z}$	$z_i > 0$	$\Psi = \arctan\left(\frac{z_i}{z_R}\right) - \arctan\left(\frac{z}{z_R}\right) - \pi$ $\arg\left(\frac{1}{1-i2\phi}\right) = \arctan\left(\frac{z_i}{z_R}\right) + \arctan\left(\frac{z_R}{z}\right)$
	$\frac{zz_i+z_R^2}{z_R(z-z_i)} > 0$	$z - z_i < 0$	$1 > \frac{z_i}{z}$	$z_i < 0$	ζ
	$\frac{zz_i+z_R^2}{z_R(z-z_i)} < 0$	$z - z_i > 0$	$1 < \frac{z_i}{z}$	$z_i > 0$	ζ
	$\frac{zz_i+z_R^2}{z_R(z-z_i)} < 0$	$z - z_i > 0$	$1 < \frac{z_i}{z}$	$z_i < 0$	ζ
	$\frac{zz_i+z_R^2}{z_R(z-z_i)} < 0$	$z - z_i > 0$	$1 > \frac{z_i}{z}$	$z_i > 0$	ζ
Case IV	$\frac{zz_i+z_R^2}{z_R(z-z_i)} < 0$	$z - z_i > 0$	$1 > \frac{z_i}{z}$	$z_i < 0$	$\Psi = \arctan\left(\frac{z_i}{z_R}\right) - \arctan\left(\frac{z}{z_R}\right)$ $\arg\left(\frac{1}{1-i2\phi}\right) = \arctan\left(\frac{z_i}{z_R}\right) + \arctan\left(\frac{z_R}{z}\right)$
Case V	$\frac{zz_i+z_R^2}{z_R(z-z_i)} < 0$	$z - z_i < 0$	$1 < \frac{z_i}{z}$	$z_i > 0$	$\Psi = \arctan\left(\frac{z_i}{z_R}\right) - \arctan\left(\frac{z}{z_R}\right) - \pi$ $\arg\left(\frac{1}{1-i2\phi}\right) = \arctan\left(\frac{z_i}{z_R}\right) + \arctan\left(\frac{z_R}{z}\right) - \pi$
	$\frac{zz_i+z_R^2}{z_R(z-z_i)} < 0$	$z - z_i < 0$	$1 < \frac{z_i}{z}$	$z_i < 0$	ζ
	$\frac{zz_i+z_R^2}{z_R(z-z_i)} < 0$	$z - z_i < 0$	$1 > \frac{z_i}{z}$	$z_i > 0$	ζ
Case VI	$\frac{zz_i+z_R^2}{z_R(z-z_i)} < 0$	$z - z_i < 0$	$1 > \frac{z_i}{z}$	$z_i < 0$	$\Psi = \arctan\left(\frac{z_i}{z_R}\right) - \arctan\left(\frac{z}{z_R}\right) - \pi$ $\arg\left(\frac{1}{1-i2\phi}\right) = \arctan\left(\frac{z_i}{z_R}\right) + \arctan\left(\frac{z_R}{z}\right)$
	$\frac{zz_i+z_R^2}{z_R(z-z_i)} = 0$		$1 < \frac{z_i}{z}$		ζ
Case VII	$\frac{zz_i+z_R^2}{z_R(z-z_i)} = 0$		$1 > \frac{z_i}{z}$	$z_i > 0$	$\Psi = -\frac{\pi}{2} = \arctan\left(\frac{z_i}{z_R}\right) - \arctan\left(\frac{z}{z_R}\right) - \pi$ $\arg\left(\frac{1}{1-i2\phi}\right) = \arctan\left(\frac{z_i}{z_R}\right) + \arctan\left(\frac{z_R}{z}\right)$
Case VIII	$\frac{zz_i+z_R^2}{z_R(z-z_i)} = 0$		$1 > \frac{z_i}{z}$	$z_i < 0$	$\Psi = -\frac{\pi}{2} = \arctan\left(\frac{z_i}{z_R}\right) - \arctan\left(\frac{z}{z_R}\right)$ $\arg\left(\frac{1}{1-i2\phi}\right) = \arctan\left(\frac{z_i}{z_R}\right) + \arctan\left(\frac{z_R}{z}\right)$

Table A.1: Cases for the different phases of the overlap integral in equation 4.6. The table summarises the results from the paragraphs above. A lightning symbol indicates a mathematical contradiction of the prerequisites and, hence, the corresponding cases are not possible. The eight possible cases are labelled with roman numbers.

Case	$\exp(i(n+m)\Psi)$	$\exp\left(i\arg\left(\frac{1}{1-i2\phi}\right)\right)$	$H_n()H_m()$	$\frac{1}{z-z_i}$	$\text{sgn}(z)$	Π
I	1	-1	1^{n+m}	1	-1	1
II	1	1	1^{n+m}	1	1	1
III	$(-1)^{n+m}$	1	$(-1)^{n+m}$	-1	-1	1
IV	1	1	1^{n+m}	1	1	1
V	$(-1)^{n+m}$	-1	$(-1)^{n+m}$	-1	1	1
VI	$(-1)^{n+m}$	1	$(-1)^{n+m}$	-1	-1	1
VII	$(-1)^{n+m}$	1	$(-1)^{n+m}$	-1	-1	1
VIII	1	1	1^{n+m}	1	1	1

Table A.2: Table of the product of all possible minus signs in the overlap integral from equation 4.6. The cases are defined in table A.1. The product is always positive as indicated by the last column of the table.

Equation 5.68

During the transformation equations 4.40, 5.10, 5.66 and 5.67 and $V = \frac{\pi\omega_0^2 L}{4}$ for the mode volume are used.

$$4\beta \frac{c}{2L} = 4 \frac{k\alpha}{\pi\omega_0^2\epsilon_0} \frac{c}{2L} \quad (\text{A.112})$$

$$= 2 \frac{ck}{L\pi\omega_0^2\epsilon_0} \frac{3\pi\epsilon_0}{k^3} \frac{\Gamma}{\Delta} \quad (\text{A.113})$$

$$= \frac{6\pi c}{L\pi\omega_0^2 k^2} \frac{\Gamma}{\Delta} \quad (\text{A.114})$$

$$= \frac{\omega}{\hbar\epsilon_0\Delta L} \frac{6\pi^2\omega_0^2\epsilon_0\hbar\Gamma}{k^3} \quad (\text{A.115})$$

$$= \frac{2|d|^2\omega}{\hbar\epsilon_0\Delta L\pi\omega_0^2} \quad (\text{A.116})$$

$$= \frac{|d|^2\omega}{2\hbar\epsilon_0\Delta V} \quad (\text{A.117})$$

$$= \frac{|d|^2 \frac{\omega}{2\hbar\epsilon_0 V}}{\Delta} \quad (\text{A.118})$$

$$= \frac{|g_0|^2}{\Delta} \quad (\text{A.119})$$

Bibliography

- [1] Max Planck. Ueber irreversible Strahlungsvorgänge. *Annalen der Physik*, 306(1):69–122, 1900.
- [2] Dieter Hoffmann. *Max Planck und die moderne Physik*. Springer-Verlag Berlin Heidelberg, Berlin, Heidelberg, 2010.
- [3] Helge Kragh. Max planck: the reluctant revolutionary. <https://physicsworld.com/a/max-planck-the-reluctant-revolutionary/>, Dec 2000. in *Physics World*, Retrieved on 2021-10-21.
- [4] A. Einstein. Über einen die Erzeugung und Verwandlung des Lichtes betreffenden heuristischen Gesichtspunkt. *Annalen der Physik*, 322(6):132–148, 1905.
- [5] Peter W. Atkins and Julio De Paula. *Physikalische Chemie*. Wiley-VCH, Weinheim, 2013.
- [6] Robert W. Brown, Yu-Chung N. Cheng, E. Mark Haacke, Michael R. Thompson, and Ramesh Venkatesan D.Sc. *Magnetic Resonance Imaging*. John Wiley & Sons, Ltd, 2014.
- [7] Elizabeth Antébi. *Die Entdeckung von Shockley, Bardeen und Brattain bei den Bell Laboratories*, pages 87–96. Birkhäuser Basel, Basel, 1983.
- [8] Christopher Gerry and Peter Knight. *Introductory Quantum Optics*. Cambridge University Press, 2004.
- [9] Paul Adrien Maurice Dirac and Niels Henrik David Bohr. The quantum theory of the emission and absorption of radiation. *Proceedings of the Royal Society of London. Series A, Containing Papers of a Mathematical and Physical Character*, 114(767):243–265, 1927.
- [10] S. Tomonaga. On a Relativistically Invariant Formulation of the Quantum Theory of Wave Fields*. *Progress of Theoretical Physics*, 1(2):27–42, 08 1946.
- [11] Julian Schwinger. Quantum Electrodynamics. I. A Covariant Formulation. *Phys. Rev.*, 74:1439–1461, Nov 1948.
- [12] R. P. Feynman. Mathematical Formulation of the Quantum Theory of Electromagnetic Interaction. *Phys. Rev.*, 80:440–457, Nov 1950.
- [13] T-H. Maiman. Stimulated Optical Radiation in Ruby. *Nature*, 187:493–494, Aug 1960.
- [14] Nick Proukakis, Simon Gardiner, Matthew Davis, and Marzena Szymańska. *Quantum Gases - Finite Temperature and Non-Equilibrium Dynamics*. IMPERIAL COLLEGE PRESS, 2013.
- [15] M. A. Baranov, M. Dalmonte, G. Pupillo, and P. Zoller. Condensed Matter Theory of Dipolar Quantum Gases. *Chemical Reviews*, 112(9):5012–5061, 2012. PMID: 22877362.

- [16] I. Bloch, J. Dalibard, and S. Nascimbène. Quantum simulations with ultracold quantum gases. *Nature Phys*, 8:267–276, Apr 2012.
- [17] D. J. Wineland, R. E. Drullinger, and F. L. Walls. Radiation-Pressure Cooling of Bound Resonant Absorbers. *Phys. Rev. Lett.*, 40:1639–1642, Jun 1978.
- [18] William D. Phillips and Harold Metcalf. Laser Deceleration of an Atomic Beam. *Phys. Rev. Lett.*, 48:596–599, Mar 1982.
- [19] Steven Chu, J. E. Bjorkholm, A. Ashkin, and A. Cable. Experimental Observation of Optically Trapped Atoms. *Phys. Rev. Lett.*, 57:314–317, Jul 1986.
- [20] E. L. Raab, M. Prentiss, Alex Cable, Steven Chu, and D. E. Pritchard. Trapping of Neutral Sodium Atoms with Radiation Pressure. *Phys. Rev. Lett.*, 59:2631–2634, Dec 1987.
- [21] Paul D. Lett, Richard N. Watts, Christoph I. Westbrook, William D. Phillips, Phillip L. Gould, and Harold J. Metcalf. Observation of Atoms Laser Cooled below the Doppler Limit. *Phys. Rev. Lett.*, 61:169–172, Jul 1988.
- [22] M. H. Anderson, J. R. Ensher, M. R. Matthews, C. E. Wieman, and E. A. Cornell. Observation of Bose-Einstein Condensation in a Dilute Atomic Vapor. *Science*, 269(5221):198–201, 1995.
- [23] K. B. Davis, M. O. Mewes, M. R. Andrews, N. J. van Druten, D. S. Durfee, D. M. Kurn, and W. Ketterle. Bose-Einstein Condensation in a Gas of Sodium Atoms. *Phys. Rev. Lett.*, 75:3969–3973, Nov 1995.
- [24] A. Einstein. *Quantentheorie des einatomigen idealen Gases*, pages 237–244. John Wiley & Sons, Ltd, 2005.
- [25] A. Einstein. *Quantentheorie des einatomigen idealen Gases. Zweite Abhandlung*, pages 245–257. John Wiley & Sons, Ltd, 2005.
- [26] Satyendra Nath Bose. Plancks Gesetz und Lichtquantenhypothese. *Zeitschrift für Physik*, 26:178–181, Dec 1924.
- [27] B. DeMarco and D. S. Jin. Onset of Fermi Degeneracy in a Trapped Atomic Gas. *Science*, 285(5434):1703–1706, 1999.
- [28] Matthias Vojta. Quantum phase transitions. *New Journal of Physics*, 66(12):2069–2110, nov 2003.
- [29] Mark J. H. Ku, Ariel T. Sommer, Lawrence W. Cheuk, and Martin W. Zwierlein. Revealing the Superfluid Lambda Transition in the Universal Thermodynamics of a Unitary Fermi Gas. *Science*, 335(6068):563–567, 2012.
- [30] Chen-Lung Hung, Victor Gurarie, and Cheng Chin. From Cosmology to Cold Atoms: Observation of Sakharov Oscillations in a Quenched Atomic Superfluid. *Science*, 341(6151):1213–1215, 2013.
- [31] Takahiro Hashimoto, Yuichi Ota, Akihiro Tsuzuki, Tsubaki Nagashima, Akiko Fukushima, Shigeru Kasahara, Yuji Matsuda, Kohei Matsuura, Yuta Mizukami, Takasada Shibauchi, Shik Shin, and Kozo Okazaki. Bose-Einstein condensation superconductivity induced by disappearance of the nematic state. *Science Advances*, 6(45):eabb9052, 2020.

- [32] T Lahaye, C Menotti, L Santos, M Lewenstein, and T Pfau. The physics of dipolar bosonic quantum gases. *Reports on Progress in Physics*, 72(12):126401, nov 2009.
- [33] Jun-Ru Li, Jeongwon Lee, Wujie Huang, Sean Burchesky, Boris Shteynas, Furkan Çağrı, Alan O. Jamison, and Wolfgang Ketterle. A stripe phase with supersolid properties in spin-orbit-coupled Bose-Einstein condensates. *Nature*, 534:91–94, mar 2017.
- [34] Axel Griesmaier, Jörg Werner, Sven Hensler, Jürgen Stuhler, and Tilman Pfau. Bose-Einstein Condensation of Chromium. *Phys. Rev. Lett.*, 94:160401, Apr 2005.
- [35] Mingwu Lu, Nathaniel Q. Burdick, Seo Ho Youn, and Benjamin L. Lev. Strongly Dipolar Bose-Einstein Condensate of Dysprosium. *Phys. Rev. Lett.*, 107:190401, Oct 2011.
- [36] K. Aikawa, A. Frisch, M. Mark, S. Baier, A. Rietzler, R. Grimm, and F. Ferlaino. Bose-Einstein Condensation of Erbium. *Phys. Rev. Lett.*, 108:210401, May 2012.
- [37] Torsten Hartmann. *An experiment apparatus for the production of ultracold bosonic dipolar ground state $^{23}\text{Na}^{39}\text{K}$ molecules and Feshbach spectroscopy in a cold mixture of ^{23}Na and ^{39}K* . PhD thesis, Leibniz Universität Hannover, 2019.
- [38] Torben A. Schulze. *Quantum degenerate mixtures of ^{23}Na – ^{39}K and coherent transfer paths in NaK molecules*. PhD thesis, Leibniz Universität Hannover, 2018.
- [39] M W Gempel, T Hartmann, T A Schulze, K K Voges, A Zenesini, and S Ospelkaus. Versatile electric fields for the manipulation of ultracold NaK molecules. *New Journal of Physics*, 18(4):045017, apr 2016.
- [40] Steven A. Moses, Jacob P. Covey, Matthew T. Miecnikowski, Deborah S. Jin, and Jun Ye. New frontiers for quantum gases of polar molecules. *Nature Physics*, 13:13–20, dec 2017.
- [41] S. Chervenkov, X. Wu, J. Bayerl, A. Rohlfes, T. Gantner, M. Zeppenfeld, and G. Rempe. Continuous Centrifuge Decelerator for Polar Molecules. *Phys. Rev. Lett.*, 112:013001, Jan 2014.
- [42] M Petzold, P Kaebert, P Gersema, M Siercke, and S Ospelkaus. A Zeeman slower for diatomic molecules. *New Journal of Physics*, 20(4):042001, apr 2018.
- [43] J. J. Zirbel, K.-K. Ni, S. Ospelkaus, T. L. Nicholson, M. L. Olsen, P. S. Julienne, C. E. Wieman, J. Ye, and D. S. Jin. Heteronuclear molecules in an optical dipole trap. *Phys. Rev. A*, 78:013416, Jul 2008.
- [44] S. Ospelkaus, A. Pe’er, K.-K. Ni, J. J. Zirbel, B. Neyenhuis, S. Kotochigova, P. S. Julienne, J. Ye, and D. S. Jin. Efficient state transfer in an ultracold dense gas of heteronuclear molecules. *Nature Physics*, 4:622–626, Jun 2008.
- [45] K.-K. Ni, S. Ospelkaus, M. H. G. de Miranda, A. Pe’er, B. Neyenhuis, J. J. Zirbel, S. Kotochigova, P. S. Julienne, D. S. Jin, and J. Ye. A High Phase-Space-Density Gas of Polar Molecules. *Science*, 322(5899):231–235, 2008.
- [46] Immanuel Bloch, Jean Dalibard, and Wilhelm Zwerger. Many-body physics with ultracold gases. *Rev. Mod. Phys.*, 80:885–964, Jul 2008.
- [47] L Guidoni and P Verkerk. Optical lattices: cold atoms ordered by light. *Journal of Optics B: Quantum and Semiclassical Optics*, 1(5):R23–R45, sep 1999.

- [48] Yewei Wu, Justin J. Burau, Kameron Mehling, Jun Ye, and Shiqian Ding. High phase-space density of laser-cooled molecules in an optical lattice. *Phys. Rev. Lett.*, 127:263201, Dec 2021.
- [49] Steven A. Moses, Jacob P. Covey, Matthew T. Miecnikowski, Bo Yan, Bryce Gadway, Jun Ye, and Deborah S. Jin. Creation of a low-entropy quantum gas of polar molecules in an optical lattice. *Science*, 350(6261):659–662, 2015.
- [50] W. Ketterle, D.S. Durfee, and D.M. Stamper-Kurn. Making, probing and understanding bose-einstein condensates. <https://arxiv.org/abs/cond-mat/9904034v2>, apr 1999. Arxiv, Retrieved on 2021-11-19.
- [51] F. Zernike. Das Phasenkontrastverfahren bei der mikroskopischen Beobachtung. *Z. techn. Physik*, 16:454–457, 1935.
- [52] C. C. Bradley, C. A. Sackett, and R. G. Hulet. Bose-Einstein Condensation of Lithium: Observation of Limited Condensate Number. *Phys. Rev. Lett.*, 78:985–989, Feb 1997.
- [53] G. Modugno, G. Ferrari, G. Roati, R. J. Brecha, A. Simoni, and M. Inguscio. Bose-Einstein Condensation of Potassium Atoms by Sympathetic Cooling. *Science*, 294(5545):1320–1322, 2001.
- [54] Tino Weber, Jens Herbig, Michael Mark, Hanns-Christoph Nägerl, and Rudolf Grimm. Bose-Einstein Condensation of Cesium. *Science*, 299(5604):232–235, 2003.
- [55] D. Rychtarik, B. Engeser, H.-C. Nägerl, and R. Grimm. Two-Dimensional Bose-Einstein Condensate in an Optical Surface Trap. *Phys. Rev. Lett.*, 92:173003, Apr 2004.
- [56] Martin Miranda, Ryotaro Inoue, Yuki Okuyama, Akimasa Nakamoto, and Mikio Kozuma. Site-resolved imaging of ytterbium atoms in a two-dimensional optical lattice. *Phys. Rev. A*, 91:063414, Jun 2015.
- [57] Waseem S. Bakr, Jonathon I. Gillen, Amy Peng, Simon Fölling, and Markus Greiner. A quantum gas microscope for detecting single atoms in a Hubbard-regime optical lattice. *Nature*, 462:74–77, Nov 2009.
- [58] Jacob F. Sherson, Christof Weitenberg, Manuel Endres, Marc Cheneau, Immanuel Bloch, and Stefan Kuhr. Single-atom-resolved fluorescence imaging of an atomic Mott insulator. *Nature*, 467:68–72, Aug 2010.
- [59] Lawrence W. Cheuk, Matthew A. Nichols, Melih Okan, Thomas Gersdorf, Vinay V. Ramasesh, Waseem S. Bakr, Thomas Lompe, and Martin W. Zwierlein. Quantum-Gas Microscope for Fermionic Atoms. *Phys. Rev. Lett.*, 114:193001, May 2015.
- [60] Maxwell F. Parsons, Florian Huber, Anton Mazurenko, Christie S. Chiu, Widagdo Setiawan, Katherine Wooley-Brown, Sebastian Blatt, and Markus Greiner. Site-Resolved Imaging of Fermionic ${}^6\text{Li}$ in an Optical Lattice. *Phys. Rev. Lett.*, 114:213002, May 2015.
- [61] Mickey McDonald, Jonathan Trisnadi, Kai-Xuan Yao, and Cheng Chin. Superresolution Microscopy of Cold Atoms in an Optical Lattice. *Phys. Rev. X*, 9:021001, Apr 2019.
- [62] M. R. Andrews, M.-O. Mewes, N. J. van Druten, D. S. Durfee, D. M. Kurn, and W. Ketterle. Direct, Nondestructive Observation of a Bose Condensate. *Science*, 273(5271):84–87, 1996.

- [63] Kali E. Wilson, Zachary L. Newman, Joseph D. Lowney, and Brian P. Anderson. In situ imaging of vortices in Bose-Einstein condensates. *Phys. Rev. A*, 91:023621, Feb 2015.
- [64] J. Smits, A. P. Mosk, and P. van der Straten. Imaging trapped quantum gases by off-axis holography. *Opt. Lett.*, 45(4):981–984, Feb 2020.
- [65] Daniel Kai Hoffmann, Benjamin Deissler, Wolfgang Limmer, and Johannes Hecker Denschlag. Holographic method for site-resolved detection of a 2D array of ultracold atoms. *Applied Physics B*, 122, 2016.
- [66] Miroslav Gajdacz, Poul L. Pedersen, Troels Mørch, Andrew J. Hilliard, Jan Arlt, and Jacob F. Sherson. Non-destructive Faraday imaging of dynamically controlled ultracold atoms. *Review of Scientific Instruments*, 84(8):083105, 2013.
- [67] Ryuta Yamamoto, Jun Kobayashi, Kohei Kato, Takuma Kuno, Yuto Sakura, and Yoshiro Takahashi. Site-resolved imaging of single atoms with a Faraday quantum gas microscope. *Phys. Rev. A*, 96:033610, Sep 2017.
- [68] M. D. Di Rosa. Laser-cooling molecules. *The European Physical Journal D - Atomic, Molecular, Optical and Plasma Physics*, 31:395–402, 2004.
- [69] E. S. Shuman, J. F. Barry, D. R. Glenn, and D. DeMille. Radiative Force from Optical Cycling on a Diatomic Molecule. *Phys. Rev. Lett.*, 103:223001, Nov 2009.
- [70] Lawrence W. Cheuk, Loïc Anderegg, Benjamin L. Augenbraun, Yicheng Bao, Sean Burchesky, Wolfgang Ketterle, and John M. Doyle. Λ -Enhanced Imaging of Molecules in an Optical Trap. *Phys. Rev. Lett.*, 121:083201, Aug 2018.
- [71] C. Gabbanini, A. Fioretti, A. Lucchesini, S. Gozzini, and M. Mazzoni. Cold Rubidium Molecules Formed in a Magneto-Optical Trap. *Phys. Rev. Lett.*, 84:2814–2817, Mar 2000.
- [72] Fredrik K. Fatemi, Kevin M. Jones, Paul D. Lett, and Eite Tiesinga. Ultracold ground-state molecule production in sodium. *Phys. Rev. A*, 66:053401, Nov 2002.
- [73] D. Wang, B. Neyenhuis, M. H. G. de Miranda, K.-K. Ni, S. Ospelkaus, D. S. Jin, and J. Ye. Direct absorption imaging of ultracold polar molecules. *Phys. Rev. A*, 81:061404, Jun 2010.
- [74] Jacob P. Covey, Steven A. Moses, Martin Gärttner, Arghavan Safavi-Naini, Matthew T. Miecnikowski, Zhengkun Fu, Johannes Schachenmayer, Paul S., Ana Maria Rey, Deborah S. Jin, and Jun Ye. Doublon dynamics and polar molecule production in an optical lattice. *Nature Communications*, 7(11279), 2016.
- [75] Kai K. Voges, Philipp Gersema, Mara Meyer zum Alten Borgloh, Torben A. Schulze, Torsten Hartmann, Alessandro Zenesini, and Silke Ospelkaus. Ultracold Gas of Bosonic $^{23}\text{Na}^{39}\text{K}$ Ground-State Molecules. *Phys. Rev. Lett.*, 125:083401, Aug 2020.
- [76] Rahul Sawant, Olivier Dulieu, and S. A. Rangwala. Detection of ultracold molecules using an optical cavity. *Phys. Rev. A*, 97:063405, Jun 2018.
- [77] M. Niranjan, Sourav Dutta, Tridib Ray, and S. A. Rangwala. Measuring spatially extended density profiles using atom-cavity collective strong coupling to higher-order modes. *Phys. Rev. A*, 99:033617, Mar 2019.
- [78] Qingze Guan, Michael Highman, Eric J. Meier, Garrett R. Williams, Vito Scarola, Brian DeMarco, Svetlana Kotochigova, and Bryce Gadway. Nondestructive dispersive imaging of rotationally excited ultracold molecules. *Phys. Chem. Chem. Phys.*, 22:20531–20544, 2020.

- [79] Daichi Okuno, Yoshiki Amano, Katsunari Enomoto, Nobuyuki Takei, and Yoshiro Takahashi. Schemes for nondestructive quantum gas microscopy of single atoms in an optical lattice. *New Journal of Physics*, 22(1):013041, Jan 2020.
- [80] C. M. Savage, S. L. Braunstein, and D. F. Walls. Macroscopic quantum superpositions by means of single-atom dispersion. *Opt. Lett.*, 15(11):628–630, Jun 1990.
- [81] Matthias Mader, Jakob Reichel, Theodor W. Hänsch, and David Hunger. A scanning cavity microscope. *Nature Communications*, 6, 2015.
- [82] Anthony E. Siegman. *Lasers*. University Science Books, 1986.
- [83] Norman Hodgson and Horst Weber. *Laser Resonators and Beam Propagation - Fundamentals, Advanced Concepts and Applications*. Springer, 2. edition, 2005.
- [84] Bahaa E. A. Saleh and Malvin C. Teich. *Fundamentals of Photonics*. Wiley-VCH, 3rd edition, 2019.
- [85] David J. Griffiths. *Introduction to electrodynamics*. Pearson, 4th edition, 2013.
- [86] Louis G. Gouy. Sur une propriété nouvelle des ondes lumineuses. *C. R. Acad. Sci. Paris* 110, page 1251, 1890.
- [87] Simin Feng and Herbert G. Winful. Physical origin of the Gouy phase shift. *Opt. Lett.*, 26(8):485–487, Apr 2001.
- [88] Miguel A. Bandres and Julio C. Gutiérrez-Vega. Ince–Gaussian modes of the paraxial wave equation and stable resonators. *J. Opt. Soc. Am. A*, 21(5):873–880, May 2004.
- [89] William H. Carter. Spot size and divergence for Hermite Gaussian beams of any order. *Appl. Opt.*, 19(7):1027–1029, Apr 1980.
- [90] Warren Nagourney. *Quantum Electronics for Atomic Physics*. Oxford University Press, 1st edition, 2010.
- [91] Markus Aspelmeyer, Tobias J. Kippenberg, and Florian Marquardt. Cavity optomechanics. *Rev. Mod. Phys.*, 86:1391–1452, Dec 2014.
- [92] Matthew Pitkin, Stuart Reid, Sheila Rowan, and Jim Hough. Gravitational Wave Detection by Interferometry (Ground and Space). *Living Reviews in Relativity*, 14, 2011.
- [93] Herbert Walther, Benjamin T H Varcoe, Berthold-Georg Englert, and Thomas Becker. Cavity quantum electrodynamics. *Reports on Progress in Physics*, 69(5):1325–1382, Apr 2006.
- [94] Dieter Meschede. *Optics, Light and Lasers: The Practical Approach to Modern Aspects of Photonics and Laser Physics*. Wiley-VCH, 3rd edition, 2017.
- [95] George B. Arfken, Hans J. Weber, and Frank E. Harris. *Mathematical Methods for Physicists : A Comprehensive Guide*. Elsevier, 7th edition, 2012.
- [96] E.T. Jaynes and F.W. Cummings. Comparison of quantum and semiclassical radiation theories with application to the beam maser. *Proceedings of the IEEE*, 51(1):89–109, 1963.
- [97] G. S. Agarwal. Vacuum-field Rabi oscillations of atoms in a cavity. *J. Opt. Soc. Am. B*, 2(3):480–485, Mar 1985.
- [98] R. Short and L. Mandel. Observation of Sub-Poissonian Photon Statistics. *Phys. Rev. Lett.*, 51:384–387, Aug 1983.

- [99] Frank Diedrich and Herbert Walther. Nonclassical radiation of a single stored ion. *Phys. Rev. Lett.*, 58:203–206, Jan 1987.
- [100] J. H. Eberly, N. B. Narozhny, and J. J. Sanchez-Mondragon. Periodic Spontaneous Collapse and Revival in a Simple Quantum Model. *Phys. Rev. Lett.*, 44:1323–1326, May 1980.
- [101] Yifu Zhu, Daniel J. Gauthier, S. E. Morin, Qilin Wu, H. J. Carmichael, and T. W. Mossberg. Vacuum Rabi splitting as a feature of linear-dispersion theory: Analysis and experimental observations. *Phys. Rev. Lett.*, 64:2499–2502, May 1990.
- [102] Vladan Vuletić and Steven Chu. Laser Cooling of Atoms, Ions, or Molecules by Coherent Scattering. *Phys. Rev. Lett.*, 84:3787–3790, Apr 2000.
- [103] Haruka Tanji-Suzuki, Ian D. Leroux, Monika H. Schleier-Smith, Marko Cetina, Andrew T. Grier, Jonathan Simon, and Vladan Vuletić. Chapter 4 - Interaction between Atomic Ensembles and Optical Resonators: Classical Description. In E. Arimondo, P.R. Berman, and C.C. Lin, editors, *Advances in Atomic, Molecular, and Optical Physics*, volume 60 of *Advances In Atomic, Molecular, and Optical Physics*, pages 201–237. Academic Press, 2011.
- [104] Valeriy Astapenko. *Polarization Bremsstrahlung on Atoms, Plasmas, Nanostructures and Solids*, Springer Series on Atomic, Optical, and Plasma Physics, volume 72. Springer, Berlin, 2013.
- [105] Alexander Lvovsky. *Quantum Physics - An Introduction Based on Photons*. Springer-Verlag Berlin Heidelberg, 2018.
- [106] Claude Cohen-Tannoudji, Jacques Dupont-Roc, and Gilbert Grynberg. *Atom - Photon Interactions*. John Wiley & Sons, Ltd, 1998.
- [107] A F J Levi. The lorentz oscillator model. In *Essential Classical Mechanics for Device Physics*, 2053-2571, pages 5–1 to 5–21. Morgan & Claypool Publishers, 2016.
- [108] H.A. Lorentz. *The Theory of Electrons and Its Applications to the Phenomena of Light and Radiant Heat*. Dover books on physics. Dover Publications, 2003. originally published in 1915.
- [109] John David Jackson. *Classical electrodynamics*. Wiley, New York, NY, 3rd edition, 1999.
- [110] I. S. Gradshteyn and I. M. Ryzhik. *Table of Integrals, Series, and Products*. Elsevier Inc., 6th edition, 2000.
- [111] Jan-Moritz Bischoff. Theory of phase contrast imaging of cold molecules. Master’s thesis, Leibniz Universität Hannover, 2014.
- [112] Hans-A. Bachor and Timothy-C. Ralph. *A Guide to Experiments in Quantum Optics*. Wiley-VCH, 3rd edition, 2019.
- [113] Ernst Abbe. Beiträge zur Theorie des Mikroskops und der mikroskopischen Wahrnehmung. *Archiv für mikroskopische Anatomie*, 9:413–468, Dec 1873.
- [114] Frank Matossi, Clemens Schaefer, and Ludwig Bergmann. *Optik. Mit 1 Ausschlagtafel*. De Gruyter, 1972.
- [115] Lord Rayleigh Sec. R. S. XV. On the theory of optical images, with special reference to the microscope. *The London, Edinburgh, and Dublin Philosophical Magazine and Journal of Science*, 42(255):167–195, 1896.

- [116] Max Born and Emil Wolf. *Principles of Optics: 60th Anniversary Edition*. Cambridge University Press, 7 edition, 2019.
- [117] W. R. Dawes. Catalogue of Micrometrical Measurements of Double Stars. *Monthly Notices of the Royal Astronomical Society*, 27:217–238, 1867.
- [118] Rodney Loudon. *The quantum theory of light*. Oxford University Press, 3rd edition, 2003.
- [119] David J. Griffiths and Darrell F. Schroeter. *Introduction to Quantum Mechanics*. Cambridge University Press, 3rd edition, 2018.
- [120] Steven Barnett and Paul Radmore. *Methods in Theoretical Quantum Optics*. Clarendon Press, 1997.
- [121] Thomas Fischer. *Controlling the motion of an atom in an optical cavity*. PhD thesis, Technische Universität München Max-Planck-Institut für Quantenoptik, 2002.
- [122] Rodney Loudon. *The quantum theory of light, Oxford science publications*. Oxford Univ. Press, 2010.
- [123] R. Paschotta. 'unstable resonators. https://www.rp-photonics.com/unstable_resonators.html. article in the RP Photonics Encyclopedia, Retrieved on 2021-11-05.
- [124] J. P. Gordon and H. Kogelnik. Equivalence relations among spherical mirror optical resonators. *The Bell System Technical Journal*, 43(6):2873–2886, 1964.
- [125] H. Kogelnik and T. Li. Laser Beams and Resonators. *Appl. Opt.*, 5(10):1550–1567, Oct 1966.
- [126] Dustin Kleckner, William T. M. Irvine, Sumant S. R. Oemrawsingh, and Dirk Bouwmeester. Diffraction-limited high-finesse optical cavities. *Phys. Rev. A*, 81:043814, Apr 2010.
- [127] Mikhail V Poplavskiy, Andrey B Matsko, Hiroaki Yamamoto, and Sergey P Vyatchanin. On fundamental diffraction limitation of finesse of a Fabry–Perot cavity. *Journal of Optics*, 20(7):075609, Jun 2018.
- [128] K. Durak, C. H. Nguyen, Vi Leong, S. Straupe, and C. Kurtsiefer. Diffraction-limited Fabry–Perot cavity in the near concentric regime. *New Journal of Physics*, 16, Oct 2014.
- [129] R. Hauck, H. P. Körtz, and H. Weber. Misalignment sensitivity of optical resonators. *Appl. Opt.*, 19(4):598–601, Feb 1980.
- [130] Martial Ducloy and Daniel Bloch. *Quantum Optics of Confined Systems, Proceedings of the NATO Advanced Study Institute, Les Houches, France, May 23–June 2, 1995, NATO ASI Series, Series E: Applied Sciences*, volume 314. Springer, Dordrecht, 1996. Proceedings of the NATO Advanced Study Institute, Les Houches, France, May 23–June 2, 1995.
- [131] T. A. Schulze, I. I. Temelkov, M. W. , T. Hartmann, H. Knöckel, S. Ospelkaus, and E. Tiemann. Multichannel modeling and two-photon coherent transfer paths in NaK. *Phys. Rev. A*, 88:023401, Aug 2013.
- [132] A Gerdes, M Hobein, H Knöckel, and E Tiemann. Ground state potentials of the NaK molecule. *The European Physical Journal D*, 49(5):67–73, Jul 2008.

- [133] Chi Huan Nguyen, Adrian Nugraha Utama, Nick Lewty, Kadir Durak, Gleb Maslennikov, Stanislav Straupe, Matthias Steiner, and Christian Kurtsiefer. Single atoms coupled to a near-concentric cavity. *Phys. Rev. A*, 96:031802, Sep 2017.
- [134] Chi Huan Nguyen, Adrian Nugraha Utama, Nick Lewty, and Christian Kurtsiefer. Operating a near-concentric cavity at the last stable resonance. *Phys. Rev. A*, 98:063833, Dec 2018.
- [135] D Hunger, T Steinmetz, Y Colombe, C Deutsch, T W Hänsch, and J Reichel. A fiber Fabry–Perot cavity with high finesse. *New Journal of Physics*, 12(6):065038, jun 2010.
- [136] Carlos Saavedra, Deepak Pandey, Wolfgang Alt, Hannes Pfeifer, and Dieter Meschede. Tunable fiber Fabry-Perot cavities with high passive stability. *Opt. Express*, 29(2):974–982, Jan 2021.
- [137] Julia Benedikter, Thomas Hümmer, Matthias Mader, Benedikt Schleder, Jakob Reichel, Theodor W Hänsch, and David Hunger. Transverse-mode coupling and diffraction loss in tunable Fabry–Pérot microcavities. *New Journal of Physics*, 17(5):053051, may 2015.
- [138] Ibrahim Khan, Khalid Saeed, and Idrees Khan. Nanoparticles: Properties, applications and toxicities. *Arabian Journal of Chemistry*, 12(7):908–931, 2019.
- [139] Lukas Novotny and Bert Hecht. *Principles of Nano-Optics*. Cambridge University Press, 2 edition, 2012.
- [140] Craig F. Bohren and Donald R. Huffman. *Absorption and Scattering of Light by Small Particles*. John Wiley and Sons, Ltd, 1998.
- [141] V. G. Farafonov and V. B. Il'in. Rayleigh approximation for light scattering at parallelepipeds. *J. Opt. Technol.*, 81(7):375–381, Jul 2014.
- [142] Viktor Myroshnychenko, Jessica Rodríguez-Fernández, Isabel Pastoriza-Santos, Alison M. Funston, Carolina Novo, Paul Mulvaney, Luis M. Liz-Marzán, and F. Javier García de Abajo. Modelling the optical response of gold nanoparticles. *Chem. Soc. Rev.*, 37:1792–1805, 2008.
- [143] Péter Dombi, Zsuzsanna Pápa, Jan Vogelsang, Sergey V. Yalunin, Murat Sivis, Georg Herink, Sascha Schäfer, Petra Groß, Claus Ropers, and Christoph Lienau. Strong-field nano-optics. *Rev. Mod. Phys.*, 92:025003, Jun 2020.
- [144] Frederick Wooten. Chapter 3 - absorption and dispersion. In Frederick Wooten, editor, *Optical Properties of Solids*, pages 42–84. Academic Press, 1972.
- [145] <https://refractiveindex.info/?shelf=main&book=Ag&page=Johnson>. Retrieved on 2021-11-28.
- [146] Yajie Jiang, Supriya Pillai, and Martin A. Green. Realistic Silver Optical Constants for Plasmonics. *Scientific Reports*, 6, 2016.
- [147] Kevin M. McPeak, Sriharsha V. Jayanti, Stephan J. P. Kress, Stefan Meyer, Stelio Iotti, Aurelio Rossinelli, and David J. Norris. Plasmonic Films Can Easily Be Better: Rules and Recipes. *ACS Photonics*, 2(3):326–333, 2015. PMID: 25950012.
- [148] I. H. Malitson. Interspecimen Comparison of the Refractive Index of Fused Silica*,†. *J. Opt. Soc. Am.*, 55(10):1205–1209, Oct 1965.

- [149] I. Bodurov, I. Vlaeva, A. Viraneva, T. Yovcheva, and S. Sainov. Modified design of a laser refractometer. *Nanoscience & Nanotechnology*, 16:31–33, 2016.
- [150] A. Ashkin, J. M. Dziedzic, J. E. Bjorkholm, and Steven Chu. Observation of a single-beam gradient force optical trap for dielectric particles. *Opt. Lett.*, 11(5):288–290, May 1986.
- [151] M. W. Gempel, T. Hartmann, T. A. Schulze, K. K. Voges, A. Zenesini, and S. Ospelkaus. An adaptable two-lens high-resolution objective for single-site resolved imaging of atoms in optical lattices. *Review of Scientific Instruments*, 90(5):053201, 2019.
- [152] Anatoliy Pinchuk, Almuth Hilger, Gero von Plessen, and Uwe Kreibig. Substrate effect on the optical response of silver nanoparticles. *Nanotechnology*, 15(12):1890–1896, December 2004.
- [153] Meindert Alexander van Dijk. *Nonlinear-optical studies of single gold nanoparticles*. PhD thesis, Universiteit Leiden, 2007.
- [154] R. Paschotta. mode matching. https://www.rp-photonics.com/mode_matching.html, Oct 2008. article in the Encyclopedia of Laser Physics and Technology, 1. edition, Wiley-VCH, ISBN 978-3-527-40828-3, Retrieved on 2021-10-21.
- [155] Adrian Nugraha Utama, Chang Hoong Chow, Chi Huan Nguyen, and Christian Kurtz. Coupling light to higher order transverse modes of a near-concentric optical cavity. *Opt. Express*, 29(6):8130–8141, Mar 2021.
- [156] Alexander T. Papageorge, Alicia J. Kollár, and Benjamin L. Lev. Coupling to modes of a near-confocal optical resonator using a digital light modulator. *Opt. Express*, 24(11):11447–11457, May 2016.
- [157] Ekbert Hering, Rolf Martin, and Martin Stohrer. *Physik für Ingenieure, Lehrbuch*. Springer Vieweg, Berlin, 2016.
- [158] Datenblatt p-611.3. https://www.physikinstrumente.de/fileadmin/user_upload/physik_instrumente/files/datasheets/P-611.3-Datenblatt.pdf. Retrieved on 2021-10-27.
- [159] <https://www.newport.com/p/M-DS65-XYZ>. Retrieved on 2021-10-27.
- [160] <https://www.newport.com/p/U200-G2K>. Retrieved on 2021-10-27.
- [161] <https://www.thorlabs.com/thorproduct.cfm?partnumber=AL4532-A>. Retrieved on 2021-12-09.
- [162] Chi Huan Nguyen. *Single atoms coupled to a near-concentric cavity*. PhD thesis, National University of Singapore, 2018.
- [163] https://docs.scipy.org/doc/scipy/reference/generated/scipy.optimize.curve_fit.html. , Retrieved on 2021-11-15.
- [164] Kai K. Voges. *An Ultracold Gas of Bosonic $^{23}\text{Na}^{39}\text{K}$ Ground-State Molecules*. PhD thesis, Leibniz Universität Hannover, 2020.
- [165] R. V. Pound. Electronic Frequency Stabilization of Microwave Oscillators. *Review of Scientific Instruments*, 17(11):490–505, 1946.

- [166] R. W. P. Drever, J. L. Hall, F. V. Kowalski, J. Hough, G. M. Ford, A. J. Munley, and H. Ward. Laser phase and frequency stabilization using an optical resonator. *Applied Physics B*, 31:97–105, Jun 1983.
- [167] Eric D. Black. An introduction to Pound–Drever–Hall laser frequency stabilization. *American Journal of Physics*, 69(1):79–87, 2001.
- [168] <https://www.qubig.com/products/electro-optic-modulators-230/phase-modulators.html>. Retrieved on 2021-12-04.
- [169] <http://www.eqphotonics.de/cms/deutsch/produkte/54,ao---modulatoren-und-frequenzschieber.html?idapp=5&idprdgrp=19>. Retrieved on 2021-12-04.
- [170] <https://www.meadowlark.com/small-512-512-spatial-light-modulator-p-139?mid=18>. Retrieved on 2021-12-04.
- [171] Alicia J Kollár, Alexander T Papageorge, Kristian Baumann, Michael A Armen, and Benjamin L Lev. An adjustable-length cavity and Bose–Einstein condensate apparatus for multimode cavity QED. *New Journal of Physics*, 17(4):043012, apr 2015.
- [172] Kevin C Cox, David H Meyer, Nathan A Schine, Fredrik K Fatemi, and Paul D Kunz. Increased atom-cavity coupling and stability using a parabolic ring cavity. *Journal of Physics B: Atomic, Molecular and Optical Physics*, 51(19):195002, sep 2018.
- [173] K. Dupraz, K. Cassou, A. Martens, and F. Zomer. The ABCD matrix for parabolic reflectors and its application to astigmatism free four-mirror cavities. *Optics Communications*, 353:178–183, 2015.
- [174] Joachim Erven and Dietrich Schwägerl. *Mathematik für Ingenieure, Oldenbourg Lehrbücher für Ingenieure*. Oldenbourg, München, 2011.

Curriculum Vitae

Personal details

Name	Jannis Schnars
Date of birth	15.12.1992
Place of birth	Bremerhaven
Current address	Beltgens Garten 7 20537 Hamburg

Research

since 08/2019	Doctoral studies at Institute of Quantum Optics University of Hanover Group of Prof. Dr. Silke Ospelkaus
05/2019 - 07/2019	Visiting scientist at Centre of Quantum Technologies National University of Singapore Group of Prof. Dr. Christian Kurtsiefer
04/2017 - 07/2019	Doctoral studies at Institute of Theoretical Physics University of Hanover Group of Prof. Dr. Klemens Hammerer

Education

10/2014 - 03/2017	Master of Science (Physics) University of Hanover
10/2011 - 09/2014	Bachelor of Science (Physics) University of Göttingen
06/2011	Abitur Waldschule Hagen-Beverstedt

Danksagung

Zum Schluss möchte ich mich noch einmal bei allen bedanken, die zum Entstehen dieser Arbeit beigetragen haben.

Zuerst möchte ich mich bei meiner Betreuerin Silke dafür bedanken, dass sie mich in ihrer Gruppe aufgenommen hat und mir die Promotion ermöglicht hat. Für diese Dinge möchte ich auch meinem Zweitgutachter Klemens danken, in dessen Gruppe ich die erste Hälfte meiner Promotionszeit verbringen durfte. Weiterhin möchte ich beiden dafür danken, dass ich auch in privat schwierigen Zeiten viel Verständnis und Unterstützung erfahren habe. Vielen Dank!

Als nächstes möchte ich mich bei Guido Pupillo bedanken, dass er sich die Zeit genommen hat, diese Arbeit als weitere Gutachter zu beurteilen. Christian Kurtsiefer möchte ich danken, dass er mich zeitweise bei seiner Gruppe in Singapur aufgenommen hat. Was ich im Labor dort über Resonatoren gelernt habe, hat mir viele Impulse für diese Arbeit gegeben.

Weiterhin möchte ich sämtlichen Kollegen danken, die mich während meiner Promotion und teilweise bereits davor begleitet haben. Alessandro und Leon danke ich, dass diese immer ein offenes Ohr für mich hatten und mir oft mit Ihren Ideen und Vorschlägen weiterhelfen konnten. Bei Torben und Torsten möchte ich mich für ihre Hilfe bei den diversen Problemen bedanken, die während der Promotion aufgetreten sind. Kai, der mich bereits während meiner Masterarbeit betreut hat, danke ich für seine Geduld bei den unzähligen Fragen mit denen ich ihn bombardiert habe. Auch Philipp, mit dem ich zeitgleich als Masterand in der POLAR Gruppe angefangen habe, danke ich, dass er mir bei vielen Problemen weiterhelfen konnte. Dieser Dank geht auch an die "jüngste" Generation an Doktoranden, Mara, Jule und Jakob. Neben den ganzen Hilfestellungen möchte ich euch allen aber auch für die vielen schönen Momente sowohl bei der Arbeit als auch nach Feierabend danken. Ob nun als frisch ernannter U-Boot Kapitän oder Mr. Monday, es war mir immer eine große Freude zur Arbeit zu kommen. Daher sehe ich auch über gelegentliche Bombardierungen mit zehn Stunden Versionen von "Taking the Hobbits to Isengard" hinweg...

Natürlich gab es diese schönen Momente nicht nur mit der POLAR Gruppe. Auch den übrigen Postdocs und Doktoranden von Silke, Mirco, Supeng, Maurice, Paul, Mariia, Timo, Julius, Erik, Julia und Wuying, danke ich für viele tolle Gespräche und Erlebnisse. Auch der Gruppe von Klemens, die mich zu Beginn meiner Promotion so freundlich aufgenommen hat, gilt mein Dank. Vielen Dank dafür an Sahand, Jonas, Alexander, Ondrej, Marius, Victor, Corentin, Kasper, Jan-Niclas und Florian. Ich habe meine Zeit bei euch in der Gruppe sehr genossen. Ein weiterer Dank gilt der gesamten Kurtsiefer-Gruppe in Singapur, die mich ebenfalls sehr freundlich bei sich aufgenommen und auch diese aufregende Stadt gezeigt haben. Ein besonderes Danke schön möchte ich dabei an Adrian ausrichten, von dem ich während meiner Zeit in Singapur nicht nur viel über beinahe-instabile Resonatoren gelernt habe, sondern den ich auch hinterher mit unzähligen Fragen löchern durfte.

Die Entstehung einer Doktorarbeit ist außerdem nur möglich, wenn auch der gesamte Universitätsbetrieb an sich läuft. Daher geht auch ein großer Dank an die verschiedenen Sekretariate, mit denen ich während meiner Promotion zu tun hatte. Vielen Dank an Birgit Gemmeke, Birgit Ohlendorf, Elke Hünitzsch und Stephanie Kaisik für eure Hilfe und das

ihr mir in meiner Zerstreutheit so oft zur Seite standet. Ebenfalls möchte ich der Werkstatt des IQO meinen Dank für die diversen Komponenten aussprechen, die für mich angefertigt wurden. Auch der technischen Leitung des HITEC möchte ich in Person von Tobias Froböse danken, für diverse Hilfestellungen während der Schlussphase meiner Promotion.

Zu guter Letzt möchte ich mich bei meiner Familie für all die Unterstützung bedanken, die ich in den vergangenen Jahren erhalten habe. Meinen Eltern, Silke und **Dr.** Ulf, danke ich dafür, dass sie mir überhaupt meine Ausbildung erst ermöglicht haben und auch bei sonstigen Problemen immer für mich da waren. Auch meiner Schwester, Lena, danke ich für die vielen schönen Momente, die wir zusammen erlebt haben. Dafür möchte ich auch meinen Schwiegereltern, Susanne und Michael, danken und auch dafür, dass sie ein so aufrichtiges Interesse an meiner Arbeit gezeigt haben. Auch meinem Schwager, Johannes, sowie Nico und Sabine möchte ich für unsere tolle gemeinsame Zeit danken. Und ein weiteres riesiges Danke gilt meiner Frau Regina. Vielen Dank, dass du immer an mich geglaubt hast, mich so oft bestärkt hast, wenn ich an mir selber gezweifelt habe und mir so oft den Rücken freigehalten hast, damit ich diese Arbeit überhaupt schreiben konnte. Danke, für alles was du für mich getan hast und auch noch tust. Der letzte Dank dieser Arbeit gilt meinem Sohn Mattis. Vielen Dank für unser gemeinsames Leben. Und vielen Dank, dass du mich jeden Tag so freudig anstrahlst.